ARISTOTLE UNIVERSITY OF THESSALONIKI
SCHOOL OF GEOLOGY
DEPARTMENT OF METEOROLOGY AND CLIMATOLOGY

ALKIVIADIS KALISORAS
Geologist

CLIMATE RESPONSES DUE TO ANTHROPOGENIC AEROSOLS RADIATIVE FORCING

MASTER THESIS

POSTGRADUATE STUDIES PROGRAMME
‘Meteorology, Climatology and Atmospheric Environment’

THESSALONIKI
2021

ALKIVIADIS KALISORAS
ΑΛΚΙΒΙΑΔΗΣ ΚΑΛΗΣΩΡΑΣ
Πτυχιούχος Γεωλόγος

CLIMATE RESPONSES DUE TO ANTHROPOGENIC AEROSOLS RADIATIVE FORCING

ΚΛΙΜΑΤΙΚΗ ΑΠΟΚΡΙΣΗ ΛΟΓΩ ΕΞΑΝΑΓΚΑΣΜΟΥ ΤΟΥ ΙΣΟΖΥΓΙΟΥ ΑΚΤΙΝΟΒΟΛΙΑΣ ΑΠΟ ΑΝΘΡΩΠΟΓΕΝΗ ΑΕΡΟΖΟΛ

Υποβλήθηκε στο Τμήμα Γεωλογίας στα πλαίσια του Προγράμματος Μεταπτυχιακών Σπουδών ‘Μετεωρολογία, Κλιματολογία και Ατμοσφαιρικό Περιβάλλον’

Ημερομηνία Προφορικής Εξέτασης: 1/11/2021
Oral Examination Date: 1/11/2021

Three-member Examining Board

Professor Zanis Prodromos, School of Geology, A.U.Th., Supervisor
Professor Balis Dimitrios, School of Physics, A.U.Th., Member
Associate Professor Tolika Konstantia, School of Geology, A.U.Th., Member

Τριμελής Εξεταστική Επιτροπή

Καθηγητής Ζάνης Πρόδρομος, Τμήμα Γεωλογίας, Α.Π.Θ., Επιβλέπων
Καθηγητής Μπαλής Δημήτριος, Τμήμα Φυσικής, Α.Π.Θ., Μέλος Τριμελούς Εξεταστικής Επιτροπής
Αναπληρώτρια Καθηγήτρια Τολίκα Κωνσταντία, Τμήμα Γεωλογίας, Α.Π.Θ., Μέλος Τριμελούς Εξεταστικής Επιτροπής

CLIMATE RESPONSES DUE TO ANTHROPOGENIC AEROSOLS RADIATIVE FORCING – *Master Thesis*

ΚΛΙΜΑΤΙΚΗ ΑΠΟΚΡΙΣΗ ΛΟΓΩ ΕΞΑΝΑΓΚΑΣΜΟΥ ΤΟΥ ΙΣΟΖΥΓΙΟΥ ΑΚΤΙΝΟΒΟΛΙΑΣ ΑΠΟ ΑΝΘΡΩΠΟΓΕΝΗ ΑΕΡΟΖΟΛ – *Μεταπτυχιακή Διπλωματική Εργασία*

<u>Citation</u>:
Kalisoras A., 2021. – Climate responses due to anthropogenic aerosols radiative forcing. Master Thesis, School of Geology, Aristotle University of Thessaloniki, 114 pp.
Καλησώρας Α., 2021. – Κλιματική απόκριση λόγω εξαναγκασμού του ισοζυγίου ακτινοβολίας από ανθρωπογενή αεροζόλ. Μεταπτυχιακή Διπλωματική Εργασία, Τμήμα Γεωλογίας Α.Π.Θ., 114 σελ.

To my parents,
Maria and Theologos

PREFACE

In the current thesis, the fast climate responses caused by present-day anthropogenic aerosols are studied using simulations from five climate models participating in the sixth phase of the Coupled Model Intercomparison Project (CMIP6). This research was conducted within the frame of the postgraduate studies programme “Meteorology, Climatology, and Atmospheric Environment” of School of Geology, of the Aristotle University of Thessaloniki (A.U.Th.).

In the first chapter, information about atmospheric aerosols, climate change, and the concept and calculation of radiative forcing are presented. The second chapter describes the climate models and simulations used in this thesis, along with the method implemented in order to calculate the radiative forcing and the rapid temperature responses. In the third chapter, the obtained results are discussed on an annual and seasonal basis, and the fourth chapter contains a summary of the results and the conclusions.

I would like to thank my supervisor, Professor Zanis Prodromos, for all these years of mentoring and support, ever since I was an undergraduate student. I would also like to thank Professor Balis Dimitrios and Associate Professor Tolika Konstantia for their insights and for being members of my examination committee. Many thanks go to Dr. Aristeidis K. Georgoulias, postdoctoral researcher at the Department of Meteorology and Climatology, School of Geology, A.U.Th., for helping me download and process the data, calculate the radiative forcing, produce most of the figures, and improve the text. Also, I would like to thank the rest of the Academic and Laboratory Teaching Staff of the Department of Meteorology and Climatology for their efforts, especially during the pandemic. Last but definitely not least, I would like to thank my family and friends, for their support over the years.

CONTENTS

ABSTRACT (ENGLISH)

In this study, the rapid climate responses caused by anthropogenic aerosol radiative forcing are examined. Using 30-year simulations with fixed sea surface temperatures (SSTs) and sea ice cover from five climate models participating in the sixth phase of the Coupled Model Intercomparison Project (CMIP6), the effective radiative forcing (ERF) and surface air temperature response to anthropogenic aerosols are estimated on an annual and seasonal basis. The fixed-SST ERF, which allows for tropospheric, stratospheric and some land surface properties to adjust, is calculated for black carbon (BC), organic carbon (OC), and sulphate aerosols (SO_4) following the method of Ghan (2013). Considering all aerosols (sulphate, BC and OC), the global multi-model mean annual ERF, ERFari (due to aerosol-radiation interactions), ERFaci (caused by aerosol-cloud interactions), and ERFalb (induced by surface albedo changes) due to present-day anthropogenic aerosols are estimated to be –1.09 (–3.28 to 0.22 in the 5th to 95th percentile range) W m^{-2}, –0.01 (–0.34 to 0.38) W m^{-2}, –1.11 (–3.42 to 0.46) W m^{-2}, and 0.03 (–1.46 to 0.47) W m^{-2}, respectively, with a global mean annual near-surface cooling of –0.03 (–0.22 to 0.18) ^{o}C. Aerosols mainly scatter incoming solar radiation and serve as cloud condensation nuclei (CCN), thus increasing the cloud albedo and lifetime, resulting in more solar radiation being reflected back to space. Therefore, they induce a negative radiative forcing at the top of the atmosphere (TOA) and cool the Earth's surface. The negative TOA forcing and cooling is predominantly observed in the Northern hemisphere (NH), especially over the emission sources, such as the industrialized areas of East Asia, the continental South Asia, Europe and North America. Sulphate aerosols strongly scatter incoming shortwave (SW) solar radiation, causing a negative ERF and a near-surface cooling, in general, and over its emission sources, in particular. For SO_4 aerosols the multi-model global mean annual ERF, ERFari, ERFaci, and ERFalb are estimated to be –1.10 (–3.32 to 0.21) W m^{-2}, –0.27 (–0.79 to 0.00) W m^{-2}, –0.84 (–2.85 to 0.58) W m^{-2}, and 0.01 (–1.52 to 0.47) W m^{-2}, respectively, with a global mean annual cooling of –0.04 (–0.27 to 0.15) ^{o}C, concentrated over the NH, while the Arctic experiences a near-surface warming. OC mainly scatters the incoming solar radiation, exerting a negative ERF and has a cooling effect on the climate system, with a spatial pattern similar to SO_4, but weaker in magnitude. For OC the global mean annual ERF, ERFari, ERFaci, and ERFalb are –0.35 (–1.34 to 0.43) W m^{-2}, –0.07 (–0.25 to 0.03) W m^{-2}, –0.29 (–1.17 to 0.41) W m^{-2}, and 0.01 (–0.44 to 0.27) W m^{-2}, respectively, and the surface air temperature response is –0.01 (–0.14 to 0.06) ^{o}C. On the other hand, BC aerosols strongly absorb solar radiation, directly and indirectly, causing a general near-surface warming. For BC the annual global mean ERF, ERFari, ERFaci, and ERFalb are estimated to be 0.18 (–0.58 to 1.20) W m^{-2}, 0.38 (0.07 to 1.03) W m^{-2}, –0.22 (–1.00 to 0.38) W m^{-2}, and 0.02 (–0.35 to 0.62) W m^{-2}, respectively, with a corresponding warming of 0.02 (–0.10 to 0.16) ^{o}C on a global scale. On a seasonal basis, both the magnitude and spatial patterns of both the ERF and surface air temperature responses vary from the mean annual state, mainly over the NH during the boreal winter and the boreal summer. There are also differences in the magnitude and the spatial patterns of

ERF, and the fast response or rapid adjustments of temperature among models, deriving from differences in their aerosol chemistry, atmospheric chemistry and processes, and land surface properties parameterization schemes.

ABSTRACT (GREEK)

Στην παρούσα εργασία, μελετώνται οι ταχείες κλιματικές αποκρίσεις που προκαλούνται από τις μεταβολές του ισοζυγίου ακτινοβολίας εξαιτίας των ανθρωπογενών ατμοσφαιρικών αιωρημάτων (αιωρούμενα σωματίδια - ΑΣ ή αεροζόλ). Χρησιμοποιώντας σετ 30-ετών προσομοιώσεων, στις οποίες οι θερμοκρασίες της θαλάσσιας επιφάνειας (ΘΘΕ) και ο θαλάσσιος πάγος διατηρούνται σταθερά, από πέντε κλιματικά μοντέλα που συμμετέχουν στην έκτη φάση του Coupled Model Intercomparison Project (CMIP6), εκτιμάται, σε ετήσιο και εποχικό επίπεδο, ο θερμικός εξαναγκασμός (effective radiative forcing - ERF) και οι αποκρίσεις της θερμοκρασίας του επιφανειακού αέρα που οφείλονται στα ανθρωπογενή αεροζόλ. Το ERF με σταθερές ΘΘΕ, το οποίο επιτρέπει την προσαρμογή των τροποσφαιρικών, στρατοσφαιρικών και κάποιων εδαφικών μεταβλητών, υπολογίζεται για τα ΑΣ του μαύρου άνθρακα (black carbon - BC) και του οργανικού άνθρακα (organic carbon - OC) και για τα θειικά ΑΣ (sulphates – SO_4) ακολουθώντας τη μέθοδο του Ghan (2013). Οι μέσες ετήσιες τιμές του συνόλου των μοντέλων για το ERF, το ERFari (λόγω των αλληλεπιδράσεων μεταξύ ΑΣ και ακτινοβολίας), το ERFaci (εξαιτίας των αλληλεπιδράσεων ανάμεσα στα ΑΣ και τα νέφη) και το ERFalb (που προκαλείται κυρίως από αλλαγές στην επιφανειακή ανακλαστικότητα) εξαιτίας των σημερινών ανθρωπογενών ΑΣ είναι –1.09 (–3.28 με 0.22 στο εύρος τιμών μεταξύ του $5^{ου}$ και του $95^{ου}$ εκατοστημορίου) W m^{-2}, –0.01 (–0.34 με 0.38) W m^{-2}, –1.11 (–3.42 με 0.46) W m^{-2} και 0.03 (–1.46 με 0.47) W m^{-2}, αντιστοίχως, με επακόλουθη μέση ετήσια επιφανειακή ψύξη της τάξης των –0.03 (–0.22 με 0.18) ^{o}C σε παγκόσμιο επίπεδο. Τα ατμοσφαιρικά αιωρήματα, κατά βάση, σκεδάζουν την εισερχόμενη ηλιακή ακτινοβολία και λειτουργούν ως πυρήνες συμπύκνωσης νεφών, αυξάνοντας, τοιουτοτρόπως, την ανακλαστικότητα και το χρόνο ζωής των νεφών, με αποτέλεσμα την ανάκλαση μεγαλύτερης ποσότητας ηλιακής ακτινοβολίας πίσω στο διάστημα. Ως εκ τούτου, προκαλούν έναν αρνητικό εξαναγκασμό στην κορυφή της ατμόσφαιρας (ΚτΑ) και ψύχουν τη γήινη επιφάνεια. Ο αρνητικός εξαναγκασμός στην ΚτΑ και η ψύξη παρατηρούνται, κατά κύριο λόγο, στο Βόρειο ημισφαίριο (ΒΗ) και ιδιαιτέρως άνωθεν των πηγών εκπομπών, όπως οι βιομηχανοποιημένες περιοχές της Α. Ασίας, της ηπειρωτικής Ν. Ασίας, της Ευρώπης και της Β. Αμερικής. Τα θειικά ΑΣ σκεδάζουν ισχυρά την εισερχόμενη μικρού μήκους κύματος ηλιακή ακτινοβολία, προκαλώντας έναν αρνητικό εξαναγκασμό και ψύξη του επιφανειακού αέρα, ιδιαίτερα στις πηγές εκπομπών του. Σε παγκόσμια βάση, οι μέσες ετήσιες τιμές των ERF, ERFari, ERFaci και ERFalb υπολογίζονται στα –1.10 (–3.32 με 0.21) W m^{-2}, –0.27 (–0.79 με 0.00) W m^{-2}, –0.84 (–2.85 με 0.58) W m^{-2} και 0.01 (–1.52 με 0.47) W m^{-2}, αντιστοίχως, με μια μέση ετήσια ψύξη στους –0.04 (–0.27 με 0.15) ^{o}C, εστιασμένη στο ΒΗ, με την Αρκτική να υπόκειται σε θέρμανση. Τα σωματίδια OC κυρίως σκεδάζουν την εισερχόμενη ηλιακή ακτινοβολία, ασκώντας έναν αρνητικό εξαναγκασμό προκαλώντας ψύξη του κλιματικού συστήματος, με χωρική κατανομή παρόμοια με αυτή των SO_4, αλλά μικρότερης ισχύος. Οι μέσες ετήσιες τιμές των ERF, ERFari, ERFaci και ERFalb είναι –0.35 (–1.34 με 0.43) W m^{-2}, –0.07 (–0.25 με 0.03) W m^{-2}, –0.29 (–1.17 με 0.41) W m^{-2} και 0.01 (–0.44 με 0.27) W m^{-2}, αντιστοίχως, με την απόκριση της θερμοκρασίας του επιφανειακού αέρα να είναι στους –0.01 (–0.14 με 0.06) ^{o}C. Αντιθέτως, τα ΑΣ του BC απορροφούν ισχυρά την ηλιακή ακτινοβολία, άμεσα και έμμεσα, προκαλώντας μια γενική θέρμανση του επιφανειακού αέρα στο ΒΗ. Οι ετήσιες μέσες τιμές των ERF, ERFari, ERFaci και ERFalb υπολογίζονται στα 0.18 (–0.58 με 1.20) W m^{-2}, 0.38 (0.07 με 1.03) W m^{-2}, –0.22 (–1.00 με 0.38) W m^{-2} και 0.02 (–0.35 to 0.62) W m^{-2}, αντίστοιχα, με μια σύμφωνη θέρμανση της τάξης των 0.02 (–0.10 με 0.16) ^{o}C σε παγκόσμια κλίμακα. Σε εποχική βάση, το μέγεθος και η χωρική κατανομή αμφότερων των ERF και των αποκρίσεων της θερμοκρασίας του επιφανειακού αέρα διαφοροποιούνται από τη μέση ετήσια κατάσταση, κυρίως στο ΒΗ κατά το χειμώνα και το θέρος του ΒΗ. Υπάρχουν, επίσης, διαφορές στην ισχύ και τα χωρικά μοτίβα του ERF και των ταχέων θερμοκρασιακών αποκρίσεων μεταξύ των μοντέλων, οι οποίες προέρχονται από τις διαφορές στα σχήματα παραμετροποιήσεών τους για τη χημεία των αεροζόλ, την ατμοσφαιρική χημεία και τις διαδικασίες της ατμόσφαιρας, καθώς και τις ιδιότητες της επιφάνειας του εδάφους.

CHAPTER 1: INTRODUCTION

1.1 Climate Change and Climate Drivers

1.1.1 The Earth's Radiative Budget

Climate is commonly defined as the average weather, or more precisely, as the statistical description with regard to the mean value and the variability of relevant quantities (typically surface variables such as temperature, precipitation and wind) over a period of time that ranges from months to thousands or millions of years (*Cubasch et al., 2013*). Typically, the period for averaging these variables is 30 years, as defined by the World Meteorological Organization (WMO). Climate change is referred to a change in the state of the climate system that can be identified by statistically significant changes in the mean and/or the variability of its properties, and that persists for an extended period of time (decades or longer) (*Cubasch et al., 2013*; *Hartmann et al., 2013*).

The climate system basically gains its energy from the Sun, as the incident solar radiation drives the climate system and atmospheric chemistry (*Ramanathan and Feng, 2009*). A portion of the incoming solar shortwave (SW) radiation is reflected back to space by air molecules (Rayleigh scattering), aerosols, clouds and by the Earth's surface, whereas the rest is absorbed by the surface, and atmospheric gases and absorbing aerosols (*Cubasch et al., 2013*; *Ramanathan and Feng, 2009*). The absorbed radiation heats the surface and the atmosphere, resulting in the emission of the energy they gained as infrared or longwave (LW) radiation (*Ramanathan and Feng, 2009*). The emitted LW radiation from the Earth's surface is mainly absorbed by greenhouse gases (GHGs), clouds and some large aerosols, all of which also emit LW towards every direction (*Cubasch et al., 2013*; *Ramanathan and Feng, 2009*).

The Earth's radiation budget is a key element of the climate system (*Hartmann et al., 2013*). One would expect the radiative energy budget of the Earth to be in balance, with the incoming radiative fluxes balancing the outgoing radiative fluxes, thus keeping the heat content of the Earth constant at steady state when averaged over a long period of time (*Bellouin et al., 2020*). However, satellite measurements suggest that there is a small positive imbalance (*Cubasch et al., 2013*), meaning that the planetary system has an excess of energy. Consequently, the Earth system gets rid of this energy surplus by warming and thus emitting greater amounts of infrared radiation, until the excess energy is released back to space and the surface–atmosphere system returns to balance (*Ramanathan and Feng, 2009*). This rationale is the physical basis of the greenhouse effect and the global warming.

The radiative balance between the net incoming solar shortwave radiation (downward solar energy minus the reflected) and the outgoing longwave radiation is influenced by global climate "drivers" (*Cubasch et al., 2013*), which are attributed to natural and anthropogenic processes (Fig. 1.1). Perturbations in the net incoming solar radiation arise from changes in solar radiative output, variations in Earth's astronomical parameters or changes in the reflectivity (albedo) of the Earth (*Cubasch et al., 2013*; *Bellouin et al., 2020*), while perturbations in the outgoing LW radiation come from changes in Earth's atmospheric and surface temperature or changes in the amount of infrared radiation emitted from the Earth's surface or atmosphere (*Cubasch et al., 2013*).

1.1.2 Climate Drivers

As far as the atmosphere is concerned, emissivity changes occur predominantly due to changes in GHG and aerosol concentrations and in cloud micro- and macro-physical properties and cloud cover. Greenhouse gases – primarily water vapour (H_2O), carbon dioxide (CO_2), nitrous oxide (N_2O), methane (CH_4), ozone (O_3), and halocarbons – absorb LW radiation at particular wavelengths within the spectrum of the radiation emitted by the Earth's atmosphere and surface, and by clouds, and emit it towards all directions, adding heat to the lower atmosphere and the surface and amplifying the greenhouse effect (*Cubasch et al., 2013*; *IPCC, 2013*).

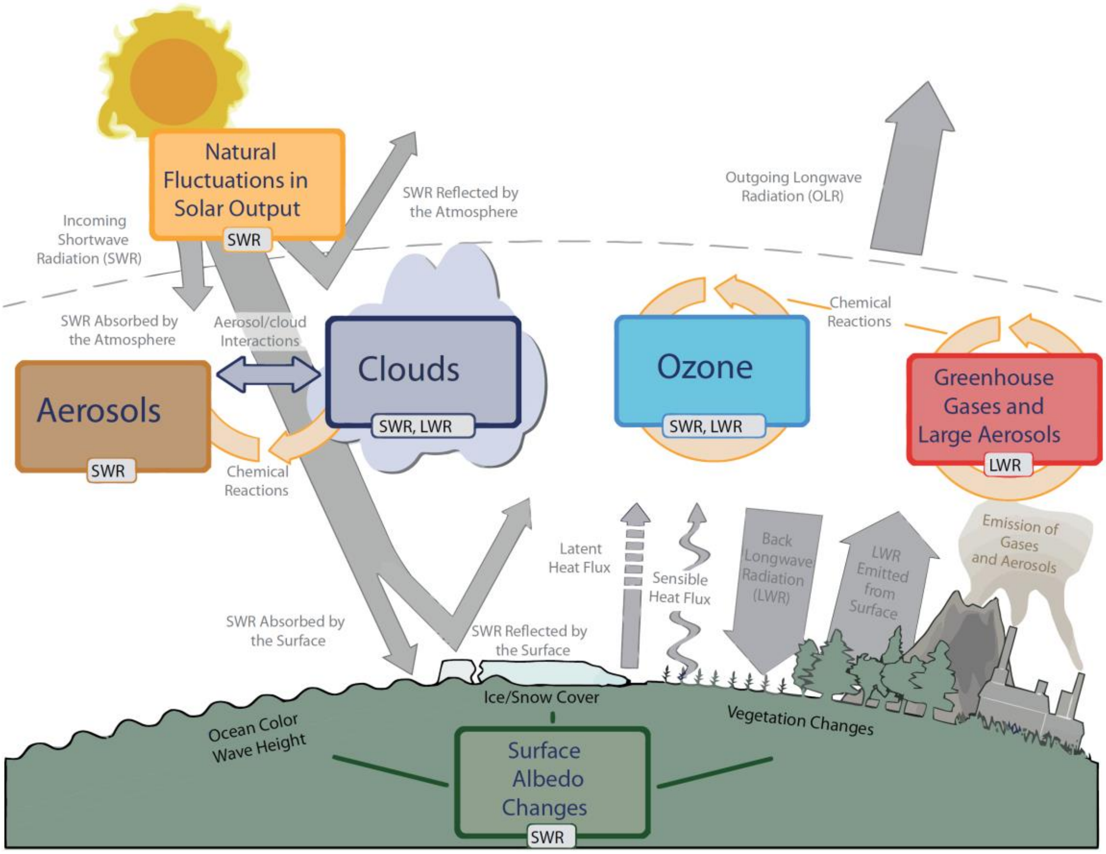

Figure 1.1. The main drivers of climate change. Global climate "drivers" influence the radiative balance between incoming SW radiation and outgoing LW radiation. Natural fluctuations in solar output (solar cycles), changes in GHG and aerosol concentrations and emissions, in cloud cover and cloud microphysical properties, and in surface albedo (changes in land surface properties or vegetation, snow or ice cover and ocean colour can cause perturbations in the energy balance of the Earth [Figure taken from *Cubasch et al., 2013*].

Water vapour (H_2O) is the foremost GHG in the atmosphere and the principal contributor to the natural greenhouse effect, but its quantity is regulated mainly by air temperature, rather than by emissions. Due to that fact, H_2O typically resides for about ten days in the atmosphere. Anthropogenic sources of water vapour have an insignificant contribution to its overall tropospheric concentrations (*Myhre et al., 2013*). On the other hand, many GHGs, such as CO_2, N_2O, CH_4, and numerous halogenated species, are adequately mixed throughout the troposphere and hence are called well-mixed greenhouse gases (WMGHGs) because their lifetimes in the atmosphere are much greater than the time scale of a few years for atmospheric mixing and are referred to as "long-lived greenhouse gases". Many WMGHGs have significant anthropogenic sources (CO_2, CH_4, N_2O), whereas others are entirely man-made, like chlorofluorocarbons (CFCs), hydrochlorofluorocarbons (HCFCs), hydrofluorocarbons (HFCs) and other chlorine- and bromine-containing substances (*Myhre et al., 2013*; *IPCC, 2013*). Carbon dioxide occurs naturally, but is also a by-product of fossil fuel and biomass burning, of industrial processes and of land use changes. Methane is the main component of natural gas and is linked with all hydrocarbon fuels, livestock breeding and agriculture. Nitrous oxide is naturally produced from numerous biological processes (e.g., microbial action), but its major anthropogenic emissions are agricultural and soil sources, along with sewage treatment, fossil fuel combustion and chemical industry (*IPCC, 2013*; *Myhre et al., 2013*). Halocarbons are powerful GHGs that absorb and emit radiation in the 8–12 μm region (atmospheric window), while many of which deplete the stratospheric ozone (especially the ones containing chlorine and bromine). CFCs were used as refrigerants and propellants in deodorizers, drug delivery pumps etc., and can be destroyed through photolysis in the stratosphere (*Myhre et al., 2013*; *Ramanathan and Feng, 2009*).

Along with WMGHGs, there is another group of compounds that are defined as "near-term climate forcers" (NTCFs) or "short-lived climate forcers" (SLCFs). SLCFs are a set of chemically reactive compounds that impact the climate system mainly within the first two decades years following their emission or formation, and most of them have relatively short atmospheric lifetimes (from hours to decades) compared to WMGHGs (hence "short-lived"). SLCFs do not accumulate in the atmosphere at long time scales, with their effect on the climate system being primarily in the near term after their emission. SLCFs include CH_4 (which is also a WMGHG), O_3 and aerosols, or their precursors, and some halogenated species that are not considered WMGHGs (*Myhre et al., 2013*; *IPCC, 2013*). Tropospheric O_3 is created both naturally and by photochemical reactions as a by-product of the oxidation of carbon monoxide (CO), methane, and non-methane hydrocarbons in the presence of nitrogen oxides (NO_x), acts as a GHG and is considered a pollutant, while stratospheric O_3 is created by the interaction between solar ultraviolet (UV) radiation and molecular oxygen (O_2) and its concentration is greatest from about 12 to 40 km above the surface of the Earth, with a maximum between about 20 and 25 km (*IPCC, 2013*; *Myhre et al., 2013*).

Aerosols, the main consideration in this thesis, are a suspension of airborne solid or liquid particles, having a size that ranges from a few nanometres to tens of micrometres, remaining in the atmosphere for at least several hours (*IPCC, 2013*; *Myhre et al., 2013*). Atmospheric particles have natural or anthropogenic sources and originate from two distinct pathways: they are either emitted directly in the liquid or solid phase (primary aerosols) or they are formed in the atmosphere through chemical reactions with gaseous precursors (secondary aerosols) (*Myhre et al., 2013*; *Boucher et al., 2013*; *Bellouin et al., 2020*). Inorganic sea salt, mineral dust, black carbon (BC) and primary biological aerosol particles (PBAPs) are considered primary aerosols, whereas inorganic species like non-sea-salt sulphate (SO_4), ammonium (NH_4) and nitrate (NO_3) mainly occur from secondary aerosol formation processes, as they are the products of reactions which involve sulphur dioxide (SO_2), ammonia (NH_3), and nitric oxide (NO) emissions (*Myhre et al., 2013*; *Boucher et al., 2013*). The term "organic aerosol" (OA) indicates carbon-containing compounds that include hydrogen and, usually, oxygen (*Bond et al., 2013*). OAs have important primary (primary organic aerosols – POAs) and secondary (secondary organic aerosols – SOAs) sources (*Boucher et al., 2013*). POAs originate from both anthropogenic (i.e., fossil fuel and biomass burning) and natural sources (like debris, spores, pollen or algae) (*Haywood and Boucher, 2000*). The majority of BC, SO_4, NO_3 and NH_4 have anthropogenic sources, while sea salt, major part of mineral dust and PBAPs originate mainly from natural sources (*Boucher et al., 2013*). Aerosols typically remain in the troposphere for a few days up to a week and have high spatio-temporal variation due to spatially inhomogeneous distribution of emission sources and to relatively rapid removal processes, such as direct deposition to the surface (dry deposition) or washout through precipitation (wet deposition) (*Bellouin et al., 2020*; *Haywood and Boucher, 2000*).

Sea spray particles are created at sea surface when bubbles burst, mostly, by breaking waves and are composed of sea salt and marine POA, the emission rate of the latter depending on the biological activities in oceanic regions (*Boucher et al., 2013*). SOAs originate from biogenic and anthropogenic sources, and result from chemical reactions of non-CH_4 hydrocarbons with the hydroxyl radical (OH), O_3, NO_3 or photolysis (*Boucher et al., 2013*; *Myhre et al., 2013*; *Hallquist et al., 2009*). Land sources of PBAPs are bacteria, pollen, lichen, fungal spores, viruses and fragments of plants and animals (*Després et al., 2012*). Mineral dust is principally released from the effects of wind erosion over deserts or other arid regions and from agricultural and industrial processes (*Boucher et al., 2013*; *Haywood and Boucher, 2000*). The main natural sources of sulphate are volcanoes (chemical conversion of gaseous SO_2 emissions; *Kasoar et al., 2016*) and from dimethylsulphide (DMS) emitted by the oceans, while SO_4 aerosol particles can form from the oxidation of SO_2 from fossil fuel burning (the main anthropogenic source; biomass burning is a relatively small contributor) and other sulphur gases from natural and anthropogenic sources (*Boucher et al., 2013*; *Haywood and Boucher, 2000*).

Black carbon (BC) is a characteristic carbonaceous material with unique physical properties that is formed mainly in flames during combustion of carbon-based fuels and is directly emitted along with other aerosols and aerosol precursor gases to the atmosphere of the Earth (*Bond et al., 2013*). It is heat resistant with a vaporization temperature near 4000 K and it is found as an aggregate of small carbon spherules that were formed in flames and rapidly coagulated, being also insoluble in water and most organic solvents (*Bond et al., 2013*; *Boucher et al., 2013*). The major sources of BC are industry, diesel engines, residential solid fuel, and open burning, especially of forests and savannas, which emit the greatest quantities globally (although there is significant uncertainty in estimating emission sources and regions due to lack of data availability). Other activities like aviation, shipping, and flaring account for a small fraction of BC emissions. BC is mostly concentrated around source regions, while it can be transported regionally and over continents during its short residence time in the atmosphere (*Bond et al., 2013*; *Ramanathan and Carmichael, 2008*). As a result, it can be found in remote regions at lower concentrations than in source regions (e.g. in the Arctic from emissions predominantly at mid-latitudes which are transported northwards; *Sand et al., 2013*). Black carbon is removed from the atmosphere within a few days to weeks through wet or dry deposition (i.e., precipitation and contact with surfaces) (*Bond et al., 2013*). All BC-emitting sources also emit POAs, along with gases which may later become SOAs in the atmosphere. Organic carbon (OC) is referred to the carbon mass included in organic aerosol particles, without considering the associated hydrogen and oxygen content, and can be emitted either as primary aerosol and by secondary formation from gaseous compounds (*Bond et al., 2013*; *Haywood and Boucher, 2000*). OC aerosols are co-emitted with BC and have approximately the same atmospheric lifetime (*Hodnebrog et al., 2016*). The mass ratio between organic aerosol and organic carbon (OA/OC) relies on the amount of oxygen that is included inside the organic molecules, with its values depending on the combustion source. When the source is coal or diesel OA/OC has lower values, whereas in the case of biomass combustion the mass ratio has higher values (*Bond et al., 2013*).

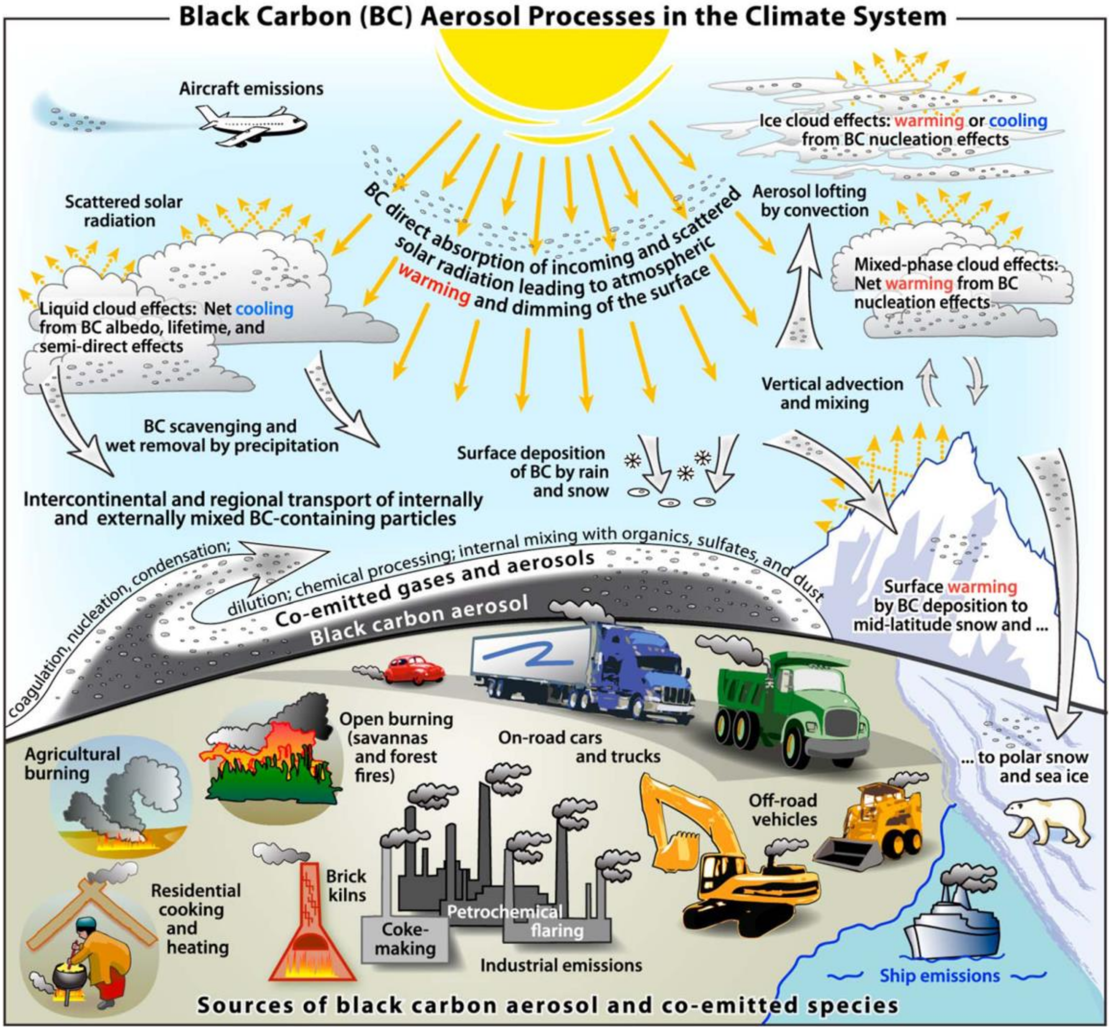

Figure 1.2. An overview of the main BC emission sources and the processes responsible for its spatial distribution in the atmosphere of the Earth [Figure taken from *Bond et al., 2013*].

Aerosol particles modify the Earth's radiative budget in various ways. Directly they absorb and scatter solar SW radiation and, to a lesser extent they absorb, scatter and emit terrestrial LW radiation (aerosol-radiation interactions – ARI) (*Boucher et al., 2013*; *Bellouin et al., 2020*). Anthropogenic aerosols partially offset (or mask) the impact of GHGs by scattering and absorbing incident radiation from the Sun, which results in a reduction of the radiation that reaches the Earth’s surface, thus cooling the surface while heating and stabilizing the atmosphere (*Undorf et al., 2018*; *Ming and Ramaswamy, 2009*).

Indirectly, aerosols modify the microphysical and radiative properties of clouds and affect their reflectivity and persistence, as they can serve as cloud condensation nuclei (CCN) for cloud droplets and ice nuclei (IN) for ice crystals (aerosol-cloud interactions – ACI) (*Boucher et al., 2013*; *Bellouin et al., 2020*; *Haywood and Boucher, 2000*; *Lohmann and Feichter, 2005*; *Rosenfeld et al., 2014a*). The indirect effect of aerosols is typically divided into two effects. The first indirect effect (or cloud albedo effect or Twomey effect) suggests that increased atmospheric concentrations of aerosols cause an increase in droplet concentration and cloud optical thickness due increased number of available CCN, with a subsequent decrease in droplet size (for fixed liquid water content) and an increase of cloud reflectivity (*Twomey, 1974, 1977*). The second indirect effect (or cloud lifetime effect or Albrecht effect) proposes that the reduction in the size of cloud droplets due to increased aerosol concentrations affects the precipitation efficiency, tending to increase the liquid water content, the cloud lifetime (*Albrecht, 1989*), and the cloud thickness (*Pincus and Baker, 1994*). There is also a semi-direct effect of aerosols, whereby aerosol absorption causes atmospheric heating, thus reducing relative humidity and consequently cloud amount (evaporation of clouds or cloud burn–off) and/or liquid water path, increasing surface insolation (*Allen and Sherwood, 2010*).

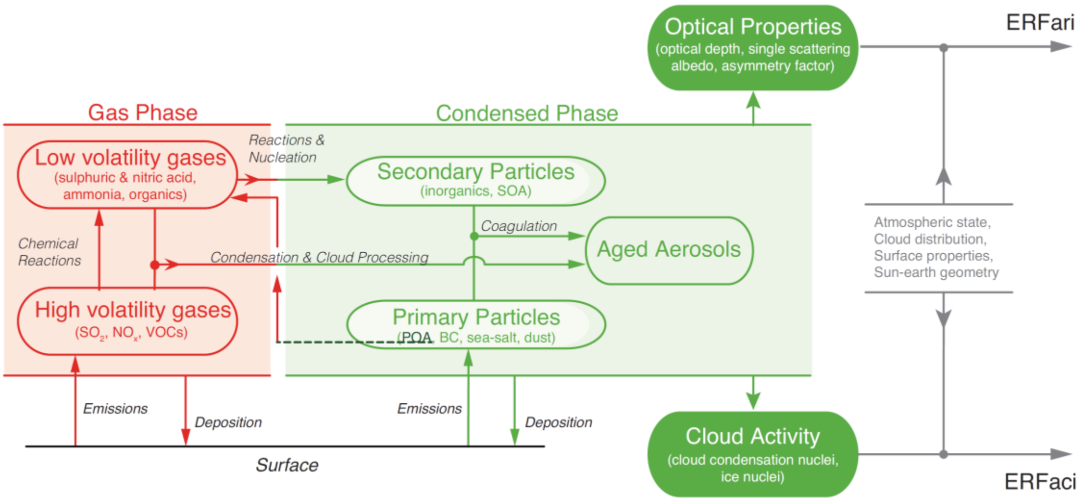

Figure 1.3. An overview of the basic aerosol and environmental processes that affect the interactions between aerosols, radiation and clouds. The red region includes gas-phase variables and processes and the green region encompasses particulate-phase variables and processes. The aerosol processes that result in forcings (ERFari and ERFaci) are described in Section 2.2 [Figure taken from *Boucher et al., 2013*].

Knowledge of ACI is essential for estimating changes in the climate system, as clouds regulate the Earth’s radiation budget to a great degree and have a globally averaged cooling effect on the Earth-atmosphere system at the top of the atmosphere (TOA) (*Lohmann and Feichter, 2005*). ACI are affected by the cloud type and the ability of aerosols to act as CCN or IN, which relies on the aerosols’ number concentration, size distribution, shape, solubility, and surface chemical properties (*Bellouin et al., 2020*). The Twomey and Albrecht effects tend to cool the Earth-atmosphere system through an increase in cloud optical depth and cloud cover, respectively, thus decreasing the net solar radiation at TOA and the surface (*Lohmann and Feichter, 2005*). As a result, aerosols can postpone or stop convection, thus preventing clouds that would reflect more solar radiation to space from forming (*Rosenfeld et al., 2014a*). Aerosols also affect the hydrological cycle by changing the occurrence and frequency of convection, and by reducing evaporation, with the latter resulting in run-off increases and suppressed evapotranspiration. (*Baker et al., 2015*; *Lohmann and Feichter, 2005*). They can generate anomalies in meridional circulation, which reduce the ascent in the northern tropics, create hemispheric temperature gradients and weaken the Hadley circulation (*Ramaswamy et al., 2019*). Aerosols can also affect the surface albedo, as absorbing particles deposited on snow-covered surfaces may decrease their reflectivity (*Bellouin et al., 2020*).

The direct, semi-direct and indirect effects of aerosols, the intensity of which differs among aerosol species (*Barlett et al., 2017*), alter global precipitation patterns, which may vary on a regional level (*Baker et al., 2015*). These effects may interact with each other and with other local, regional or global processes, complicating their impacts on precipitation and clouds (*Barlett et al., 2017*). For instance, the aerosol direct radiative effects can modify clouds by changing the atmospheric heating rate locally, while aerosols serving as CCN and IN influence the composition and radiative properties of clouds, simultaneously affecting precipitation formation mechanisms, which in turn affect the cloud dynamic and radiative properties, with the latter altering the thermal structure that further changes the cloud dynamics (*Rosenfeld et al., 2014a*).

The majority of aerosols predominantly scatter solar SW radiation (*Myhre et al., 2013*), producing a net cooling effect globally (*Liu et al., 2018*). From the aerosol particles of interest here, SO_4 particles strongly scatter incoming solar SW radiation, which subsequently increases the Earth’s albedo and cools the surface. Sulphate aerosols also act as CCN, meaning that they will nucleate additional cloud droplets under supersaturated conditions, a process that increases cloud albedo and again has a cooling effect on the Earth system (*Kasoar et al., 2016*). OAs and OC reflect the incoming solar radiation in general (*Myhre et al., 2013*; *Bond et al., 2013*). Although OC and BC are co-emitted and have quite similar atmospheric lifetimes, OC scatters sunlight to a much greater degree than BC, thus cooling the atmosphere-surface system (*Hodnebrog et al., 2016*; *Boucher et al., 2013*). However, there is a portion of OA compounds that absorbs sunlight and reduces the albedo of snow and ice cover, called absorbing organic carbon or brown carbon (BrC), which is a complex mixture of organic compounds and is emitted along with BC or may originate from local soils (*Bond et al., 2013*).

On the other hand, there are aerosols that absorb solar radiation to various extents, with BC being the most absorbing aerosol particle (*Myhre et al., 2013*). It strongly absorbs visible light at all visible wavelengths (*Bond et al., 2013*). BC absorbs sunlight directly, heating the air around it and reducing the amount of sunlight that reaches the Earth’s surface and is reflected back to space (*Bond et al., 2013*; *Chen et al., 2010*). The BC absorption of direct solar radiation decreases surface insolation, resulting in dimming, which is amplified by direct and indirect effects of non-BC aerosols and can impact atmospheric and surface temperatures and the hydrological cycle on a global and regional scale (*Ramanathan and Carmichael, 2008*; *Ramanathan and Feng, 2009*). Additionally, when BC is situated above a reflective surface (like snow or clouds), it also absorbs the solar radiation that is reflected from that surface (*Bond et al., 2013*), a process with potentially large effect in the Arctic (*Sand et al., 2013*; *Stjern et al., 2019*). BC interaction with solar radiation depends on its altitude and position relative to clouds (*Bond et al., 2013*). When high in the atmosphere, BC absorption considerably enhances as it absorbs the solar radiation reflected by low clouds

(*Ramanathan and Carmichael, 2008*). BC changes the net energy balance at the top of the atmosphere (TOA) more when above a bright reflective surface or cloud layer than over a dark one (*Bond et al., 2013*).

During or shortly after its emission, BC becomes internally mixed with other aerosols (such as sulphates and organic material), which can affect its lifetime in the atmosphere and its ability to act as CCN or IN (*Bond et al., 2013*). Particles consisting of a mixture of BC and non-absorbing, hygroscopic components (e.g., sulphate) absorb more solar radiation than pure BC, but they are removed from the atmosphere via wet deposition faster than unmixed BC (*Chen et al., 2010*). While newly emitted BC particles are hydrophobic and small in size, making them poor CCN, aging of BC (i.e., internal mixing or coating with more soluble/hydrophilic compounds after emission) can enhance its CCN activity (*Bond et al., 2013*). Therefore, BC aerosols can influence the properties and lifetime of clouds through microphysical interactions (indirect effects), and cloud distribution by altering tropospheric stability (*Sand et al., 2013*). Cloud cover is reduced when absorbing aerosols are embedded in the cloud layer (*Boucher et al., 2013*; *Rosenfeld et al., 2014a*), while BC can affect clouds through changes in the atmospheric thermal structure (semi-direct effect), or in the liquid cloud droplet number concentration, ice crystal number concentration, or a combination of the two in mixed-phase clouds (indirect effects), with each of aforementioned processes influencing the cloud albedo and distribution, thus changing the Earth's radiative balance (*Bond et al., 2013*). If BC is set inside cloud droplets, it shows greater absorption than pure or coated BC, resulting in cloud albedo reductions, heating and dissipation of clouds (*Bond et al., 2013*). BC creates a warming effect also when deposited on snow or ice by reducing their surface albedo and thus increasing solar radiation absorption (*Bond et al., 2013*), it contributes to the retreat of the Arctic sea ice and can induce changes to monsoon systems (*Ramanathan and Carmichael, 2008*).

From the above, one can easily understand that aerosols are one of the most important drivers of observed past and projected future climate change (*Voigt et al., 2017*). Currently, climate change is caused by the interaction of climate drivers such as changing concentrations of GHGs and aerosol emissions from anthropogenic and natural sources, among others (*Samset et al., 2016*). Altering the anthropogenic emission rates of aerosols and GHGs can cause perturbations in the radiative budget of the Earth or, in other words, a (radiative) forcing (see Section 1.2). Forcings act on the global mean temperature of the surface through the global radiative (energy) budget (*Boucher et al., 2013*). In response to the imposed forcing agents, which alter the internal energy flows of the climate system, rapid adjustments (or fast responses) may occur in the troposphere (*Boucher et al., 2013*; *Chung and Soden, 2015a*). These responses are generally fast, with the majority of them occurring within a few weeks after the initial perturbation, because they do not operate through changes in the global mean surface temperature, which are slowed down by the high heat capacity of the oceans. On the contrary, climate feedbacks act on longer timescales and are related to changes in variables of the climate system that are mediated by a global mean surface temperature change (*Boucher et al., 2013*); they contribute to amplify or damp the initial radiative perturbation caused by a forcing agent (*Thornhill et al., 2021b*) through changes in climate variables in response to changes in the global mean surface temperature (*Chung and Soden, 2015a*). Therefore, in a broader sense, climate change is the result of responses and feedbacks due to forcings from drivers acting on the climate system globally.

1.1.3 Climate Change Indicators

There are plenty of climate change indicators such as changes in the temperature of the Earth's surface, in the amount of water vapour within the atmosphere, in precipitation amount and rate, in the frequency of severe event occurrence, in glaciers, in land and ocean ice, and in sea level (*Cubasch et al., 2013*). The Intergovernmental Panel on Climate Change (IPCC) in its Fifth Assessment Report (AR5) in 2013 has documented numerous changes in climate variables during the last century.

Based on the conclusions of AR5, since the late 1900s, globally averaged land-surface air temperature (LSAT) has risen, with an increase in the warming trend since the 1970s, while global average sea surface temperatures (SSTs) have increased since the beginning of the 20th century. Near surface temperatures averaged over the globe have risen since the end of the 19th century. Each of the last three decades has been warmer than all previous ones recorded by instruments, with the first decade of the 21st century being the warmest. Based on measurements from satellites and radiosondes, it has been observed that since the second half of the 20th century the troposphere has warmed and the stratosphere has cooled on a global scale even though there is disagreement in the rate of temperature changes. Temperature extremes also seem to have changed since the mid-20th century globally, as it is very likely that the number of cold days and nights has decreased, whereas the number of warm days and nights has increased overall (*Hartmann et al., 2013*). As suggested by climate models and observations, the Arctic has undergone considerably larger warming than the globally averaged temperature increase since preindustrial times, with conspicuous sea ice cover reductions and increasing Arctic CH_4 emissions from permafrost fragmentation (*Stjern et al., 2019*).

When it comes to precipitation changes, the available records, which are incomplete globally due to insufficient data especially prior to 1950, show mixed and statistically insignificant long-term trends in reported global mean changes. Global datasets since 1900 indicate a likely overall increase in precipitation when averaged over Northern hemisphere (NH) mid-latitude land areas, while there is low confidence in long-term trends in zonally averaged precipitation for all other zones due to sparsity of data, low quality or lack of agreement among the estimates (*Hartmann et al., 2013*). In general, it is expected that precipitation will increase in the "wettest" latitudes, whereas a decrease may be observed over "dry" latitudes, or in other words, wet regions will get wetter and dry regions will get drier (*Held and Soden, 2006*). On a regional scale, the response is more unclear due to local circulation shifts, although there is some evidence that the dry zones in the subtropics are broadening due to the contraction of tropical convergence zones and the poleward movement and strengthening of storm tracks (*Boucher et al., 2013*). In areas with increased winter temperatures (e.g., in N. America, Europe, E. Asia and S. Asia), there seems to be a reduction in snowfall events, whereas no conclusions can be drawn for the changes in Antarctic snowfall (*Hartmann et al., 2013*). As far as precipitation extremes are concerned, their intensity is expected to increase with global warming, at a greater rate than that of the mean precipitation (*Boucher et al., 2013*). It is likely that more regions (such as N. America and Europe) had a statistically significant increase in the number of heavy precipitation events than a statistically significant decrease since 1950, with the trends having strong regional variations. There is low confidence in large scale changes in extreme extratropical cyclone intensity since the 20th century or in long-term changes in the activity of tropical cyclones, although there is evidence for an increase in both intensity and frequency of the strongest tropical cyclones in the N. Atlantic basin since the 1970s. Generally, changes in extremes for climate variables other than temperature are more incoherent due to data limitations, seasonal variability, and inconsistencies among studies and regions (*Hartmann et al., 2013*).

As studied in Hartmann et al. (2013), other signs of climate change include a very likely increase of global near-surface air specific humidity and tropospheric water vapour at near-global spatial scales since the 1970s, with a recent abatement of near-surface moistening over land. While there is not sufficient evidence to support a global-scale trend in drought or dryness (i.e., lack of rainfall) since the 1950s, the intensity and frequency of drought has likely increased in the Mediterranean and W. African regions and decreased in N.W. Australia and the central part of N. America since the mid-20th century. For the period 1979-2012, it is likely that the sea level pressure has decreased over the tropical Atlantic and increased over large regions of the S. Atlantic and the Pacific, while the tropospheric geopotential height (GPH) has decreased at Southern hemisphere (SH) high latitudes in boreal winter and increased in the subtropical region and at NH high latitudes, whereas the lower-stratopheric GPH over Antarctica has decreased in spring and summer. Moreover, there is evidently broadening of the tropical belt and a poleward shift of jet streams, storm tracks, and circulation features since the 1970s.

1.2 The Concept of Radiative Forcing

1.2.1 Definitions of Radiative Forcing

As mentioned in Section 1.1, numerous drivers cause perturbations to the Earth's radiative budget and contribute to climate change. Theoretically, one could assess the impact of a single factor (driver) on the climate system by observing how the climate responds to that particular factor, which is difficult to isolate. Thus, the scientific community has used a variety of metrics to study the relation between cause and effect and to estimate the climate impact of individual drivers, with radiative forcing (RF) being one of the most widely used metrics (*Myhre et al., 2013*).

RF is defined in Myhre et al. (2013) as "the net change in the energy balance of the Earth system due to some imposed perturbation". It is typically expressed in Watts per square meter (W m^{-2}) averaged over a specific time period and quantifies the energy imbalance arising from the imposed change. Frequently, the forcing is presented as the value due to changes between two specific times, such as pre-industrial to present-day (commonly in control and perturbed simulations of climate models, respectively). RF is a quantitative tool used to compare and estimate the potential climate response to different imposed agents, particularly global mean temperature response (*Myhre et al., 2013*). RF was created as a means to quantify the radiation balance perturbations caused by WMGHGs and solar irradiance changes, and was later extended to short-lived gases that show strong spatio-temporal variability (*Ramaswamy et al., 2019*).

In simpler terms, radiative forcing offers a metric for quantifying how human activities and natural agents change the energy flow into and out of the climate system (*Ramaswamy et al., 2019*). At first, a radiative perturbation forced on the climate system exerts a temporary imbalance on the energy budget (*Bellouin et al., 2020*). This perturbation of the energy balance commences all other changes of the climate that occur due to an external forcing (*Ramaswamy et al., 2019*). A temperature change is the climate system's response in an attempt to restore radiative equilibrium (Planck response or Planck feedback; *Ramaswamy et al., 2019*) until a new steady state is reached, whereby its heat content yet again remains almost constant (*Bellouin et al., 2020*). A positive (negative) forcing is translated as a net radiative gain (loss), which results in a warming (cooling) of the climate and an increase (decrease) of the thermal energy emitted to space until the balance is restored (*Ramaswamy et al., 2019*).

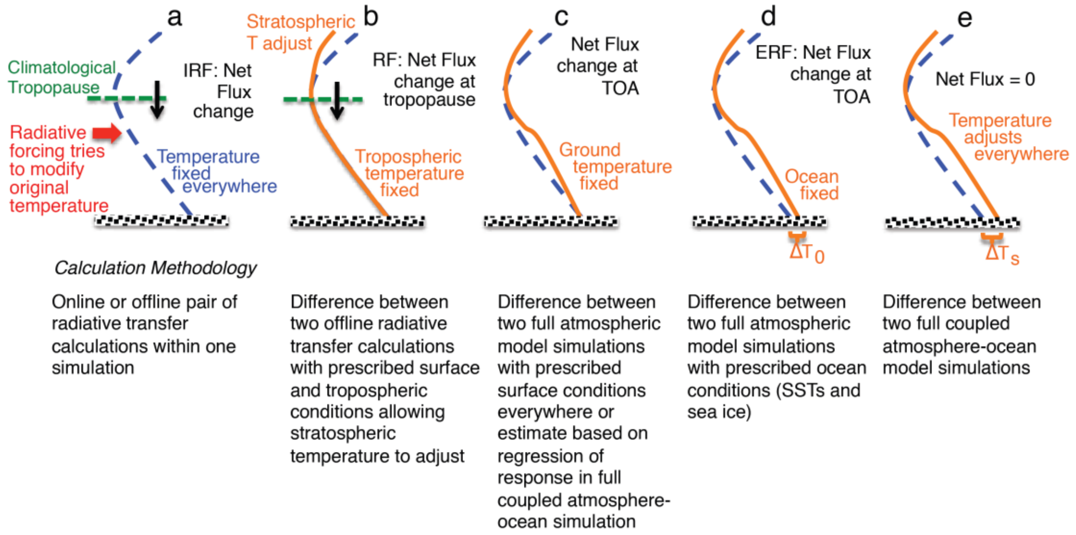

Calculation Methodology

Online or offline pair of radiative transfer calculations within one simulation

Difference between two offline radiative transfer calculations with prescribed surface and tropospheric conditions allowing stratospheric temperature to adjust

Difference between two full atmospheric model simulations with prescribed surface conditions everywhere or estimate based on regression of response in full coupled atmosphere-ocean simulation

Difference between two full atmospheric model simulations with prescribed ocean conditions (SSTs and sea ice)

Difference between two full coupled atmosphere-ocean model simulations

Figure 1.4. A schematic representation of (a) IRF, (b) SARF, (c) flux change when the temperature of the surface is held fixed over the entire Earth (a method of ERF calculation), (d) ERF with atmospheric and land temperature allowed to adjust while ocean conditions are held fixed and (e) the equilibrium response to the climate forcing agent. ΔT_0 is the land temperature response and ΔT_S is the full surface temperature response [Figure taken from *Myhre et al., 2013*].

Different definitions of radiative forcing have been developed over the years (Fig. 1.4), each with its own advantages and limitations. The instantaneous radiative forcing (IRF) is referred to “an instantaneous change in the net (down minus up) radiative flux (SW plus LW) owing to an imposed change” (*Myhre et al., 2013*). IRF is commonly defined either at the climatological tropopause or at the top of the atmosphere (TOA), with the former indicating the global mean surface temperature response more accurately in cases when the two values differ (*Myhre et al., 2013*).

Since the Third Assessment Report (TAR) of the IPCC, the term “radiative forcing” has been defined as “the change in net irradiance at the tropopause after allowing for stratospheric temperatures to adjust to radiative equilibrium, while tropospheric and surface temperatures along with state variables like water vapour and cloud cover were held fixed at the unperturbed values” (*Myhre et al., 2013*). This stratospherically adjusted radiative forcing (SARF) captures surface and tropospheric temperature responses more appropriately than IRF, primarily for agents that largely modify stratospheric temperatures (such as CO_2 and O_3) (*Myhre et al., 2013*). SARF is thought to be good measure of the RF affecting the climate system and the long-term climate change because stratospheric temperature adjusts more rapidly than the tropospheric temperature, which is strongly coupled to the ocean, and many forcing agents have longer lifetimes than the stratospheric radiative relaxation time (*Hansen et al., 2005*).

SARF is a useful tool that enables an appropriate comparison of the relative importance of the potential effect on climate for many forcing agents. However, IRF and SARF do not accurately estimate the temperature response for all forcing agents nor do they include alterations in cloudiness driven by forcings and other rapid adjustments responsible for global energy balance changes (*Myhre et al., 2013*; *Forster et al. 2016*). Because tropospheric rapid adjustments can either enhance or reduce the flux perturbations and lead to important differences in the forcings that drive long-term climate change, there came the need for a new definition of radiative forcing that includes these rapid adjustments (*Myhre et al., 2013*). While the majority of the adjustments occur shortly after the imposed forcing, there does not exist a fundamental timescale based on which rapid adjustments are distinguished from feedback responses. Theoretically, the timescales of the two can overlap substantially (*Sherwood et al., 2015*).

Therefore, the effective radiative forcing (ERF) concept was introduced in the Fifth Assessment Report (AR5). ERF is defined as “the change in net TOA downward radiative flux after allowing for atmospheric temperatures, water vapour and clouds to adjust, but with global mean surface temperature or a portion of surface conditions unchanged” (*Myhre et al., 2013*). ERF estimates the eventual global mean temperature response in a better manner, as it accounts for additional rapid adjustments, the majority of which happen on time scales of seasons or less. However, it does not describe regional climate changes. This applies to all forcing agents, but particularly to the heterogeneously distributed forcings, as they trigger climate feedbacks based on their regional distribution (*Myhre et al., 2013*).

1.2.2 ERF Calculation Methods and Limitations

There is no perfect method to determine ERF (*Boucher et al., 2013*). One of the main methods used to calculate ERF (Fig. 1.5) is by holding sea surface temperatures (SSTs) and sea ice cover (SIC) fixed at climatological values, but allowing all other parts of the system to respond until they reach a steady state (*Hansen et al., 2005*). In this approach, the climate response to a forcing agent accounts for land surface responses (weakly connecting them to feedback processes as a result), excluding slow ocean responses (*Myhre et al., 2013, 2017*). Arguably it would be more consistent to keep both land and surface temperatures fixed (*Shine et al. 2003*), but this would be difficult to apply in some climate models (*Ramaswamy et al., 2019*). In the fixed-SST method, the TOA radiative flux imbalance is the sum of the direct radiative forcing and the rapid adjustments (*Forster et al., 2016*; *Chung and Soden, 2015a*). Another common method (Fig. 1.5) is by analyzing the transient global mean surface temperature response to an instantaneous perturbation. First, the TOA net radiative imbalance is regressed against the surface temperature change in coupled climate model simulations. The initial ERF is derived from the extrapolation of that regression line to zero surface temperature change (*Gregory et al., 2004*).

In the fixed-SST method land surface properties such as temperature, vegetation, and snow and ice cover are allowed to adjust. Thus the effects of the forcing agent and the rapid adjustments to that particular agent are considered in the ERF (same as in SARF, but with stratospheric temperature adjustments only considered). In the case of aerosols, the cloud rapid adjustments account for the effects of indirect and semi-direct forcings (see Section 1.1) (*Myhre et al., 2013*). Calculation of ERF using the fixed-SST method leads to much smaller uncertainty due to internal variability than using the regression method in simulations of similar length, making the former probably a better indicator of very small forcings (*Forster et al., 2016*; *Myhre et al., 2013*). Forster et al. (2016) found that 30-year integrations are sufficient to limit global forcing to within 0.1 W m^{-2} when keeping SSTs constant, making it a more accurate and computationally efficient method. Richardson et al. (2019) concluded that ERF definition based on fixed-SST experiments is the best predictor of the climate responses among various forcing agents. Furthermore, the fixed-SST technique yields a smaller spread across models and is available for a greater number of forcing agents in the latest climate models than forcing calculated with the use of the regression method (*Myhre et al., 2013*). The fixed-SST technique separates forcing and feedback by their timescales, because it accounts for land surface and atmosphere responses, which have short timescales, but does not include responses with longer timescales (*Forster et al., 2016*).

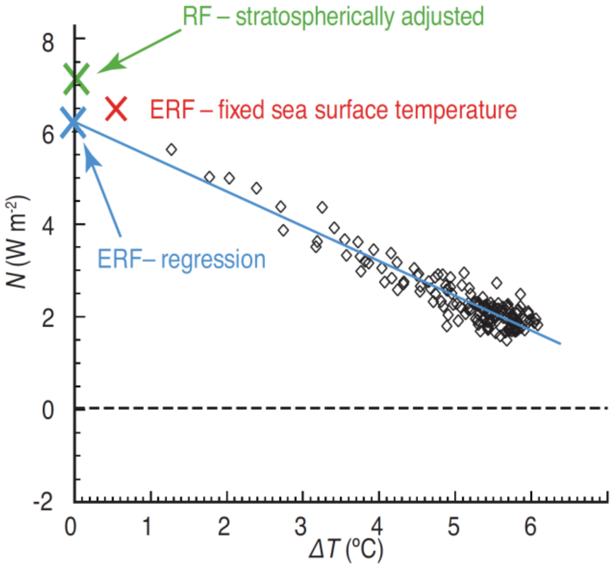

Figure 1.5. SARF and ERF estimates for the example of 4 × CO_2 experiments in one climate model. *N* denotes the TOA net energy imbalance and *ΔT* the global mean surface temperature change. The fixed-SST ERF estimate is derived from an atmosphere–land model averaged over a 30-year period. The regression ERF estimate is from 150 years of a coupled model simulation after an abrupt quadrupling of CO_2, with the *N* from individual years in this regression shown as black diamonds. SARF is the energy imbalance at tropopause from radiation calculations at 1 × and 4 × CO_2 concentrations [Figure taken from *Boucher et al., 2013*].

However, there are some disadvantages to the fixed-SST approach. Although the ERF calculated with constant SSTs accounts for a portion of land area responses, its value is slightly less than it would be if the surface temperature was constant everywhere. While possible to adjust for this in the global mean forcing, the land response will create artificial gradients in land–sea temperatures, which could bring about small local climate responses (*Myhre et al., 2013*). Land surface temperatures changes can lead to small changes of global mean surface temperature, making it more difficult to distinguish forcings from responses (*Forster et al., 2016*; *Sherwood et al., 2015*), as land surface temperature responses and feedbacks from land surface temperature changes are included in the calculation of adjustments (*Chung and Soden, 2015b*). In order to separate forcing and response, globally averaged feedback based “corrections” have been applied to the land surface-based global temperatures change in the implementation of the fixed-SST method, but they do not work well (*Hansen et al., 2005*; *Sherwood et al., 2015*).

On the other hand, the regression approach allows for forcing and response to be examined from a single model integration (*Forster et al., 2016*). The regression approach allows tropospheric, stratospheric and land surface feedback mechanisms to act (*Hansen et al., 2005*), neatly separating adjustments from global-mean temperature change (*Sherwood et al., 2015*). However, the regression method does not include a global mean temperature response and can be complicated by natural variability or time-varying feedbacks (*Myhre et al., 2013*; *Boucher et al., 2013*; *Sherwood et al., 2015*). Moreover, ERF values depend on the type of regression and change substantially as more years are included in the regression, which are needed to reduce the uncertainty in ERF (*Forster et al., 2016*). It should also be noted that the separation of the instantaneous forcing from the radiative adjustments is not possible using either the regression or the fixed-SST methods (*Chung and Soden, 2015b*). In this work, only the fixed-SST approach is considered.

Both the ERF and SARF concepts have merits and disadvantages. ERF is easier to estimate than the traditionally used definitions of radiative forcing in global climate models (GCMs) and represents the eventual temperature response more accurately (*Forster et al., 2016*). However, ERF is highly depended on its method of calculation (*Forster et al., 2016*) and is restricted only to forcing mechanisms that are of sufficient magnitude in order for their impact on TOA fluxes to become distinct from the noise deriving from the climate model's own internal variability (*Ramaswamy et al., 2019*). Meteorological variability can also complicate the identification of ERF from small forcings that are more easily isolated in radiative transfer calculations performed for SARF (*Myhre et al., 2013*). In contrast, SARF is sensitive to the choice of tropopause level, whose definition can be quite nebulous and may differ among climate models (*Myhre et al., 2013*; *Hansen et al., 2005*; *Shine et al. 2003*). Despite all that, several studies show that SARF is a good estimate of ERF in the majority of the cases, as they are nearly equal, with the exceptions of forcings related to BC (*Bond et al., 2013*). ERF is a better indicator of these effects, along with others, including all aerosol–cloud interactions. While ERF and SARF are generally quite similar when it comes to WMGHG quantification, ERF is usually more fitting for characterizing NTCF climate responses (*Myhre et al., 2013*).

However, ERF estimates tend to have a larger uncertainty range than SARF estimates, because rapid adjustments differ in intensity across climate models due to their more complicated nature and less theoretical understanding (especially cloud adjustments resulting from complex interactions between processes that may or may not be adequately represented in climate models), thus complicating the distinction between adjustments and feedbacks arbitrated by surface temperature change (*Myhre et al., 2013*; *Ramaswamy et al., 2019*). In order to examine and quantify the importance of climate feedback processes consistently among individual climate models, the radiative kernel technique was developed (*Chung and Soden, 2015a, b*). Radiative kernels describe the differential response of TOA radiative fluxes to incremental changes in climate variables, and can help detect the inconsistencies in transient climate response among climate models through accurate decomposition of TOA radiative flux imbalances (*Chung and Soden, 2015a*).

Generally, the most broadly used definitions of forcing and the majority of forcing-based metrics are proportionate to the eventual temperature response on a global scale, and do not estimate impacts like changes in global precipitation (which are more limited by surface and atmospheric energy, rather than energy budget perturbations at TOA or tropopause; *Andrews et al., 2010*), extreme events, etc., or regional temperatures, which can be considerably different from the global mean (*Myhre et al.,* *2013*). These metrics help understand the factors that drive global mean temperature changes, but they give little insight on the factors driving broader climate change (*Myhre et al.*, *2013*). In particular, the SARF and ERF concepts do not consider the complex nature of certain climate forcers, they cannot characterize sufficiently nor reduce the uncertainties in the determination of the forcings and their precursor parameters (i.e., emissions), and their reliance on numerical models for forcing estimations (since it is difficult to verify the theoretically developed concept of RF against observations or measure parameters relevant to forcing estimates) makes them susceptible to inconsistencies among different model estimates (*Ramaswamy et al., 2019*). It is clear that a metric relying exclusively on radiative perturbations cannot allow comparison of non-radiative forcings, and provides a limited perspective on the relative contribution of radiative forcing to climate change (*Myhre et al., 2013*).

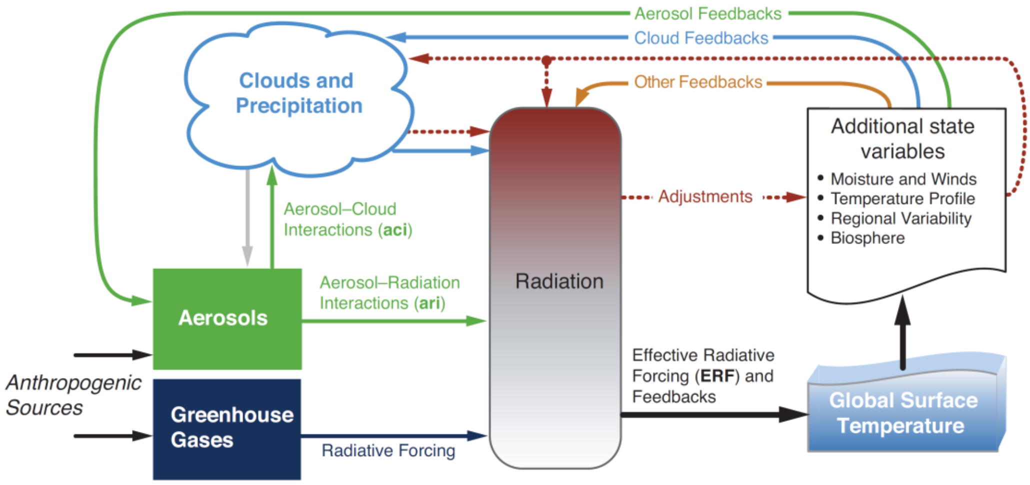

Figure 1.6. An overview of forcing and feedback pathways involving GHGs, aerosols and clouds. Forcing mechanisms are shown as straight green and dark blue arrows. Rapid adjustments are indicated by brown dashed arrows and feedbacks by curving arrows. The final temperature response relies on the ERF imposed on the climate system, that is, after considering rapid adjustments and feedback processes [Figure taken from *Boucher et al., 2013*].

1.2.3 ERF and Climate Impacts of Anthropogenic Aerosols

Anthropogenic aerosols influence the energy balance of the surface and the atmosphere by scattering and absorption of solar radiation, affect clouds (and vice versa; *Rosenfeld et al., 2014a*) and precipitation (e.g., *Gu et al., 2016*; *Tang et al., 2018*; *Undorf et al., 2018*), and can perturb the Earth’s hydrological cycle (*Andrews et al. 2010*; *Hoose et al., 2009*). The sign and magnitude of the ARI forcing depends on the radiation wavelength and the physical and chemical properties of the aerosol particles, along with environmental factors, like the incident radiation amount, relative humidity, and the reflectivity of the underlying surface (*Bellouin et al., 2020*). Scattering aerosols (like SO_4 and OC), which reflect solar radiation back to space, increase the planetary albedo and exert a negative TOA forcing (*Ramanathan and Carmichael, 2008*), resulting in a decrease in global mean surface temperature (*Baker et al., 2015*). Over the historical period, aerosols have a net negative radiative forcing, mainly confined to the NH (*Ramaswamy et al., 2019*) and around industrialized regions, such as N. America, Europe, E. Asia and S. Asia (*Kasoar et al., 2018*). Therefore, anthropogenic aerosol species induce a preferential cooling of the NH (*Ramaswamy et al., 2019*), with the surface temperature of some NH regions being more sensitive to aerosol perturbations than others (*Richardson et al., 2019*). This causes a meridional shift in the Intertropical Convergence Zone (ITCZ) towards the warmer hemisphere (there is a pronounced southward shift in tropical precipitation), which induces local precipitation changes in the tropics and the monsoon regions (*Baker et al., 2015*; *Ramaswamy et al., 2019*; *Voigt et al., 2017*). Moreover, hydrophilic aerosol particles acting as CCN allow the formation of a greater amount of small sized cloud droplets, increasing the cloud amount, albedo and lifetime, thus contributing to the negative forcing (*Baker et al., 2015*; *Ramanathan and Carmichael, 2008*). By reducing the amount of droplets large enough to precipitate, they can cause regional precipitation decreases (*Baker et al., 2015*). CCN serving aerosols brighten clouds through the Twomey effect and reflect more solar radiation back to space, cooling the layer below cloud tops (*Rosenfeld et al., 2014a*). It should be noted that the globally averaged impact of aerosols does not necessarily reflect the regional climate responses, which can be substantial in magnitude even if the global forcing is small (*Barlett et al., 2017*).

The SO_4 radiative forcing is globally negative and strongest over NH industrial regions, especially during the warm period when the insolation is at its highest (*Haywood and Boucher, 2000*), being the main aerosol driver of surface temperature for present-day emissions (*Baker et al., 2015*). Biomass burning aerosols may exert either a net cooling or a net warming effect depending on their type and the reflectivity of the underlying surface (*Chand et al., 2009*). On average, fossil fuel (biomass burning) BC and OC combined have a positive (negative) forcing (*Hansen et al., 2005*; *Haywood and Boucher, 2000*). BC absorbs incoming solar radiation, having a positive TOA forcing and a net warming effect on the atmosphere, with the local impact of BC on the surface temperature relying on its altitude; BC in low levels can warm the surface through LW radiation emission, while BC in higher levels can decrease the surface temperature via absorption of a portion of the solar radiation before it reaches the surface (*Ramanathan and Carmichael, 2008*; *Baker et al., 2015*). The forcing from BC cloud effects is positive over the industrial era with considerable uncertainty (*Bond et al., 2013*). BC solar heating can reduce the relative humidity of the cloud layer it resides, causing cloud drops to evaporate and thus decreasing the albedo and amount of low clouds (especially if it is embedded in cloud droplets), consequently intensifying the positive BC forcing and the Earth-atmosphere system warming (*Ramanathan and Carmichael, 2008*; *Lohmann and Feichter, 2005*). Allen et al. (2019) found substantial global annual mean reductions in low- and mid-level clouds, along with weaker decreases in high-level clouds, leading to a positive semi-direct effect, suggesting that cloud adjustments tend to warm the climate system. BC forcing is greater when above low clouds than under clear sky conditions, whereas when situated below clouds, it has a decreased contribution to forcing (*Bond et al., 2013*). BC deposition on ice and snow surfaces can decrease their albedo and darken them, inducing a positive forcing on the climate and enhancing the local surface temperature response (*Ramanathan and Carmichael,* 2008; *Ramaswamy et al., 2019*; *Bond et al., 2013*). Small reductions in snow albedo can have significant adjusted forcing, as the resulting warming influences the snow grain size, along with its sublimation and melt rates, thus amplifying the radiative forcing (*Bond et al., 2013*).

BC forcing due to the direct effect and snowpack change provokes a warming of the troposphere and the top of the cryosphere, leading to additional changes in surface temperature, precipitation, clouds and circulation (*Bond et al., 2013*). Forcing from BC mainly warms the mid- and high latitudes of NH and may cause regional circulation and precipitation changes, including a northward shift of the ITCZ, changes in the Asian Monsoon precipitation patterns, and the Arctic warming (*Bond et al., 2013*). The impacts of BC forcing on the Arctic surface temperature are complicated, because they depend on the location and altitude of the forcing (*Sand et al., 2013*; *Baker et al., 2015*; *Stjern et al., 2019*). During winter, BC is most intensely transported northward and has a longer lifetime, resulting in a BC concentration maximum in the Arctic in late winter and spring, with the high concentrations remaining until the melting season (*Sand et al., 2013*). BC has intricate effects on precipitation patterns, because it warms the atmosphere, but may either cool or warm the surface, reducing or increasing surface evaporation and resulting precipitation (*Andrews et al., 2010*; *Baker et al., 2015*). The net effect on precipitation and clouds strongly relies on the region and vertical profile of BC (*Andrews et al., 2010*; *Baker et al., 2015*; *Hodnebrog et al., 2016*). On a global scale, the altitude of absorbing aerosols affects the sign and magnitude of globally averaged precipitation changes. Unless BC is near the surface, there appears to be a net decrease in precipitation (*Hodnebrog et al., 2016*) through rapid adjustments (*Bond et al., 2013*). BC can either enhance or reduce cloud cover, depending on its location and the cloud type. BC at high altitudes stabilizes the atmosphere, leading to increased stratocumulous clouds formation (*Ramanathan and Carmichael, 2008*; *Baker et al., 2015*). It should be noted that temperature, cloud, and in some cases, precipitation responses to absorbing aerosols are controlled by rapid adjustments, which lead to a negative radiative perturbation, thus partly counterbalancing the positive direct forcing of absorbing aerosols, eventually causing a quite weak surface temperature response (*Allen et al., 2019*).

As stated in AR5, the total anthropogenic net TOA ERF is positive over the industrial era (1750-2011 period) with a value of 2.3 (1.1 to 3.3) W m^{-2}, (the uncertainty values in the parenthesis represent the 5–95% (90%) confidence range), and has increased at a greater rate since 1970 (*Myhre et al., 2013*). While anthropogenic increases in WMGHGs have largely enhanced the greenhouse effect due to LW radiation absorption, with their ERF estimated at 2.83 (2.26 to 3.40) W m^{-2}, aerosols partly offset this forcing, but with larger uncertainties (*Myhre et al., 2013*). In IPCC AR5, the aerosol ERF was separated into forcing from aerosol-radiation interactions (ERFari) and aerosol-cloud interactions (ERFaci). The total net ERF due to aerosols (ERFari+aci), including rapid adjustments, like changes to cloud lifetime and altitude, and microphysical effects of aerosols on clouds, but without the effects of absorbing aerosol on ice and snow, was estimated to be –0.9 (–1.9 to –0.1) W m^{-2} (*Boucher et al., 2013*; *Myhre et al., 2013*). The ERFari was estimated to be –0.45 (–0.95 to +0.05) W m^{-2} (*Boucher et al., 2013*; *Myhre et al., 2013*), while Myhre et al. (2013) estimated an ERFaci, which they defined as ERFari+aci minus ERFari, and represented only aerosol induced rapid adjustments initiated by aerosol-cloud interactions, at –0.45 (–1.2 to 0.0) W m^{-2}. The ERFari+aci does not necessarily equal the sum of ERFari and ERFaci due to nonlinearities in forcings and rapid adjustments (*Boucher et al., 2013*), and it was coincidental that the two were equal. There are numerous climate model estimates of ERFari+aci, which may vary due to the selection of a different year as a pre-industrial period, to the different method of ERFari+aci calculation among models or to the different aerosol–cloud interaction processes considered (*Boucher et al., 2013*).

Myhre et al. (2017) showed that there is stronger positive radiative forcing of aerosols and O_3 over the 1990–2015 period than reported in IPCC AR5, with the globally averaged total forcing being almost +0.2 W m^{-2} due to considerable reductions in global mean SO_2 emissions and higher BC emissions. Shindell et al. (2013) estimated a mean 1850 to 2000 aerosol ERF value of −1.2 ±0.5 W m^{-2}, with the largest negative values over and near Europe, N. America, and east and south Asia, and positive values over the Sahara, parts of the Himalayas/Karakoram, and over both the polar regions. Shindell et al. (2015) estimated a global historical aerosol forcing at –1.0 ±0.4 W m^{-2} and found that large aerosol forcings in eastern N. America and Europe likely moderated the local WMGHG warming. Zanis et al. (2012) found that anthropogenic aerosols caused a negative RF and small changes in the near-surface temperature over Europe during the 1996–2007 period, with cooling south of the latitudinal zone 50^{o}-55° N and warming northwards. Zelinka et al. (2014) estimated a SW ERFari+aci of −1.40 ±0.56 W m^{-2}, 25% of which from ERFari (−0.35 ±0.20 W m^{-2}), which was largest near emission sources and accounted for aerosol scattering (−0.62 ±0.30 W m^{-2}) and aerosol absorption (+0.26 ±0.12 W m^{-2}), and 75% from ERFaci (−1.04 ±0.67 W m^{-2}), which was large close to and downwind of emission sources and consisted of −0.99 ±0.54 W m^{-2} from increased cloud scattering, along with much smaller contributions from increased cloud amount and absorption.

Recent studies used simulations from climate models participating in the sixth phase of the Coupled Model Intercomparison Project (CMIP6; *Eyring et al., 2016*). Michou et al. (2020) calculated the anthropogenic aerosol ERF using 30-year fixed-SST simulations from the CNRM-CM6-1 and CNRM-ESM2-1 models and estimated an overall ERF, ERFari and ERFaci of −1.10, −0.36, and −0.81 W m^{-2} for CNRM-CM6-1 and −0.74 , −0.21, and −0.61 W m^{-2} for CNRM-ESM2-1, respectively. They also calculated the overall ERF, ERFari and ERFaci due to BC (0.11, 0.13, and −0.03 W m^{-2}, respectively), due to OC (−0.17, −0.07, and −0.14 W m^{-2}, respectively), and due to SO$_4$ (−0.75, −0.29, and −0.53 W m^{-2}, respectively) using the CNRM-ESM2-1 model (*Michou et al., 2020*). Oshima et al. (2020) used the MRI-ESM2.0 model to estimate the overall ERF, ERFari, ERFaci and ERFalb (i.e., the ERF caused by surface albedo changes) due to anthropogenic aerosols (−1.22, −0.32, −0.98, and 0.08 W m^{-2}, respectively), due to BC (0.24, 0.25, −0.09, and 0.07 W m^{-2}, respectively), due to OC (−0.33, −0.07, −0.21, and −0.05 W m^{-2}, respectively), and due to SO$_4$ (−1.38, −0.48, −0.94, and 0.05 W m^{-2}, respectively). Smith et al. (2020) estimated the multi-model mean present-day aerosol ERF to be −1.01 ±0.23 W m^{-2} from 17 models using the fixed-SST method and the total ERFari+aci to be −1.04 ±0.20 W m^{-2}, 22% of which from ERFari (−0.23 W m^{-2}) and 78% from ERFaci (−0.81 W m^{-2}), using the approximate partial radiative perturbation (APRP) method. Thornhill et al. (2021a) estimated the multi-model mean total ERF for the aerosols at −1.01 ±0.25 W m^{-2}, for BC at 0.15 ±0.17 W m^{-2}, for OC at −0.25 ±0.09 W m^{-2}, and for SO$_4$ at −1.03 ±0.37 W m^{-2} from 10 models. Zanis et al. (2020) using simulations from 10 models calculated the multi-model mean global fixed-SST ERF due to anthropogenic aerosols at −1.00 ±0.24 W m^{-2} (−1.46 ±0.44 W m^{-2} in NH and −0.54 ±0.18 W m^{-2} in SH) on an annual level, as well as during the boreal winter (DJF) with a value of −0.76 ±0.26 W m^{-2} (−1.00 ±0.42 W m^{-2} in NH and −0.53 ±0.20 W m^{-2} in SH) and in the boreal summer (JJA) valued at −1.12 ±0.35 W m^{-2} (−1.79 ±0.67 W m^{-2} in NH and −0.46 ±0.14 W m^{-2} in SH).

Numerous researches examining the effects of aerosols on the Earth's climate have been conducted. Zanis et al. (2020) investigated the fast responses on pre-industrial climate in response to anthropogenic aerosol ERF using the fixed-SST method finding that there is a cooling over the NH land regions, in particular, with the largest cooling over India and E. Asia, while there was an apparent warming in the Arctic during the winter. They also detected the strongest fast precipitation responses in the tropics, with a reduction over continental areas and a southward shift of the tropical rain belt (away from the cooled hemisphere), along with a weakening of the monsoon systems over the globe (*Zanis et al., 2020*). Thornhill et al. (2018) studied the impact of biomass burning aerosols on the regional climate in South America and they found that increased emissions in September (peak biomass emissions month) caused substantial burning off and cloud cover change due to reduced deep convection, while the mean surface temperature decreased by 0.14±0.24^{o}C and then mean precipitation decreased by 14.5% in the peak biomass region due to changes in cloud cover and microphysical properties. According to Hodnebrog et al. (2016), the local anthropogenic biomass burning emissions of BC and OC are the main cause of S. African dry season precipitation reduction during the last century.

Furthermore, many studies examining the effects of aerosol emission or concentration increases on the climate system have been published. Liu et al. (2018) found that the ITCZ experiences a southward (northward) shift when SO_4 (BC) aerosols increase and the storm tracks move towards the equator when the Asian SO_4 aerosols increase, while there is a decrease in precipitation over Europe (especially the Mediterranean) when the Asian BC increases. Zhang et al. (2021) found that an increase in BC (SO_2) emissions induces a decrease in global-mean precipitation, dominated by fast (slow) responses, with a reduction in extratropical precipitation and a northward (southward) shift of the ITCZ, along with tropical rainfall. Similar results were derived from other papers studying the impacts of SO_2 emission or SO_4 concentration increases on the climate system, which, on average, showed negative radiative forcing over the emission region, temperature decreases concentrated on the NH with considerable responses in the Arctic, precipitation reductions and a southward shift of the ITCZ (*Lewinschal et al., 2019*; *Richardson et al., 2019*; *Samset et al., 2016*). Barlett et al. (2017) showed that increased SO_4 aerosols mainly from E. Asia impact the regional climate (surface cooling, E. Asian monsoon circulation weakening, S. Asian monsoon suppression) and remote areas of the NH (shift of W. African monsoon rainfall, temperature anomalies in northern mid-latitudes), while Liu et al. (2018) concluded that, although European aerosols are more efficient in driving global changes, Asian SO_4 aerosols influence local precipitation more effectively than European SO_4 aerosols do for Europe. As far as BC is concerned, increases in its emissions or concentrations produce a strong heating near the tropopause (*Richardson et al., 2019*), generate positive (negative) temperature (precipitation) response, while the mean precipitation change is dominated by fast responses, and is generally negative at most latitudes, with a northward shift of the ITCZ (*Samset et al., 2016*). Sand et al. (2013) found that increased BC forcing over the Arctic reduces the local surface air temperature (despite the positive TOA radiative forcing) with a parallel increase in sea ice fraction (in spite of the greater sunlight absorption) due to surface dimming and the weakening of northward heat transport caused by a meridional temperature gradient decrease. However, they detected that BC forcing at the mid-latitudes substantially warms the Arctic surface and reduces the sea-ice fraction, concluding that BC forcing outside the Arctic could be more significant to its climate change than the forcing within the Arctic itself (*Sand et al., 2013*). The analysis of Stjern et al. (2017) showed that increased BC concentrations produced a positive ERF, a warming globally and in the Arctic, in particular, and an increase (decrease) in Low-level (high-level) cloud amounts. Temperature and cloud responses to BC forcing were dominated by rapid adjustments, while the rapid temperature response was especially strong above 400 hPa (*Stjern et al., 2017*). Smith et al. (2018) found similar results to increased BC emissions or concentrations, which induced a strong negative total adjustment, with the largest negative (positive) contributions being the tropospheric temperature and clouds (water vapour). BC forcing caused a warming and wetting throughout the atmosphere connected to a large cloud fraction reduction, especially at higher levels (*Smith et al., 2018*). Tang et al. (2018) found that increases in BC concentrations or emission induce a local heating and an apparent precipitation reduction in the Mediterranean, by creating an enhanced positive sea level pressure pattern akin to the North Atlantic Oscillation–Arctic Oscillation.

Aerosols can also exert a radiative forcing after they are removed from the atmosphere (*Bellouin et al., 2020*). The predominant effect of aerosol removal is the loss of present-day SO_4 induced cooling. On a global scale, aerosol removal enhances the climate impacts already expected for the near future (*Samset et al., 2018*). In general, reductions in aerosol emissions cause a net precipitation increase due to greater surface insolation, resulting in more available heat for evaporation and convection (*Westervelt et al., 2018*). Samset et al. (2018) showed that removing anthropogenic aerosols increases the global mean surface temperature (0.5–1.1°C), precipitation (2.0–4.6%) and extreme weather indices, with extreme events having a higher sensitivity to aerosol reductions over the major aerosol emission regions. Westervelt et al. (2018) found that when regional aerosol emissions are reduced, regional and global precipitation mostly increases, with the strongest responses occurring for SO_2 European and U.S. emissions reductions. They detected the strongest precipitation responses in the tropics, which affect the El Niño–Southern Oscillation, while Sahel precipitation increases in response to remote aerosol reductions due to a northward shift of the ITCZ (*Westervelt et al., 2018*). BC radiative forcing ceases within weeks after the termination of emissions due to its short atmospheric lifetime (*Bond et al., 2013*). Chen et al. (2010) found that a 50% decrease in BC/OC emissions, results in a reduction in global cloud radiative forcing (a reverse “cloud albedo effect”). Baker et al. (2015) concluded that reductions in SO_2 emissions have a strong response, with an increase in surface temperature mainly in the NH mid- and, particularly, high latitudes, a corresponding increase in global mean precipitation, and a northward shift of the ITCZ, while removal of BC and OC emissions had much weaker responses, with the latter exhibiting similar response patterns to the removal of SO_2, including a weak northward ITCZ shift and corresponding precipitation changes. Other studies agree that SO_2 emission or SO_4 concentration reductions lead to positive ERF concentrated near the source region, global surface temperature increases, concentrated over the NH with an amplification of warming towards the Arctic region (*Kasoar et al., 2016, 2018*; *Conley et al., 2018*)

The ERF concept gives rise to many uncertainties. As it can be estimated mostly through model simulations, it is prone to generate numerous uncertainties that may be due to its calculation approach (e.g., *Forster et al., 2016*; *Hansen et al., 2005*), the method of estimating climate forcing, responses, and feedbacks (e.g., *Lewinschal et al., 2019*; *Lohmann et al., 2010*; *Samset et al., 2016*; *Zanis et al., 2012*), the inadequate theoretical underpinning of the aerosol-cloud interactions (e.g., *Rosenfeld et al., 2014b*), the limitations of the ERF concept itself (e.g., *Myhre et al., 2013*), the uncertainties in the aerosol pre-industrial or present-day emissions, concentrations or sources (e.g., *Wan et al., 2021*; *Wilcox et al., 2015*), the uncertainties in the effects of natural drivers, such as natural aerosols (e.g., *Carslaw et al., 2013*), the models’ representation of aerosols, ARI, ACI or atmospheric and aerosol chemistry (e.g., *Ghan et al., 2012*; *Hoose et al., 2009*; *Kasoar et al., 2016*; *Bellouin et al., 2020*; *Allen et al., 2019*; *Rosenfeld et al., 2014a*; *Rotstayn and Liu, 2005*; *Sand et al., 2013*; *Westervelt et al., 2018*; *Wilcox et al., 2015*; *Zelinka et al., 2014*), the modeled natural climate variability and meteorology or the simulated climate responses and feedbacks (e.g., *Baker* *et al., 2015*; *Wilcox et al., 2015*; *Zelinka et al., 2020*), the models’ ability to simulate sub-grid scale features and phenomena (*Allen et al., 2019*), the models’ internal variability, biases, and parameterization schemes (e.g., *Zanis et al., 2012*; *Zelinka et al., 2020*), etc.

Over the last decades, the Coupled Model Intercomparison Project (CMIP) has systematically tried to understand the radiative forcing due to aerosols and reactive gases. Currently in its sixth phase (CMIP6; *Eyring et al., 2016*), the interest is focused on the ways the Earth system responds to forcing and the methods of evaluating future climate change, along with discovering the sources and ramifications of model biases. CMIP6 endorses 21 MIPs, two of which are of interest here. The Radiative Forcing Model Intercomparison Project (RFMIP; *Pincus et al., 2016*) addresses the question of how the Earth system reacts to radiative forcing by examining ERF and its components and by identifying robust model responses to aerosol RF. The Aerosol Chemistry Model Intercomparison Project (AerChemMIP; *Collins et al., 2017*) is designed to quantify the impacts of NTCFs, N_2O and O_3-depleting halocarbons on climate and air quality through targeted simulations with CMIP6 climate model containing an interactive representation of atmospheric chemistry and tropospheric aerosols. In this study, models participating in AerChemMIP and RFMIP are used to examine the ERF of BC, OC and sulphate aerosols, as well as their impact on surface air temperature.

CHAPTER 2: DATA AND METHODOLOGY

2.1 Models and Data

In the present work, simulations from state-of-the-art Earth System Models (ESMs) participating in CMIP6 (*Eyring et al., 2016*) were used (Table 2.1). The five models included in this study are CNRM-ESM2-1, GFDL-ESM4, MPI-ESM-1-2-HAM, MRI-ESM2-0, and NorESM2-LM, with the latter providing two physics variants, r1i1p1f1 and r1i1p2f1 (hereafter “p1” and “p2”, respectively), with aerosol treatments that are different enough to justify treating the variants as separate models, bringing the total to six. The main characteristics of each model’s atmospheric chemistry and aerosol schemes are summarized below.

Table 2.1. Information on model atmospheric resolution (horizontal and vertical levels), type, variant label and references. Each experiment (see Table 2.2) has a variant label $r_a i_b p_c f_d$, where *a* is the realization index, *b* is the initialization index, *c* is the physics index and *d* is the forcing index.

Model Name	Atmospheric Resolution (lon x lat)	Model Type	Variant Label	References/DOI
CNRM-ESM2-1	1.4^{o} x 1.4^{o} 91 levels top level: 78.4 Km	ESM fully interact. aerosols	r1i1p1f2	Seferian (2019a-e) Séférian et al. (2019) Michou et al. (2020)
GFDL-ESM4	1.25^{o} x 1^{o} 49 levels top level: 0.01 hPa	ESM interact. aerosols	r1i1p1f1	Horowitz et al. (2018a-e) Horowitz et al. (2020) Dunne et al. (2020)
MPI-ESM-1-2-HAM	1.875^{o} x 1.875^{o} 47 levels top level: 0.01 hPa	ESM interact. aerosols	r1i1p1f1	Neubauer et al. (2019b, c) Neubauer et al. (2020a-c) Mauritsen et al. (2019) Tegen et al. (2019) Neubauer et al. (2019a) Lohmann and Neubauer (2018)
MRI-ESM2-0	1.125^{o} x 1.125^{o} 80 levels top level: 0.01 hPa	ESM interact. aerosols	r1i1p1f1	Yukimoto et al. (2019a-f) Oshima et al. (2020) Kawai et al. (2019)
NorESM2-LM	2.5^{o} x 1.875^{o} 32 levels top level: 3 hPa	ESM interact. aerosols	r1i1p1f1 r1i1p2f1	Oliviè et al. (2019a-e)[a] Kirkevåg et al. (2018) Seland et al. (2020)

[a] In the references, versions 20191108 and 20190815 are referred to r1i1p1f1, and version 20200218 to r1i1p2f1.

The CNRM-ESM2-1 model (*Séférian et al., 2019*; *Michou et al., 2020*) uses the Reactive Processes Ruling the Ozone Budget in the Stratosphere Version 2 (REPROBUS-C_v2) atmospheric chemistry scheme, in which chemical evolution is calculated only above the 560 hPa level. Below that level, the concentrations of the species are relaxed either toward the yearly evolving global mean abundances (*Meinshausen et al., 2017*) or toward the 560-hPa value. The Tropospheric Aerosols for ClimaTe In CNRM (TACTIC_v2) interactive tropospheric aerosol scheme is also used in CNRM-ESM2-1, which implements a sectional representation of BC, organic matter, sulfates (SO_4), sea-salt and desert dust. The SO_4 precursors evolve in SO_4 aerosols with dependence on latitude (*Séférian et al., 2019*). Biomass burning and anthropogenic emissions are provided by van Marle et al. (2017) and Hoesly et al. (2018), respectively. The cloud droplet number concentration is dependent on the concentrations of sea-salt, sulfate and organic matter, thus representing the cloud albedo (or Twomey) effect, but not any other aerosol-cloud effects.

The GFDL-ESM4 model (*Dunne et al., 2020*; *Horowitz et al., 2020*) consists of the Geophysical Fluid Dynamics Laboratory (GFDL)'s Atmosphere Model version 4.1 (AM4.1), which includes an interactive tropospheric and stratospheric gas-phase and aerosol chemistry scheme. In contrast to the previous model version (AM4.0), nitrate and ammonium aerosols are treated explicitly, the rate of aging of BC and OC from hydrophobic to hydrophilic forms changes depending on the calculated concentrations of hydroxyl radical (OH), and oxidation of SO_2 and dimethyl sulfide (DMS) to produce SO_4 aerosols is driven by the gas-phase oxidant concentrations (OH, O_3 and H_2O_2) and cloud pH (*Horowitz et al., 2020*). The time series of monthly biomass burning and anthropogenic emissions of ozone precursors, aerosols and aerosol precursors are derived from van Marle et al. (2017) and Hoesly et al. (2018), respectively.

The MPI-ESM-1-2-HAM model (*Mauritsen et al., 2019*; *Tegen et al., 2019*; *Neubauer et al., 2019a*; *Lohmann and Neubauer, 2018*) is the latest version of the Max Planck Institute for Meteorology Earth System Model (MPI-ESM1.2) coupled with the Hamburg Aerosol Model version 2.3 (HAM2.3). It contains the atmospheric general circulation model developed by the Max Planck Institute for Meteorology (ECHAM6.3). The ECHAM6.3–HAM2.3 uses a two-moment cloud microphysics scheme in order to study aerosol–cloud interactions and improve the simulation of clouds. The aerosol–cloud interactions are simulated in liquid, mixed-phase and ice clouds (*Neubauer et al., 2019a*). The aerosol microphysics module HAM calculates the evolution of an aerosol ensemble considering the species BC, OC, sulfate, sea salt and mineral dust. In its default version, HAM simulates the aerosol spectrum as the superposition of 7 lognormal modes (nucleation, Aitken, accumulation and coarse modes) (*Tegen et al., 2019*). As far as emissions are concerned, the default version of ECHAM6.3–HAM2.3 uses the Atmospheric Chemistry and Climate Model Intercomparison Project (ACCMIP) emission dataset (*Lamarque et al., 2010*) for anthropogenic and biomass burning emissions (*Tegen et al., 2019*), while for anthropogenic aerosol emissions the Global Fire Assimilation System (GFAS) (*Kaiser et al., 2012*) or the Community Emissions Data System (CEDS) (*Hoesly et al., 2018*) datasets can be used (*Neubauer et al., 2019a*).

The MRI-ESM2 model (*Yukimoto et al., 2019a*; *Oshima et al., 2020*; *Kawai et al., 2019*) includes the MRI Chemistry Climate Model version 2.1 (MRI-CCM2.1) atmospheric chemistry model, which computes the evolution and distribution of ozone and other trace gases in the troposphere and middle atmosphere, and the Model of Aerosol Species in the Global Atmosphere mark-2 revision 4-climate

(MASINGAR mk-2r4c) aerosol model, which contains BC, OC, non sea-salt sulfate, mineral dust, sea salt and aerosol precursor gases (e.g. SO_2 and DMS), assuming external mixing for all aerosol species (*Yukimoto et al., 2019a*). In MASINGAR mk-2r4c the conversion rate of hydrophobic to hydrophilic BC is depended on the rate at which condensable materials cover hydrophobic BC, an approach that could reproduce the seasonal variations of BC mass concentrations that are observed over the Arctic region (*Oshima et al., 2020*).

NorESM2-LM (*Kirkevåg et al., 2018*; *Seland et al., 2020*) is the "low resolution" version of the second version of the coupled Norwegian Earth System Model (NorESM2). It employs the CAM6-Nor atmosphere model, which uses parameterisation schemes for aerosols and aerosol–radiation–cloud interactions, and the OsloAero6 atmospheric aerosol module, which describes the formation and evolution of BC, OC, sulfate, dust, sea salt and secondary organic aerosol. Anthropogenic emissions of BC, organic matter and SO_2 are prescribed based on Hoesly et al. (2018), while biomass burning emissions follow van Marle et al. (2017). The oxidant concentrations of OH, ozone, NO_3 and HO_2 are prescribed by 3D monthly mean fields (*Seland et al., 2020*).

Table 2.2. List of fixed-SST ERF simulations. The 30 year experiments used pre-industrial climatological average SST and sea ice distributions. The year indicates that the emissions or concentrations were fixed to that year (modified from *Collins et al., 2017*).

Experiment name	**CH_4**	**N_2O**	**Aerosol precursors**	**Ozone precursors**	**CFC/ HCFC**	**MIP**
piClim-control	1850	1850	1850	1850	1850	RFMIP/ AerChemMIP
piClim-aer	1850	1850	2014	1850	1850	RFMIP/ AerChemMIP
piClim-BC	1850	1850	1850 (non-BC) 2014 (BC)	1850	1850	AerChemMIP
piClim-OC	1850	1850	1850 (non-OC) 2014 (OC)	1850	1850	AerChemMIP
piClim-SO_2	1850	1850	1850 (non-SO_2) 2014 (SO_2)	1850	1850	AerChemMIP

The simulations mentioned in the beginning of this chapter were carried out within the framework of RFMIP (*Pincus et al., 2016*) and AerChemMIP (*Collins et al., 2017*), which are endorsed by the CMIP6 (*Eyring et al., 2016*). All the models carried out five time-slice experiments (Table 2.2); one control simulation (piClim-control) and four perturbation experiments (piClim-aer, piClim-BC, piClim-OC, piClim-SO_2) covering a period of at least 30 years in total and using fixed climatological average sea surface temperatures (SSTs) and sea ice distributions corresponding to the year 1850, which is considered as a pre-industrial period that matches the onset of the majority of surface temperature records and also the start of the historical climate simulations of the Coupled Model Intercomparison Project (CMIP; *Eyring et al., 2016*). The number of years chosen for these experiments is the minimum value in order to minimize internal variability (mainly from clouds), which generates substantial interannual variability in the ERFs (*Forster et al., 2016*). It should be noted that concentrations of well-mixed greenhouse gases (WMGHGs), emissions of O_3 precursors and O_3 depleting halocarbons, land use and solar irradiance forcings are also set to pre-industrial values (1850).

The control simulation (piClim-control) uses set 1850 values for the CH_4, N_2O, aerosol and aerosol precursors, O_3 precursors and halocarbons emissions or concentrations. Each perturbation experiment is run similarly for the 30-year period following the control experiment, keeping the SSTs and sea ice fixed to pre-industrial levels, but setting one or more of the specified species (concentrations or emissions) to present-day (2014) values (*Collins et al., 2017*). Consequently, in perturbation experiments piClim-BC, piClim-OC, piClim-SO_2, only the BC, OC, SO_2 precursor emissions, respectively, are set to 2014 values while all forcings are set to 1850 values, and in piClim-aer experiment the anthropogenic aerosol precursor emissions are set to 2014 values with all forcings set to 1850 values.

2.2 Calculation Method

As discussed in Chapter 1, ERF represents the change in the net TOA radiative flux after allowing for atmospheric temperatures, water vapor and clouds to adjust but with global mean surface temperature or a portion of surface conditions unchanged. In this study, the fast responses to forcing from aerosols is investigated by fixing SSTs and sea ice cover (SIC) at climatological values, allowing all other parts of the system to respond until reaching steady state (*Hansen et al., 2005*). This allows for ERF to be diagnosed as the difference in the net TOA flux between the perturbed experiments (piClim-aer, piClim-BC, piClim-OC, piClim-SO_2) and the control (piClim-control) simulation (*Hansen et al.*, 2005; *Sherwood et al., 2015*; *Smith et al., 2020*; *Zanis et al., 2020*; *Thornhill et al., 2021a*), in order to estimate the fast responses of pre-industrial climate to present-day aerosols without any ocean response to climate change since SSTs and SIC are fixed (*Zanis et al., 2020*). The fixed-SST ERF estimates are more insensitive to internal climate variability as this method utilizes the long averaging times and the absence or equalization of interannual ocean variability in the perturbed and control simulations (*Sherwood et al., 2015*). In this work, the effect of aerosols only on the net radiative flux at TOA (ERF) and the surface air temperature are considered.

The ERF (measured in W m^{-2}) is calculated following the method of Ghan (2013). In order to quantify the magnitude of various processes to the overall ERF, the effective radiative forcing is analyzed into three main components: (a) ERFari, which accounts for the aerosol-radiation interactions (i.e., scattering and absorption of radiation by anthropogenic aerosols; Eq. 1), (b) ERFaci, which represents the effects of aerosols on cloud radiative forcing (aerosol-cloud interactions; Eq. 2), and (c) ERFalb, which is largely the contribution of changes in surface albedo that are induced by anthropogenic aerosols (Eq. 3) (*Ghan, 2013*). Consequently, the sum of ERFari, ERFaci, and ERFalb gives an approximation of the overall effective radiative forcing of the aerosols species (Eq. 4):

$$\mathrm{ERFari} = \Delta(F - F_{af}), \quad (1)$$

$$\mathrm{ERFaci} = \Delta(F_{af} - F_{csaf}), \quad (2)$$

$$\mathrm{ERFalb} = \Delta F_{csaf}\,, \quad (3)$$

$$\mathrm{ERF} = \mathrm{ERFari} + \mathrm{ERFaci} + \mathrm{ERFalb}, \quad (4)$$

where F is the net (downward minus upward) TOA radiative flux, F_{af} (af: aerosol-free) is the flux calculated ignoring the scattering and absorption of radiation by aerosols, F_{csaf} (cs: clear-sky) is the flux calculated neglecting the scattering and absorption of radiation by both aerosols and clouds and Δ denotes the difference between the perturbation (piClim-aer, piClim-BC, piClim-OC, piClim-SO_2) and the control (piClim-control) experiment (i.e., perturbation minus control).

This approach was implemented for both the shortwave (SW) and longwave (LW) radiation. Moreover the sum of SW and LW radiation was calculated in order to estimate the total ERF for each component (Eq. 5-8):

$$\text{ERFari\_total} = \text{ERFari\_sw} + \text{ERFari\_lw}, \tag{5}$$

$$\text{ERFaci\_total} = \text{ERFaci\_sw} + \text{ERFaci\_lw}, \tag{6}$$

$$\text{ERFalb\_total} = \text{ERFalb\_sw} + \text{ERFalb\_lw}, \tag{7}$$

$$\text{ERF\_total} = \text{ERFari\_total} + \text{ERFaci\_total} + \text{ERFalb\_total}, \tag{8}$$

Due to differences in the spatial horizontal resolution of the models (Table 2.1), all data were brought to a common spatial grid (2.8125^o x 2.8125^o) by applying bilinear interpolation prior to processing. For the sake of consistency, the first 30 years were selected for all simulations. The effective radiative forcing was calculated using the above approach based on Ghan (2013) and the surface temperature changes (indicating the fast responses) were estimated by subtracting the piClim-control experiment from the perturbation experiments for each model individually. A multi-model ensemble for the ERF components and temperature change was created, the results of which are presented in Chapter 3 on an annual and seasonal basis, i.e., for the boreal winter/austral summer (December, January, February – DJF), for the boreal spring/austral autumn (March, April, May – MAM), for the boreal summer/austral winter (June, July, August – JJA), and for the boreal autumn/austral spring (September, October, November – SON). Each individual model's results for ERF and temperature (annual and seasonal) are given separately in Appendices A-E. A paired sample t-test was conducted to the results in order to check their statistical significance at the 95% confidence level.

CHAPTER 3: RESULTS

In this chapter, the ERF estimation and global spatial pattern using the fixed-SST method following Ghan (2013) are presented on an annual and seasonal basis averaged over the globe (Section 3.1), along with the annual and seasonal spatial pattern of the surface temperature fast responses (Section 3.2) for the all-aerosol, BC, OC and SO$_2$ perturbation simulations. The only the multi-model ensemble results are shown here, whereas the results for each individual model can be found in Appendices A through E. The spatial patterns of the ERF components at TOA and the temperature response for each model are shown in Appendix A and E, respectively, tables with ERF values for all experiments on an annual and seasonal level for every model are shown in Appendix B, while barplots and boxplots of annual and seasonal ERF values for all simulations for each individual model are presented in Appendix C and D, respectively.

3.1 Effective Radiative Forcing

3.1.1 Annual

As it can be seen in Fig. 3.1, the globally averaged annual multi-model ensemble total (SW + LW) overall ERF of anthropogenic aerosols (piClim-aer minus piClim-control; Fig. 3.1 first row) is estimated to be –1.09 W m^{-2} (Fig. 3.1a), in good agreement with other studies that examined the ERF using CMIP6 models (e.g., *Zanis et al., 2020*; *Thornhill et al., 2021a*; *Smith et al., 2020*). The lowest values are found predominantly over East and South Asia, along with the Arabian sea and over some parts of Indonesia, S. Africa, S. America, E. Europe and N. Pacific Ocean, while its highest values are over the Alaska, N.W. Canada and Central Africa. The annual global average SW ERF of anthropogenic aerosols is –1.46 W m^{-2}, while the annual global mean LW ERF is 0.37 W m^{-2} (Table 3.1 and Figure 3.6). The total annual global mean ERFari is almost zero (–0.01 W m^{-2}; Fig. 3.1b), with a peak negative value over the Indian Peninsula. The annual SW and LW ERFari are found to be –0.02 W m^{-2} and 0.01 W m^{-2}, respectively. The globally averaged annual ERFaci is strongly negative (–1.11 W m^{-2}; Fig. 3.1c), with a pattern almost identical to that of the overall total ERF and its SW and LW components estimated at –1.40 W m^{-2} and 0.29 W m^{-2}, respectively. The annual global mean ERFalb is calculated at 0.03 W m^{-2}, but it has lower statistical significance globally than the other ERF components (Fig. 3.1d), with its highest values over the Himalayas, in particular, and the adjacent regions in S. Asia, whereas negative values are found over the Arctic. The globally averaged annual SW ERFalb is –0.03 W m^{-2}, while its LW counterpart is 0.06 W m^{-2}.

As far as the BC simulation is concerned (piClim-BC minus piClim-control; Fig. 3.1 second row), the annual global mean overall total (SW + LW) ERF value for the model ensemble is calculated at 0.18 W m^{-2}, peaking over South and mainly, East Asia, with quite high values over parts of Central Africa and Russia, as well (Fig. 3.1e). Its SW and LW components are of equal magnitude (0.09 W m^{-2} each; Table 3.1). The annual total ERFari is positive all over the globe (Fig. 3.1f) and is estimated to be 0.38 W m^{-2}, with no contribution from its LW component. Its highest values are found predominantly over the E. Asia and downwind Pacific Ocean regions, and the Himalayan region. The annual total ERFaci is negative (Fig. 3.1g) and has a value of –0.22 W m^{-2} when averaged over the globe. It is most negative over the N. Pacific, while its SW and LW components are estimated to be –0.37 W m^{-2} and 0.15 W m^{-2}, respectively. The mean annual LW and SW ERFalb are –0.06 W m^{-2} and 0.08 W m^{-2}, respectively, leading to a globally averaged annual total ERFalb of 0.02 W m^{-2} for BC, with the greatest values of the latter located over S. Asia, parts of North and N.E. Russia and the Northeastern part of N. America (Fig. 3.1h).

Table 3.1. Global mean TOA values of the overall ERF (denoted as ERF), ERFari (ARI), ERFaci (ACI), ERFalb (ALB), and globally averaged surface air temperature change (TAS) on an annual and seasonal basis for the piClim-aer, piClim-BC, piClim-OC, and piClim-SO_2 experiments for the multi-model ensemble.

ENSEMBLE		**ERF**			**ARI**			**ACI**			**ALB**			**TAS**
		total	sw	lw	total	sw	lw	total	sw	lw	total	sw	lw	
ANNUAL	aer	-1.09	-1.46	0.37	-0.01	-0.02	0.01	-1.11	-1.40	0.29	0.03	-0.03	0.06	-0.03
	BC	0.18	0.09	0.09	0.38	0.38	0.00	-0.22	-0.37	0.15	0.02	0.08	-0.06	0.02
	OC	-0.35	-0.40	0.06	-0.07	-0.07	0.00	-0.29	-0.33	0.04	0.01	0.00	0.01	-0.01
	SO2	-1.10	-1.39	0.29	-0.27	-0.27	0.01	-0.84	-1.04	0.20	0.01	-0.08	0.09	-0.04
DJF	aer	-0.84	-1.12	0.28	-0.02	-0.03	0.01	-0.82	-1.08	0.26	0.01	0.00	0.01	0.00
	BC	0.20	0.04	0.16	0.28	0.28	0.00	-0.10	-0.28	0.17	0.02	0.03	-0.02	0.02
	OC	-0.35	-0.36	0.01	-0.05	-0.05	0.00	-0.30	-0.32	0.02	0.00	0.01	-0.02	0.00
	SO2	-0.98	-1.10	0.13	-0.22	-0.23	0.01	-0.73	-0.86	0.13	-0.02	-0.01	-0.01	0.00
MAM	aer	-1.23	-1.60	0.37	0.03	0.03	0.00	-1.30	-1.60	0.30	0.04	-0.03	0.07	-0.03
	BC	0.33	0.23	0.10	0.44	0.44	0.00	-0.21	-0.35	0.14	0.10	0.14	-0.04	0.03
	OC	-0.29	-0.34	0.04	-0.05	-0.06	0.01	-0.25	-0.27	0.02	0.01	0.00	0.01	-0.02
	SO2	-1.34	-1.61	0.27	-0.27	-0.26	0.00	-1.04	-1.23	0.19	-0.04	-0.12	0.08	-0.05
JJA	aer	-1.19	-1.60	0.41	0.02	0.00	0.02	-1.24	-1.52	0.28	0.03	-0.09	0.11	-0.05
	BC	0.08	0.10	-0.01	0.45	0.45	0.01	-0.35	-0.46	0.11	-0.03	0.11	-0.14	0.04
	OC	-0.33	-0.40	0.07	-0.07	-0.08	0.00	-0.26	-0.31	0.05	0.00	-0.02	0.02	-0.01
	SO2	-1.11	-1.55	0.44	-0.29	-0.30	0.01	-0.86	-1.10	0.23	0.04	-0.15	0.19	-0.07
SON	aer	-1.10	-1.50	0.40	-0.05	-0.07	0.02	-1.09	-1.42	0.33	0.04	-0.02	0.06	-0.03
	BC	0.12	0.00	0.13	0.36	0.35	0.00	-0.21	-0.38	0.17	-0.03	0.02	-0.05	0.02
	OC	-0.41	-0.51	0.10	-0.09	-0.10	0.00	-0.35	-0.41	0.06	0.02	-0.01	0.03	-0.02
	SO2	-0.96	-1.30	0.34	-0.29	-0.30	0.01	-0.74	-0.98	0.24	0.07	-0.02	0.09	-0.04

Regarding the OC experiment (piClim-OC minus piClim-control; Fig. 3.1 third row), it exerts a negative TOA annual total ERF overall (Fig. 3.1i), with a value of –0.35 W m^{-2} mainly due to its SW rather than its LW component (–0.40 W m^{-2} and 0.06 W m^{-2}, respectively; Table 3.1). The negative values peak over E. Asia and the N. Pacific Ocean region downwind, and Indonesia, whereas the positive ones over the Northwestern part of N. America. OC exhibits a low total annual ERFari of –0.07 W m^{-2} entirely due to its SW component and appears to peak over the Himalayas and W. Indonesia, while over the rest of the globe it is close to zero (Fig. 3.1j). The annual

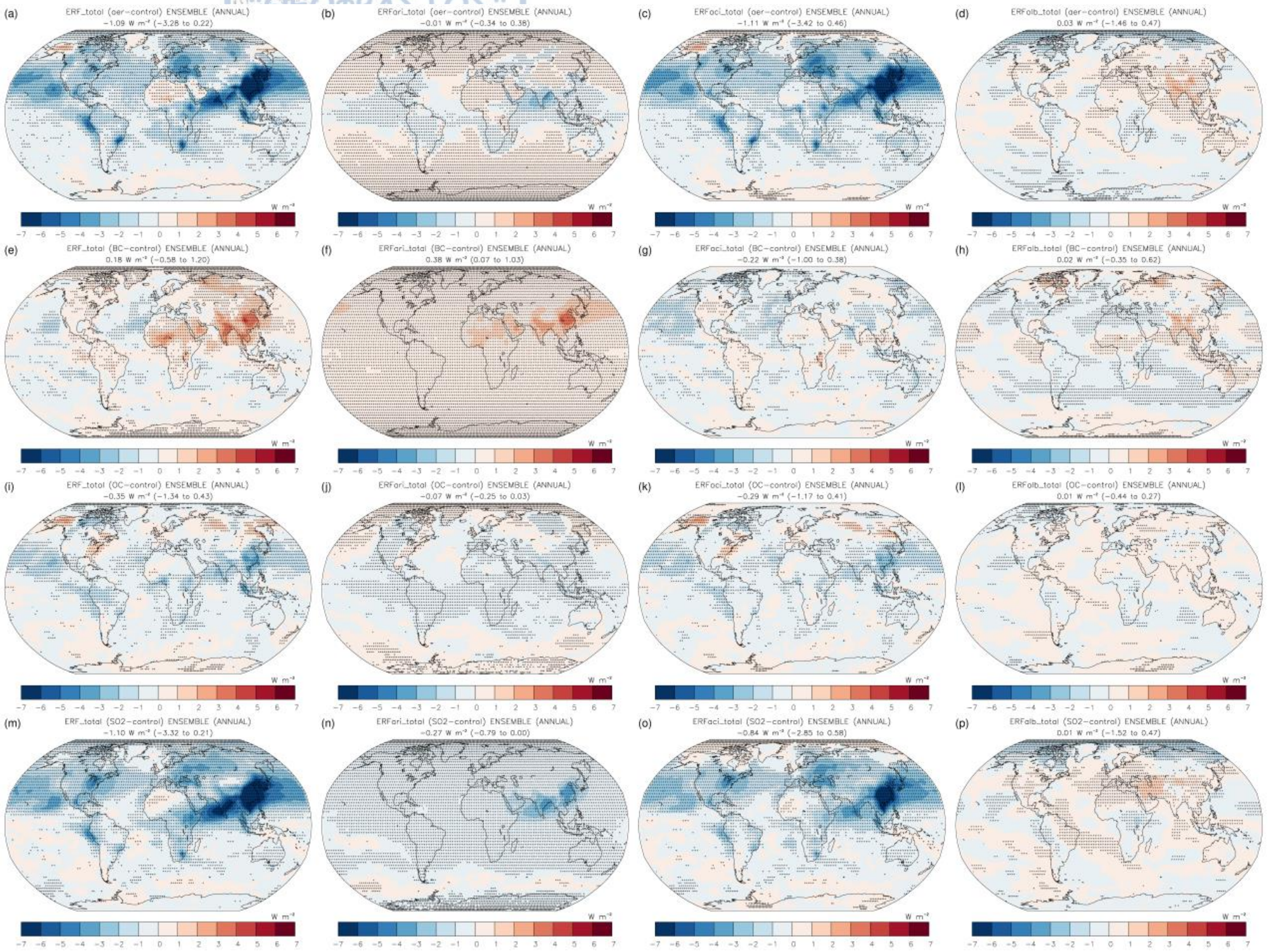

Figure 3.1. Spatial TOA distribution of the annual mean total (SW + LW) ERF (first column), ERFari (second column), ERFaci (third column), and ERFalb (fourth column) in the piClim-aer (first row), piClim-BC (second row), piClim-OC (third row), and piClim-SO_2 (fourth column) experiment for the multi-model ensemble. The black crosses indicate the statistically important values in the 95% confidence level. The global field means (5th to 95th percentiles in the parenthesis) are shown in W m^{-2}.

total ERFaci for OC is –0.29 W m^{-2} mostly due to its SW component, which is estimated to be –0.33 W m^{-2}, whereas the annual LW ERFaci is –0.06 W m^{-2}. The annual total ERFaci dominates the TOA horizontal distribution of the overall total ERF, as the spatial pattern of the two are almost identical (Fig. 3.1k). The annual global mean ERFalb is found to be nearly zero (0.01 W m^{-2}) with negligible spatial variation (Fig. 3.1l).

SO_2 (piClim-SO_2 minus piClim-control; Fig. 3.1 fourth row) produces a globally averaged annual total ERF of –1.10 W m^{-2}, which is slightly greater in magnitude than the total ERF of anthropogenic aerosols, indicating that it plays a dominant role in the overall TOA radiative forcing. Its value is due to its strong SW ERF component, which is estimated to be –1.39 W m^{-2}, while its LW counterpart is –0.29 W m^{-2} (Table 3.1). The SO_2 annual total ERF is highly negative over a large area covering East Asia, Western N. Pacific, India and the Arabian Sea, with other regions, such as parts of East and South Africa, Western S. America, E. Europe, Eastern N. Pacific and Eastern N. America also exhibiting significant negative TOA total ERF (Fig. 3.1m). The global mean annual total ERFari is –0.27 W m^{-2} almost entirely due to its SW component and has a distinct signal over East and South Asia (Fig. 3.1n). The annual TOA total ERFaci is estimated at –0.84 W m^{-2}, because of its SW component averaging at –1.04 W m^{-2} over the globe, while LW ERFaci is 0.20 W m^{-2}. ERFaci has a spatial pattern analogous to that of the overall ERF (Fig. 3.1o), but weaker in magnitude (except for E. Asia) and with positive values in the Arctic. The annual SW and LW ERFalb nearly counterbalance each other, producing an annual total TOA ERFalb of 0.01 W m^{-2} (Fig. 3.1p), with the most negative (positive) values located over the Arctic (Middle East).

3.1.2 DJF

During the boreal winter (DJF; Fig. 3.2), the total (SW + LW) all-aerosol TOA ERF is slightly weaker at –0.84 W m^{-2}, but is more pronounced and statistically significant only over the areas that had the most negative annual ERF values (i.e., East and South Asia, East Indonesia, Arabian Sea, South Africa, and parts of Central and South America; Fig. 3.2a), with its SW (LW) component estimated to be –1.12 W m^{-2} (0.28 W m^{-2}). The global mean all-aerosol ERFari (Fig. 3.2b) is of similar magnitude and pattern as the annual ERFari, but with more negative forcing over the Indian Peninsula. It is estimated at –0.02 W m^{-2}, with its SW and LW components being –0.03 W m^{-2} and 0.01 W m^{-2}, respectively. The total ERFaci in DJF (Fig. 3.2c) is less negative than its annual value (–0.82 W m^{-2}) and has an almost identical spatial pattern with the overall all-aerosol ERF. The global mean all-aerosol total ERFalb in DJF is 0.01 W m^{-2} due only to its LW component (Table 3.1) and is statistically important only over S. Asia, where it peaks (Fig. 3.2d).

In DJF, the TOA BC total ERF (Fig. 3.2e) is almost the same as the annual total ERF, with a value of 0.20 W m^{-2} mostly due to its LW component (0.16 W m^{-2}), being statistically significant in E. Asia, where it peaks, S. Asia and the Arabian Peninsula, and is dominated by ERFari (Fig. 3.2f), which is estimated to be 0.28 W m^{-2} solely due to its SW component and is also highest in East Asia. ERFaci and ERFalb caused by BC in DJF are estimated at –0.10 W m^{-2} and 0.02 W m^{-2}, respectively, and are generally not statistically significant (Fig. 3.2g and h, respectively).

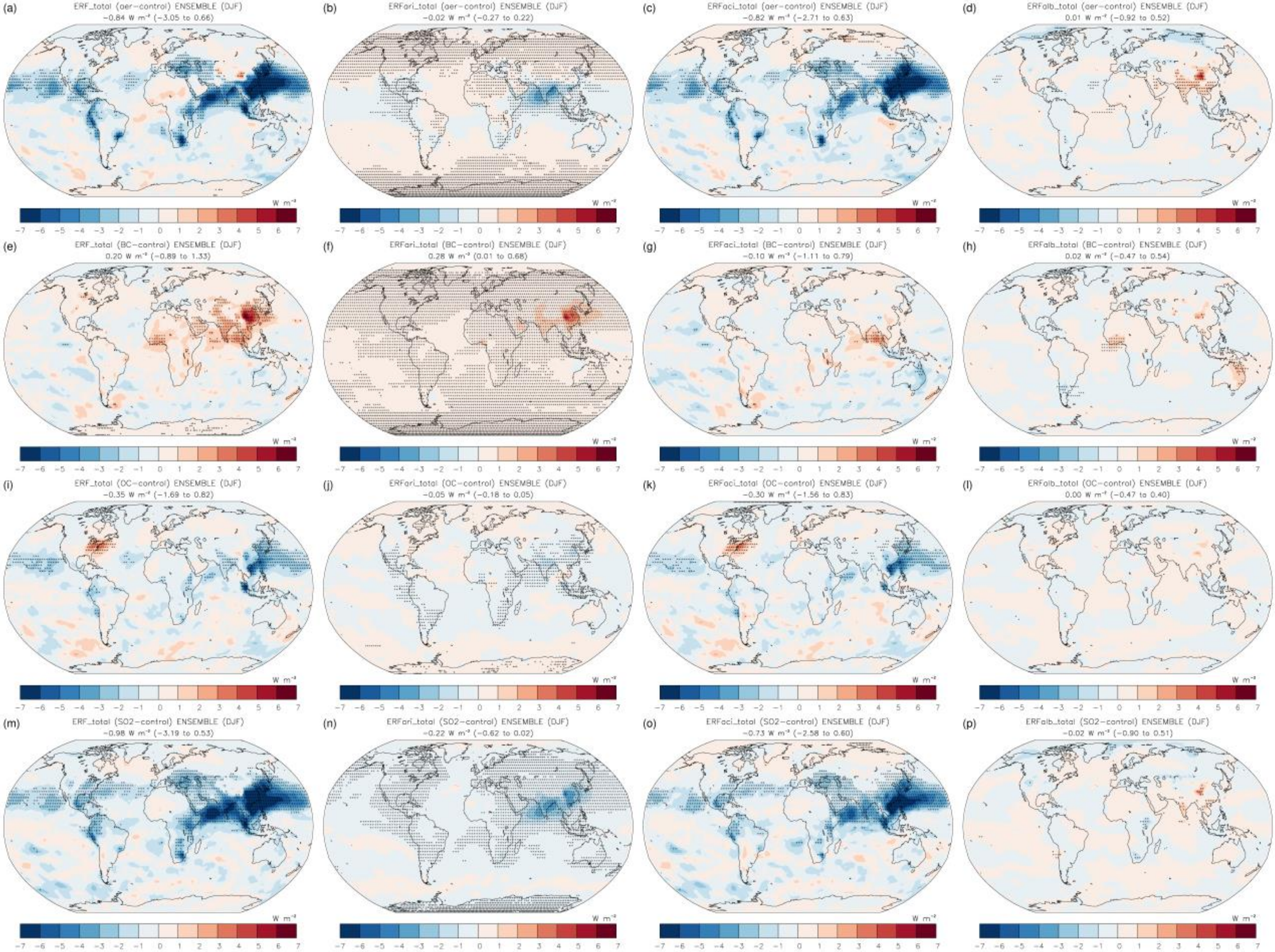

Figure 3.2. As in Fig. 3.1, but for DJF.

The total DJF ERF due to OC (Fig. 3.2i) is identical with its annual value (–0.35 W m^{-2}), its horizontal distribution is analogous to its annual spatial pattern, but with more pronounced peak regions, is statistically important only over Eastern N. America (where it is most positive), E. Indonesia and E. Asia and downwind N. Pacific (where the most negative forcing is located), and is dominated by ERFaci (Fig. 3.2k), which is of similar magnitude (–0.30 W m^{-2} almost entirely due to its SW component). The DJF total OC ERFari and ERFalb (Fig. 3.2j and l, respectively) have nearly the same values with their annual counterparts (–0.05 W m^{-2} and 0.00 W m^{-2}, respectively, with DJF ERFari entirely due to its SW component), but are much less statistically significant.

The total SO_2 ERF in DJF is less negative than its annual value (–0.98 W m^{-2} mostly due to its SW component), especially in the mid- and high latitudes of NH, peaks in South and East Asia (Fig. 3.2m), with the latter peak region appearing to have shifted eastwards downwind the N. Pacific (same as in the case of the total all-aerosol overall ERF), and is clearly dominated by ERFaci (with a value of –0.73 W m^{-2} mainly due to its SW component), with which shares a common spatial pattern (Fig. 3.2o). ERFari is akin to its annual value (–0.22 W m^{-2} almost solely due to its SW component) and spatial pattern (Fig. 3.2n), but more positive, especially in the Arctic, and generally less statistically significant, while ERFalb becomes slightly negative (–0.02 W m^{-2} with equal contribution from its SW and LW components), but is not statistically significant (Fig. 3.2p).

3.1.3 MAM

In boreal spring (MAM; Fig. 3.3) the all-aerosol total ERF is more negative than its annual value (–1.23 W m^{-2} with a strongly negative SW component that is estimated at –1.60 W m^{-2}), and is again dominated by ERFaci, which is even more negative (–1.30 W m^{-2} with equally negative SW component). Both ERF and ERFaci have spatial patterns similar to each other and their annual counterparts, but with much more negative values over the entire N. Pacific Ocean, Eastern N. America, and Central and Eastern Europe (Fig. 3.3a and c, respectively). All-aerosol total TOA ERFarci has an almost identical horizontal distribution to its annual and DJF counterparts (Fig. 3.3b), but has a positive value estimated to be 0.03 W m^{-2} due solely to its SW component (Table 3.1). ERFalb is of almost the same magnitude in MAM as annually (estimated at 0.04 W m^{-2}) and has a spatial pattern resembling both the annual and DJF ERFalb distribution, but with more positive values over the continental S. Asia (Fig. 3.3d).

The global mean MAM total ERF due to BC is almost twice as much as its annual value (0.36 W m^{-2} with the SW value being greater than double compared to the LW component) and with higher positive values over the entire Eurasia, along with Central Africa and the Arctic (Fig. 3.3e). The total ERFari is also stronger, with a value of 0.44 W m^{-2} entirely due to its SW component, peaking again in E. Asia, but having more positive values all over the N. Pacific and the Arctic (Fig. 3.3f). The global mean TOA ERFaci is similar to the annual ERFaci value (–0.21 W m^{-2}) with a resembling spatial pattern, but much less statistically significant (Fig. 3.3g), while the total MAM ERFalb due to BC is more positive, with a globally averaged value of 0.10 W m^{-2}, especially over the Himalayan region (where it peaks), Russia, Myanmar, and Thailand, but statistically significant mostly in the aforementioned regions (Fig. 3.3h).

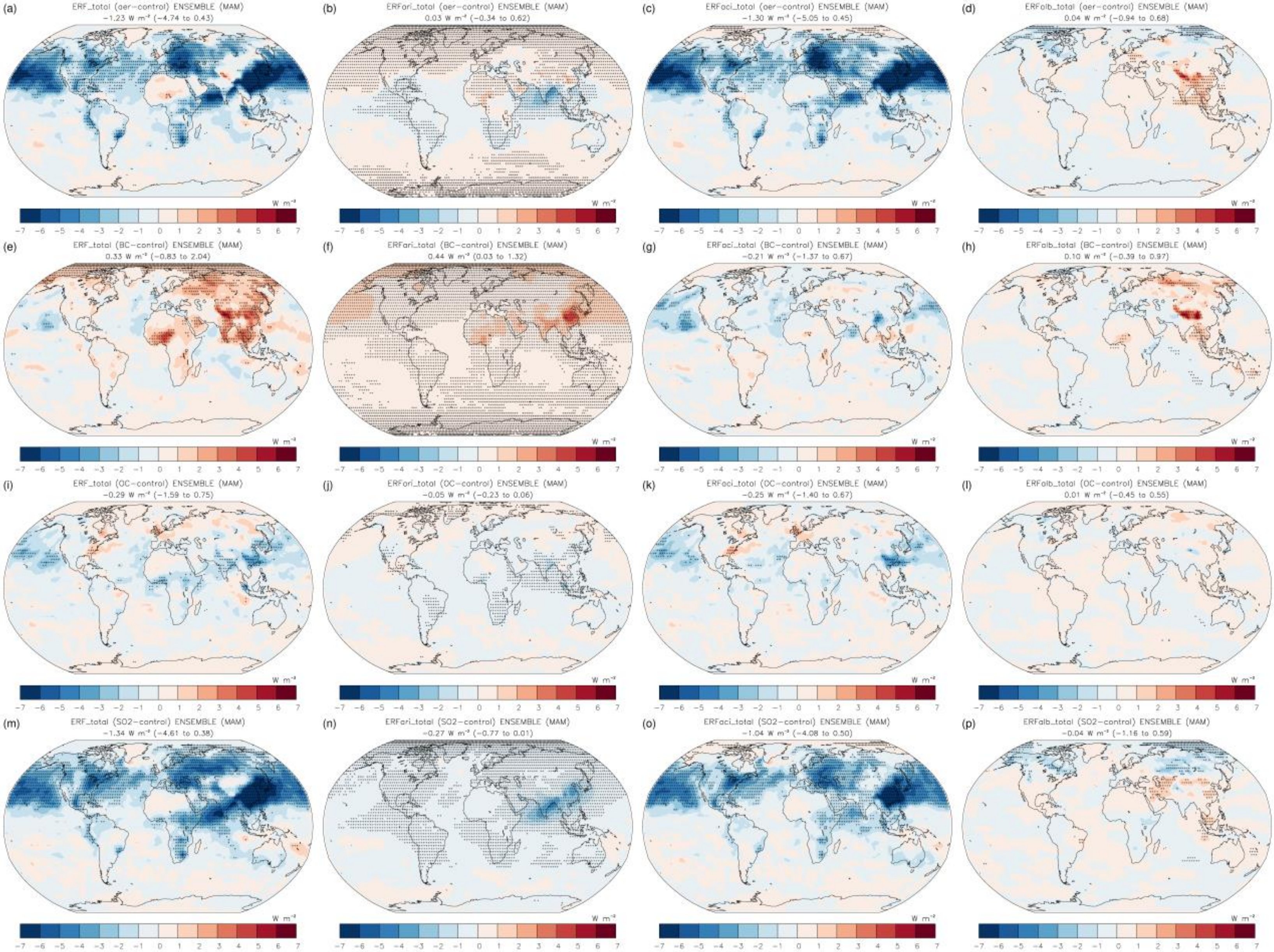

Figure 3.3. As in Fig. 3.1, but for MAM.

The globally averaged TOA MAM total ERF caused by OC is slightly less negative and estimated at –0.29 W m^{-2} (mainly due to its SW component) and its TOA distribution is quite similar to its mean annual, but much less statistically significant (Fig. 3.3i). The MAM ERFari has the same value to its DJF counterpart (almost entirely due to its SW component), with almost identical spatial pattern and statistical significance (Fig. 3.3j). ERFaci is estimated to be –0.25 W m^{-2} (basically due to its SW component), which is a bit less negative than its annual and DJF counterparts, and peaks in E. Asia and some parts of the N. Pacific Ocean, where it is statistically significant (Fig. 3.3k). The OC MAM ERFalb is equal to the global mean annual value (solely due to its LW component), with a spatial pattern akin to the annual, but without statistical significance (Fig. 3.3l).

As in the all-aerosol case, the MAM SO_2 global mean total ERF is more negative than both the annual and DJF, with an estimated value of –1.34 W m^{-2} (with almost equally strong SW ERF as that in the all-aerosol case), has a nearly identical spatial distribution to its annual counterpart, but with stronger negative forcing over the entire N. Pacific Ocean, Eastern N. America and Eurasia, and more positive values over Greenland and east of Australia (Fig. 3.3m). As for the mean annual state and DJF, in the case of SO_2 for MAM, the total ERF is dominated by ERFaci, whose total TOA global mean value is –1.04 W m^{-2} (mostly due to its SW component) and spatial pattern is almost the same as for the total ERF, but with more confined peak regions in E. Asia and the Northern continental Eurasia, and stronger positive forcing over the Arctic (Fig. 3.3o). ERFari has a value equal to its annual global mean (nearly solely due to its SW component) and a horizontal TOA distribution almost identical to both the annual and DJF patterns (Fig. 3.3n). The SO_2 MAM total ERFalb is estimated to be –0.04 W m^{-2}, with statistical significance only over the areas with the most positive (Middle East, Central and East Asia) and negative (Central Russia and oceanic parts within the Arctic Circle) values (Fig. 3.3p).

3.1.4 JJA

During boreal summer (JJA; Fig. 3.4), the all-aerosol global mean annual total ERF is estimated at –1.19 W m^{-2}, less than its MAM value but still more negative than its annual value. It generally follows the annual spatial pattern (Fig. 3.4a), but with stronger negative forcing over the Indian Peninsula, Russia, the easternmost edge of the S. Pacific adjacent to S. America, E. Europe, the northern parts of N. America and the Arctic, and a pronounced region of peaking positive forcing over Alaska. The total JJA annual ERFaci has a similar TOA distribution (Fig. 3.4c), but with positive values over the Arctic and a global mean value of –1.24 W m^{-2}, mainly due to its SW component, which is highly negative, as in the case of the total ERF (Table 3.1). The total ERFari is 0.02 W m^{-2}, solely due to its LW component (the MAM all-aerosol ERFari is also positive, with almost the same magnitude, but due only to its SW component), and its spatial pattern resembles the annual, but with more negative values over Eurasia and without the peak negative forcing over India (Fig. 3.4b). The global mean JJA total ERFalb is the same as the annual, with a quite similar, though much less statistically significant, TOA distribution, but with more negative values over the Arctic, and more distinct positive forcing over the Western N. America, E. Europe, Central and South continental Asia (Fig. 3.4d).

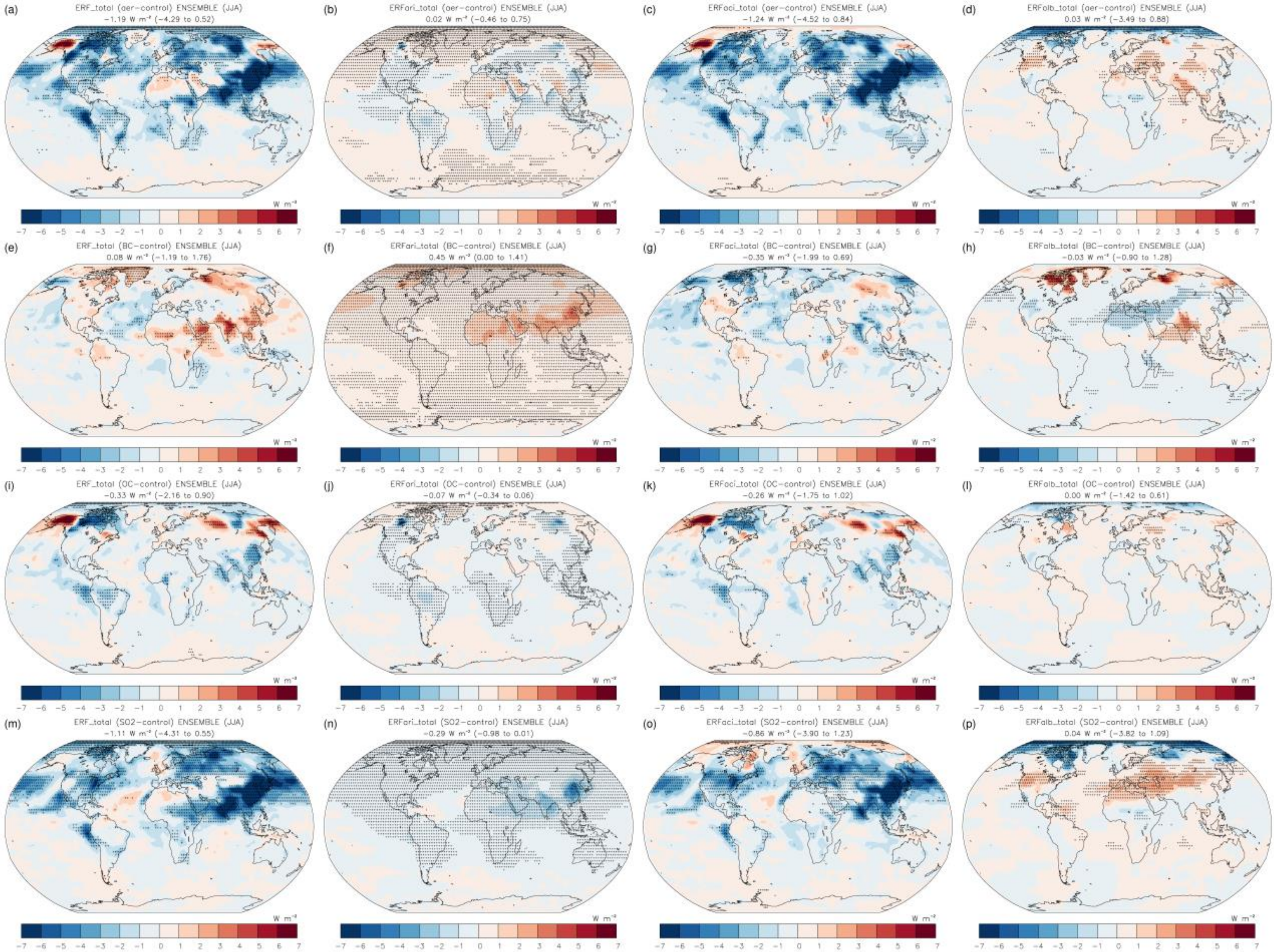

Figure 3.4. As in Fig. 3.1, but for JJA.

The JJA BC total ERF is estimated to be 0.08 W m^{-2} mainly due to its SW component, and peaks over the Indian and Arabian Peninsulas, and N. Russia (Fig. 3.4e). The JJA total ERFari is of almost equal magnitude as its MAM counterpart (0.45 W m^{-2} due to its SW component), and has a spatial TOA distribution similar to MAM, but with a weaker positive forcing over E. Asia and the N. Pacific, and more positive values over N. Africa and S. Asia (Fig. 3.4f). ERFaci is most negative in JJA, with a value of –0.35 W m^{-2} (basically due to its SW component), and has a unique spatial pattern, with the negative (positive) forcing peaking over the northern parts of N. America, the easternmost edge of Russia and in N. India (Central Russia) (Fig. 3.4g). The global mean BC total ERFalb is slightly negative, with a value of –0.03 W m^{-2}, with the strongest positive forcing found over the northeastern part of N. America and N. Russia, followed by the Indian Peninsula and the northeastern tip of Russia, along with a negative forcing extending from Central Asia to N. Africa and the Mediterranean Sea (Fig. 3.4h).

In the case of OC, while the global mean JJA total ERF is of similar magnitude to the annual and DJF values (–0.33 W m^{-2}, basically due to its SW component), it exhibits a special TOA distribution, of little statistical significance, however, with distinct regions of positive and negative forcing (Fig. 3.4i). The most positive (negative) values are found over Alaska, N.E. Asia and Central Russia (the northern half of N. America, a small region in Central Russia, E. China, India, and the oceanic region just west of S. America), a spatial pattern that shares with ERFaci, which is estimated to be –0.26 W m^{-2} (again mainly due to SW ERFaci; Fig. 3.4k). The global mean JJA ERFari is equally strong as its annual counterpart, but less statistically significant, and with two pronounced peak negative regions in Canada and Central Russia (Fig. 3.4j). ERFalb has a globally averaged value of 0.00 W m^{-2} (with equally strong but of opposite sign SW and LW components), with more negative forcing over the Arctic and Northeastern N. America, but with no statistical significance (Fig. 3.4l).

Regarding SO_2, it exerts a global mean JJA total ERF almost identical to its annual mean (–1.11 W m^{-2}) and has a similar TOA pattern, but with stronger negative forcing over the mid- and high latitudes of NH (Fig. 3.4m). The JJA total ERFari is of similar magnitude to its annual and MAM counterpart (–0.29 W m^{-2} almost solely due to its SW component) and its spatial pattern remains almost identical, but with less negative forcing over the Indian Peninsula (Fig. 3.4n). The JJA SO_2 ERFaci and ERFalb, although of similar strength to their annual mean values when averaged over the globe (–0.86 W m^{-2} and 0.04 W m^{-2}, respectively), their spatial distributions is an enhanced version of their respective annual spatial patterns, in which the forcing becomes more negative (positive) over areas that exhibited quite weaker negative (positive) values. Compared to their respective annual TOA patterns, the JJA ERFaci is more negative (positive) in the low and mid-latitudes of NH (in the Arctic Circle), while the reverse is true for the JJA ERFalb (Fig. 3.4o and p, respectively).

3.1.5 SON

In the boreal autumn (SON; Fig. 3.5) the all-aerosol total ERF is –1.10 W m^{-2} (almost equal to its annual mean value) with a similar spatial pattern to the annual TOA horizontal distribution, but with generally weaker (stronger) negative forcing over the N. Pacific (S. Africa and westernmost edge of S. America), and more positive values over the Arctic and the Sahara (Fig. 3.5a), a pattern that shares with the

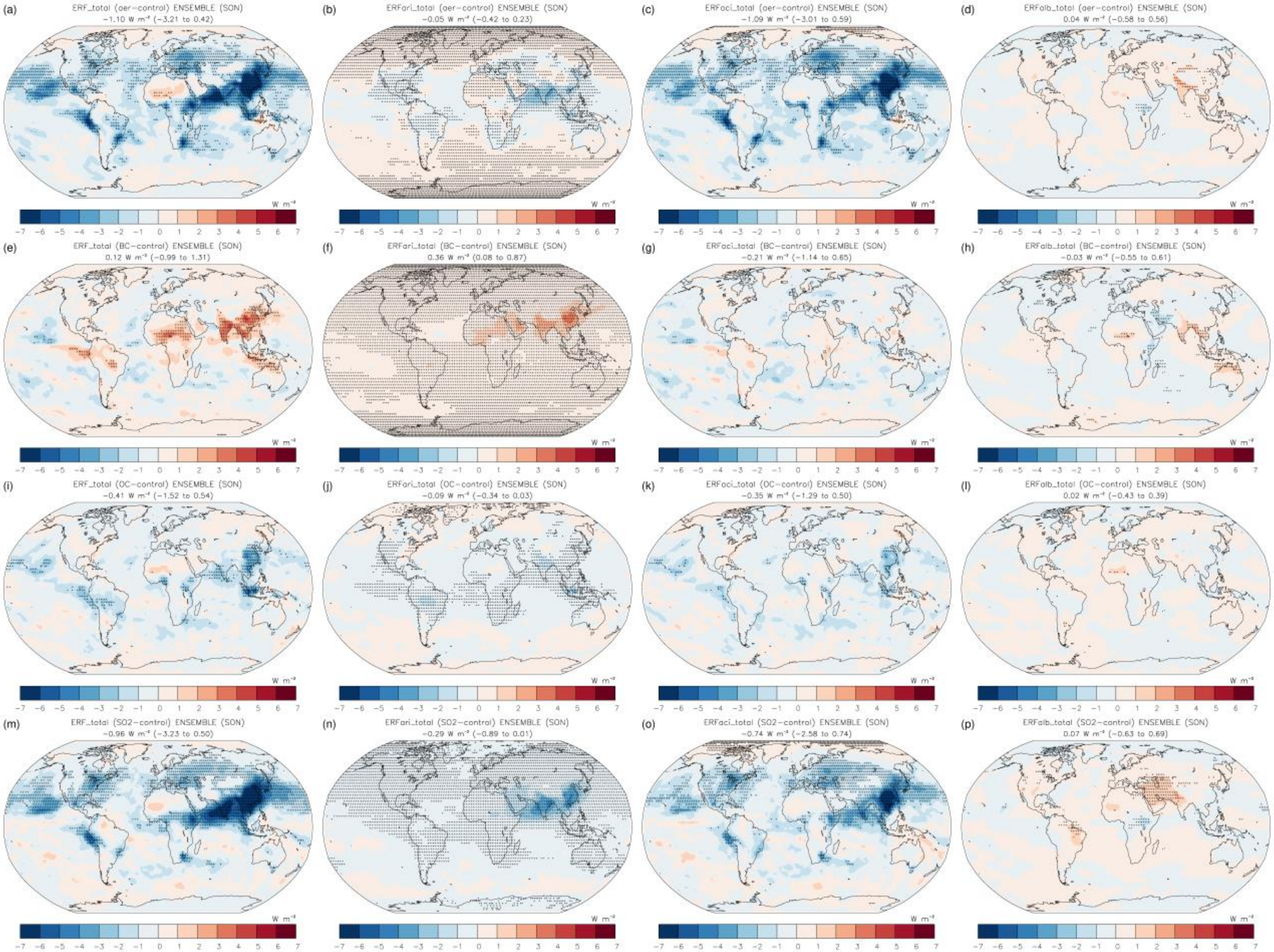

Figure 3.5. As in Fig. 3.1, but for SON.

SON total ERFaci (except for the Saharan region), which is estimated to be –1.09 W m^{-2} (Fig. 3.5c). The SON ERFari is –0.05 W m^{-2} and its TOA pattern is identical to the annual (Fig. 3.5b). The all-aerosol global mean total ERFalb is of similar magnitude to the other seasons (0.04 W m^{-2}), but is generally very close to zero all around the globe, except for the Himalayas, where it is most positive (Fig. 3.5d).

The SON globally averaged BC total ERF is 0.12 W m^{-2} and has a spatial pattern very similar to the annual, but less statistically significant (Fig. 3.5e). The SON BC ERFari is positive all over the globe, with a value and TOA distribution similar to the annual (0.36 W m^{-2} solely due to its SW component), but with weaker positive forcing over the N. Pacific (Fig. 3.5f). In a similar manner, SON ERFaci is of almost identical global mean value (–0.21 W m^{-2} a) and spatial pattern to the annual, but not statistically significant (Fig. 3.5g). The SON BC total ERFalb retains its JJA global mean value and its spatial horizontal pattern at TOA resembles the annual pattern, but lacks statistical significance nearly all over the globe (Fig. 3.5h).

In the OC simulation, the total ERF attains its most negative global mean in SON, with an estimated value of –0.41 W m^{-2}, mainly due to its SW component, and exhibits more pronounced negative forcing over E. Asia and Indonesia (Fig. 3.5i), although it generally lacks statistical significance over the globe. The SON total ERFari is estimated at –0.09 W m^{-2} due to its SW component (Table 3.1), with a similar, yet less statistically significant, spatial pattern to the annual (Fig. 3.5j). The total ERFaci, although more negative during SON when averaged globally (–0.35 W m^{-2} predominantly due to its SW contribution) and with a spatial distribution resembling the annual pattern, it lacks statistical significance in nearly the entire globe (Fig. 3.5k). The same applies to the OC SON total ERFalb, whose global mean is estimated at 0.02 W m^{-2} (Fig. 3.5l).

Regarding the SO_2 experiment, the SON total ERF is slightly less negative than its annual counterpart (–0.94 W m^{-2} basically due to its strongly negative SW component) and its TOA distribution is pretty much the same, but with less negative forcing and statistical significance in the NH high latitudes than the annual (Fig. 3.5m). It is again dominated by ERFaci, which is estimated at –0.74 W m^{-2} (mainly due to its SW contribution) and has a nearly identical TOA spatial distribution, except for the weaker negative forcing over the Indian Peninsula and the Eastern N. Pacific Ocean (Fig. 3.5o). The total ERFari is –0.29 W m^{-2} (almost solely due to its SW component) and has the same spatial pattern at TOA as the annual ERFari (Fig. 3.5n). The SO_2 total ERFalb exhibits its most positive value in SON, which is estimated to be 0.07 W m^{-2} and produces a spatial pattern at TOA akin to the annual, but with weaker negative forcing in the Arctic and much less statistical significance globally (Fig. 3.5p).

3.1.6 Intermodel Differences

It is implied that the above analysis represents only an average state derived from the combination of the six CMIP6 model configurations used in this work. Each individual model produces results that may differ in magnitude, sign and/or spatial pattern on an annual and/or seasonal level (Appendices A and C). For instance, while similar in sign, the magnitude and spatial TOA pattern of the all-aerosol and SO_2 annual total ERFaci that CNRM-ESM2-1 produces differs significantly from the ones presented here for the ensemble (Fig. A1), whereas MPI-ESM-1-2-HAM appears to overestimate (relative to the ensemble mean) the forcing due to ACI in all experiments (Fig.

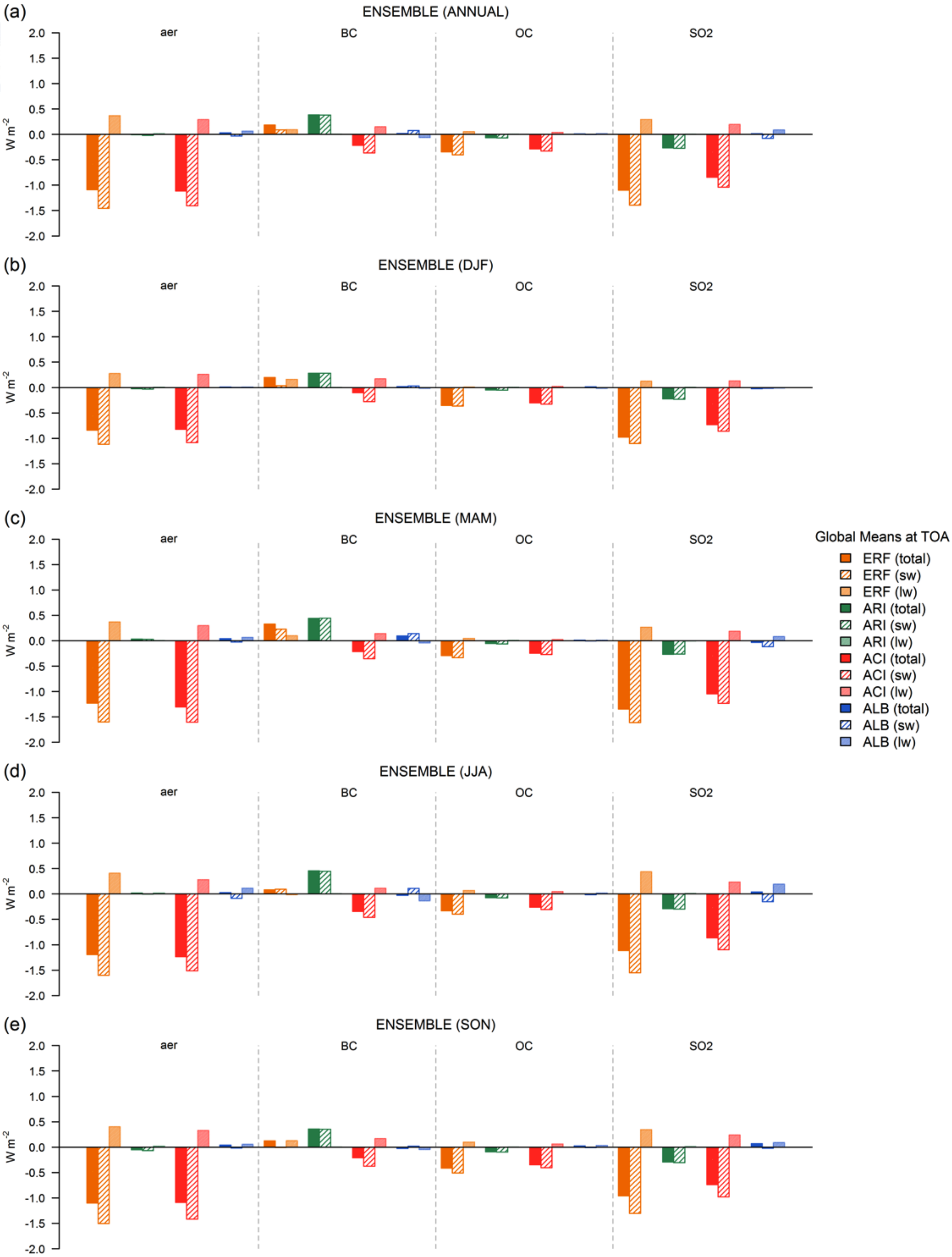

Figure 3.6. Barplots of the globally averaged (a) annual, (b) DJF, (c) MAM, (d) JJA, and (e) SON SW, LW, and total (SW + LW) TOA ERF components (overall ERF, ERFari, ERFaci, ERFalb) for the piClim-aer, piClim-BC, piClim-OC, and piClim-SO_2 simulations for the multi-model ensemble.

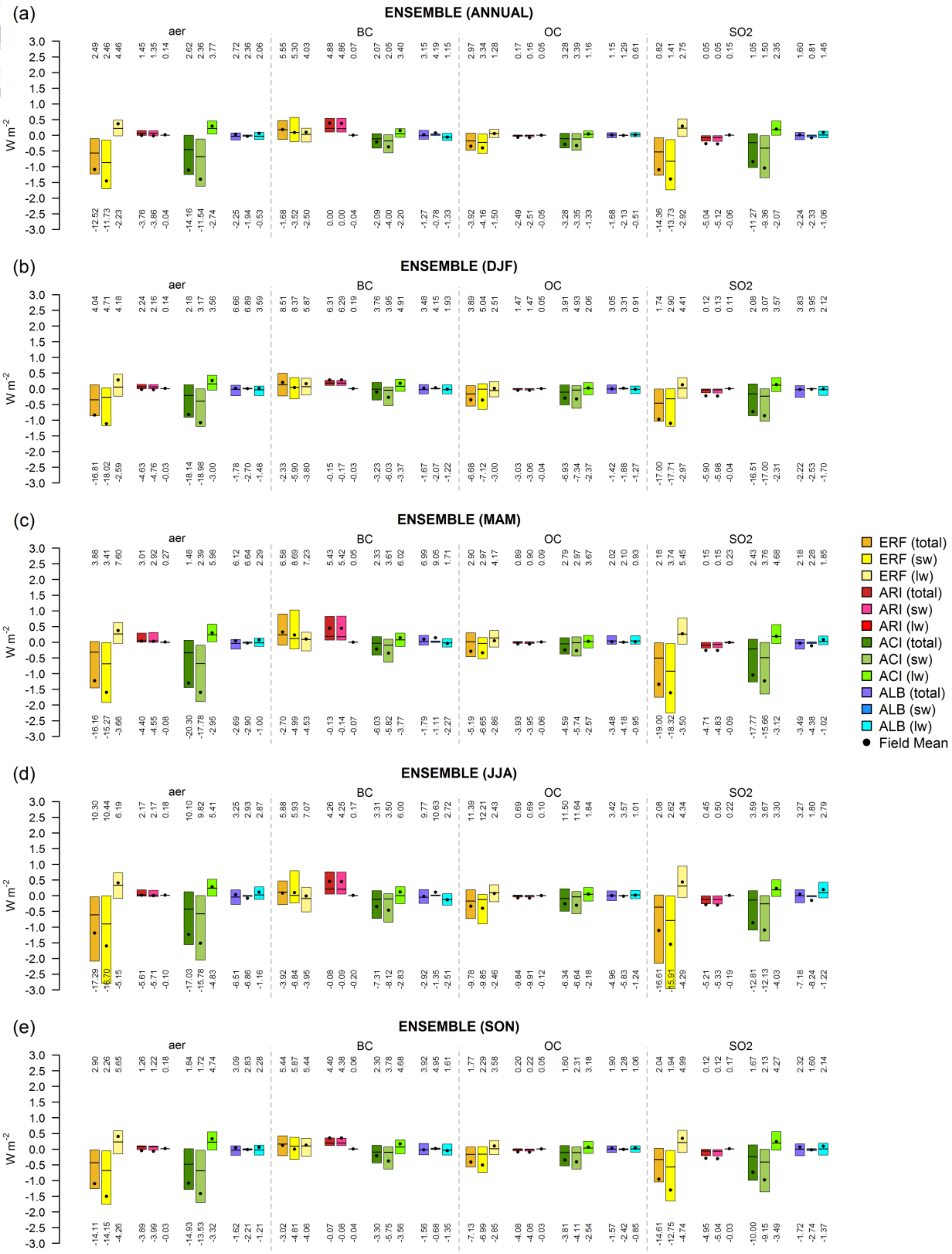

Figure 3.7. Boxplots of the (a) annual, (b) DJF, (c) MAM, (d) JJA, and (e) SON SW, LW, and total (SW + LW) TOA ERF components (overall ERF, ERFari, ERFaci, ERFalb) for the piClim-aer, piClim-BC, piClim-OC, and piClim-SO2 simulations for the multi-model ensemble. Each box's lower (upper) limit is the 25th (75th) percentile, the black horizontal lines denote the median (50th percentile), the black circles are the global field means at TOA, and the numbers on the lower (upper) bounds of each subplot denote the minimum (maximum) field values.

A11). The GFDL-ESM4 and MRI-ESM2-0 models quite accurately capture the “hot-spots” of negative forcing over East and South Asia (Fig. A6 and Fig. A16, respectively), but the latter produces a strong positive (negative) annual total ERF over S. Asia and the Maritime Continent (Easternmost Tropical S. Pacific) in the BC (all-aerosol and SO_2) simulation. The NoeESM2-LM (p1) and (p2) models overestimate (underestimate), relative to the ensemble mean, the annual negative forcing due to ACI over the N. Pacific (E. Asia) in the all-aerosol and SO_2 simulations (Fig. A21 and Fig. A26, respectively), while the NorESM2-LM (p2) model produces a much stronger positive (negative) annual total ERFaci (ERFalb) over the Arctic in the same simulations than presented here. It is not uncommon for the seasonal results to vary even further.

The overall total (SW + LW) ERF and total ERFaci show considerably larger spread in the anthropogenic aerosol and SO_2 experiments due to the much greater interquartile range of their respective SW components, which is true both on annual and seasonal level (Fig. 3.7). In contrast, ERFalb exhibits a narrower spread throughout the season in all simulations, while the total ERFari has a larger interquartile range in MAM and JJA only in the BC experiment due to the larger SW ERFari spread. The large spread of SW ERF and SW ERFaci is a robust feature among all models (Appendix D), although some exhibit larger interquartile range in their respective LW component (e.g., MRI-ESM2-0). Generally, the majority of the models shows little spread in ERFari (except for MPI-ESM-1-2-HAM and GFDL-ESM4 in the BC simulations, with the latter exhibiting substantial interquartile range in the all-aerosol experiment as well), while the LW ERFalb spread, and consequently the total ERFalb spread increase in CNRM-ESM2-1 and GFDL-ESM4. The nearly zero multi-model ensemble annual total ERFari derives from the combination of positive (i.e., GFDL-ESM4 and MPI-ESM-1-2-HAM), negative (i.e., CNRM-ESM2-1 and MRI-ESM2-0), and almost zero (NorESM2-LM (p1) and (p2)) respective annual total ERFari values of the individual models, which end up counterbalancing each other.

3.2 Surface Air Temperature Response

3.2.1 All-aerosol Experiment

The global surface air temperature response on an annual and seasonal basis is presented in Fig. 3.8. In the all-aerosol experiment (Fig. 3.8; first row), the global mean annual response is a decrease by 0.03 ^{o}C (Table 3.1 and Fig. 3.9). Eurasia appears to experience a surface cooling, concentrated in East and South Asia (particularly in the Himalayas), followed by E. Europe and N. America, while there is an apparent warming in the Arctic Circle (excluding Greenland and the Northeastern N. America) and the Antarctic (Fig. 3.8a). The areas experiencing surface cooling generally correspond to the regions of strong negative TOA forcing (especially in E. Asia), but this is not the case for the Arctic (Greenland), over which a weak negative (positive) overall ERF was induced and should experience a(n) decrease (increase) in their surface temperature on an annual level. This also applies to Antarctica, over which a negligible and statistically insignificant overall ERF was caused, but undergoes a pronounced and, for the most part, statistically significant warming (probably due to warm air advection; *Zanis et al., 2020*). In DJF, the global mean surface temperature is unchanged. A dipole of warming in N. Russia and cooling in East and South continental Asia is produced, which cannot be justified by the TOA overall ERF (Fig.

3.8b). There is generally substantial warming in the Arctic Circle (excluding Greenland), and cooling in Central Asia and the Arabian Peninsula, but both are statistically insignificant. During MAM, the global mean temperature change is –0.03 ^{o}C, with Eurasia and N. America (the Arctic) experiencing more (less) pronounced cooling (warming) than in DJF (Fig. 3.8c), while there seems to be a greater warming effect over Antarctica, but much like the Arctic, it is statistically insignificant. With the exception of the N. Pacific, regions that where under a negative forcing in MAM undergo a surface cooling. In boreal summer (JJA; Fig. 3.8d), the globally averaged surface temperature decreases by 0.05 ^{o}C, with a general cooling effect over the NH land areas and parts of the Arctic, consistent with the negative forcing induced at TOA. There is also a statistically insignificant warming over Antarctica. In SON, the global mean temperature change is the same as the mean annual with a similar pattern, which is quite consistent to the total ERF pattern, but with greater, yet not statistically significant, warming over N. Russia, the Arctic and Antarctica (Fig. 3.8e).

3.2.2 BC Experiment

In the BC simulation (Fig. 3.8; second row), the annual globally averaged temperature change is an increase by 0.02 ^{o}C, with the warming peaking over the Himalayan region, along with Central and N.E. Asia and N. America. This spatial pattern is not quite consistent with the annual total ERF or ERFari, for that matter, as the greatest positive forcing was caused over E. Asia, where seems to be negligible and statistically insignificant surface temperature change (Fig. 3.8f). During boreal winter (DJF; Fig. 3.8g), the global mean surface temperature rises by 0.02 ^{o}C, with the strongest warming occurring over the Himalayas and the Tibetan Plateau, and less pronounced warming (and statistically not significant) over the whole Eurasia, north of Alaska and over and around Greenland, while there is cooling over Australia, the northern half of N. America, north of Russia and the northeastern edge of Asia, a spatial pattern utterly inconsistent with the DJF total ERF. In MAM (Fig. 3.8h), the global average surface temperature change is +0.03 ^{o}C, with an intense and statistically significant (insignificant) warming over the Tibetan Plateau (the northeastern part of N. America), consistent with the MAM total ERFalb (inconsistent with the MAM forcing over the area). During the austral winter (JJA; Fig. 3.8i), the global mean temperature response is +0.04 ^{o}C, with statistically significant warming (cooling) over North and Central Asia, Greenland and most of N. America (the Indian Peninsula), not quite consistent with the pattern of the JJA forcing. In SON, the mean surface temperature increases by 0.02 ^{o}C, with a statistically significant warming only over the Tibetan Plateau, and spatial pattern that does not correspond to that of the forcing (Fig. 3.8j).

3.2.3 OC Experiment

Regarding the effects of OC to temperature (Fig. 3.8; third row), it causes a mean annual surface temperature decrease of –0.01 ^{o}C, with the most pronounced cooling regions being E. Europe, E. Asia and the northern edge of N. America (Fig. 3.8k), with the last two corresponding to the negative annual forcing. In austral summer (DJF; Fig. 3.8l), the global mean surface temperature remains unchanged, but there is a distinct warming over central Europe and in small region in N. Russia, while cool-

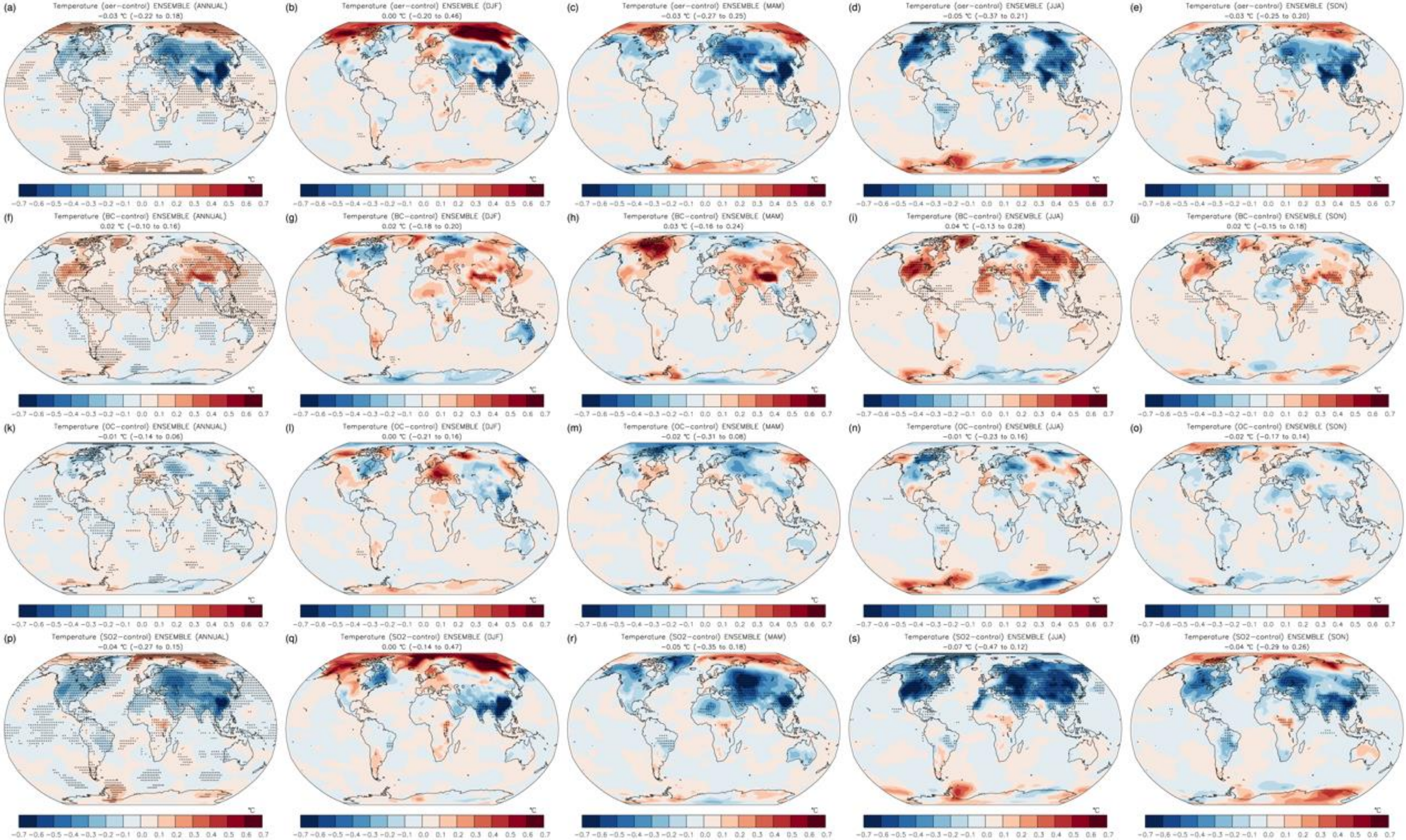

Figure 3.8. Spatial pattern of the annual (first column), DJF (second column), MAM (third column), JJA (fourth column), and SON (fifth column) global mean surface temperature response in the piClim-aer (first row), piClim-BC (second row), piClim-OC (third row), and piClim-SO_2 (fourth column) experiment for the multi-model ensemble. The black crosses indicate the statistically important values in the 95% confidence level. The global field means (5th to 95th percentiles in the parenthesis) are shown in degrees Celsius.

ing occurs over the Northeastern N. America, the eastern edge of Russia and in E. Asia, where it is statistically significant and corresponding to the negative DJF forcing. During boreal spring (MAM; Fig. 3.8m), there is a global mean cooling of 0.02 ^{o}C, with the high NH latitudes experiencing a general cooling (except for the eastern tip of Russia, which warms), a spatial pattern not consistent with the TOA forcing. In JJA the global mean surface temperature change is –0.01 ^{o}C, with a pattern quite consistent to the TOA forcing and similar to the annual, but with more pronounced warming and cooling regions and a distinct dipole of warming and cooling in Antarctica (Fig. 3.8n). OC in SON induces a global mean cooling equal to that in MAM, with a general warming of the Arctic and cooling of NH low and mid-latitudes, none of which is either statistically significant or corresponding to the SON forcing at TOA (Fig. 3.8o).

3.2.4 SO_2 Experiment

In the SO_2 experiment (Fig. 3.8; fourth row), the global average annual response of the surface temperature is –0.04 ^{o}C (Fig. 3.8p), quite consistent (inconsistent) with the negative forcing over the NH mid- and low latitude land areas (the Arctic), which experience cooling (warming). While there is not a change in the global mean DJF surface temperature (Fig. 3.8q), East and South Asia (the NH high latitudes) undergo substantial cooling (warming), which is consistent (inconsistent) with the TOA forcing. The global temperature change in MAM is –0.05 ^{o}C (Fig. 3.8r) and has a spatial pattern similar to the annual, but with stronger cooling over E. Europe, W. Asia, and Greenland, which agrees with the negative TOA forcing over Eurasia and N. America. In boreal summer (JJA; Fig. 3.8s), SO_2 is responsible for a statistically significant cooling over the NH land areas (consistent with the total SO_2 ERF pattern), which results in a global mean cooling of –0.07 ^{o}C. In MAM, the global mean surface temperature decreases by 0.04 ^{o}C (Fig. 3.8t), with NH the low and mid-latitude land regions experiencing cooling and the NH high latitudes, along with Antarctica, undergoing a statistically insignificant warming. This spatial pattern is quasi-similar with the SON total forcing at TOA.

3.2.5 Intermodel Differences

As in the case of ERF, each model yields a surface temperature response that may differ substantially from the multi-model ensemble results annually and/or seasonally. For instance, CNRM-ESM2-1 exhibits greater warming over N. America and significant cooling in the Arctic during the boreal winter in all simulations and stronger annual cooling over Asia (Fig. E1), while GFDL-ESM4 produces greater warming (cooling) in the BC (all-aerosol) experiment over NH land areas both on an annual and seasonal level (Fig. E2). MPI-ESM-1-2-HAM shows much greater cooling of the NH in the SO_2 and all-aerosol simulations and substantial DJF warming over Eurasia and the Arctic in the BC perturbation experiment (Fig. E3), whereas MRI-ESM2-0 produces extreme seasonal variations in the poles in all simulations (Fig. E4). In the all-aerosol and SO_2 experiments, both the NorESM2-LM (p1) and (p2) models (Fig. E5 and Fig. E6, respectively) generate considerable annual, DJF, MAM, and SON warming in the Arctic and most regions within the NH high latitudes. In the case of NorESM2-LM (p2), this also happens in the BC perturbation experiment.

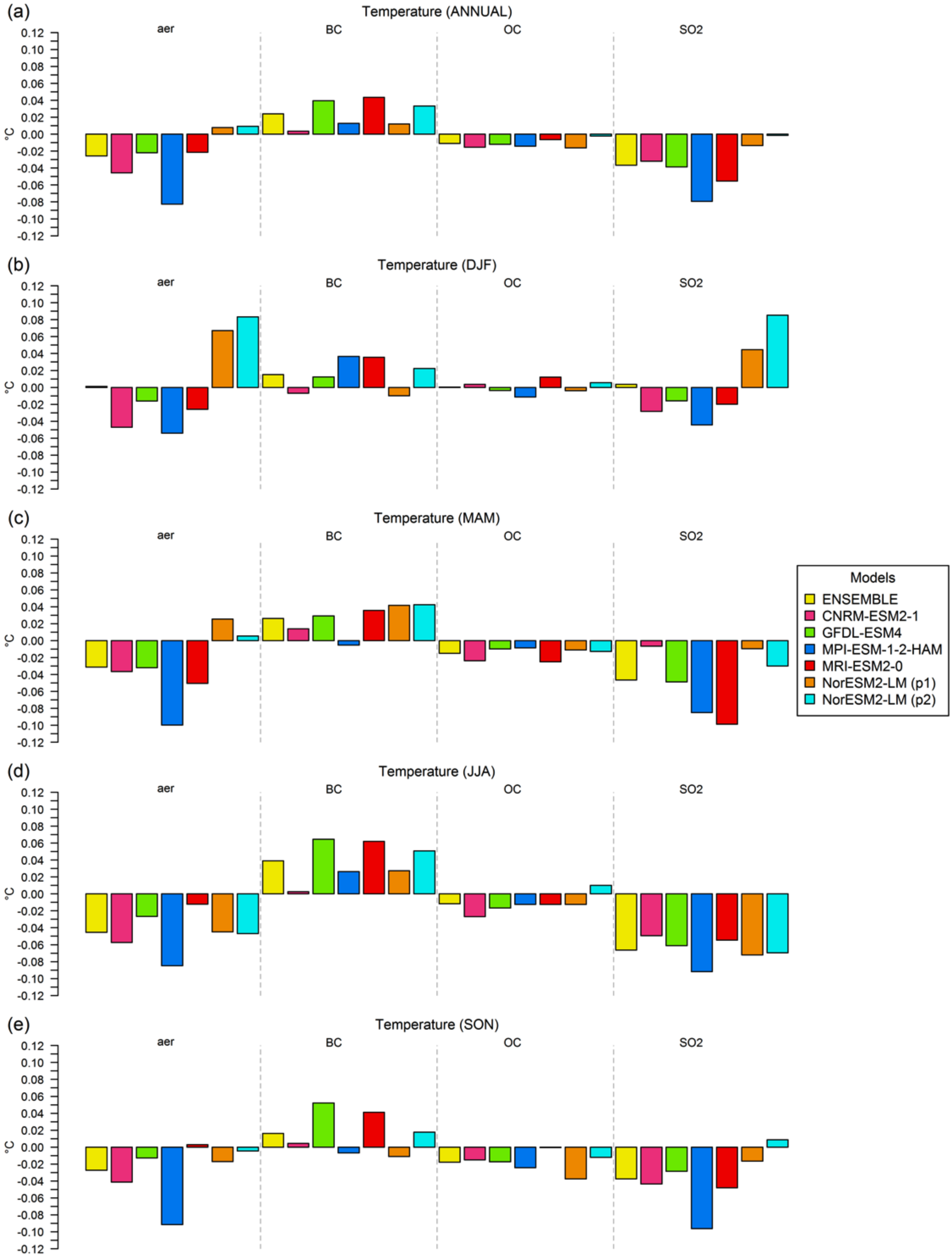

Figure 3.9. Barplots of the global mean (a) annual, (b) DJF, (c) MAM, (d) JJA, and (e) SON temperature change for the piClim-aer, piClim-BC, piClim-OC, and piClim-SO_2 simulations for all the models of this study and their multi-model ensemble.

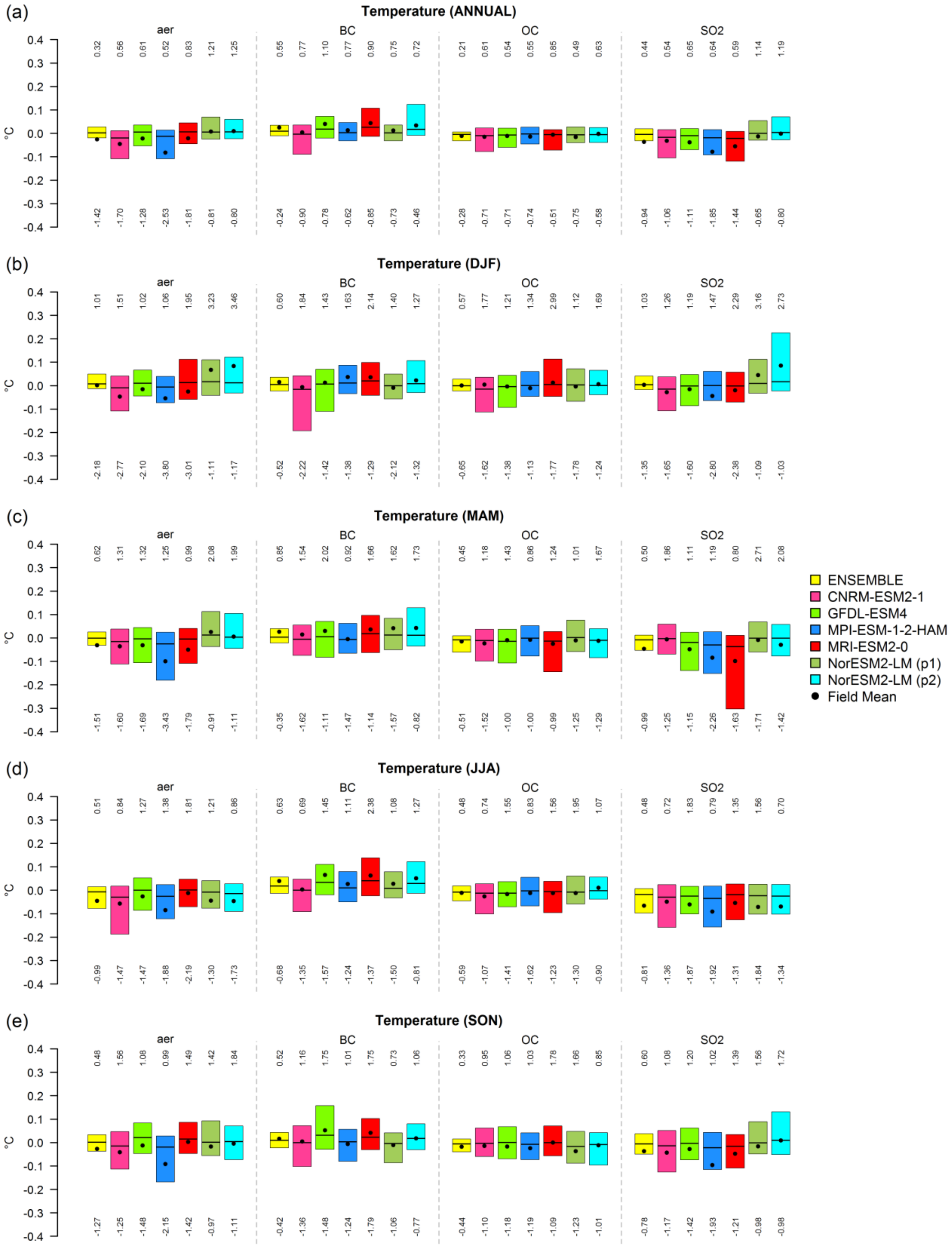

Figure 3.10. Boxplots of the (a) annual, (b) DJF, (c) MAM, (d) JJA, and (e) SON surface temperature change for the piClim-aer, piClim-BC, piClim-OC, and piClim-SO_2 simulations for all individual models participating in this study and their multi-model ensemble. Each box's lower (upper) limit is the 25th (75th) percentile, the black horizontal lines denote the median (50th percentile), the black circles are the global field means, and the numbers on the lower (upper) bounds of each subplot denote the minimum (maximum) field values.

The spread of surface temperature change is small in the ensemble, as well as among models (with a few isolated exceptions, such as the DJF NorESM2-LM (p2) or the MAM MRI-ESM2-0 temperature response both in the SO_2 simulation), with their respective medians being nearly equal to each other and to the ensemble median, for the most part, both annually and seasonally (Fig. 3.10).

CHAPTER 4: SUMMARY AND CONCLUSIONS

In this study, the rapid responses of the climate system caused by anthropogenic aerosol radiative forcing were investigated. In particular, the surface air temperature responses to the radiative forcing exerted by black carbon (BC), organic carbon (OC), sulphur dioxide (SO_2), which is the gaseous precursor of sulphate, and their combination was examined using simulations of climate models participating in the sixth phase of the Coupled Model Intercomparison Project (CMIP6).

The fixed-SST effective radiative forcing (ERF) approach was implemented, which accounts for tropospheric and land rapid adjustments, but not for changes in sea surface temperatures (SSTs) or sea ice, is more accurate, more computationally efficient, requires shorter simulations and gives rise to less uncertainties. The ERF due to aerosol-radiation interactions (ERFari), due to aerosol-cloud interactions (ERFaci), and due to changes in surface albedo induced by anthropogenic aerosols (ERFalb) were calculated following the method of Ghan (2013), and the overall ERF for the shortwave (SW) and longwave (LW) radiation, as well as their sum (SW + LW, denoted as total) was estimated.

Five climate models taking part in the CMIP6 were used, namely CNRM-ESM2-1, GFDL-ESM4, MPI-ESM-1-2-HAM, MRI-ESM2-0, and NorESM2-LM with two physics variations (denoted as “p1 and “p2”) different enough for them to be considered as separate models. From them, a multi-model ensemble was calculated in order to study the average ERF and temperature responses avoiding each individual model’s possible biases. Five simulations run under the recommendations of the Radiative Forcing Model Intercomparison Project (RFMIP) and the Aerosol Chemistry Model Intercomparison Project (AerChemMIP) were used, namely a control simulation with all forcings set to the year 1850 using aerosol precursors emission of 1850 (piClim-control), and four perturbation simulations with all forcings set to 1850 but using anthropogenic aerosol (piClim-aer), BC (piClim-BC), OC (piClim-OC), and SO_2 (piClim-SO_2) precursor emissions of the year 2014, respectively. The ERF components and surface air temperature responses to present-day aerosol species were estimated by subtracting the piClim-control simulation from the four perturbation simulations.

The multi-model ensemble global mean annual total (SW + LW) ERF at TOA due to present-day anthropogenic aerosols (piClim-aer experiment) is estimated to be –1.09 (–3.28 to 0.22 in the 5th to 95th percentile range) W m^{-2}, which is a bit more negative than the ERF calculated in other studies using multiple CMIP6 models (e.g., *Zanis et al., 2020*; *Smith et al., 2020*; *Thornhill et al., 2021a*). Its decomposition in ERFari, ERFaci and ERFalb gives an estimate of –0.01 (–0.34 to 0.38) W m^{-2}, –1.11 (–3.42 to 0.46) W m^{-2}, and 0.03 (–1.46 to 0.47) W m^{-2}, respectively, on an annual level in the all-aerosol experiment. ERFari (ERFaci) is less (more) negative than the respective values estimated by Smith et al. (2020), which is expected as they used a different calculation method. The ERF, ERFari, ERFaci, and ERFalb values calculated with the CNRM-ESM2-1 and MRI-ESM2-0 models in this work are identical with those estimated by Michou et al. (2020) and Oshima et al. (2020), respectively. The overall ERF is dominated by ERFaci, the SW component of both of which largely contributes to their respective total values, due to aerosol cloud interactions. Aerosols serve as

CCN or IN, thus increasing the cloud albedo and lifetime, resulting in more solar radiation being reflected back to space and a negative TOA forcing. This is especially true over industrialized areas, such as E. Asia and the continental S. Asia, where the negative TOA ERF is concentrated, consistent with the findings of other papers (e.g., *Zanis et al., 2020*; *Oshima et al., 2020*; *Michou et al., 2020*). The negative annual global mean ERF has cooling effect on the surface, with an annual surface air temperature change of –0.03 (–0.22 to 0.18) ^{o}C, mainly confined in the NH continental regions, and especially over E. Asia and India, over which the strongest negative ERF was exerted, while there is a slight warming signal over the Arctic, again consistent with the results of Zanis et al. (2020). The all-aerosol DJF total ERF, ERFari, ERFaci, and ERFalb are estimated to be –0.84 (–3.05 to 0.66) W m^{-2}, –0.02 (–0.27 to 0.22) W m^{-2}, –0.82 (–2.71 to 0.63) W m^{-2}, and 0.01 (–0.92 to 0.52) W m^{-2}, respectively, with a global mean surface temperature response of 0.00 (–0.20 to 0.46) ^{o}C. There is a strong near-surface cooling over the continental East and South Asia and a stronger (slight) warming over the Arctic (Europe). The near-surface warming cannot be explained by the ERF pattern, but is justified by the aerosol-induced circulation changes, that cause warm air advection and subsidence over the specified areas (*Zanis et al., 2020*). The globally averaged total ERF, ERFari, ERFaci, and ERFalb in MAM are –1.23 (–4.74 to 0.43) W m^{-2}, 0.03 (–0.34 to 0.62) W m^{-2}, –1.30 (–5.05 to 0.45) W m^{-2}, and 0.04 (–0.94 to 0.68) W m^{-2}, respectively. The total ERF is much more negative over E. Asia, the N. Pacific Ocean, E. Europe and the Arabian Sea due to the much stronger ERFaci over these regions, while the global mean temperature change is –0.03 (–0.27 to 0.25) ^{o}C, with a spatial pattern almost identical to the annual, but with more pronounced warming (cooling) over the Arctic and Antarctica (Europe). In JJA, anthropogenic aerosols induce a total ERF, ERFari, ERFaci, and ERFalb equal to –1.19 (–4.29 to 0.52) W m^{-2}, 0.02 (–0.46 to 0.75) W m^{-2}, –1.24 (–4.52 to 0.84) W m^{-2}, and 0.03 (–3.49 to 0.88) W m^{-2}, respectively, and a surface temperature response of –0.05 (–0.37 to 0.21) ^{o}C. There is a strong JJA ERFalb over the Arctic, which is probably responsible for the slight regional cooling during the boreal summer and a stronger warming over Antarctica unjustifiable by the ERF pattern. In SON, the ERF, ERFari, ERFaci, and ERFalb have a global mean of –1.10 (–3.21 to 0.42) W m^{-2}, –0.05 (–0.42 to 0.23) W m^{-2}, –1.09 (–3.01 to 0.59) W m^{-2}, and 0.04 (–0.58 to 0.56) W m^{-2}, respectively, with a near-surface global mean cooling of –0.03 (–0.25 to 0.20) ^{o}C. The NH experiences a general cooling, especially in E. Asia and the Himalayan region, except for the Arctic and Antarctica, which exhibit a stronger warming than the annual, while the largest negative ERF is found over E. Asia and the Arabian Sea.

In the BC simulation, the NH experiences a general near-surface warming on an annual and seasonal basis, with the strongest warming during the boreal summer and spring. The annual global mean total ERF, ERFari, ERFaci, and ERFalb are estimated to be 0.18 (–0.58 to 1.20) W m^{-2}, 0.38 (0.07 to 1.03) W m^{-2}, –0.22 (–1.00 to 0.38) W m^{-2}, and 0.02 (–0.35 to 0.62) W m^{-2}, respectively, with a corresponding warming of 0.02 (–0.10 to 0.16) ^{o}C on a global scale. The greatest positive ERF is mainly limited over E. Asia and India, almost exclusively from the ERFari contribution due to emission of BC from industry and transport. However, the strongest near-surface warming is detected over the Himalayas, while the aforementioned regions experience, if anything, a slight cooling, possibly due to weaker insolation induced by BC absorption. During the boreal winter, the globally averaged ERF, ERFari, ERFaci, and ERFalb are calculated to be 0.20 (–0.89 to 1.33) W m^{-2}, 0.28 (0.01 to 0.68) W m^{-2}, –0.10 (–1.11 to 0.79) W m^{-2}, and 0.02 (–0.47 to 0.54) W m^{-2}, respectively, with a near-surface temperature rise of 0.02 (–0.18 to 0.20) °C globally. The ERF and temperature changes peak over the same regions, but the northern part of N. America experiences a near-surface cooling. In MAM, the average total ERF, ERFari, ERFaci, and ERFalb are 0.33 (–0.83 to 2.04) W m^{-2}, 0.44 (0.03 to 1.32) W m^{-2}, –0.21 (–1.37 to 0.67) W m^{-2}, and 0.10 (–0.39 to 0.97) W m^{-2}, respectively, with a global temperature increase of 0.03 (–0.16 to 0.24) °C, the strongest of which detected over the Himalayas due to the strong positive ERFalb, possibly due to BC deposition on snow. In JJA, the ERF, ERFari, ERFaci, and ERFalb are valued at 0.08 (–1.19 to 1.76) W m^{-2}, 0.45 (0.00 to 1.41) W m^{-2}, –0.35 (–1.99 to 0.69) W m^{-2}, and –0.03 (–0.90 to 1.28) W m^{-2}, respectively, on a global scale, which result in a considerable general near-surface warming in NH continental regions (except for India, E. Europe and Alaska), that is globally estimated to be 0.04 (–0.13 to 0.28) °C. ERFaci and ERFalb have opposite signs throughout the NH, while ERFari is positive in the low and high NH latitudes. In SON, the global mean ERF, ERFari, ERFaci, and ERFalb are estimated to be 0.12 (–0.99 to 1.31) W m^{-2}, 0.36 (0.08 to 0.87) W m^{-2}, –0.21 (–1.14 to 0.65) W m^{-2}, and –0.03 (–0.55 to 0.61) W m^{-2}, respectively, with a slightly weaker warming, which is globally calculated to be 0.02 (–0.15 to 0.18) °C, and has a spatial pattern almost opposite to that of DJF, unjustifiable by the ERF distribution for the most part.

OC is mainly a scattering aerosol that exerts a negative ERF on the climate system and tends to cool it. The negative ERF is mainly concentrated over East and South Asia (except for JJA) and its overall ERF is dominated by ERFaci annually and on a seasonal basis. In more detail, the global mean annual ERF, ERFari, ERFaci, and ERFalb are –0.35 (–1.34 to 0.43) W m^{-2}, –0.07 (–0.25 to 0.03) W m^{-2}, –0.29 (–1.17 to 0.41) W m^{-2}, and 0.01 (–0.44 to 0.27) W m^{-2}, respectively, and the surface air temperature response is –0.01 (–0.14 to 0.06) °C with an additional weak near-surface cooling (warming) over East (West) Europe. During the boreal winter, the ERF, ERFari, ERFaci, and ERFalb are estimated at –0.35 (–1.69 to 0.82) W m^{-2}, –0.05 (–0.18 to 0.05) W m^{-2}, –0.30 (–1.56 to 0.83) W m^{-2}, and 0.00 (–0.47 to 0.40) W m^{-2}, respectively, with a global temperature response of 0.00 (–0.21 to 0.16) °C, that exhibits two pronounced dipoles of near-surface warming-cooling (E. Europe-E. Asia and N.W. Russia-E. Russia, respectively) that cannot be explained by ERF. In MAM, the ERF, ERFari, ERFaci, and ERFalb are valued at –0.29 (–1.59 to 0.75) W m^{-2}, –0.05 (–0.23 to 0.06) W m^{-2}, –0.25 (–1.40 to 0.67) W m^{-2}, and 0.01 (–0.45 to 0.55) W m^{-2}, respectively, on a global scale, with a global mean cooling of –0.02 (–0.31 to 0.08) °C concentrated on the mid- high NH latitudes. In austral winter the globally averaged ERF, ERFari, ERFaci, and ERFalb are –0.33 (–2.16 to 0.90) W m^{-2}, –0.07 (–0.34 to 0.06) W m^{-2}, –0.26 (–1.75 to 1.02) W m^{-2}, and 0.00 (–1.42 to 0.61) W m^{-2}, respectively, causing near-surface cooling of –0.01 (–0.23 to 0.16) °C globally, with an unjustifiable by the ERF pattern warming-cooling dipole in Antarctica. In SON, the global mean ERF, ERFari, ERFaci, and ERFalb are estimated at –0.41 (–1.52 to 0.54) W m^{-2}, –0.09 (–0.34 to 0.03) W m^{-2}, –0.35 (–1.29 to 0.50) W m^{-2}, and 0.02 (–0.43 to 0.39) W m^{-2}, respectively, with a slightly stronger global cooling of –0.02 (–0.17 to 0.14) °C. ERFari has a negative global mean value on an annual and seasonal basis as it scatters the incoming SW radiation. In MAM (SON), the Arctic experiences a near-surface cooling (warming) despite the weak regional ERF. East Europe and West Asia exhibit an apparent cooling both annually and seasonally, except for the boreal winter, during which there is a strong warming over Central and Eastern Europe. E. Asia, over which the strongest negative ERF is detected, has only a weak cooling signal. None of the aforementioned temperature response patterns are compatible with the ERF spatial distribution.

SO_2 is the gaseous precursor of sulphates, which highly scatter the incoming SW solar radiation, causing a negative ERF and a near-surface cooling over the NH, in general, and over the emission sources (i.e., continental East and South Asia, followed by Europe and N. America), in particular. Annually, the global mean ERF, ERFari, ERFaci, and ERFalb are estimated to be –1.10 (–3.32 to 0.21) W m^{-2}, –0.27 (–0.79 to 0.00) W m^{-2}, –0.84 (–2.85 to 0.58) W m^{-2}, and 0.01 (–1.52 to 0.47) W m^{-2}, respectively, with a global mean annual cooling of –0.04 (–0.27 to 0.15) ^{o}C, concentrated over the NH (and especially large over E. Asia), while the Arctic experiences a near-surface warming. ERFaci dominates the overall ERF annually and seasonally as sulphate is a great CCN, which results in cloud albedo and fraction increases, and greater amount of SW radiation being reflected back to space. ERFari is almost exclusively negative all around the globe on an annual and seasonal basis due to SW radiation scattering from SO_4 particles. During the boreal winter, the globally averaged total (SW + LW) ERF, ERFari, ERFaci, and ERFalb are –0.98 (–3.19 to 0.53) W m^{-2}, –0.22 (–0.62 to 0.02) W m^{-2}, –0.73 (–2.58 to 0.60) W m^{-2}, and –0.02 (–0.90 to 0.51) W m^{-2}, respectively, with a global mean temperature response of 0.00 (–0.14 to 0.47) ^{o}C due to near-surface cooling (warming) over E. Asia, India, and Eastern N. America (the Arctic, Europe, and Northwestern N. America), which could be justified from aerosol-induced circulation changes rather than the ERF TOA pattern. In MAM, the ERF, ERFari, ERFaci, and ERFalb are valued at –1.34 (–4.61 to 0.38) W m^{-2}, –0.27 (–0.77 to 0.01) W m^{-2}, –1.04 (–4.08 to 0.50) W m^{-2}, and –0.04 (–1.16 to 0.59) W m^{-2}, respectively, on a global scale, causing a global mean temperature decrease of –0.05 (–0.35 to 0.18) ^{o}C, confined over the NH continental regions. During the boreal summer, the globally averaged ERF, ERFari, ERFaci, and ERFalb are estimated at –1.11 (–4.31 to 0.55) W m^{-2}, –0.29 (–0.98 to 0.01) W m^{-2}, –0.86 (–3.90 to 1.23) W m^{-2}, and 0.04 (–3.82 to 1.09) W m^{-2}, respectively. Over the NH, in areas where ERFaci is negative, ERFalb has positive values, but the combined radiative forcing is negative nearly all over the NH, inducing the strongest near-surface cooling over the land regions north of the Equator, with a global mean value of –0.07 (–0.47 to 0.12) ^{o}C. In SON, the global mean ERF, ERFari, ERFaci, and ERFalb are –0.96 (–3.23 to 0.50) W m^{-2}, –0.29 (–0.89 to 0.01) W m^{-2}, –0.74 (–2.58 to 0.74) W m^{-2}, and 0.07 (–0.63 to 0.69) W m^{-2}, respectively, with a global mean reduction in the surface air temperature by –0.04 (–0.29 to 0.26) ^{o}C, corresponding to a near-surface cooling (warming) over the NH low and mid-latitudes (the polar regions).

There are bound to be differences and inconsistencies among individual models. This is caused by differences in the aerosol parameterization schemes developed for each climate model, which affect the aerosol size distribution, emissions or concentrations, vertical extension, interaction with radiation, clouds, and other atmospheric constituents, among others. Also, every model has different parameterization schemes for atmospheric chemistry, land surface (soil, snow, vegetation, hydrology, carbon cycle, etc.), and atmospheric processes (e.g., convection, clouds, gravity waves, turbulence, etc.), which also influence the aerosol lifetimes and the mechanisms through which they could induce a climate forcing. Consequently, the magnitude and spatial patterns of forcings and rapid responses a climate model generates are affected by its parameterization schemes. Therefore, it is only logical that one climate model's results may diverge to some degree from another model's results and/or from their multi-model ensemble results. This also explains the intermodel differences in the ERF and temperature change values spread witnessed in Chapter 3.

The above results generally agree with the findings of other studies (e.g., *Zanis et al., 2020*; *Smith et al., 2020*, *Thornhill et al., 2021a*; *Oshima et al., 2020*; *Michou et al., 2020*). Despite the intermodel differences and the uncertainties rising from the ERF calculation approach, there is a general agreement that sulphates are the main driver of the aerosol ERF pattern and the induced surface temperature response. The results of this study show that anthropogenic aerosols combined, and OC and SO_2 individually have a negative total (SW + LW) annual ERF and tend to cool the surface over the NH continental regions due to the large contribution of ACI to the overall ERF, whereas BC has a positive total ERF and causes near-surface warming primarily due to ARI, along with albedo changes of the surface it is deposited on. The small magnitude of BC ERFaci could be caused by many processes occurring between BC and clouds that offset each other. In order to conduct a more thorough analysis of the aerosol-induced fast climate responses, other variables, such as precipitation and atmospheric circulation, along with the vertical distribution of anthropogenic aerosols (which is crucial, especially in the case of BC), the macro- and micro-physical properties of clouds and the liquid water path should also be considered. Furthermore, a greater number of climate model simulations should be included, in order to bypass any individual model biases deriving from their parameterizations on aerosol and atmospheric chemistry and/or meteorology. Consequently, this study should be considered only as a first analysis of present-day anthropogenic aerosol ERF, along with its components, and the rapid temperature responses they cause on an annual and seasonal basis, without considering important factors that could help explain the spatial patterns of ERF and near-surface temperature changes.

BIBLIOGRAPHY

Albrecht, B. A., 1989: Aerosols, cloud microphysics, and fractional cloudiness, Science, 245, 1227–1230, https://doi.org/10.1126/science.245.4923.1227.

Allen, R. J., Amiri-Farahani, A., Lamarque, J.-F. Smith, C., Shindell, D., Hassan, T., and Chung, C. E., 2019: Observationally constrained aerosol–cloud semi-direct effects, npj Clim. Atmos. Sci. 2, 16, https://doi.org/10.1038/s41612-019-0073-9.

Allen, R. J., and Sherwood, S. C., 2010: Aerosol-cloud semi-direct effect and land-sea temperature contrast in a GCM, Geophys. Res. Lett., 37, L07702, https://doi.org/10.1029/2010GL042759.

Andrews, T., P. M. Forster, O. Boucher, N. Bellouin, and A. Jones, 2010: Precipitation, radiative forcing and global temperature change, Geophys. Res. Lett., 37, L14701, https://doi.org/10.1029/2010GL043991.

Baker, L. H., Collins, W. J., Olivié, D. J. L., Cherian, R., Hodnebrog, Ø., Myhre, G., and Quaas, J., 2015: Climate responses to anthropogenic emissions of short-lived climate pollutants, Atmos. Chem. Phys., 15, 8201–8216, https://doi.org/10.5194/acp-15-8201-2015.

Bartlett, R.E., Bollasina, M.A., Booth, B.B.B., Dunstone, N. J., Marenco, F., Messori, G., and Bernie, D. J., 2018: Do differences in future sulfate emission pathways matter for near-term climate? A case study for the Asian monsoon, Clim Dyn 50, 1863–1880, https://doi.org/10.1007/s00382-017-3726-6.

Bellouin, N., Quaas, J., Gryspeerdt, E., Kinne, S., Stier, P., Watson-Parris, D., Boucher, O., Carslaw, K. S., Christensen, M., Daniau, A.-L., Dufresne, J.-L., Feingold, G., Fiedler, S., Forster, P., Gettelman, A., Haywood, J. M., Lohmann, U., Malavelle, F., Mauritsen, T., McCoy, D. T., Myhre, G., Mülmenstädt, J., Neubauer, D., Possner, A., Rugenstein, M., Sato, Y., Schulz, M., Schwartz, S. E., Sourdeval, O., Storelvmo, T., Toll, V., Winker, D., and Stevens, B., 2020: Bounding global aerosol radiative forcing of climate change, Reviews of Geophysics, 58, e2019RG000660, https://doi.org/10.1029/2019RG000660.

Bond, T. C., S. J. Doherty, D. W. Fahey, P. M. Forster, T. Berntsen, B. J. DeAngelo, M. G. Flanner, S. Ghan, B. Kärcher, D. Koch, S. Kinne, Y. Kondo, P. K. Quinn, M. C. Sarofim, M. G. Schultz, M. Schulz, C. Venkataraman, H. Zhang, S. Zhang, N. Bellouin, S. K. Guttikunda, P. K. Hopke, M. Z. Jacobson, J. W. Kaiser, Z. Klimont, U. Lohmann, J. P. Schwarz, D. Shindell, T. Storelvmo, S. G. Warren, and C. S. Zender, 2013: Bounding the role of black carbon in the climate system: A scientific assessment, J. Geophys. Res. Atmos., 118, 5380–5552, https://doi.org/10.1002/jgrd.50171.

Boucher, O., D. Randall, P. Artaxo, C. Bretherton, G. Feingold, P. Forster, V.-M. Kerminen, Y. Kondo, H. Liao, U. Lohmann, P. Rasch, S.K. Satheesh, S. Sherwood, B. Stevens and X.Y. Zhang, 2013: Clouds and Aerosols. In: Climate Change 2013: The Physical Science Basis. Contribution of Working Group I to the Fifth Assessment Report of the Intergovernmental Panel on

Climate Change [Stocker, T.F., D. Qin, G.-K. Plattner, M. Tignor, S.K. Allen, J. Boschung, A. Nauels, Y. Xia, V. Bex and P.M. Midgley (eds.)]. Cambridge University Press, Cambridge, United Kingdom and New York, NY, USA.

Carslaw, K. S., Lee, L. A., Reddington, C. L., Pringle, K. J., Rap, A., Forster, P. M., Mann, G. W., Spracklen, D. V., Woodhouse, M. T., Regayre, L. A., and Pierce, J. R., 2013: Large contribution of natural aerosols to uncertainty in indirect forcing, Nature 503, 67–71, https://doi.org/10.1038/nature12674.

Chand, D., Wood, R., Anderson, T. L., Satheesh, S. K., and Charlson, R. J., 2009: Satellite-derived direct radiative effect of aerosols dependent on cloud cover, Nature Geosci 2, 181–184, https://doi.org/10.1038/ngeo437.

Chen, W.-T., Lee, Y. H., Adams, P. J., Nenes, A., and Seinfeld, J. H., 2010: Will black carbon mitigation dampen aerosol indirect forcing?, Geophys. Res. Lett., 37, L09801, https://doi.org/10.1029/2010GL042886.

Chung, E.-S. and Soden, B. J., 2015a: An assessment of direct radiative forcing, radiative adjustments, and radiative feedbacks in coupled ocean–atmosphere models, Journal of Climate, 28, 4152–4170, https://doi.org/10.1175/JCLI-D-14-00436.1.

Chung, E.-S. and Soden, B. J., 2015b: An assessment of methods for computing radiative forcing in climate models, Environ. Res. Lett. 10, 074004, https://doi.org/10.1088/1748-9326/10/7/074004.

Collins,W. J., Lamarque, J.-F., Schulz, M., Boucher, O., Eyring, V., Hegglin, M. I., Maycock, A., Myhre, G., Prather, M., Shindell, D., and Smith, S. J., 2017: AerChemMIP: quantifying the effects of chemistry and aerosols in CMIP6, Geosci. Model Dev., 10, 585–607, https://doi.org/10.5194/gmd-10-585-2017.

Conley, A. J., Westervelt, D. M., Lamarque, J.-F., Fiore, A. M., Shindell, D., Correa, G., Faluvegi, G., and Horowitz, L. W., 2018: Multimodel surface temperature responses to removal of U.S. sulfur dioxide emissions, Journal of Geophysical Research: Atmospheres, 123, 2773–2796, https://doi.org/10.1002/2017JD027411.

Cubasch, U., D. Wuebbles, D. Chen, M.C. Facchini, D. Frame, N. Mahowald, and J.-G. Winther, 2013: Introduction. In: Climate Change 2013: The Physical Science Basis. Contribution of Working Group I to the Fifth Assessment Report of the Intergovernmental Panel on Climate Change [Stocker, T.F., D. Qin, G.-K. Plattner, M. Tignor, S.K. Allen, J. Boschung, A. Nauels, Y. Xia, V. Bex and P.M. Midgley (eds.)]. Cambridge University Press, Cambridge, United Kingdom and New York, NY, USA.

Després, V. R., Huffman, J. A., Burrows, S. M., Hoose, C., Safatov, A. S., Buryak, G., Fröhlich-Nowoisky, J., Elbert, W., Andreae, M. O., Pöschl, U., and Jaenicke, R., 2012: Primary biological aerosol particles in the atmosphere: a review, Tellus B: Chemical and Physical Meteorology, 64, https://doi.org/10.3402/tellusb.v64i0.15598.

Dunne, J. P., Horowitz, L. W., Adcroft, A. J., Ginoux, P., Held, I. M., John, J. G., Krasting, J. P., Malyshev, S., Naik, V., Paulot, F., Shevliakova, E., Stock, C. A., Zadeh, N., Balaji, V., Blanton, C., Dunne, K. A., Dupuis, C., Durachta, J., Dussin, R., Gauthier, P. P. G., Griffies, S. M., Guo, H., Hallberg, R. W., Harrison, M., He, J., Hurlin, W., McHugh, C., Menzel, R., Milly, P. C. D., Nikonov, S., Paynter, D. J., Ploshay, J., Radhakrishnan, A., Rand, K., Reichl, B. G., Robinson, T., Schwarzkopf, D. M., Sentman, L. T., Underwood, S., Vahlenkamp, H., Winton, M., Wittenberg, A. T., Wyman, B., Zeng, Y., and Zhao,

M. , 2020: The GFDL Earth System Model version 4.1 (GFDL-ESM4.1): Overall coupled model description and simulation characteristics, Journal of Advances in Modeling Earth Systems, 12, e2019MS002015, https://doi.org/10.1029/2019ms002015.

Eyring, V., Bony, S., Meehl, G. A., Senior, C. A., Stevens, B., Stouffer, R. J., and Taylor, K. E., 2016: Overview of the Coupled Model Intercomparison Project Phase 6 (CMIP6) experimental design and organization, Geosci. Model Dev., 9, 1937–1958, https://doi.org/10.5194/gmd-9-1937-2016.

Forster, P. M., Richardson, T., Maycock, A. C., Smith, C. J., Samset, B. H., Myhre, G., Andrews, T., Pincus, R., and Schulz, M., 2016: Recommendations for diagnosing effective radiative forcing from climate models for CMIP6, J. Geophys. Res.-Atmos.,121,12460–12475, https://doi.org/10.1002/2016JD025320.

Ghan, S. J., 2013: Technical Note: Estimating aerosol effects on cloud radiative forcing, Atmos. Chem. Phys., 13, 9971–9974, https://doi.org/10.5194/acp-13-9971-2013.

Ghan, S. J., Liu, X., Easter, R. C., Zaveri, R., Rasch, P. J., Yoon, J.-H., and Eaton, B., 2012: Toward a minimal representation of aerosols in climate models: Comparative decomposition of aerosol direct, semidirect, and indirect radiative forcing, Journal of Climate, 25, 6461–6476, https://doi.org/10.1175/JCLI-D-11-00650.1.

Gregory, J. M., Ingram, W. J., Palmer, M. A., Jones, G. S., Stott, P. A., Thorpe, R. B., Lowe, J. A., Johns, T. C., and Williams, K. D., 2004: A new method for diagnosing radiative forcing and climate sensitivity, Geophys. Res. Lett., 31, L03205, https://doi.org/10.1029/2003GL018747.

Gu, Y., Liou, K.N., Jiang, J.H., Fu, R., Lu, S., Xue, Y., 2016: A GCM investigation of impact of aerosols on the precipitation in Amazon during the dry to wet transition, Clim Dyn 48, 2393–2404, https://doi.org/10.1007/s00382-016-3211-7.

Hallquist, M., Wenger, J. C., Baltensperger, U., Rudich, Y., Simpson, D., Claeys, M., Dommen, J., Donahue, N. M., George, C., Goldstein, A. H., Hamilton, J. F., Herrmann, H., Hoffmann, T., Iinuma, Y., Jang, M., Jenkin, M. E., Jimenez, J. L., Kiendler-Scharr, A., Maenhaut, W., McFiggans, G., Mentel, Th. F., Monod, A., Prévôt, A. S. H., Seinfeld, J. H., Surratt, J. D., Szmigielski, R., and Wildt, J., 2009: The formation, properties and impact of secondary organic aerosol: current and emerging issues, Atmos. Chem. Phys., 9, 5155–5236, https://doi.org/10.5194/acp-9-5155-2009.

Hansen, J., Sato, M., Ruedy, R., Nazarenko, L., Lacis, A., Schmidt, G. A., Russell, G., Aleinov, I., Bauer, M., Bauer, S., Bell, N., Cairns, B., Canuto, V., Chandler, M., Cheng, Y., Del Genio, A., Faluvegi, G., Fleming, E., Friend, A., Hall, T., Jackman, C., Kelley, M., Kiang, N., Koch, D., Lean, J., Lerner, J., Lo, K., Menon, S., Miller, R., Minnis, P., Novakov, T., Oinas, V., Perlwitz, Ja., Perlwitz, Ju., Rind, D., Romanou, A., Shindell, D., Stone, P., Sun, S., Tausnev, N., Thresher, D., Wielicki, B., Wong, T., Yao, M., and Zhang, S., 2005: Efficacy of Climate Forcings, J. Geophys. Res., 110, D18104, https://doi.org/10.1029/2005JD005776.

Hartmann, D.L., A.M.G. Klein Tank, M. Rusticucci, L.V. Alexander, S. Brönnimann, Y. Charabi, F.J. Dentener, E.J. Dlugokencky, D.R. Easterling, A. Kaplan, B.J. Soden, P.W. Thorne, M. Wild and P.M. Zhai, 2013: Observations: Atmosphere and Surface. In: Climate Change 2013: The Physical Science Basis.

Contribution of Working Group I to the Fifth Assessment Report of the Intergovernmental Panel on Climate Change [Stocker, T.F., D. Qin, G.-K. Plattner, M. Tignor, S.K. Allen, J. Boschung, A. Nauels, Y. Xia, V. Bex and P.M. Midgley (eds.)]. Cambridge University Press, Cambridge, United Kingdom and New York, NY, USA.

Haywood, J., and Boucher, O., 2000: Estimates of the direct and indirect radiative forcing due to tropospheric aerosols: A review, Rev. Geophys., 38(4), 513–543, https://doi.org/10.1029/1999RG000078.

Held, I. M., and Soden, B. J., 2006: Robust responses of the hydrological cycle to global warming. J. Clim. 19, 5686–5699, https://doi.org/10.1175/JCLI3990.1.

Hodnebrog, Ø., Myhre, G., Forster, P. M., Sillmann, J., and Samset, B. H., 2016: Local biomass burning is a dominant cause of the observed precipitation reduction in southern Africa, Nature Communications 7, 11236, https://doi.org/10.1038/ncomms11236.

Hoesly, R. M., Smith, S. J., Feng, L., Klimont, Z., Janssens-Maenhout, G., Pitkanen, T., Seibert, J. J., Vu, L., Andres, R. J., Bolt, R. M., Bond, T. C., Dawidowski, L., Kholod, N., Kurokawa, J.-I., Li, M., Liu, L., Lu, Z., Moura, M. C. P., O'Rourke, P. R., and Zhang, Q., 2018: Historical (1750–2014) anthropogenic emissions of reactive gases and aerosols from the Community Emissions Data System (CEDS), Geosci. Model Dev., 11, 369–408, https://doi.org/10.5194/gmd-11-369-2018.

Hoose, C., Kristjánsson, J. E., Iversen, T., Kirkevåg, A., Seland, Ø., and Gettelman, A., 2009: Constraining cloud droplet number concentration in GCMs suppresses the aerosol indirect effect, Geophys. Res. Lett., 36, L12807, https://doi.org/10.1029/2009GL038568.

Horowitz, L. W., Naik, V., Paulot, F., Ginoux, P. A., Dunne, J. P., Mao, J., Schnell, J., Chen, X., He, J., John, J. G., Lin, M., Lin, P., Malyshev, S., Paynter, D., Shevliakova, E., and Zhao, M., 2020: The GFDL Global Atmospheric Chemistry-Climate Model AM4.1: Model Description and Simulation Characteristics, Journal of Advances in Modeling Earth Systems, 12, e2019MS002032, https://doi.org/10.1029/2019MS002032.

Horowitz, L. W., Naik, V., Sentman, L., Paulot, F., Blanton, C., McHugh, C., Radhakrishnan, A., Rand, K., Vahlenkamp, H., Zadeh, N. T., Wilson, C., Ginoux, P., He, J., John, J. G., Lin, M., Paynter, D. J, Ploshay, J., Zhang, A., Zeng, Y., 2018a: NOAA-GFDL GFDL-ESM4 model output prepared for CMIP6 AerChemMIP piClim-control, Version 20180701, Earth System Grid Federation, https://doi.org/10.22033/ESGF/CMIP6.8654.

Horowitz, L. W., Naik, V., Sentman, L., Paulot, F., Blanton, C., McHugh, C., Radhakrishnan, A., Rand, K., Vahlenkamp, H., Zadeh, N. T.; Wilson, C., Ginoux, P., He, J., John, J. G.; Lin, M., Paynter, D. J, Ploshay, J., Zhang, A., Zeng, Y., 2018b: NOAA-GFDL GFDL-ESM4 model output prepared for CMIP6 AerChemMIP piClim-aer, Version 20180701, Earth System Grid Federation, https://doi.org/10.22033/ESGF/CMIP6.8651.

Horowitz, L. W., Naik, V., Sentman, L., Paulot, F., Blanton, C., McHugh, C., Radhakrishnan, A., Rand, K., Vahlenkamp, H., Zadeh, N. T., Wilson, C., Ginoux, P., He, J., John, J. G., Lin, M., Paynter, D. J, Ploshay, J., Zhang, A., Zeng, Y., 2018c: NOAA-GFDL GFDL-ESM4 model output prepared for CMIP6 AerChemMIP piClim-BC, Version 20180701, Earth System Grid Federation, https://doi.org/10.22033/ESGF/CMIP6.8639.

Horowitz, L. W., Naik, V., Sentman, L., Paulot, F., Blanton, C., McHugh, C., Radhakrishnan, A., Rand, K., Vahlenkamp, H., Zadeh, N. T., Wilson, C., Ginoux, P., He, J., John, J. G., Lin, M., Paynter, D. J, Ploshay, J., Zhang, A., Zeng, Y., 2018d: NOAA-GFDL GFDL-ESM4 model output prepared for CMIP6 AerChemMIP piClim-OC, Version 20180701, Earth System Grid Federation, https://doi.org/10.22033/ESGF/CMIP6.8647.

Horowitz, L. W., Naik, V., Sentman, L., Paulot, F., Blanton, C., McHugh, C., Radhakrishnan, A., Rand, K., Vahlenkamp, H., Zadeh, N. T., Wilson, C., Ginoux, P., He, J., John, J. G., Lin, M., Paynter, D. J, Ploshay, J., Zhang, A., Zeng, Y., 2018e: NOAA-GFDL GFDL-ESM4 model output prepared for CMIP6 AerChemMIP piClim-SO2, Version 20180701, Earth System Grid Federation, https://doi.org/10.22033/ESGF/CMIP6.8648.

IPCC, 2013: Annex III: Glossary [Planton, S. (ed.)]. In: Climate Change 2013: The Physical Science Basis. Contribution of Working Group I to the Fifth Assessment Report of the Intergovernmental Panel on Climate Change [Stocker, T.F., D. Qin, G.-K. Plattner, M. Tignor, S.K. Allen, J. Boschung, A. Nauels, Y. Xia, V. Bex and P.M. Midgley (eds.)]. Cambridge University Press, Cambridge, United Kingdom and New York, NY, USA.

Kaiser, J. W., Heil, A., Andreae, M. O., Benedetti, A., Chubarova, N., Jones, L., Morcrette, J.-J., Razinger, M., Schultz, M. G., Suttie, M., and van der Werf, G. R., 2012: Biomass burning emissions estimated with a global fire assimilation system based on observed fire radiative power, Biogeosciences, 9, 527–554, https://doi.org/10.5194/bg-9-527-2012.

Kasoar, M., Voulgarakis, A., Lamarque, J.-F., Shindell, D. T., Bellouin, N., Collins, W. J., Faluvegi, G., and Tsigaridis, K., 2016: Regional and global temperature response to anthropogenic SO2 emissions from China in three climate models, Atmos. Chem. Phys., 16, 9785–9804, https://doi.org/10.5194/acp-16-9785-2016.

Kasoar, M., Shawki, D., and Voulgarakis, A., 2018: Similar spatial patterns of global climate response to aerosols from different regions, npj Clim Atmos Sci 1, 12 , https://doi.org/10.1038/s41612-018-0022-z.

Kawai, H., Yukimoto, S., Koshiro, T., Oshima, N., Tanaka, T., Yoshimura, H., and Nagasawa, R., 2019: Significant improvement of cloud representation in the global climate model MRI-ESM2, Geosci. Model Dev., 12, 2875–2897, https://doi.org/10.5194/gmd-12-2875-2019.

Kirkevåg, A., Grini, A., Olivié, D., Seland, Ø., Alterskjær, K., Hummel, M., Karset, I. H. H., Lewinschal, A., Liu, X., Makkonen, R., Bethke, I., Griesfeller, J., Schulz, M., and Iversen, T., 2018: A production-tagged aerosol module for Earth system models, OsloAero5.3 – extensions and updates for CAM5.3-Oslo, Geosci. Model Dev., 11, 3945–3982, https://doi.org/10.5194/gmd-11-3945-2018.

Lamarque, J.-F., Bond, T. C., Eyring, V., Granier, C., Heil, A., Klimont, Z., Lee, D., Liousse, C., Mieville, A., Owen, B., Schultz, M. G., Shindell, D., Smith, S. J., Stehfest, E., Van Aardenne, J., Cooper, O. R., Kainuma, M., Mahowald, N., McConnell, J. R., Naik, V., Riahi, K., and van Vuuren, D. P., 2010: Historical (1850–2000) gridded anthropogenic and biomass burning emissions of reactive gases and aerosols: methodology and application, Atmos. Chem. Phys., 10, 7017–7039, https://doi.org/10.5194/acp-10-7017-2010.

Lewinschal, A., Ekman, A. M. L., Hansson, H.-C., Sand, M., Berntsen, T. K., and Langner, J., 2019: Local and remote temperature response of regional SO2 emissions, Atmos. Chem. Phys., 19, 2385–2403, https://doi.org/10.5194/acp-19-2385-2019.

Liu, L., Shawki, D., Voulgarakis, A., Kasoar, M., Samset, B. H., Myhre, G., Forster, P. M., Hodnebrog, Ø., Sillman, J., Aalbergsjø, S. G., Boucher, O., Faluvegi, G., Iversen, T., Kirkevåg, A., Lamarque, J.-F., Olivié, D., Richadson, T., Shindell, D., and Takemura, T., 2018: A PDRMIP multimodel study on the impacts of regional aerosol forcings on global and regional precipitation, J. of Climate, 31, 4429–4447, https://doi.org/10.1175/JCLI-D-17-0439.1.

Lohmann, U. and Feichter, J., 2005: Global indirect aerosol effects: a review, Atmos. Chem. Phys., 5, 715–737, https://doi.org/10.5194/acp-5-715-2005.

Lohmann, U. and Neubauer, D., 2018: The importance of mixed-phase and ice clouds for climate sensitivity in the global aerosol–climate model ECHAM6-HAM2, Atmos. Chem. Phys., 18, 8807–8828, https://doi.org/10.5194/acp-18-8807-2018.

Lohmann, U., Rotstayn, L., Storelvmo, T., Jones, A., Menon, S., Quaas, J., Ekman, A. M. L., Koch, D., and Ruedy, R., 2010: Total aerosol effect: radiative forcing or radiative flux perturbation?, Atmos. Chem. Phys., 10, 3235–3246, https://doi.org/10.5194/acp-10-3235-2010.

Mauritsen, T., Bader, J., Becker, T., Behrens, J., Bittner, M., Brokopf, R., Brovkin, V., Claussen, M., Crueger, T., Esch, M., Fast, I., Fiedler, S., Fläschner, D., Gayler, V., Giorgetta, M., Goll, D. S., Haak, H., Hagemann, S., Hedemann, C., Hohenegger, C., Ilyina, T., Jahns, T., Jimenéz-de-la-Cuesta, D., Jungclaus, J., Kleinen, T., Kloster, S., Kracher, D., Kinne, S., Kleberg, D., Lasslop, G., Kornblueh, L., Marotzke, J., Matei, D., Meraner, K., Mikolajewicz, U., Modali, K., Möbis, B., Müller, W. A., Nabel, J. E. M. S., Nam, C. C. W., Notz, D., Nyawira, S.-S., Paulsen, H., Peters, K., Pincus, R., Pohlmann, H., Pongratz, J., Popp, M., Raddatz, T. J., Rast, S., Redler, R., Reick, C. H., Rohrschneider, T., Schemann, V., Schmidt, H., Schnur, R., Schulzweida, U., Six, K. D., Stein, L., Stemmler, I., Stevens, B., Storch, J.-S., Tian, F., Voigt, A., Vrese, P., Wieners, K.-H., Wilkenskjeld, S., Winkler, A., and Roeckner, E., 2019: Developments in the MPI-M Earth System Model version 1.2 (MPI-ESM1.2) and its response to increasing CO2, Journal of Advances in Modeling Earth Systems, 11, 998–1038, https://doi.org/10.1029/2018MS001400.

Meinshausen, M., Vogel, E., Nauels, A., Lorbacher, K., Meinshausen, N., Etheridge, D. M., Fraser, P. J., Montzka, S. A., Rayner, P. J., Trudinger, C. M., Krummel, P. B., Beyerle, U., Canadell, J. G., Daniel, J. S., Enting, I. G., Law, R. M., Lunder, C. R., O'Doherty, S., Prinn, R. G., Reimann, S., Rubino, M., Velders, G. J. M., Vollmer, M. K., Wang, R. H. J., and Weiss, R., 2017: Historical greenhouse gas concentrations for climate modelling (CMIP6), Geosci. Model Dev., 10, 2057–2116, https://doi.org/10.5194/gmd-10-2057-2017.

Michou, M., Nabat, P., Saint-Martin D., Bock, J., Decharme, B., Mallet M., Roehrig, R., Séférian, R., Sénési, S., and Voldoire, A., 2020: Present-day and historical aerosol and ozone characteristics in CNRM CMIP6 simulations, Journal of Advances in Modeling Earth Systems, 12, e2019MS001816, https://doi.org/10.1029/2019MS001816.

Ming, Y., and Ramaswamy, V., 2009: Nonlinear climate and hydrological responses to aerosol effects, Journal of Climate, 22, 1329–1339, https://doi.org/10.1175/2008JCLI2362.1.

Myhre, G., Aas, W., Cherian, R., Collins, W., Faluvegi, G., Flanner, M., Forster, P., Hodnebrog, Ø., Klimont, Z., Lund, M. T., Mülmenstädt, J., Lund Myhre, C., Olivié, D., Prather, M., Quaas, J., Samset, B. H., Schnell, J. L., Schulz, M., Shindell, D., Skeie, R. B., Takemura, T., and Tsyro, S., 2017: Multi-model simulations of aerosol and ozone radiative forcing due to anthropogenic emission changes during the period 1990–2015, Atmos. Chem. Phys., 17, 2709–2720, https://doi.org/10.5194/acp-17-2709-2017.

Myhre, G., D. Shindell, F.-M. Bréon, W. Collins, J. Fuglestvedt, J. Huang, D. Koch, J.-F. Lamarque, D. Lee, B. Mendoza, T. Nakajima, A. Robock, G. Stephens, T. Takemura and H. Zhang, 2013: Anthropogenic and Natural Radiative Forcing. In: Climate Change 2013: The Physical Science Basis. Contribution of Working Group I to the Fifth Assessment Report of the Intergovernmental Panel on Climate Change [Stocker, T.F., D. Qin, G.-K. Plattner, M. Tignor, S.K. Allen, J. Boschung, A. Nauels, Y. Xia, V. Bex and P.M. Midgley (eds.)]. Cambridge University Press, Cambridge, United Kingdom and New York, NY, USA.

Neubauer, D., Ferrachat, S., Siegenthaler-Le Drian, C., Stier, P., Partridge, D. G., Tegen, I., Bey, I., Stanelle, T., Kokkola, H., and Lohmann, U., 2019a: The global aerosol–climate model ECHAM6.3–HAM2.3 – Part 2: Cloud evaluation, aerosol radiative forcing, and climate sensitivity, Geosci. Model Dev., 12, 3609–3639, https://doi.org/10.5194/gmd-12-3609-2019.

Neubauer, D., Ferrachat, S., Siegenthaler-Le Drian, C., Stoll, J., Folini, D. S., Tegen, I., Wieners, K.-H., Mauritsen, T., Stemmler, I., Barthel, S., Bey, I., Daskalakis, N., Heinold, B., Kokkola, H., Partridge, D., Rast, S., Schmidt, H., Schutgens, N., Stanelle, T., Stier, P., Watson-Parris, D., Lohmann, U., 2019b: HAMMOZ-Consortium MPI-ESM1.2-HAM model output prepared for CMIP6 RFMIP piClim-control, Version 20190627, Earth System Grid Federation, https://doi.org/10.22033/ESGF/CMIP6.14730.

Neubauer, D., Ferrachat, S., Siegenthaler-Le Drian, C., Stoll, J., Folini, D. S., Tegen, I., Wieners, K.-H., Mauritsen, T., Stemmler, I., Barthel, S., Bey, I., Daskalakis, N., Heinold, B., Kokkola, H., Partridge, D., Rast, S., Schmidt, H., Schutgens, N., Stanelle, T., Stier, P., Watson-Parris, D., Lohmann, U., 2019c: HAMMOZ-Consortium MPI-ESM1.2-HAM model output prepared for CMIP6 RFMIP piClim-aer, Version 20190627, Earth System Grid Federation, https://doi.org/10.22033/ESGF/CMIP6.14728.

Neubauer, D., Ferrachat, S., Siegenthaler-Le Drian, C., Stoll, J., Folini, D. S., Tegen, I., Wieners, K.-H., Mauritsen, T., Stemmler, I., Barthel, S., Bey, I., Daskalakis, N., Heinold, B., Kokkola, H., Partridge, D., Rast, S., Schmidt, H., Schutgens, N., Stanelle, T., Stier, P., Watson-Parris, D., Lohmann, U., 2020a: HAMMOZ-Consortium MPI-ESM1.2-HAM model output prepared for CMIP6 AerChemMIP piClim-BC, Version 20200120, Earth System Grid Federation, https://doi.org/10.22033/ESGF/CMIP6.5024.

Neubauer, D., Ferrachat, S., Siegenthaler-Le Drian, C., Stoll, J., Folini, D. S., Tegen, I., Wieners, K.-H., Mauritsen, T., Stemmler, I., Barthel, S., Bey, I., Daskalakis, N., Heinold, B., Kokkola, H., Partridge, D., Rast, S., Schmidt, H., Schutgens, N., Stanelle, T., Stier, P., Watson-Parris, D., Lohmann, U., 2020b:

HAMMOZ-Consortium MPI-ESM1.2-HAM model output prepared for CMIP6 AerChemMIP piClim-OC, Version 20200120, Earth System Grid Federation, https://doi.org/10.22033/ESGF/CMIP6.5032.

Neubauer, D., Ferrachat, S., Siegenthaler-Le Drian, C., Stoll, J., Folini, D. S., Tegen, I., Wieners, K.-H., Mauritsen, T., Stemmler, I., Barthel, S., Bey, I., Daskalakis, N., Heinold, B., Kokkola, H., Partridge, D., Rast, S., Schmidt, H., Schutgens, N., Stanelle, T., Stier, P., Watson-Parris, D., Lohmann, U., 2020c: HAMMOZ-Consortium MPI-ESM1.2-HAM model output prepared for CMIP6 AerChemMIP piClim-SO2, Version 20200120, Earth System Grid Federation, https://doi.org/10.22033/ESGF/CMIP6.5033.

Oliviè, D. J. L., Bentsen, M., Seland, Ø., Toniazzo, T., Gjermundsen, A., Graff, L. S., Debernard, J. B., Gupta, A. K., He, Y., Kirkevåg, A., Schwinger, J., Tjiputra, J., Aas, K. S., Bethke, I., Fan, Y., Griesfeller, J., Grini, A., Guo, C., Ilicak, M., Karset, I. H. H., Landgren, O. A., Liakka, J., Moseid, K. O., Nummelin, A., Spensberger, C., Tang, H., Zhang, Z., Heinze, C., Iversen, T., Schulz, M., 2019a: NCC NorESM2-LM model output prepared for CMIP6 RFMIP piClim-control, Version 20190815 & Version 20200218, Earth System Grid Federation, https://doi.org/10.22033/ESGF/CMIP6.8179.

Oliviè, D. J. L., Bentsen, M., Seland, Ø., Toniazzo, T., Gjermundsen, A., Graff, L. S., Debernard, J. B., Gupta, A. K., He, Y., Kirkevåg, A., Schwinger, J., Tjiputra, J., Aas, K. S., Bethke, I., Fan, Y., Griesfeller, J., Grini, A., Guo, C., Ilicak, M., Karset, I. H. H., Landgren, O. A., Liakka, J., Moseid, K. O., Nummelin, A., Spensberger, C., Tang, H., Zhang, Z., Heinze, C., Iversen, T., Schulz, M., 2019b: NCC NorESM2-LM model output prepared for CMIP6 RFMIP piClim-aer, Version 20190815 & Version 20200218, Earth System Grid Federation, https://doi.org/10.22033/ESGF/CMIP6.8169.

Oliviè, D. J. L., Bentsen, M., Seland, Ø., Toniazzo, T., Gjermundsen, A., Graff, L. S., Debernard, J. B., Gupta, A. K., He, Y., Kirkevåg, A., Schwinger, J., Tjiputra, J., Aas, K. S., Bethke, I., Fan, Y., Griesfeller, J., Grini, A., Guo, C., Ilicak, M., Karset, I. H. H., Landgren, O. A., Liakka, J., Moseid, K. O., Nummelin, A., Spensberger, C., Tang, H., Zhang, Z., Heinze, C., Iversen, T., Schulz, M., 2019c: NCC NorESM2-LM model output prepared for CMIP6 AerChemMIP piClim-BC, Version 20191108 & Version 20200218, Earth System Grid Federation, https://doi.org/10.22033/ESGF/CMIP6.8125.

Oliviè, D. J. L., Bentsen, M., Seland, Ø., Toniazzo, T., Gjermundsen, A., Graff, L. S., Debernard, J. B., Gupta, A. K., He, Y., Kirkevåg, A., Schwinger, J., Tjiputra, J., Aas, K. S., Bethke, I., Fan, Y., Griesfeller, J., Grini, A., Guo, C., Ilicak, M., Karset, I. H. H., Landgren, O. A., Liakka, J., Moseid, K. O., Nummelin, A., Spensberger, C., Tang, H., Zhang, Z., Heinze, C., Iversen, T., Schulz, M., 2019d: NCC NorESM2-LM model output prepared for CMIP6 AerChemMIP piClim-OC, Version 20191108 & Version 20200218, Earth System Grid Federation, https://doi.org/10.22033/ESGF/CMIP6.8157.

Oliviè, D. J. L., Bentsen, M., Seland, Ø., Toniazzo, T., Gjermundsen, A., Graff, L. S., Debernard, J. B., Gupta, A. K., He, Y., Kirkevåg, A., Schwinger, J., Tjiputra, J., Aas, K. S., Bethke, I., Fan, Y., Griesfeller, J., Grini, A., Guo, C., Ilicak, M., Karset, I. H. H., Landgren, O. A., Liakka, J., Moseid, K. O., Nummelin, A., Spensberger, C., Tang, H., Zhang, Z., Heinze, C., Iversen, T., Schulz, M., 2019e: NCC NorESM2-LM model output prepared for CMIP6 AerChemMIP piClim-SO2, Version 20191108 & Version 20200218, Earth System Grid Federation, https://doi.org/10.22033/ESGF/CMIP6.8161.

Oshima, N., Yukimoto, S., Deushi, M., Koshiro, T., Kawai, H., Tanaka, T. Y., and Yoshida, K., 2020: Global and Arctic effective radiative forcing of anthropogenic gases and aerosols in MRI-ESM2.0, Progress in Earth and Planetary Science, 7, 38, https://doi.org/10.1186/s40645-020-00348-w.

Pierce D., 2019. ncdf4: Interface to Unidata netCDF (Version 4 or Earlier) Format Data Files. R package version 1.17. https://CRAN.R-project.org/package=ncdf4

Pincus, R., and Baker, M., 1994: Effect of precipitation on the albedo susceptibility of clouds in the marine boundary layer. Nature 372, 250–252. https://doi.org/10.1038/372250a0.

Pincus, R., Forster, P. M., and Stevens, B., 2016: The Radiative Forcing Model Intercomparison Project (RFMIP): experimental protocol for CMIP6, Geosci. Model Dev., 9, 3447–3460, https://doi.org/10.5194/gmd-9-3447-2016.

R Core Team, 2021: R: A language and environment for statistical computing. R Foundation for Statistical Computing, Vienna, Austria. URL https://www.R-project.org/.

Ramanathan, V., and Carmichael, G., 2008: Global and regional climate changes due to black carbon, Nature Geosci 1, 221–227, https://doi.org/10.1038/ngeo156.

Ramanathan, V., and Feng, Y., 2009: Air pollution, greenhouse gases and climatechange: Global and regional perspectives, Atmos. Environ., 43, 37–50, https://doi.org/10.1016/j.atmosenv.2008.09.063.

Ramaswamy, V., Collins, W., Haywood, J., Lean, J., Mahowald, N., Myhre, G., Naik, V., Shine, K. P., Soden, B., Stenchikov, G., and Storelvmo, T., 2019: Radiative forcing of climate: The historical evolution of the radiative forcing concept, the forcing agents and their quantification, and applications. Meteorological Monographs, 59, 14.1–14.101. https://doi.org/10.1175/AMSMONOGRAPHS-D-19-0001.1.

Richardson, T. B., Forster, P. M., Smith, C. J., Maycock, A. C., Wood, T., Andrews, T., Boucher, O., Faluvegi, G., Fläschner, D., Hodnebrog, Ø., Kasoar, M., Kirkevåg, A., Lamarque, J.-F., Mülmenstädt, J., Myhre, G., Olivié, D., Portmann, R. W., Samset, B. H., Shawki, D., Shindell, D., Stier, P., Takemura, T., Voulgarakis, A., and Watson-Parris, D., 2019: Efficacy of climate forcings in PDRMIP models, Journal of Geophysical Research: Atmospheres, 124, 12,824–12,844, https://doi.org/10.1029/2019JD030581.

Rosenfeld, D., Andreae, M. O., Asmi, A., Chin, M., de Leeuw, G., Donovan, D. P., Kahn, R., Kinne, S., Kivekäs, N., Kulmala, M., Lau, W., Schmidt, K. S., Suni, T., Wagner, T., Wild, M., and Quaas, J., 2014a: Global observations of aerosol-cloud-precipitation-climate interactions, Rev. Geophys., 52, 750–808, https://doi.org/10.1002/2013RG000441.

Rosenfeld, D., Sherwood, S., Wood, R., and Donner, L., 2014b: Climate effects of aerosol-cloud interactions, Science, 343(6169), 379–380, https://doi.org/10.1126/science.1247490.

Rotstayn, L. D., and Liu, Y., 2005: A smaller global estimate of the second indirect aerosol effect, Geophys. Res. Lett., 32, L05708, https://doi.org/10.1029/2004GL021922.

Samset, B. H., Myhre, G., Forster, P. M., Hodnebrog, Ø., Andrews, T., Faluvegi, G., Fläschner, D., Kasoar, M., Kharin, V., Kirkevåg, A., Lamarque, J.-F., Olivié, D., Richardson, T., Shindell, D., Shine, K. P., Takemura, T., and Voulgarakis, A., 2016: Fast and slow precipitation responses to individual climate forcers: A PDRMIP multimodel study, Geophys. Res. Lett., 43, 2782–2791, https://doi.org/10.1002/2016GL068064.

Samset, B. H., Sand, M., Smith, C. J., Bauer, S. E., Forster, P. M., Fuglestvedt, J. S., Osprey, S., and Schleussner, C.-F., 2018: Climate impacts from a removal of anthropogenic aerosol emissions, Geophysical Research Letters, 45, 1020–1029, https://doi.org/10.1002/2017GL076079.

Sand, M., Berntsen, T. K., Kay, J. E., Lamarque, J. F., Seland, Ø., and Kirkevåg, A., 2013: The Arctic response to remote and local forcing of black carbon, Atmos. Chem. Phys., 13, 211–224, https://doi.org/10.5194/acp-13-211-2013.

Seferian, R., 2019a: CNRM-CERFACS CNRM-ESM2-1 model output prepared for CMIP6 RFMIP piClim-control, Version 20190219, Earth System Grid Federation, https://doi.org/10.22033/ESGF/CMIP6.9646.

Seferian, R., 2019b: CNRM-CERFACS CNRM-ESM2-1 model output prepared for CMIP6 RFMIP piClim-aer, Version 20190219, Earth System Grid Federation, https://doi.org/10.22033/ESGF/CMIP6.9644.

Seferian, R., 2019c: CNRM-CERFACS CNRM-ESM2-1 model output prepared for CMIP6 AerChemMIP piClim-BC, Version 20190219, Earth System Grid Federation, https://doi.org/10.22033/ESGF/CMIP6.4137.

Seferian, R., 2019d: CNRM-CERFACS CNRM-ESM2-1 model output prepared for CMIP6 AerChemMIP piClim-OC, Version 20190219, Earth System Grid Federation, https://doi.org/10.22033/ESGF/CMIP6.4145.

Seferian, R., 2019e: CNRM-CERFACS CNRM-ESM2-1 model output prepared for CMIP6 AerChemMIP piClim-SO2, Version 20190219, Earth System Grid Federation, https://doi.org/10.22033/ESGF/CMIP6.4146.

Séférian, R., Nabat, P., Michou, M., Saint-Martin, D., Voldoire, A., Colin, J., Decharme, B., Delire, C., Berthet, S., Chevallier, M., Sénési, S., Franchisteguy, L., Vial, J., Mallet, M., Joetzjer, E., Geoffroy, O., Guérémy, J.-F., Moine, M.-P., Msadek, R., Ribes, A., Rocher, M., Roehrig, R., Salas-y-Mélia, D., Sanchez, E., Terray, L., Valcke, S., Waldman, R., Aumont, O., Bopp, L., Deshayes, J., Éthé, C., and Madec, G., 2019: Evaluation of CNRM Earth-System model, CNRM-ESM2-1: role of Earth system processes in present-day and future climate, Journal of Advances in Modeling Earth Systems., 11, 4182–4227, https://doi.org/10.1029/2019MS001791.

Seland, Ø., Bentsen, M., Olivié, D., Toniazzo, T., Gjermundsen, A., Graff, L. S., Debernard, J. B., Gupta, A. K., He, Y.-C., Kirkevåg, A., Schwinger, J., Tjiputra, J., Aas, K. S., Bethke, I., Fan, Y., Griesfeller, J., Grini, A., Guo, C., Ilicak, M., Karset, I. H. H., Landgren, O., Liakka, J., Moseid, K. O., Nummelin, A., Spensberger, C., Tang, H., Zhang, Z., Heinze, C., Iversen, T., and Schulz, M., 2020: Overview of the Norwegian Earth System Model (NorESM2) and key climate response of CMIP6 DECK, historical, and scenario simulations, Geosci. Model Dev., 13, 6165–6200, https://doi.org/10.5194/gmd-13-6165-2020.

Sherwood, S. C., Bony, S., Boucher, O., Bretherton, C., Forster, P. M., Gregory, J. M., and Stevens, B., 2015: Adjustments in the Forcing-Feedback Framework for Understanding Climate Change, B. Am. Meteorol. Soc., 96, 217–228, https://doi.org/10.1175/BAMS-D-13-00167.1.

Shindell, D. T., Faluvegi, G., Rotstayn, L., and Milly, G., 2015: Spatial patterns of radiative forcing and surface temperature response, J. Geophys. Res. Atmos., 120, 5385–5403, https://doi.org/10.1002/2014JD022752.

Shindell, D. T., Lamarque, J.-F., Schulz, M., Flanner, M., Jiao, C., Chin, M., Young, P. J., Lee, Y. H., Rotstayn, L., Mahowald, N., Milly, G., Faluvegi, G., Balkanski, Y., Collins, W. J., Conley, A. J., Dalsoren, S., Easter, R., Ghan, S., Horowitz, L., Liu, X., Myhre, G., Nagashima, T., Naik, V., Rumbold, S. T., Skeie, R., Sudo, K., Szopa, S., Takemura, T., Voulgarakis, A., Yoon, J.-H., and Lo, F., 2013: Radiative forcing in the ACCMIP historical and future climate simulations, Atmos. Chem. Phys., 13, 2939–2974, https://doi.org/10.5194/acp-13-2939-2013.

Shine, K. P., Cook, J., Highwood, E. J., and Joshi, M. M., 2003: An alternative to radiative forcing for estimating the relative importance of climate change mechanisms, Geophysical Research Letters, 30 (20), 2047, https://doi.org/10.1029/2003GL018141.

Smith, C. J., Kramer, R. J., Myhre, G., Alterskjær, K., Collins, W., Sima, A., Boucher, O., Dufresne, J.-L., Nabat, P., Michou, M., Yukimoto, S., Cole, J., Paynter, D., Shiogama, H., O'Connor, F. M., Robertson, E., Wiltshire, A., Andrews, T., Hannay, C., Miller, R., Nazarenko, L., Kirkevåg, A., Olivié, D., Fiedler, S., Lewinschal, A., Mackallah, C., Dix, M., Pincus, R., and Forster, P. M., 2020: Effective radiative forcing and adjustments in CMIP6 models, Atmos. Chem. Phys., 20, 9591–9618, https://doi.org/10.5194/acp-20-9591-2020.

Smith, C. J., Kramer, R. J., Myhre, G., Forster, P. M., Soden, B. J., Andrews, T., Boucher, O., Faluvegi, G., Fläschner, D., Hodnebrog, Ø., Kasoar, M., Kharin, V., Kirkevåg, A., Lamarque, J.-F., Mülmenstädt, J., Olivié, D., Richardson, T., Samset, B. H., Shindell, D., Stier, P., Takemura, T., Voulgarakis, A., and Watson-Parris, D., 2018: Understanding rapid adjustments to diverse forcing agents, Geophysical Research Letters, 45, 12,023–12,031, https://doi.org/10.1029/2018GL079826.

Stjern, C. W., Lund, M. T., Samset, B. H., Myhre, G., Forster, P. M., Andrews, T., Boucher, O., Faluvegi, G., Fläschner, D., Iversen, T., Kasoar, M., Kharin, V., Kirkevåg, A., Lamarque, J.-F., Olivié, D., Richardson, T., Sand, M., Shawki, D., Shindell, D., Smith, C. J., Takemura, T., and Voulgarakis, A., 2019: Arctic amplification response to individual climate drivers, Journal of Geophysical Research: Atmospheres, 124, 6698–6717, https://doi.org/10.1029/2018JD029726.

Stjern, C. W., Samset, B. H., Myhre, G., Forster, P. M., Hodnebrog, Ø. Andrews, T., Boucher, O., Faluvegi, G., Iversen, T., Kasoar, M., Kharin, V., Kirkevåg, A., Lamarque, J.-F., Olivié, O., Richardson, T., Shawki, D., Shindell, D., Smith, C. J., Takemura, T., and Voulgarakis, A., 2017: Rapid adjustments cause weak surface temperature response to increased black carbon concentrations, Journal of Geophysical Research: Atmospheres, 122, 11,462–11,481, https://doi.org/10.1002/2017JD027326.

Tang, T., Shindell, D., Samset, B. H., Boucher, O., Forster, P. M., Hodnebrog, Ø., Myhre, G., Sillmann, J., Voulgarakis, A., Andrews, T., Faluvegi, G., Fläschner, D., Iversen, T., Kasoar, M., Kharin, V., Kirkevåg, A., Lamarque, J.-F., Olivié, D., Richardson, T., Stjern, C. W., and Takemura, T., 2018: Dynamical response of Mediterranean precipitation to greenhouse gases and aerosols, Atmos. Chem. Phys., 18, 8439–8452, https://doi.org/10.5194/acp-18-8439-2018.

Tegen, I., Neubauer, D., Ferrachat, S., Siegenthaler-Le Drian, C., Bey, I., Schutgens, N., Stier, P., Watson-Parris, D., Stanelle, T., Schmidt, H., Rast, S., Kokkola, H., Schultz, M., Schroeder, S., Daskalakis, N., Barthel, S., Heinold, B., and Lohmann, U., 2019: The global aerosol–climate model ECHAM6.3–HAM2.3 – Part 1: Aerosol evaluation, Geosci. Model Dev., 12, 1643–1677, https://doi.org/10.5194/gmd-12-1643-2019.

Thornhill, G. D., Collins, W. J., Kramer, R. J., Olivié, D., Skeie, R. B., O'Connor, F. M., Abraham, N. L., Checa-Garcia, R., Bauer, S. E., Deushi, M., Emmons, L. K., Forster, P. M., Horowitz, L. W., Johnson, B., Keeble, J., Lamarque, J.-F., Michou, M., Mills, M. J., Mulcahy, J. P., Myhre, G., Nabat, P., Naik, V., Oshima, N., Schulz, M., Smith, C. J., Takemura, T., Tilmes, S., Wu, T., Zeng, G., and Zhang, J., 2021a: Effective radiative forcing from emissions of reactive gases and aerosols – a multi-model comparison, Atmos. Chem. Phys., 21, 853–874, https://doi.org/10.5194/acp-21-853-2021.

Thornhill, G., Collins, W., Olivié, D., Skeie, R. B., Archibald, A., Bauer, S., Checa-Garcia, R., Fiedler, S., Folberth, G., Gjermundsen, A., Horowitz, L., Lamarque, J.-F., Michou, M., Mulcahy, J., Nabat, P., Naik, V., O'Connor, F. M., Paulot, F., Schulz, M., Scott, C. E., Séférian, R., Smith, C., Takemura, T., Tilmes, S., Tsigaridis, K., and Weber, J., 2021b: Climate-driven chemistry and aerosol feedbacks in CMIP6 Earth system models, Atmos. Chem. Phys., 21, 1105–1126, https://doi.org/10.5194/acp-21-1105-2021.

Thornhill, G. D., Ryder, C. L., Highwood, E. J., Shaffrey, L. C., and Johnson, B. T., 2018: The effect of South American biomass burning aerosol emissions on the regional climate, Atmos. Chem. Phys., 18, 5321–5342, https://doi.org/10.5194/acp-18-5321-2018.

Twomey, S., 1974: Pollution and the planetary albedo, Atmospheric Environment, 8, 1251-1256, https://doi.org/10.1016/0004-6981(74)90004-3.

Twomey, S., 1977: The Influence of Pollution on Shortwave Albedo of Clouds, Journal of the Atmospheric Sciences, 34, 1149–1152, https://doi.org/10.1175/1520-0469(1977)034<1149:TIOPOT>2.0.CO;2.

Undorf, S., Polson, D., Bollasina, M. A., Ming, Y., Schurer, A., and Hegerl, G. C., 2018: Detectable impact of local and remote anthropogenic aerosols on the 20th century changes of West African and South Asian monsoon precipitation, Journal of Geophysical Research: Atmospheres, 123, 4871–4889, https://doi.org/10.1029/2017JD027711.

Urbanek S., 2013: png: Read and write PNG images. R package version 0.1-7. https://CRAN.R-project.org/package=png.

van Marle, M. J. E., Kloster, S., Magi, B. I., Marlon, J. R., Daniau, A.-L., Field, R. D., Arneth, A., Forrest, M., Hantson, S., Kehrwald, N. M., Knorr, W., Lasslop, G., Li, F., Mangeon, S., Yue, C., Kaiser, J. W., and van der Werf, G. R., 2017: Historic global biomass burning emissions for CMIP6 (BB4CMIP) based on merging satellite observations with proxies and fire models (1750–2015), Geosci. Model Dev., 10, 3329–3357, https://doi.org/10.5194/gmd-10-3329-2017.

Voigt, A., Pincus, R., Stevens, B., Bony, S., Boucher, O., Bellouin, N., Lewinschal, A., Medeiros, B., Wang, Z., and Zhang, H., 2017: Fast and slow shifts of the zonal-mean intertropical convergence zone in response to an idealized anthropogenic aerosol, J. Adv. Model. Earth Syst., 9, 870–892, https://doi.org/10.1002/2016MS000902.

Wan, J. S., Hamilton, D. S., and Mahowald, N. M., 2021: Importance of uncertainties in the spatial distribution of preindustrial wildfires for estimating aerosol radiative forcing, Geophysical Research Letters, 48, e2020GL089758, https://doi.org/10.1029/2020GL089758.

Westervelt, D. M., Conley, A. J., Fiore, A. M., Lamarque, J.-F., Shindell, D. T., Previdi, M., Mascioli, N. R., Faluvegi, G., Correa, G., and Horowitz, L. W., 2018: Connecting regional aerosol emissions reductions to local and remote precipitation responses, Atmos. Chem. Phys., 18, 12461–12475, https://doi.org/10.5194/acp-18-12461-2018.

Wilcox, L. J., Highwood, E. J., Booth, B. B. B., and Carslaw, K. S., 2015: Quantifying sources of inter-model diversity in the cloud albedo effect, Geophys. Res. Lett., 42, 1568–1575, https://doi.org/10.1002/2015GL063301.

Yukimoto, S., Kawai, H., Koshiro, T., Oshima, N., Yoshida, K., Urakawa, S., Tsujino, H., Deushi, M., Tanaka, T., Hosaka, M., Yabu, S., Yoshimura, H., Shindo, E., Mizuta, R., Obata, A., Adachi, Y., and Ishii, M., 2019a: The Meteorological Research Institute Earth System Model Version 2.0, MRI-ESM2.0: Description and Basic Evaluation of the Physical Component, J. Meteor. Soc. Japan., 97, 931–965, https://doi.org/10.2151/jmsj.2019-051.

Yukimoto, S., Koshiro, T., Kawai, H., Oshima, N., Yoshida, K., Urakawa, S., Tsujino, H., Deushi, M., Tanaka, T., Hosaka, M., Yoshimura, H., Shindo, E., Mizuta, R., Ishii, M., Obata, A., Adachi, Y., 2019b: MRI MRI-ESM2.0 model output prepared for CMIP6 RFMIP piClim-control, Version 20200114, Earth System Grid Federation, https://doi.org/10.22033/ESGF/CMIP6.6888.

Yukimoto, S., Koshiro, T., Kawai, H., Oshima, N., Yoshida, K., Urakawa, S., Tsujino, H., Deushi, M., Tanaka, T., Hosaka, M., Yoshimura, H., Shindo, E., Mizuta, R., Ishii, M., Obata, A., Adachi, Y., 2019c: MRI MRI-ESM2.0 model output prepared for CMIP6 RFMIP piClim-aer, Version 20200114, Earth System Grid Federation, https://doi.org/10.22033/ESGF/CMIP6.6885.

Yukimoto, S., Koshiro, T., Kawai, H., Oshima, N., Yoshida, K., Urakawa, S., Tsujino, H., Deushi, M., Tanaka, T., Hosaka, M., Yoshimura, H., Shindo, E., Mizuta, R., Ishii, M., Obata, A., Adachi, Y., 2019d: MRI MRI-ESM2.0 model output prepared for CMIP6 AerChemMIP piClim-BC, Version 20200218, Earth System Grid Federation, https://doi.org/10.22033/ESGF/CMIP6.6874.

Yukimoto, S., Koshiro, T., Kawai, H., Oshima, N., Yoshida, K., Urakawa, S., Tsujino, H., Deushi, M., Tanaka, T., Hosaka, M., Yoshimura, H., Shindo, E., Mizuta, R., Ishii, M., Obata, A., Adachi, Y., 2019e: MRI MRI-ESM2.0 model output prepared for CMIP6 AerChemMIP piClim-OC, Version 20200218, Earth System Grid Federation, https://doi.org/10.22033/ESGF/CMIP6.6882.

Yukimoto, S., Koshiro, T., Kawai, H., Oshima, N., Yoshida, K., Urakawa, S., Tsujino, H., Deushi, M., Tanaka, T., Hosaka, M., Yoshimura, H., Shindo, E., Mizuta, R., Ishii, M., Obata, A., Adachi, Y., 2019f: MRI MRI-ESM2.0 model output prepared for CMIP6 AerChemMIP piClim-SO2, Version 20200218, Earth System Grid Federation, https://doi.org/10.22033/ESGF/CMIP6.6883.

Zanis, P., Akritidis, D., Georgoulias, A. K., Allen, R. J., Bauer, S. E., Boucher, O., Cole, J., Johnson, B., Deushi, M., Michou, M., Mulcahy, J., Nabat, P., Olivié, D., Oshima, N., Sima, A., Schulz, M., Takemura, T., and Tsigaridis, K., 2020: Fast responses on pre-industrial climate from present-day aerosols in a CMIP6 multi-model study, Atmos. Chem. Phys., 20, 8381–8404, https://doi.org/10.5194/acp-20-8381-2020.

Zanis, P., Ntogras, C., Zakey, A., Pytharoulis, I., and Karacostas, T., 2012: Regional climate feedback of anthropogenic aerosols over Europe using RegCM3, Clim Res, 52, 267-278, https://doi.org/10.3354/cr01070.

Zelinka, M. D., Andrews, T., Forster, P. M., and Taylor, K. E., 2014: Quantifying components of aerosol-cloud-radiation interactions in climate models, J. Geophys. Res. Atmos., 119, 7599–7615, https://doi.org/10.1002/2014JD021710.

Zelinka, M. D., Myers, T. A., McCoy, D. T., Po-Chedley, S., Caldwell, P. M., Ceppi, P., Klein, S. A., and Taylor, K. E., 2020: Causes of higher climate sensitivity in CMIP6 models, Geophysical Research Letters, 47, e2019GL085782, https://doi.org/10.1029/2019GL085782.

Zhang, S., Stier, P., and Watson-Parris, D., 2021: On the contribution of fast and slow responses to precipitation changes caused by aerosol perturbations, Atmos. Chem. Phys., 21, 10179–10197, https://doi.org/10.5194/acp-21-10179-2021.

ABBREVIATIONS

Acronym	Explanation	Acronym	Explanation
ACI	Aerosol-cloud interactions	JJA	June-July-August
AerChemMIP	Aerosol Chemistry Model Intercomparison Project	LSAT	Land-surface air temperature
af	Aerosol-free	LW	Longwave
APRP	Approximate partial radiative perturbation method	MAM	March-April-May
AR5	Fifth Assessment Report	MIP	Model Intercomparison Project
ARI	Aerosol-radiation interactions	N_2O	Nitrous oxide
BC	Black carbon	NH	Northern hemisphere
BrC	Brown carbon	NH_3	Ammonia
CCN	Cloud condensation nuclei	NH_4	Ammonium
CFC	Chlorofluorocarbon	NO	Nitric oxide
CH_4	Methane	NO_3	Nitrate
CMIP	Coupled Model Intercomparison Project	NO_x	Nitrogen oxides
CMIP6	Coupled Model Intercomparison Project Phase 6	NTCF	Near-term climate forcer
CO	Carbon monoxide	O_2	Molecular oxygen
CO_2	Carbon dioxide	O_3	Ozone
cs	Clear-sky	OA	Organic aerosol
csaf	Clear-sky aerosol-free	OC	Organic carbon
DJF	December-January-February	OH	Hydroxyl radical
DMS	Dimethylsulphide	PBAP	Primary biological aerosol particle
ERF	Effective radiative forcing	POA	Primary organic aerosol
ERFaci	Effective radiative forcing due to aerosol-cloud interactions	RF	Radiative forcing
ERFalb	Effective radiative forcing due to changes in surface albedo induced by anthropogenic aerosols	RFMIP	Radiative Forcing Model Intercomparison Project
ERFari	Effective radiative forcing due to aerosol-radiation interactions	SARF	Stratospherically adjusted radiative forcing
ERFari+aci	Total net effective radiative forcing due to aerosols	SH	Southern hemisphere
ESM	Earth System Model	SIC	Sea ice cover
F	Net (downward minus upward) radiative flux at the top of the atmosphere	SLCF	Short-lived climate forcer
GCM	Global climate model	SO_2	Sulphur dioxide
GHG	Greenhouse gas	SO_4	Sulphate
GPH	Geopotential height	SOA	Secondary organic aerosol
H_2O	Water vapour	SON	September-October-November
HCFC	Hydrochlorofluorocarbon	SST	Sea surface temperature
HFC	Hydrofluorocarbon	SW	Shortwave
hPa	Hectopascal	TAR	Third Assessment Report
IN	Ice nuclei	TOA	Top of the atmosphere
IPCC	Intergovernmental Panel on Climate Change	UV	Ultraviolet
IRF	Instantaneous radiative forcing	WMGHG	Well-mixed greenhouse gas
ITCZ	Intertropical Convergence Zone	WMO	World Meteorological Organization

APPENDIX A: ERF spatial pattern for each model

CNRM-ESM2-1

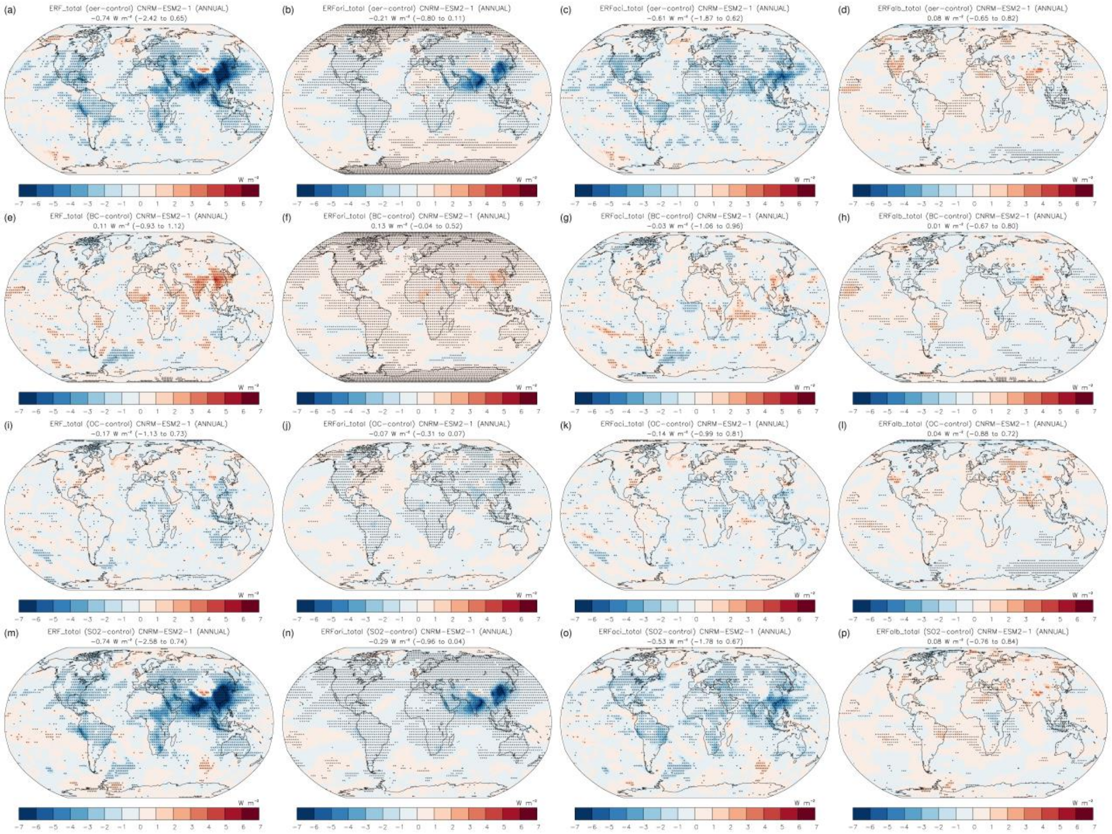

Figure A1. Spatial TOA distribution of the annual mean total (SW + LW) ERF (first column), ERFari (second column), ERFaci (third column), and ERFalb (fourth column) in the piClim-aer (first row), piClim-BC (second row), piClim-OC (third row), and piClim-SO_2 (fourth column) experiment for the CNRM-ESM2-1 model. The black crosses indicate the statistically important values in the 95% confidence level. The global field means (5th to 95th percentiles in the parenthesis) are shown in W m^{-2}.

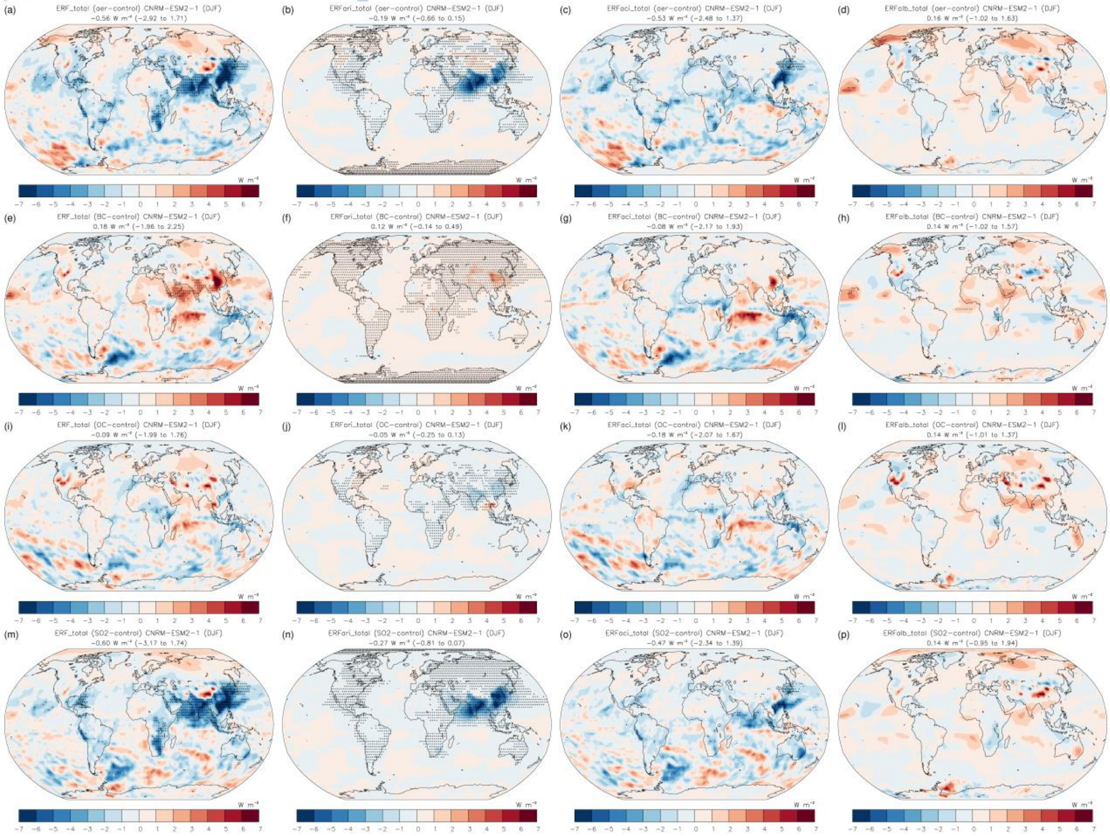

Figure A2. As in Fig. A1, but for DJF.

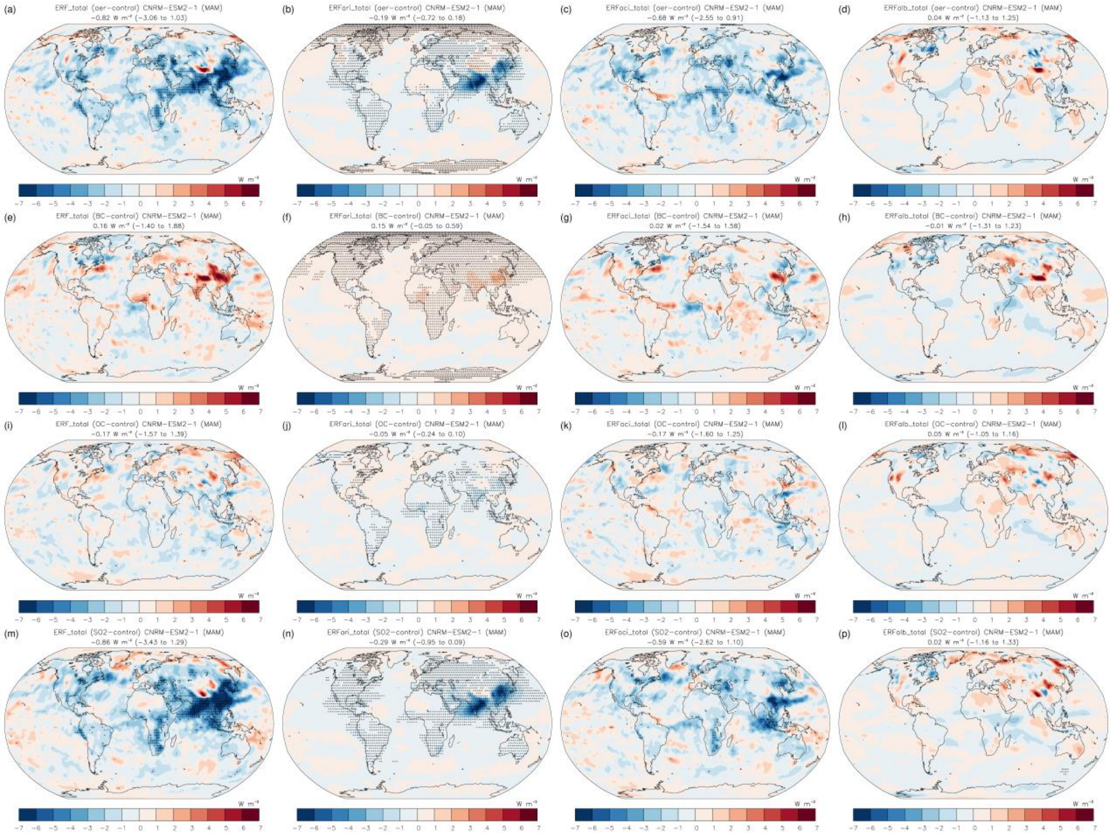

Figure A3. As in Fig. A1, but for MAM.

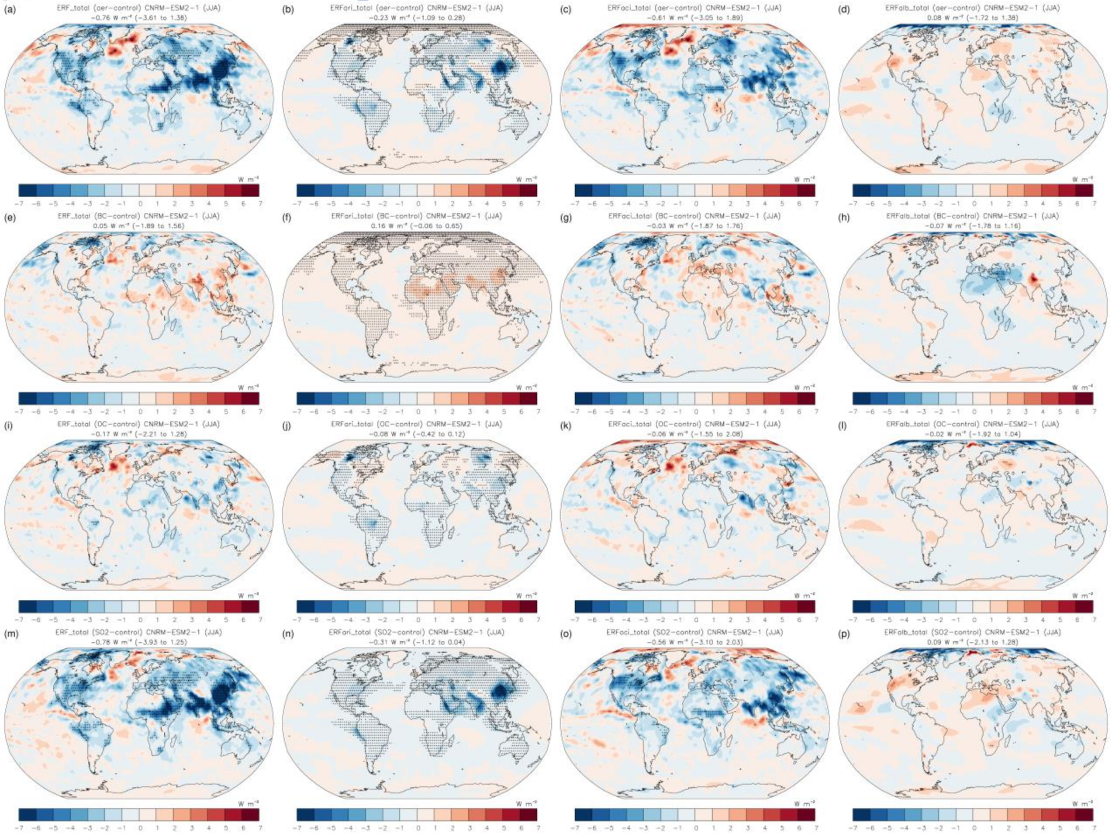

Figure A4. As in Fig. A1, but for JJA.

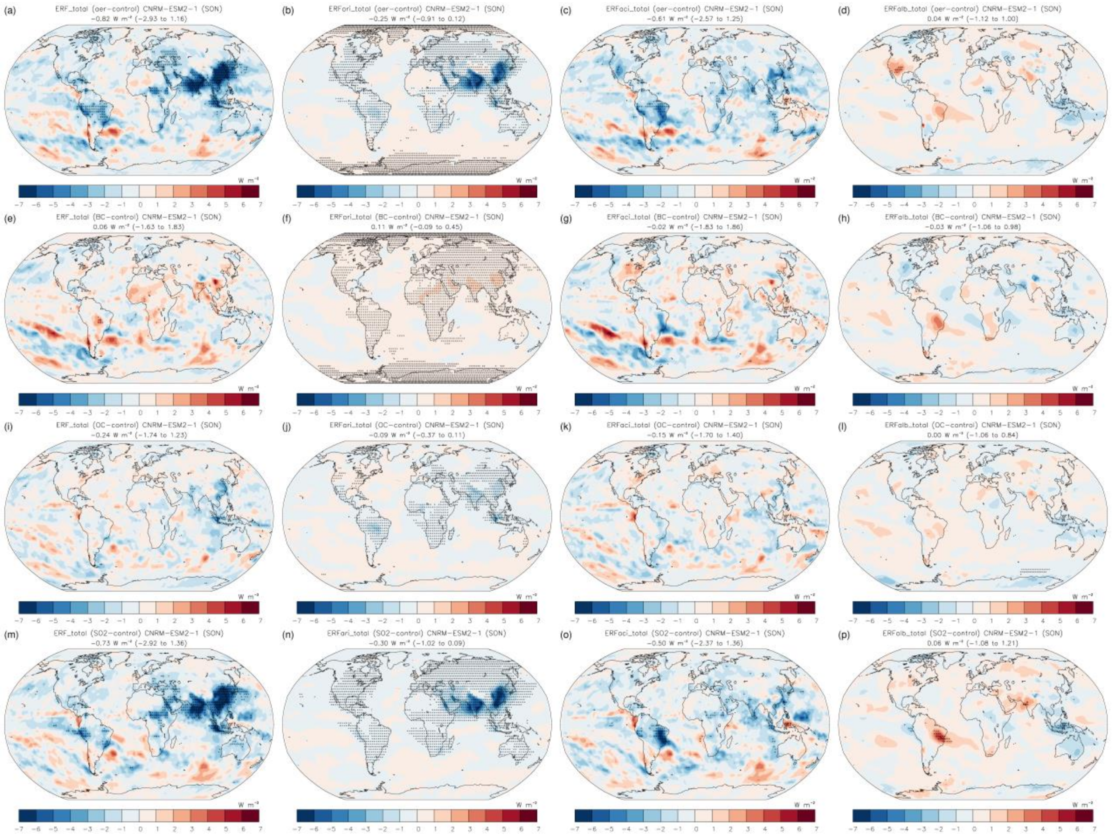

Figure A5. As in Fig. A1, but for SON.

GFDL-ESM4

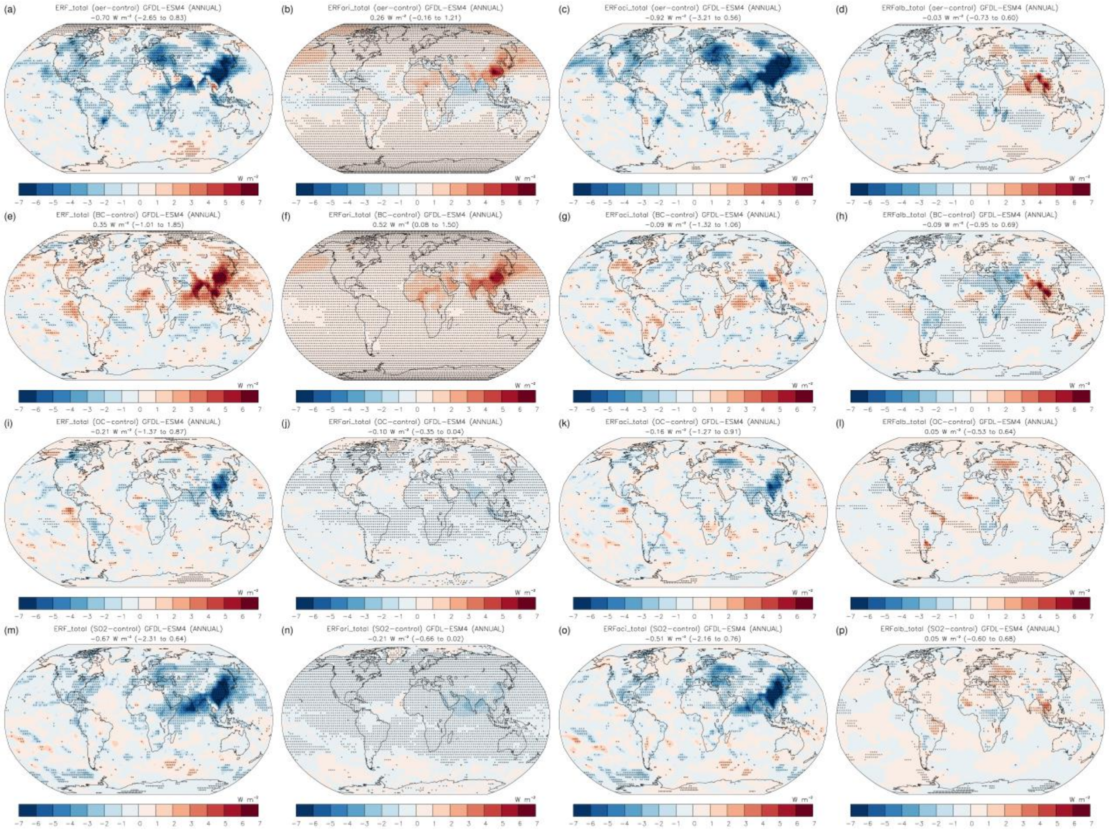

Figure A6. Spatial TOA distribution of the annual mean total (SW + LW) ERF (first column), ERFari (second column), ERFaci (third column), and ERFalb (fourth column) in the piClim-aer (first row), piClim-BC (second row), piClim-OC (third row), and piClim-SO_2 (fourth column) experiment for the GFDL-ESM4 model. The black crosses indicate the statistically important values in the 95% confidence level. The global field means (5th to 95th percentiles in the parenthesis) are shown in W m^{-2}.

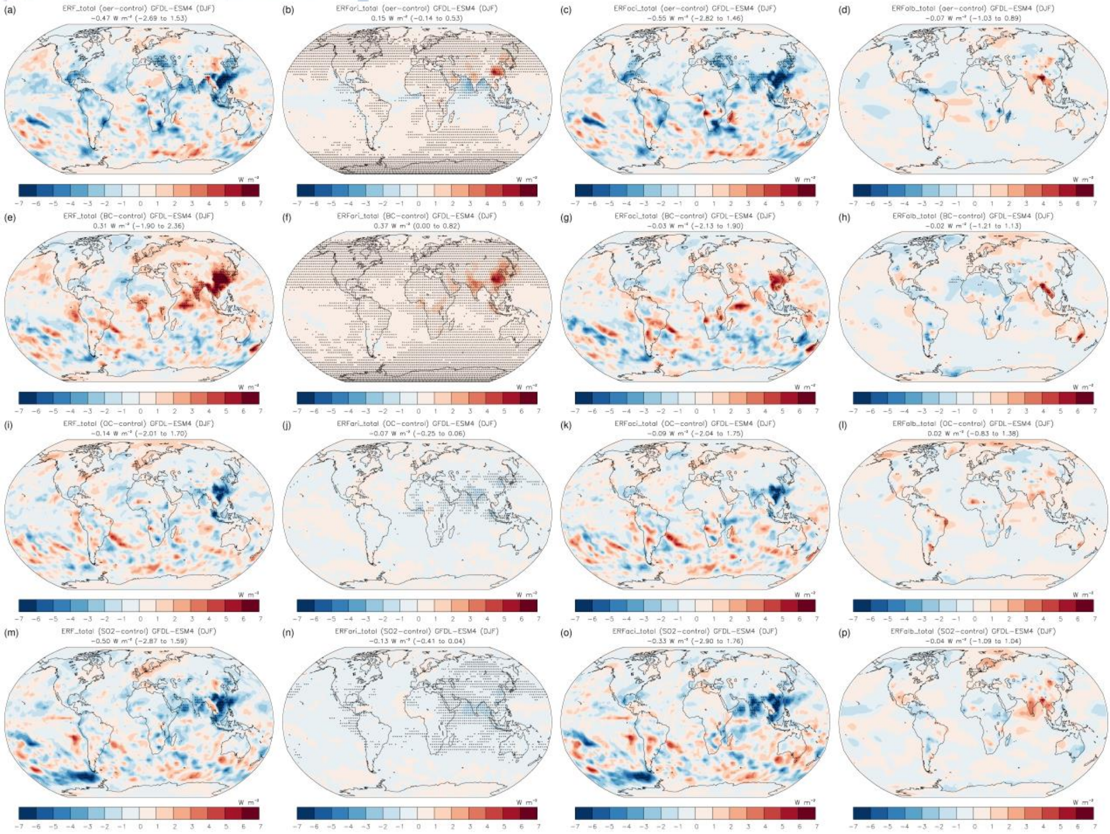

Figure A7. As in Fig. A6, but for DJF.

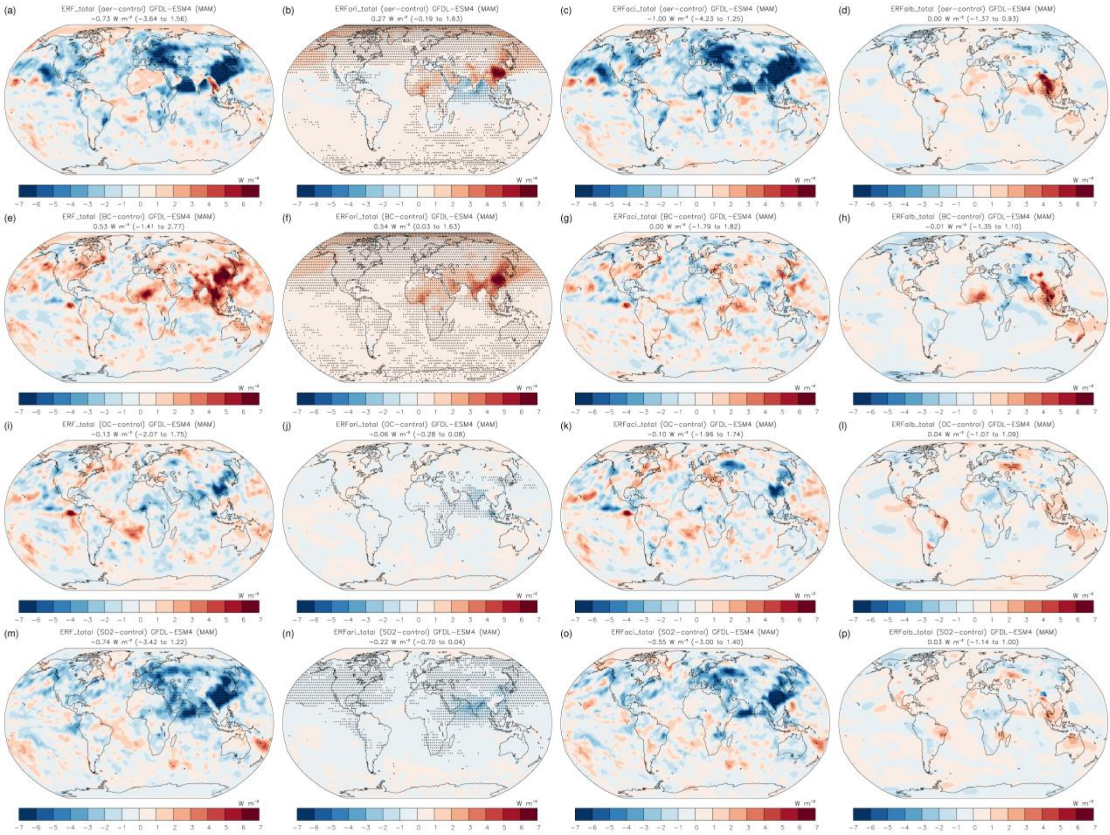

Figure A8. As in Fig. A6, but for MAM.

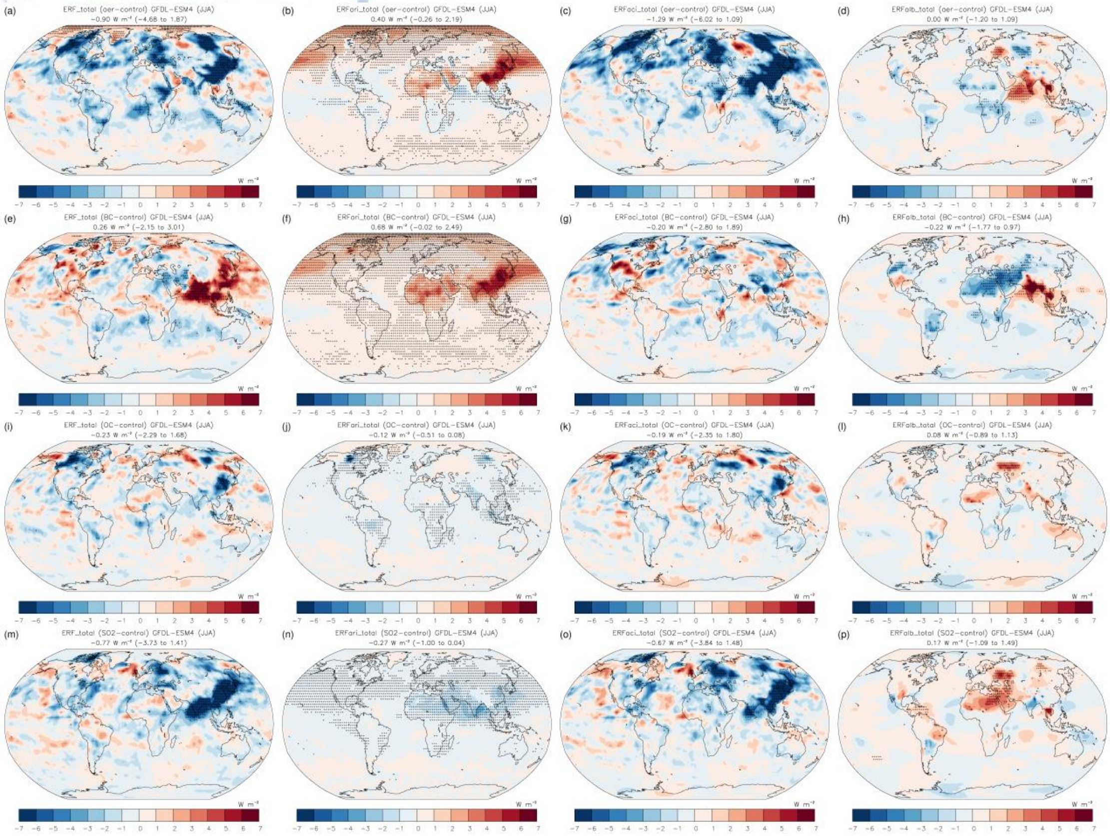

Figure A9. As in Fig. A6, but for JJA.

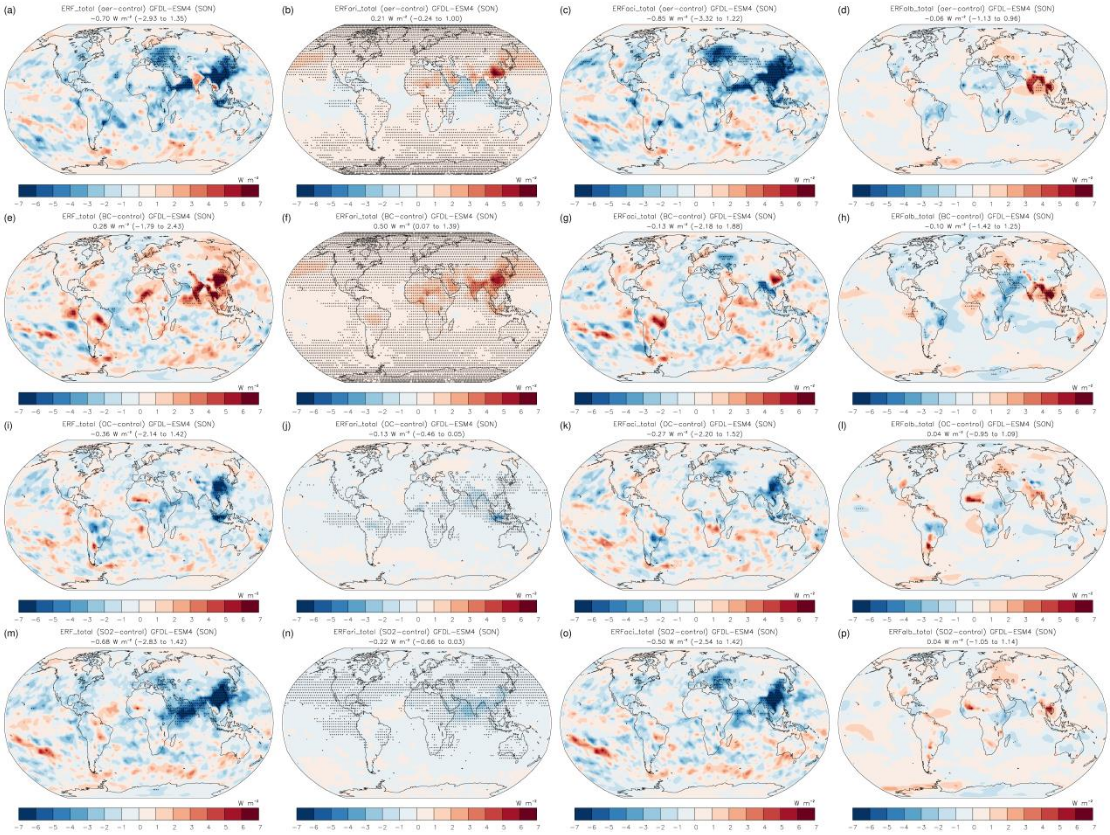

Figure A10. As in Fig. A6, but for SON.

MPI-ESM-1-2-HAM

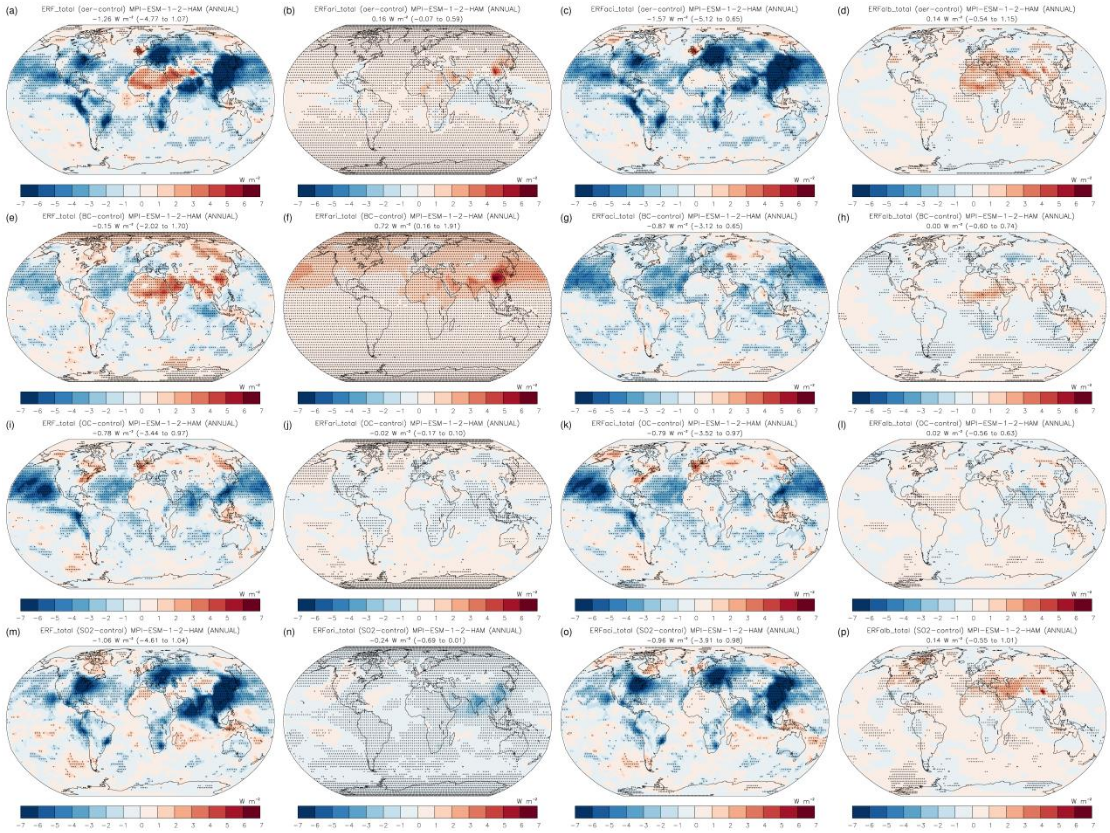

Figure A11. Spatial TOA distribution of the annual mean total (SW + LW) ERF (first column), ERFari (second column), ERFaci (third column), and ERFalb (fourth column) in the piClim-aer (first row), piClim-BC (second row), piClim-OC (third row), and piClim-SO_2 (fourth column) experiment for the MPI-ESM-1-2-HAM model. The black crosses indicate the statistically important values in the 95% confidence level. The global field means (5th to 95th percentiles in the parenthesis) are shown in W m^{-2}.

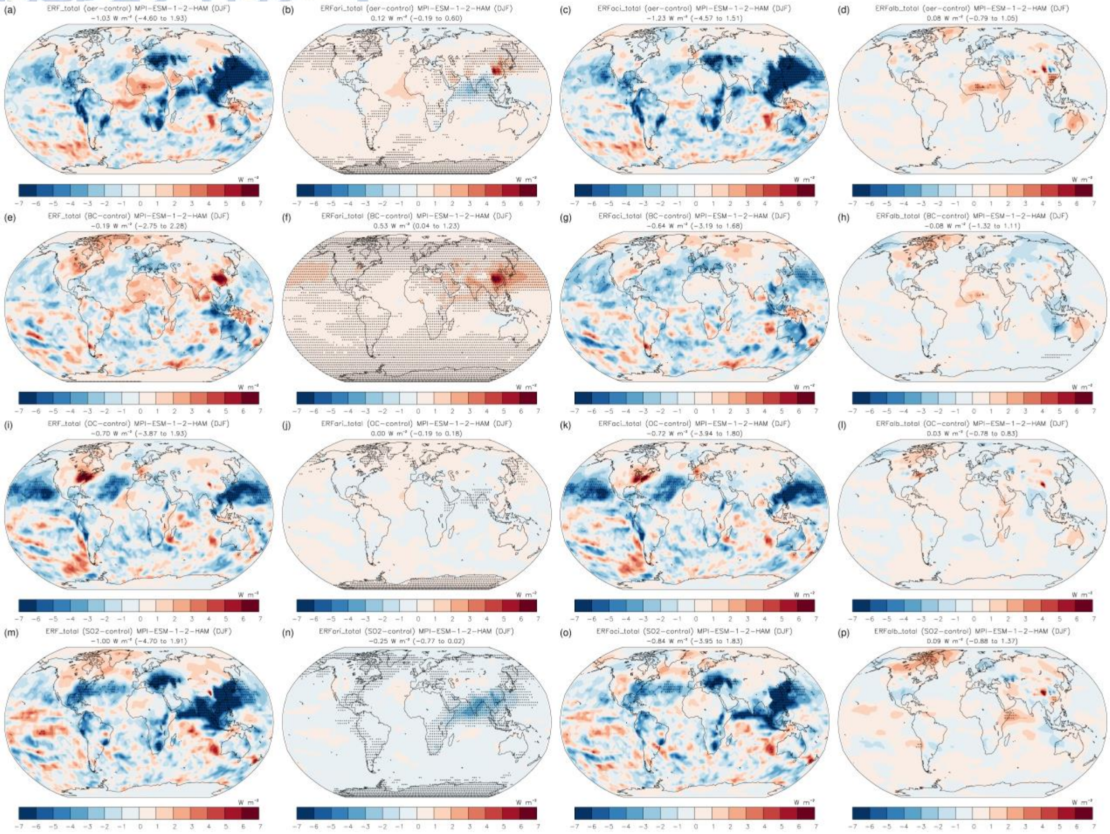

Figure A12. As in Fig. A11, but for DJF.

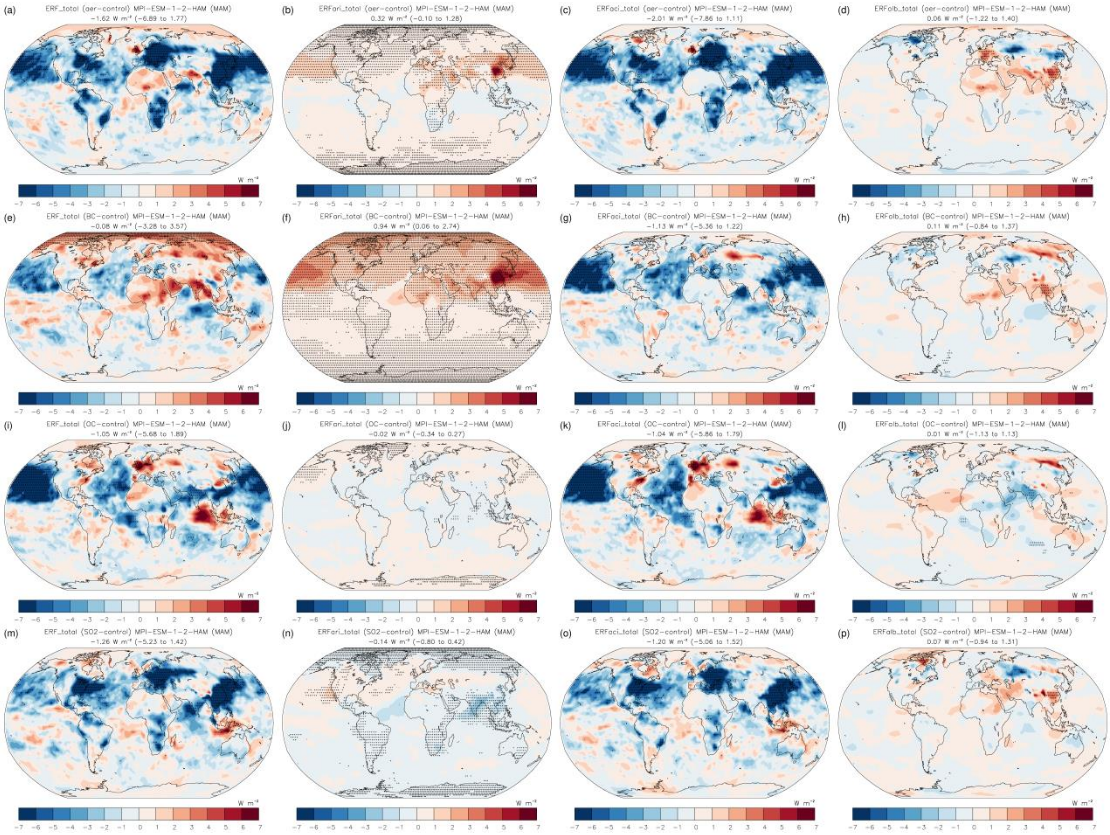

Figure A13. As in Fig. A11, but for MAM.

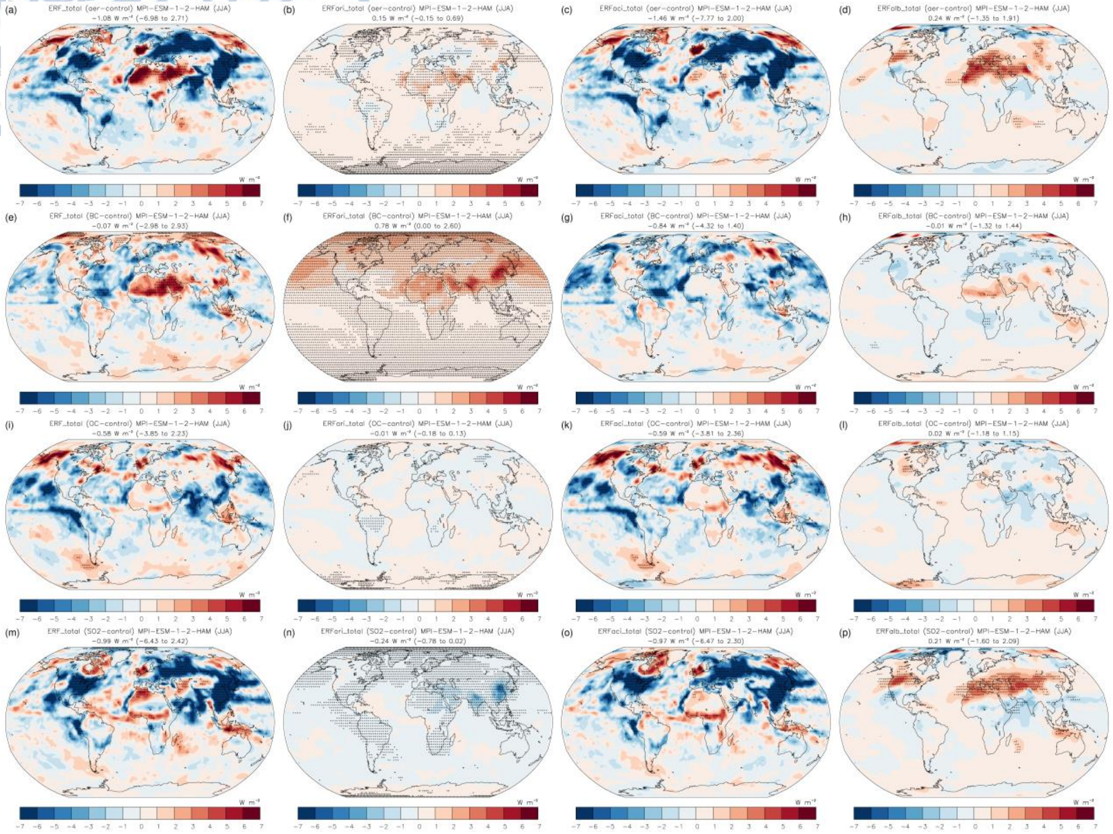

Figure A14. As in Fig. A11, but for JJA.

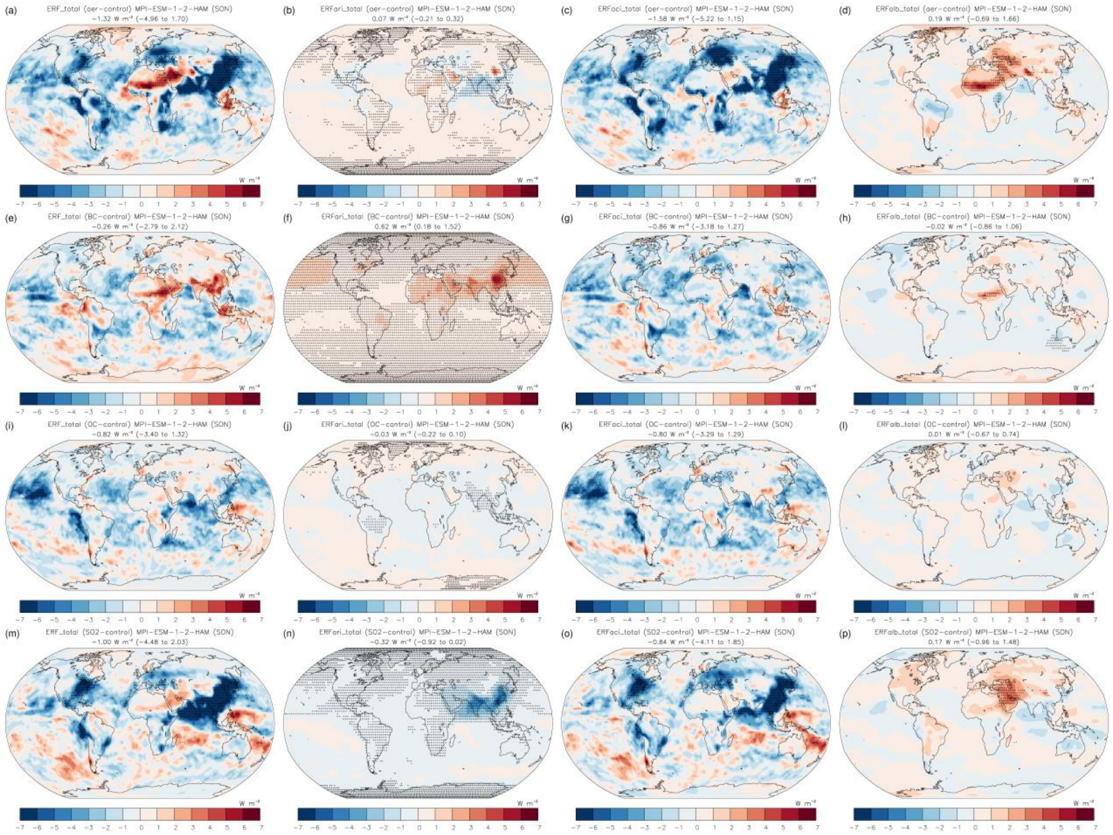

Figure A15. As in Fig. A11, but for SON.

MRI-ESM2-0

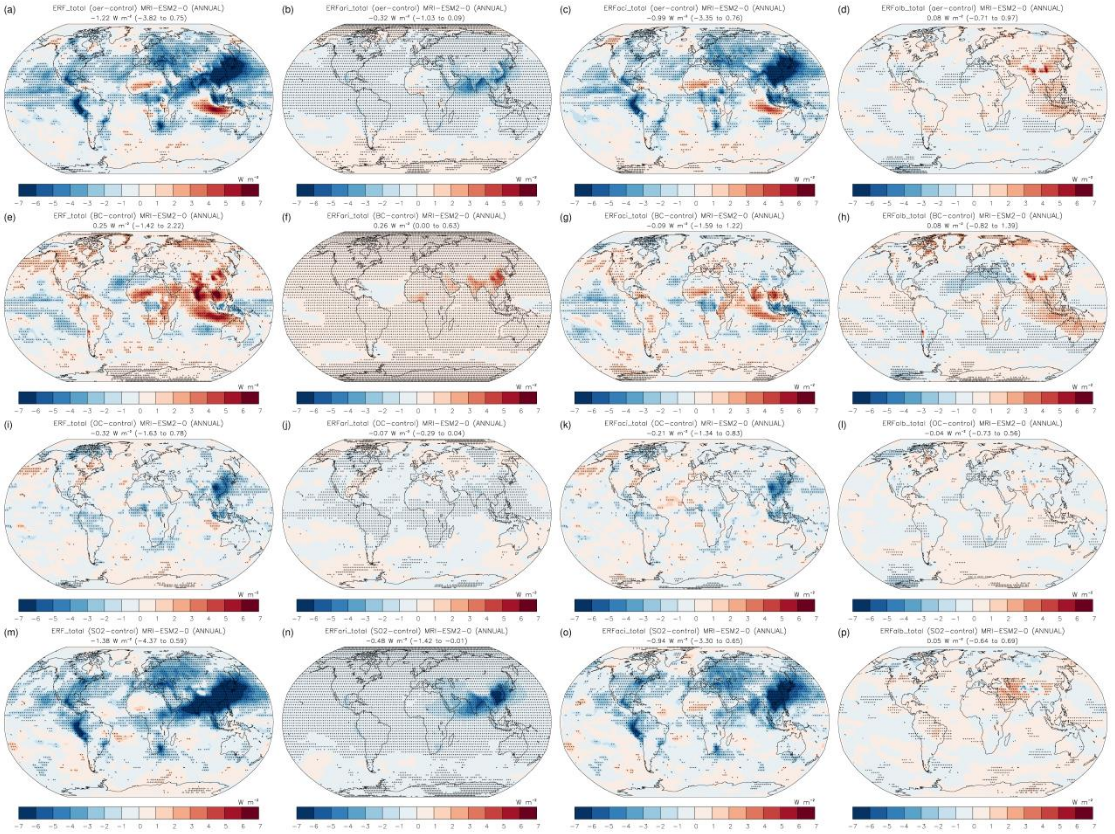

Figure A16. Spatial TOA distribution of the annual mean total (SW + LW) ERF (first column), ERFari (second column), ERFaci (third column), and ERFalb (fourth column) in the piClim-aer (first row), piClim-BC (second row), piClim-OC (third row), and piClim-SO_2 (fourth column) experiment for the MRI-ESM2-0 model. The black crosses indicate the statistically important values in the 95% confidence level. The global field means (5th to 95th percentiles in the parenthesis) are shown in W m^{-2}.

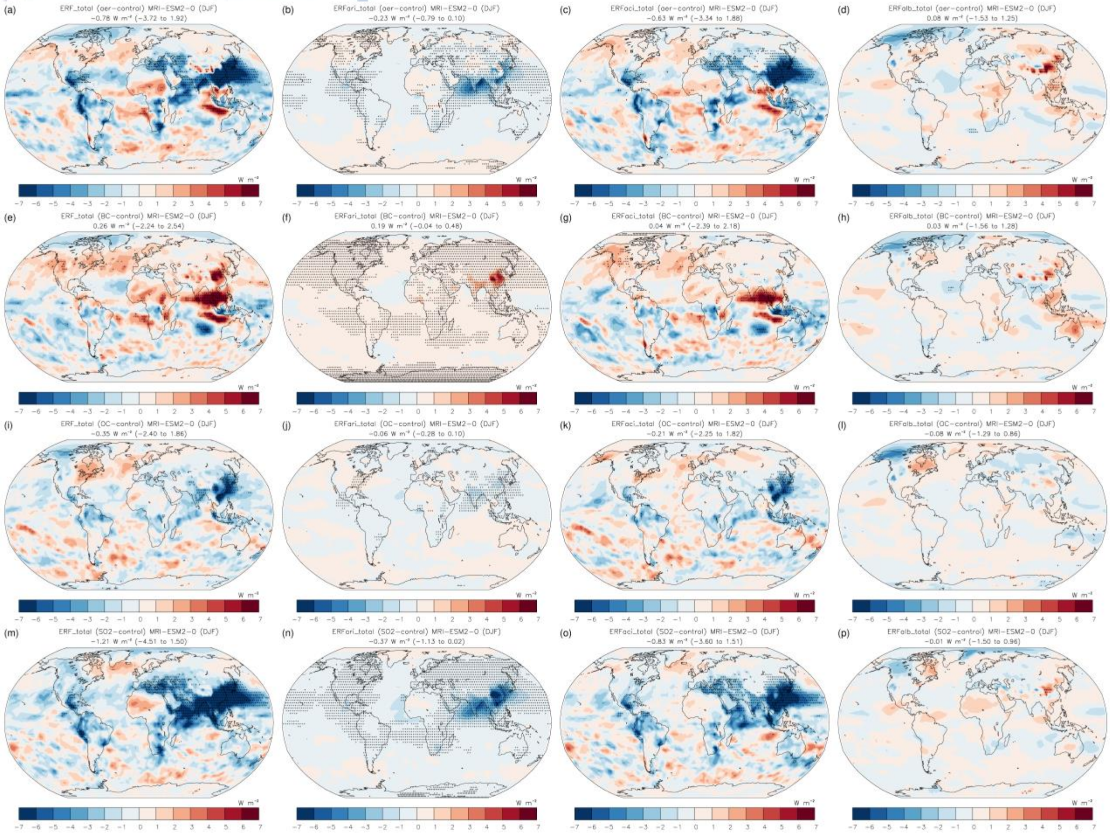

Figure A17. As in Fig. A16, but for DJF.

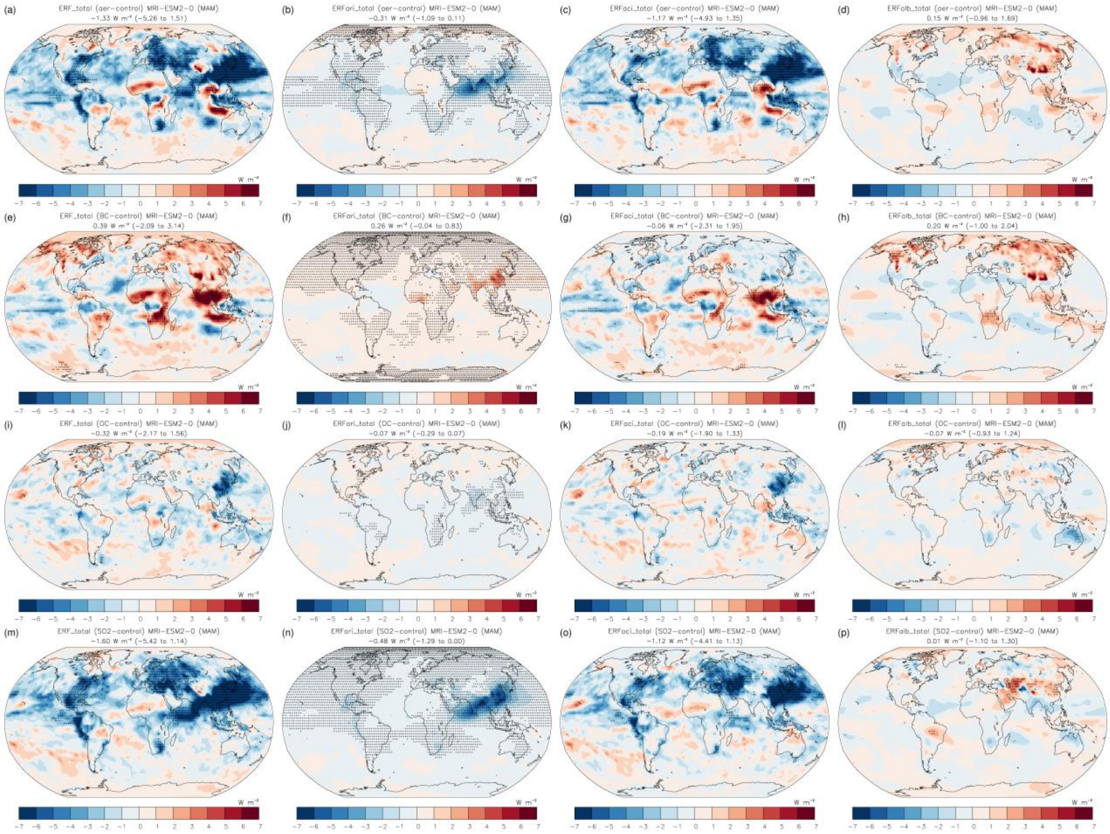

Figure A18. As in Fig. A16, but for MAM.

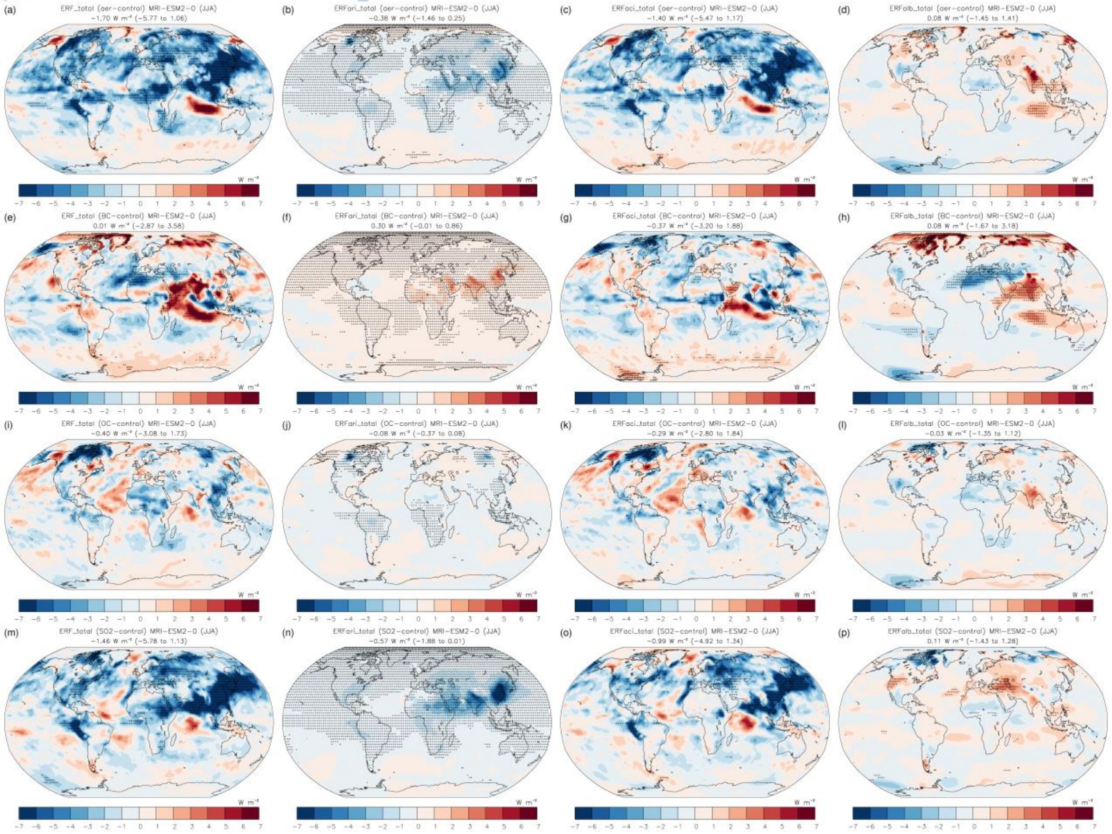

Figure A19. As in Fig. A16, but for JJA.

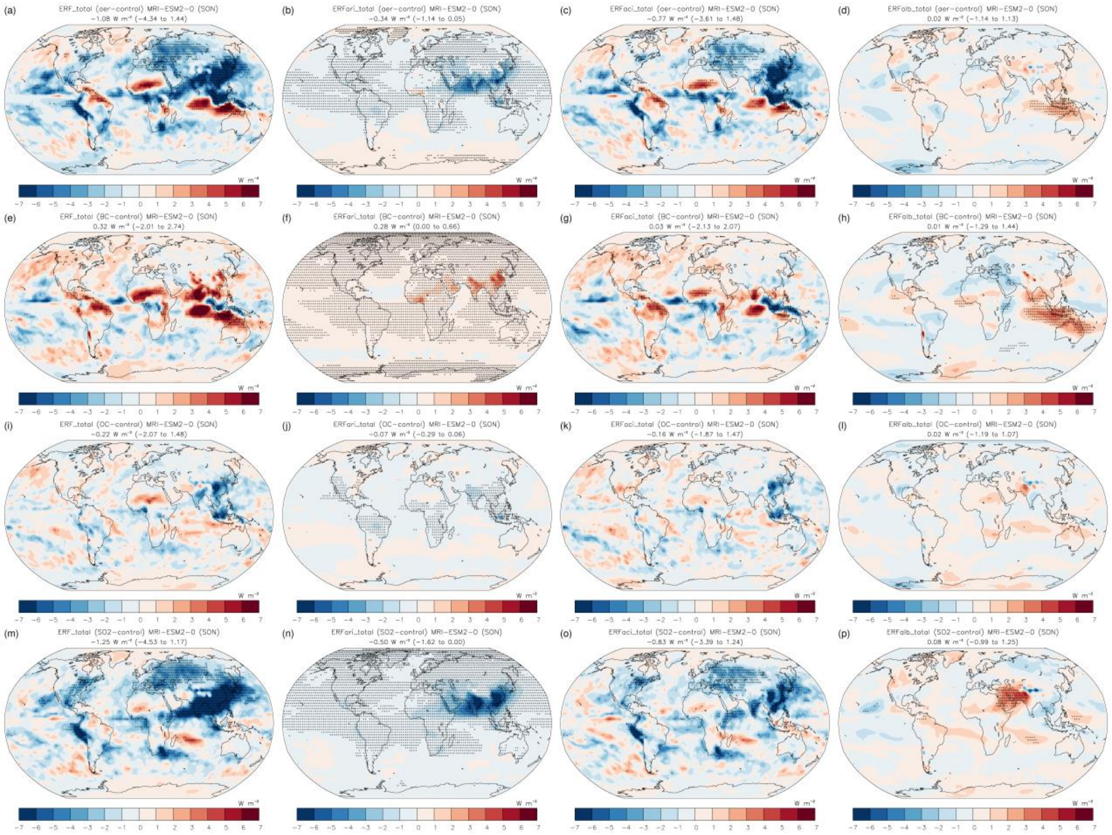

Figure A20. As in Fig. A16, but for SON.

NorESM2-LM (p1)

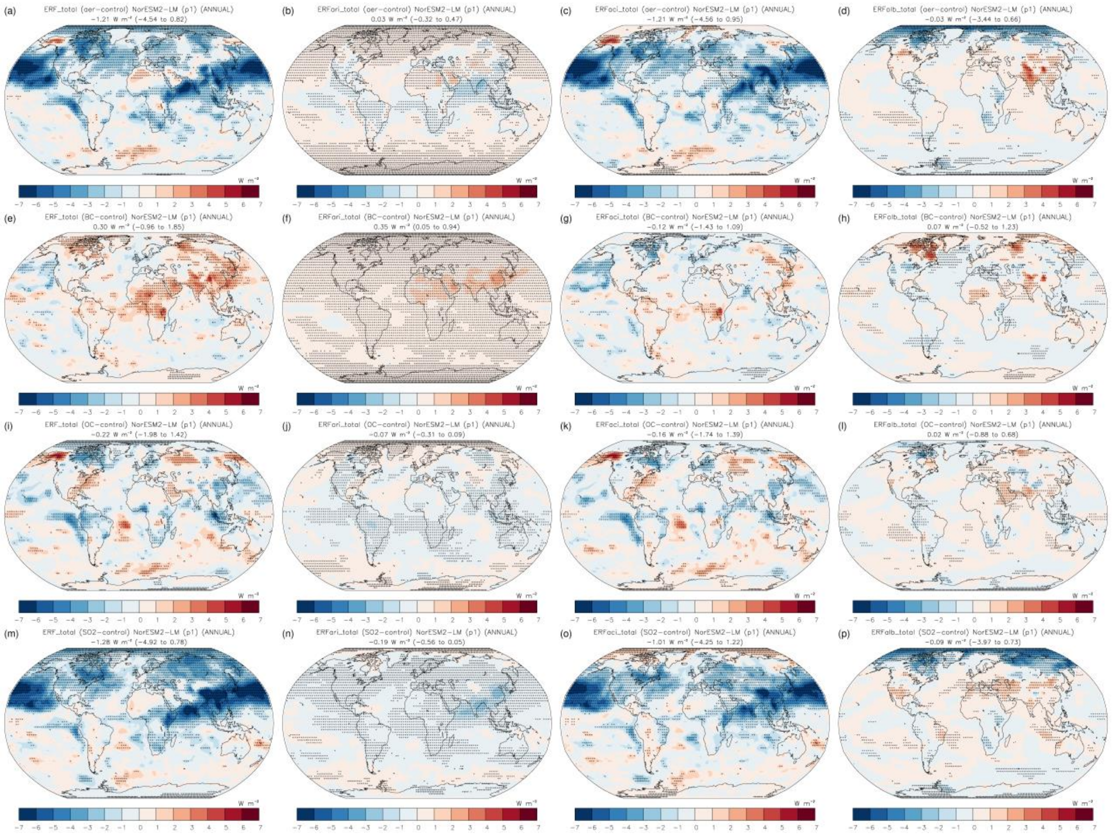

Figure A21. Spatial TOA distribution of the annual mean total (SW + LW) ERF (first column), ERFari (second column), ERFaci (third column), and ERFalb (fourth column) in the piClim-aer (first row), piClim-BC (second row), piClim-OC (third row), and piClim-SO_2 (fourth column) experiment for the NorESM2-LM (p1) model. The black crosses indicate the statistically important values in the 95% confidence level. The global field means (5th to 95th percentiles in the parenthesis) are shown in W m^{-2}.

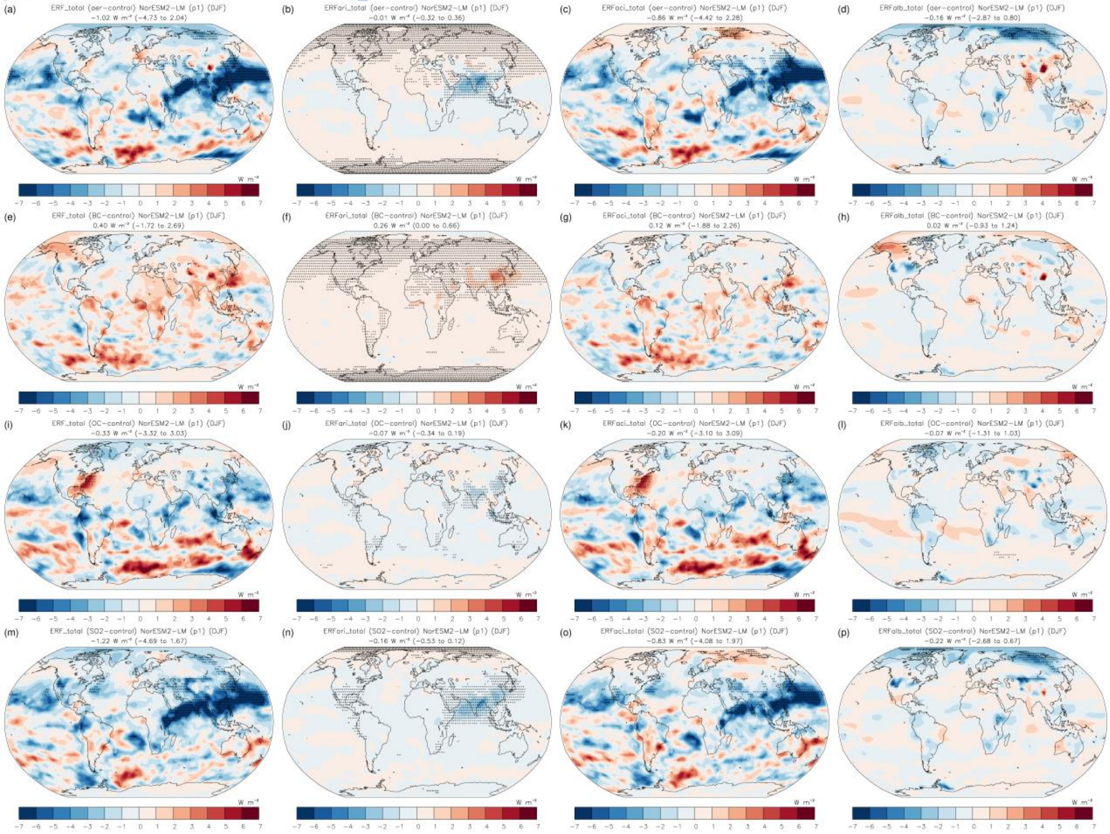

Figure A22. As in Fig. A21, but for DJF.

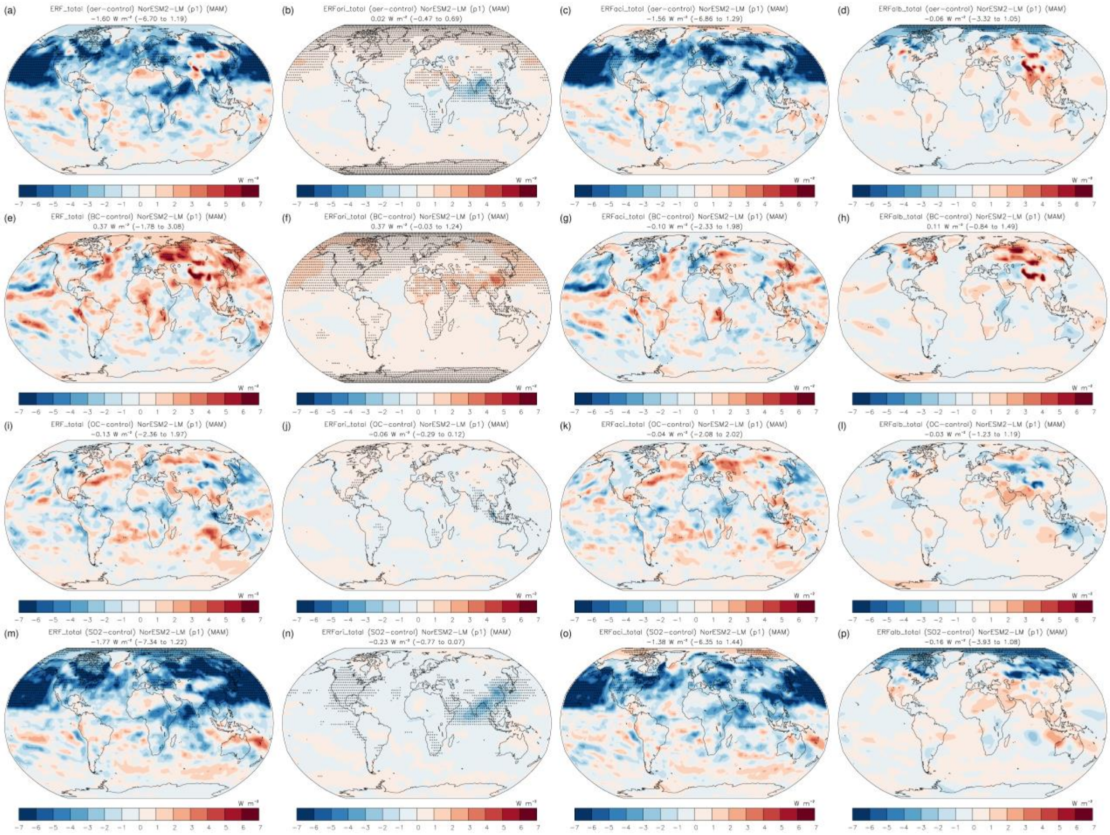

Figure A23. As in Fig. A21, but for MAM.

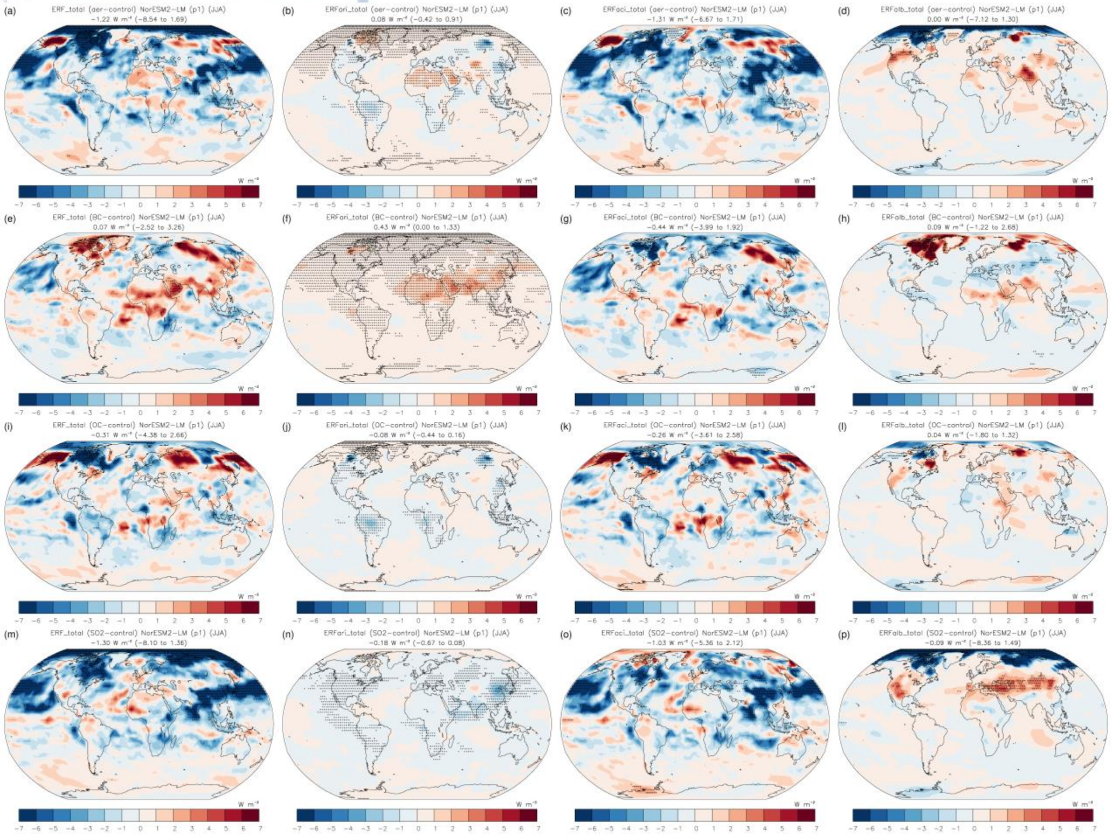

Figure A24. As in Fig. A21, but for JJA.

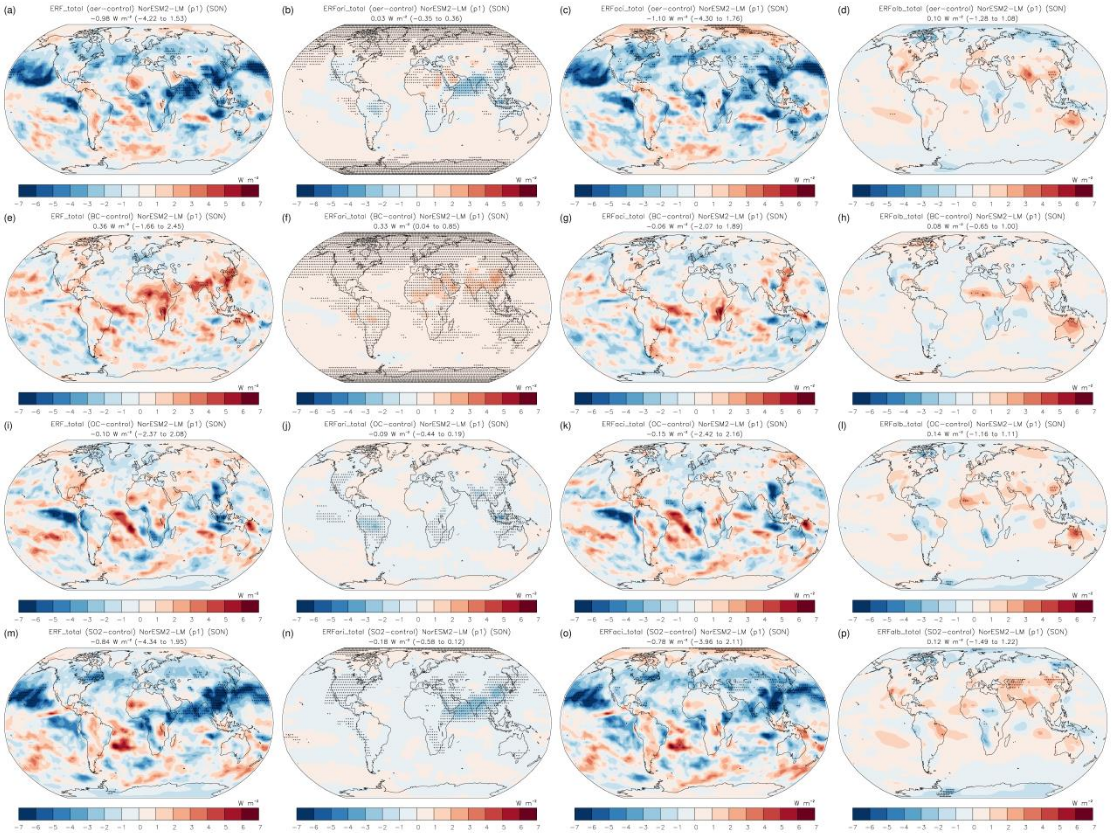

Figure A25. As in Fig. A21, but for SON.

NorESM2-LM (p2)

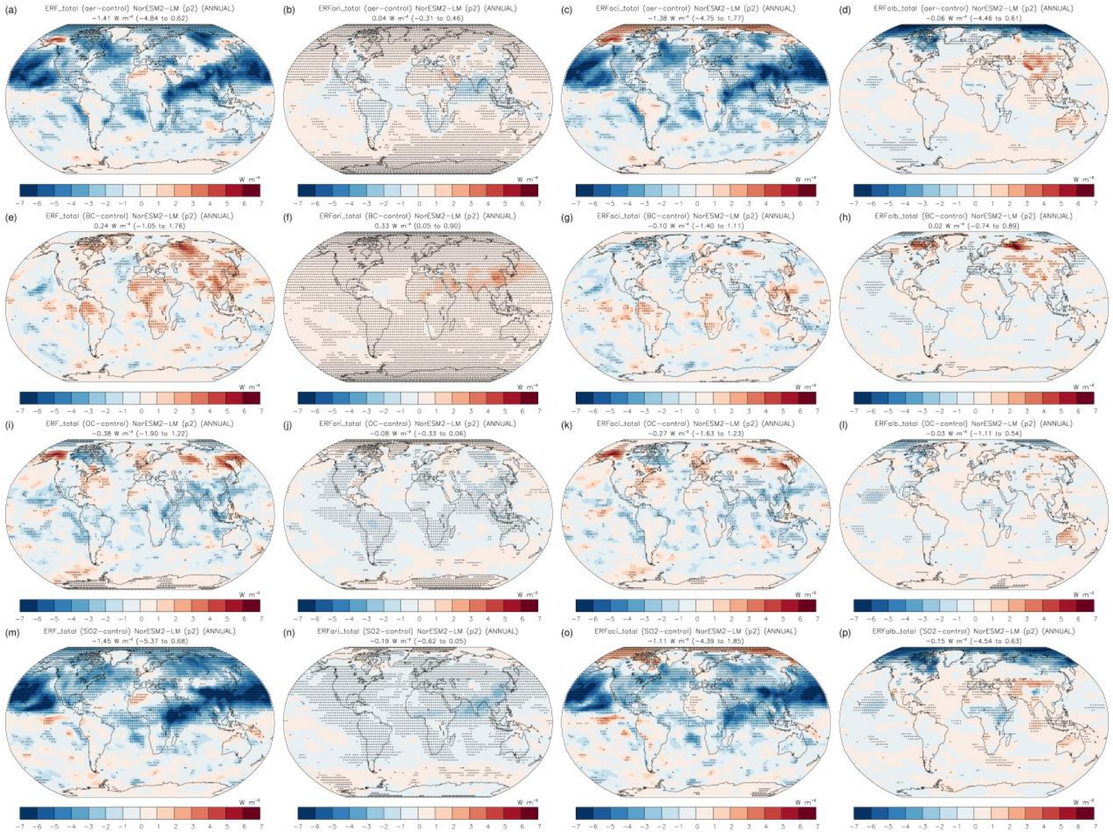

Figure A26. Spatial TOA distribution of the annual mean total (SW + LW) ERF (first column), ERFari (second column), ERFaci (third column), and ERFalb (fourth column) in the piClim-aer (first row), piClim-BC (second row), piClim-OC (third row), and piClim-SO_2 (fourth column) experiment for the NorESM2-LM (p2) model. The black crosses indicate the statistically important values in the 95% confidence level. The global field means (5th to 95th percentiles in the parenthesis) are shown in W m^{-2}.

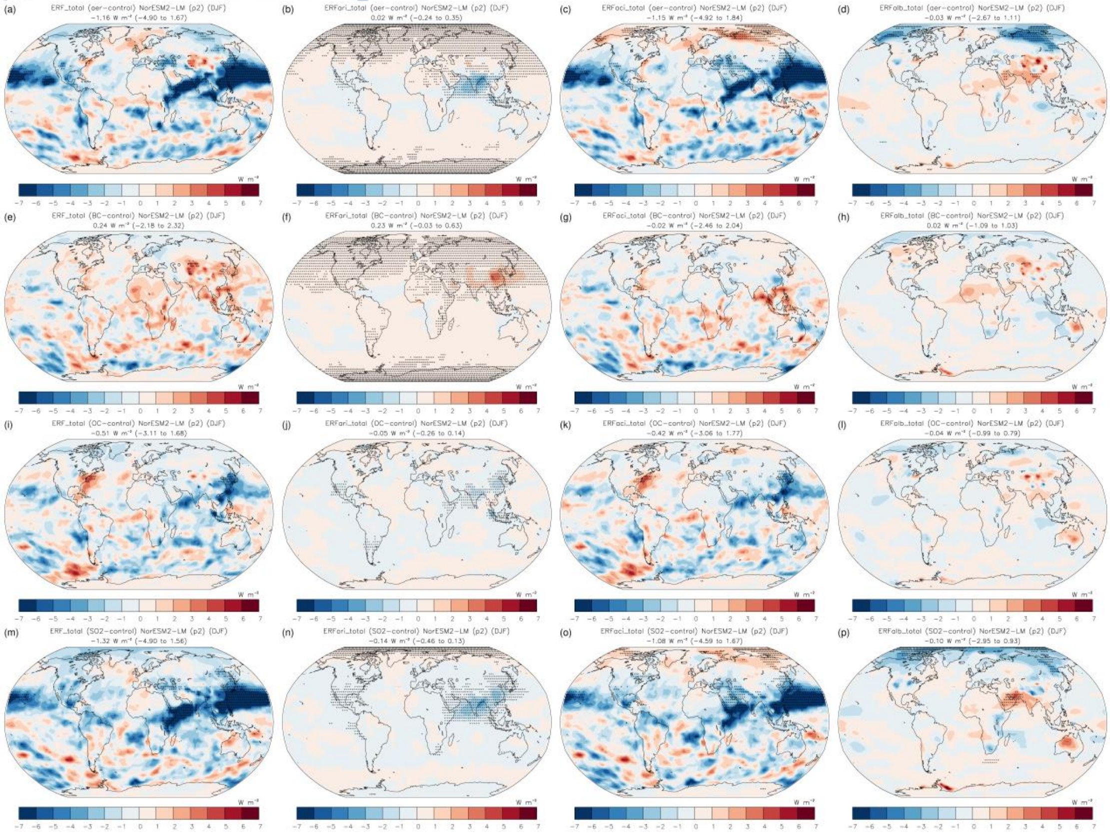

Figure A27. As in Fig. A26, but for DJF.

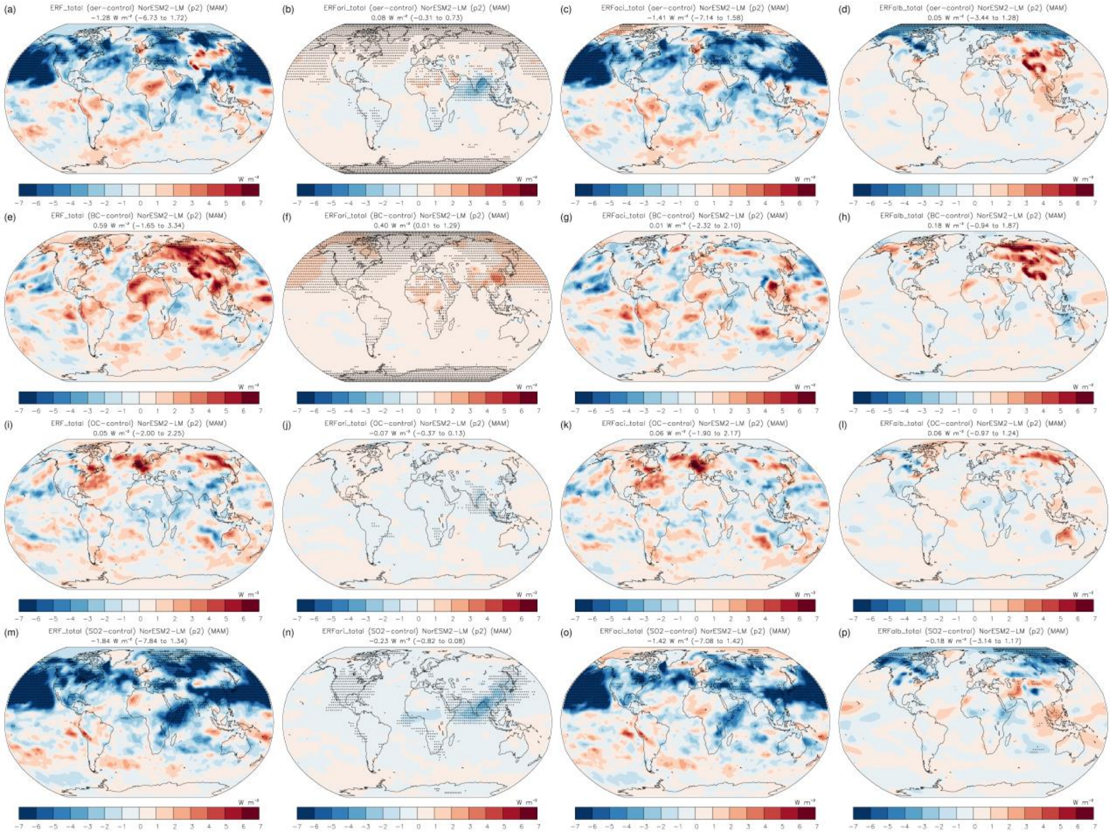

Figure A28. As in Fig. A26, but for MAM.

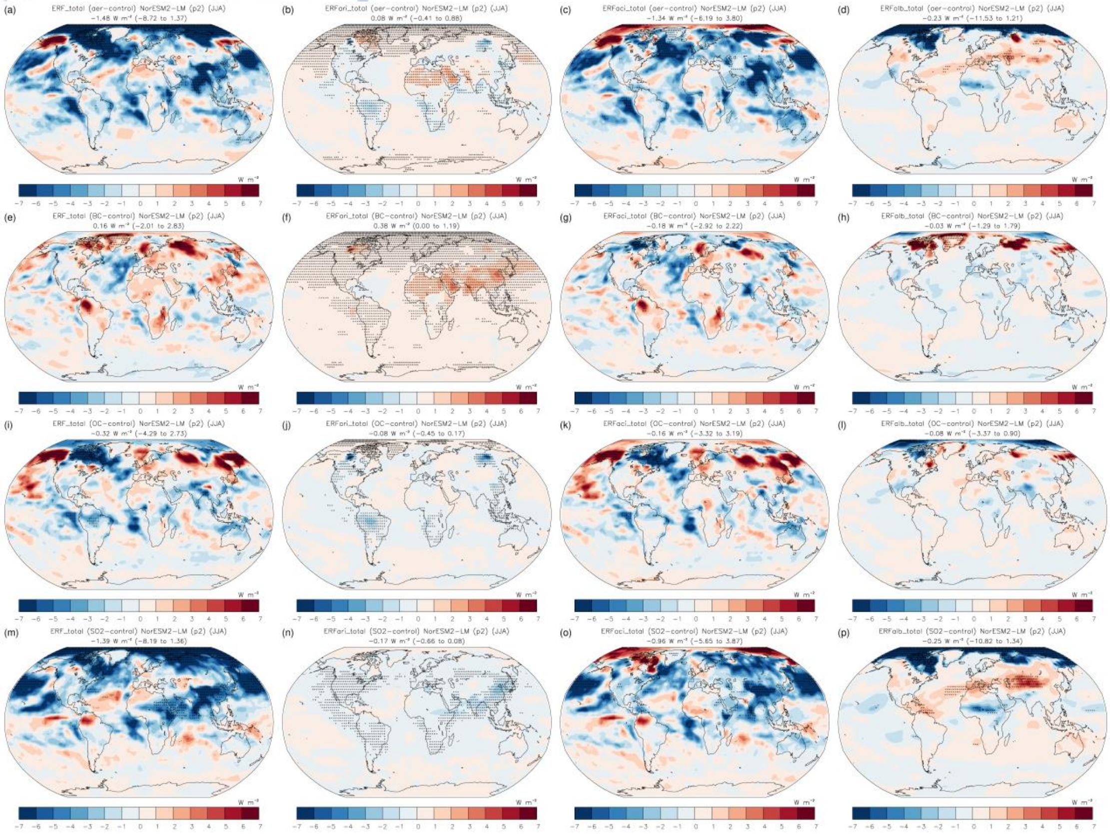

Figure A29. As in Fig. A26, but for JJA.

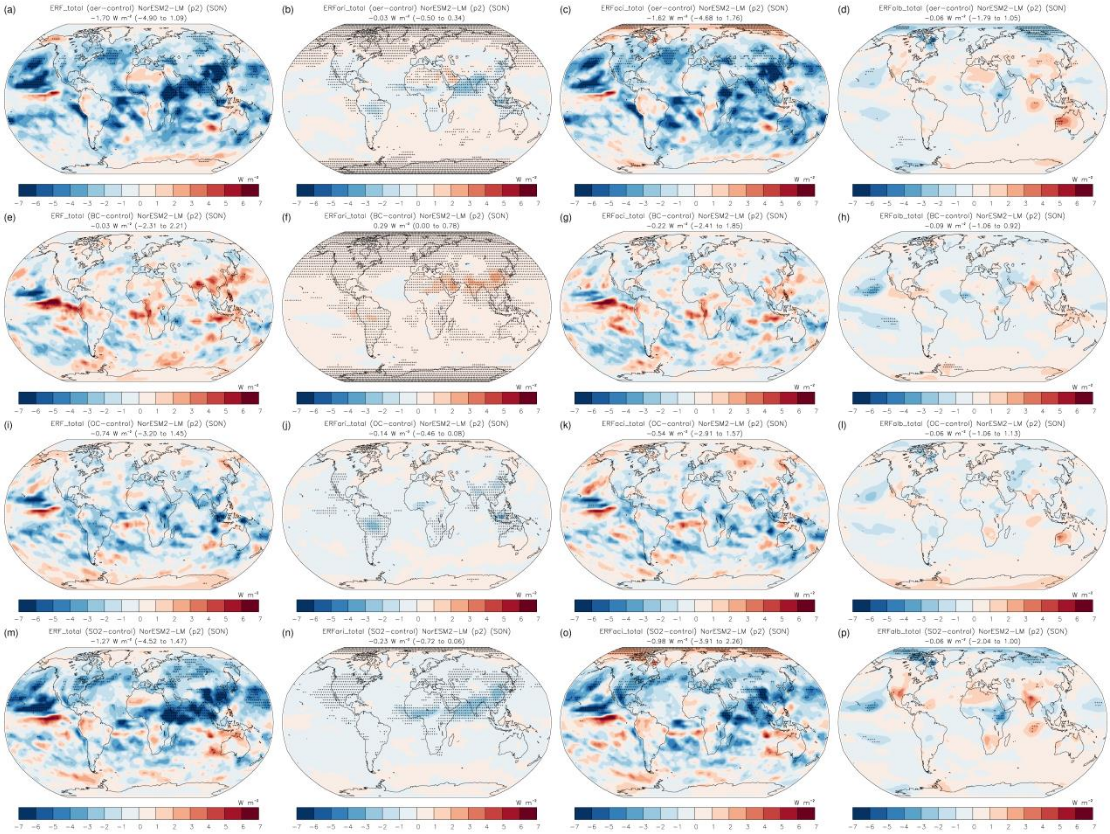

Figure A30. As in Fig. A26, but for SON.

APPENDIX B: Global field mean values for each model

Table B1. Global mean TOA values of the overall ERF (denoted as ERF), ERFari (ARI), ERFaci (ACI), ERFalb (ALB), and globally averaged surface air temperature change (TAS) on an annual and seasonal basis for the piClim-aer, piClim-BC, piClim-OC, and piClim-SO2 experiments for the CNRM-ESM2-1 model.

CNRM-ESM2-1		**ERF**			**ARI**			**ACI**			**ALB**			**TAS**
		total	sw	lw	total	sw	lw	total	sw	lw	total	sw	lw	
ANNUAL	aer	-0.74	-0.82	0.08	-0.21	-0.22	0.00	-0.61	-0.59	-0.02	0.08	-0.01	0.09	-0.05
	BC	0.11	0.15	-0.03	0.13	0.13	0.00	-0.03	-0.01	-0.02	0.01	0.02	-0.01	0.00
	OC	-0.17	-0.23	0.06	-0.07	-0.07	0.00	-0.14	-0.18	0.04	0.04	0.02	0.03	-0.02
	SO2	-0.74	-0.84	0.10	-0.29	-0.29	0.00	-0.53	-0.55	0.02	0.08	0.01	0.07	-0.03
DJF	aer	-0.56	-0.78	0.21	-0.19	-0.20	0.00	-0.53	-0.57	0.04	0.16	-0.01	0.17	-0.05
	BC	0.18	0.02	0.16	0.12	0.12	0.00	-0.08	-0.13	0.05	0.14	0.03	0.11	-0.01
	OC	-0.09	-0.24	0.16	-0.05	-0.05	0.00	-0.18	-0.28	0.10	0.14	0.09	0.05	0.00
	SO2	-0.60	-0.73	0.13	-0.27	-0.28	0.00	-0.47	-0.49	0.02	0.14	0.03	0.11	-0.03
MAM	aer	-0.82	-0.82	0.00	-0.19	-0.19	0.00	-0.68	-0.63	-0.05	0.04	0.00	0.04	-0.04
	BC	0.16	0.26	-0.11	0.15	0.15	0.00	0.02	0.06	-0.04	-0.01	0.05	-0.06	0.01
	OC	-0.17	-0.22	0.04	-0.05	-0.05	0.00	-0.17	-0.20	0.02	0.05	0.03	0.02	-0.02
	SO2	-0.86	-0.83	-0.02	-0.29	-0.29	0.00	-0.59	-0.60	0.01	0.02	0.05	-0.03	-0.01
JJA	aer	-0.76	-0.84	0.08	-0.23	-0.23	0.01	-0.61	-0.58	-0.04	0.08	-0.03	0.11	-0.06
	BC	0.05	0.20	-0.15	0.16	0.15	0.00	-0.03	0.05	-0.08	-0.07	0.00	-0.07	0.00
	OC	-0.17	-0.19	0.02	-0.08	-0.09	0.00	-0.06	-0.05	-0.01	-0.02	-0.05	0.03	-0.03
	SO2	-0.78	-0.92	0.14	-0.31	-0.31	0.00	-0.56	-0.57	0.01	0.09	-0.04	0.13	-0.05
SON	aer	-0.82	-0.85	0.03	-0.25	-0.25	0.01	-0.61	-0.59	-0.02	0.04	-0.01	0.05	-0.04
	BC	0.06	0.10	-0.04	0.11	0.11	0.00	-0.02	0.00	-0.01	-0.03	0.00	-0.03	0.00
	OC	-0.24	-0.27	0.03	-0.09	-0.09	0.00	-0.15	-0.18	0.02	0.00	0.00	0.00	-0.02
	SO2	-0.73	-0.88	0.15	-0.30	-0.30	0.00	-0.50	-0.56	0.06	0.06	-0.02	0.09	-0.04

Table B2. As in Table B1, but for GFDL-ESM4.

GFDL-ESM4		**ERF**			**ARI**			**ACI**			**ALB**			**TAS**
		total	sw	lw	total	sw	lw	total	sw	lw	total	sw	lw	
ANNUAL	aer	-0.70	-0.59	-0.11	0.26	0.24	0.02	-0.92	-0.77	-0.15	-0.03	-0.06	0.02	-0.02
	BC	0.35	0.62	-0.27	0.52	0.51	0.01	-0.09	0.08	-0.18	-0.09	0.03	-0.11	0.04
	OC	-0.21	-0.21	0.00	-0.10	-0.09	0.00	-0.16	-0.13	-0.04	0.05	0.01	0.04	-0.01
	SO2	-0.67	-0.76	0.08	-0.21	-0.22	0.01	-0.51	-0.51	0.00	0.05	-0.02	0.08	-0.04
DJF	aer	-0.47	-0.33	-0.14	0.15	0.13	0.01	-0.55	-0.42	-0.12	-0.07	-0.04	-0.03	-0.02
	BC	0.31	0.42	-0.11	0.37	0.36	0.01	-0.03	0.05	-0.09	-0.02	0.01	-0.03	0.01
	OC	-0.14	-0.12	-0.01	-0.07	-0.07	0.00	-0.09	-0.07	-0.02	0.02	0.02	0.00	0.00
	SO2	-0.50	-0.44	-0.05	-0.13	-0.14	0.01	-0.33	-0.29	-0.03	-0.04	-0.01	-0.03	-0.02
MAM	aer	-0.73	-0.76	0.03	0.27	0.25	0.02	-1.00	-0.91	-0.09	0.00	-0.10	0.10	-0.03
	BC	0.53	0.67	-0.14	0.54	0.54	0.01	0.00	0.12	-0.12	-0.01	0.01	-0.02	0.03
	OC	-0.13	-0.14	0.02	-0.06	-0.06	0.00	-0.10	-0.07	-0.03	0.04	-0.01	0.05	-0.01
	SO2	-0.74	-0.90	0.15	-0.22	-0.23	0.01	-0.55	-0.57	0.02	0.03	-0.09	0.13	-0.05
JJA	aer	-0.90	-0.74	-0.16	0.40	0.38	0.02	-1.29	-1.08	-0.22	0.00	-0.04	0.03	-0.03
	BC	0.26	0.74	-0.47	0.68	0.66	0.02	-0.20	0.06	-0.26	-0.22	0.02	-0.24	0.06
	OC	-0.23	-0.26	0.03	-0.12	-0.11	-0.01	-0.19	-0.16	-0.03	0.08	0.01	0.07	-0.02
	SO2	-0.77	-1.03	0.26	-0.27	-0.28	0.00	-0.67	-0.74	0.07	0.17	-0.01	0.19	-0.06
SON	aer	-0.70	-0.53	-0.17	0.21	0.19	0.02	-0.85	-0.67	-0.19	-0.06	-0.05	-0.01	-0.01
	BC	0.28	0.65	-0.37	0.50	0.49	0.01	-0.13	0.11	-0.23	-0.10	0.06	-0.15	0.05
	OC	-0.36	-0.33	-0.03	-0.13	-0.13	0.00	-0.27	-0.20	-0.07	0.04	0.00	0.03	-0.02
	SO2	-0.68	-0.65	-0.03	-0.22	-0.22	0.00	-0.50	-0.45	-0.05	0.04	0.02	0.02	-0.03

Table B3. As in Table B1, but for MPI-ESM-1-2-HAM.

MPI-ESM-1-2-HAM		ERF			ARI			ACI			ALB			TAS
		total	sw	lw	total	sw	lw	total	sw	lw	total	sw	lw	
ANNUAL	aer	-1.26	-1.53	0.27	0.16	0.19	-0.03	-1.57	-1.67	0.10	0.14	-0.05	0.19	-0.08
	BC	-0.15	0.04	-0.19	0.72	0.71	0.01	-0.87	-0.71	-0.16	0.00	0.04	-0.04	0.01
	OC	-0.78	-0.85	0.06	-0.02	-0.04	0.02	-0.79	-0.80	0.02	0.02	0.00	0.02	-0.01
	SO2	-1.06	-1.35	0.28	-0.24	-0.20	-0.04	-0.96	-1.10	0.14	0.14	-0.05	0.19	-0.08
DJF	aer	-1.03	-1.18	0.15	0.12	0.13	-0.01	-1.23	-1.28	0.05	0.08	-0.03	0.11	-0.05
	BC	-0.19	-0.04	-0.15	0.53	0.51	0.01	-0.64	-0.59	-0.05	-0.08	0.03	-0.11	0.04
	OC	-0.70	-0.79	0.09	0.00	-0.02	0.02	-0.72	-0.77	0.05	0.03	0.00	0.02	-0.01
	SO2	-1.00	-1.19	0.19	-0.25	-0.24	-0.01	-0.84	-0.93	0.10	0.09	-0.02	0.11	-0.04
MAM	aer	-1.62	-1.86	0.24	0.32	0.40	-0.08	-2.01	-2.14	0.13	0.06	-0.11	0.18	-0.10
	BC	-0.08	0.13	-0.21	0.94	0.95	-0.02	-1.13	-0.89	-0.24	0.11	0.07	0.05	-0.01
	OC	-1.05	-1.10	0.05	-0.02	-0.06	0.04	-1.04	-1.04	0.00	0.01	0.00	0.01	-0.01
	SO2	-1.26	-1.51	0.24	-0.14	-0.04	-0.10	-1.20	-1.38	0.18	0.07	-0.10	0.17	-0.08
JJA	aer	-1.08	-1.44	0.37	0.15	0.17	-0.03	-1.46	-1.57	0.11	0.24	-0.04	0.28	-0.08
	BC	-0.07	0.14	-0.21	0.78	0.77	0.01	-0.84	-0.68	-0.16	-0.01	0.05	-0.07	0.03
	OC	-0.58	-0.66	0.09	-0.01	-0.03	0.01	-0.59	-0.62	0.03	0.02	-0.02	0.04	-0.01
	SO2	-0.99	-1.36	0.37	-0.24	-0.20	-0.04	-0.97	-1.09	0.13	0.21	-0.07	0.28	-0.09
SON	aer	-1.32	-1.63	0.31	0.07	0.07	0.00	-1.58	-1.70	0.12	0.19	0.00	0.19	-0.09
	BC	-0.26	-0.05	-0.21	0.62	0.61	0.01	-0.86	-0.68	-0.18	-0.02	0.02	-0.04	-0.01
	OC	-0.82	-0.85	0.03	-0.03	-0.05	0.01	-0.80	-0.79	-0.01	0.01	-0.01	0.02	-0.02
	SO2	-1.00	-1.33	0.33	-0.32	-0.32	-0.01	-0.84	-0.99	0.15	0.17	-0.03	0.19	-0.10

Table B4. As in Table B1, but for MRI-ESM2-0.

MRI-ESM2-0		ERF			ARI			ACI			ALB			TAS
		total	sw	lw	total	sw	lw	total	sw	lw	total	sw	lw	
ANNUAL	aer	-1.22	-2.75	1.52	-0.32	-0.32	0.00	-0.99	-2.48	1.48	0.08	0.05	0.04	-0.02
	BC	0.25	-1.22	1.46	0.26	0.26	0.00	-0.09	-1.62	1.53	0.08	0.15	-0.07	0.04
	OC	-0.32	-0.50	0.18	-0.07	-0.07	0.00	-0.21	-0.42	0.21	-0.04	-0.01	-0.03	-0.01
	SO2	-1.38	-1.91	0.53	-0.48	-0.49	0.00	-0.94	-1.37	0.42	0.05	-0.05	0.10	-0.06
DJF	aer	-0.78	-2.06	1.28	-0.23	-0.24	0.01	-0.63	-1.86	1.23	0.08	0.04	0.04	-0.03
	BC	0.26	-0.98	1.24	0.19	0.19	0.00	0.04	-1.25	1.29	0.03	0.08	-0.05	0.04
	OC	-0.35	-0.39	0.04	-0.06	-0.06	0.00	-0.21	-0.33	0.12	-0.08	0.00	-0.08	0.01
	SO2	-1.21	-1.48	0.26	-0.37	-0.38	0.00	-0.83	-1.09	0.26	-0.01	-0.01	0.00	-0.02
MAM	aer	-1.33	-2.70	1.37	-0.31	-0.32	0.00	-1.17	-2.47	1.30	0.15	0.09	0.06	-0.05
	BC	0.39	-1.01	1.40	0.26	0.26	0.00	-0.06	-1.52	1.46	0.20	0.26	-0.06	0.04
	OC	-0.32	-0.43	0.11	-0.07	-0.07	0.00	-0.19	-0.35	0.16	-0.07	-0.02	-0.05	-0.02
	SO2	-1.60	-1.98	0.39	-0.48	-0.48	0.00	-1.12	-1.42	0.29	0.01	-0.08	0.09	-0.10
JJA	aer	-1.70	-3.49	1.79	-0.38	-0.38	0.00	-1.40	-3.14	1.74	0.08	0.04	0.04	-0.01
	BC	0.01	-1.56	1.56	0.30	0.30	0.00	-0.37	-2.08	1.70	0.08	0.22	-0.14	0.06
	OC	-0.40	-0.65	0.25	-0.08	-0.07	0.00	-0.29	-0.55	0.27	-0.03	-0.02	-0.01	-0.01
	SO2	-1.46	-2.35	0.89	-0.57	-0.57	0.00	-0.99	-1.69	0.70	0.11	-0.08	0.19	-0.05
SON	aer	-1.08	-2.75	1.66	-0.34	-0.34	0.00	-0.77	-2.43	1.65	0.02	0.02	0.01	0.00
	BC	0.32	-1.33	1.65	0.28	0.28	0.00	0.03	-1.65	1.68	0.01	0.04	-0.02	0.04
	OC	-0.22	-0.54	0.32	-0.07	-0.07	0.00	-0.16	-0.45	0.28	0.02	-0.01	0.04	0.00
	SO2	-1.25	-1.82	0.57	-0.50	-0.51	0.00	-0.83	-1.27	0.44	0.08	-0.04	0.12	-0.05

Table B5. As in Table B1, but for NorESM2-LM (p1).

NorESM2-LM (p1)		**ERF**			**ARI**			**ACI**			**ALB**			**TAS**
		total	sw	lw	total	sw	lw	total	sw	lw	total	sw	lw	
ANNUAL	aer	-1.21	-1.41	0.21	0.03	-0.01	0.04	-1.21	-1.37	0.16	-0.03	-0.04	0.01	0.01
	BC	0.30	0.48	-0.18	0.35	0.35	0.00	-0.12	0.03	-0.16	0.07	0.10	-0.03	0.01
	OC	-0.22	-0.27	0.05	-0.07	-0.07	0.00	-0.16	-0.17	0.01	0.02	-0.02	0.04	-0.02
	SO2	-1.28	-1.69	0.41	-0.19	-0.22	0.03	-1.01	-1.31	0.31	-0.09	-0.16	0.07	-0.01
DJF	aer	-1.02	-1.02	-0.01	-0.01	-0.03	0.02	-0.86	-0.99	0.13	-0.16	0.00	-0.16	0.07
	BC	0.40	0.46	-0.07	0.26	0.26	0.00	0.12	0.21	-0.09	0.02	-0.01	0.02	-0.01
	OC	-0.33	-0.23	-0.10	-0.07	-0.07	0.00	-0.20	-0.13	-0.07	-0.07	-0.03	-0.04	0.00
	SO2	-1.22	-1.32	0.11	-0.16	-0.18	0.02	-0.83	-1.06	0.22	-0.22	-0.09	-0.13	0.04
MAM	aer	-1.60	-1.74	0.15	0.02	-0.02	0.04	-1.56	-1.71	0.16	-0.06	-0.01	-0.05	0.03
	BC	0.37	0.58	-0.21	0.37	0.36	0.00	-0.10	0.03	-0.13	0.11	0.19	-0.08	0.04
	OC	-0.13	-0.12	0.00	-0.06	-0.06	0.00	-0.04	-0.01	-0.03	-0.03	-0.06	0.03	-0.01
	SO2	-1.77	-2.18	0.41	-0.23	-0.26	0.03	-1.38	-1.68	0.30	-0.16	-0.24	0.08	-0.01
JJA	aer	-1.22	-1.48	0.26	0.08	0.03	0.05	-1.31	-1.38	0.07	0.00	-0.13	0.13	-0.04
	BC	0.07	0.49	-0.42	0.43	0.42	0.00	-0.44	-0.13	-0.31	0.09	0.20	-0.12	0.03
	OC	-0.31	-0.31	0.01	-0.08	-0.08	0.00	-0.26	-0.24	-0.02	0.04	0.01	0.03	-0.01
	SO2	-1.30	-1.82	0.52	-0.18	-0.22	0.04	-1.03	-1.30	0.27	-0.09	-0.30	0.21	-0.07
SON	aer	-0.98	-1.42	0.43	0.03	-0.01	0.04	-1.10	-1.38	0.28	0.10	-0.02	0.12	-0.02
	BC	0.36	0.39	-0.03	0.33	0.33	0.00	-0.06	0.04	-0.10	0.08	0.01	0.07	-0.01
	OC	-0.10	-0.40	0.30	-0.09	-0.09	0.00	-0.15	-0.31	0.15	0.14	0.00	0.15	-0.04
	SO2	-0.84	-1.45	0.62	-0.18	-0.21	0.03	-0.78	-1.22	0.44	0.12	-0.02	0.14	-0.02

Table B6. As in Table B1, but for NorESM2-LM (p2).

NorESM2-LM (p2)		**ERF**			**ARI**			**ACI**			**ALB**			**TAS**
		total	sw	lw	total	sw	lw	total	sw	lw	total	sw	lw	
ANNUAL	aer	-1.41	-1.63	0.22	0.04	0.00	0.04	-1.38	-1.55	0.17	-0.06	-0.08	0.02	0.01
	BC	0.24	0.46	-0.22	0.33	0.32	0.00	-0.10	0.02	-0.13	0.02	0.12	-0.10	0.03
	OC	-0.38	-0.35	-0.02	-0.08	-0.08	0.00	-0.27	-0.27	0.00	-0.03	0.00	-0.03	0.00
	SO2	-1.45	-1.80	0.35	-0.19	-0.22	0.03	-1.11	-1.40	0.29	-0.15	-0.18	0.03	0.00
DJF	aer	-1.16	-1.33	0.18	0.02	0.00	0.02	-1.15	-1.38	0.23	-0.03	0.04	-0.07	0.08
	BC	0.24	0.35	-0.11	0.23	0.23	0.00	-0.02	0.06	-0.07	0.02	0.06	-0.04	0.02
	OC	-0.51	-0.41	-0.10	-0.05	-0.05	0.00	-0.42	-0.37	-0.05	-0.04	0.01	-0.05	0.01
	SO2	-1.32	-1.44	0.12	-0.14	-0.16	0.02	-1.08	-1.30	0.22	-0.10	0.01	-0.11	0.09
MAM	aer	-1.28	-1.72	0.44	0.08	0.05	0.03	-1.41	-1.74	0.33	0.05	-0.02	0.08	0.01
	BC	0.59	0.74	-0.15	0.40	0.40	0.00	0.01	0.08	-0.08	0.18	0.25	-0.07	0.04
	OC	0.05	0.00	0.05	-0.07	-0.07	0.00	0.06	0.04	0.02	0.06	0.03	0.03	-0.01
	SO2	-1.84	-2.27	0.43	-0.23	-0.26	0.03	-1.42	-1.75	0.33	-0.18	-0.25	0.07	-0.03
JJA	aer	-1.48	-1.61	0.13	0.08	0.03	0.05	-1.34	-1.34	0.00	-0.23	-0.31	0.08	-0.05
	BC	0.16	0.55	-0.39	0.38	0.37	0.00	-0.18	0.03	-0.21	-0.03	0.15	-0.18	0.05
	OC	-0.32	-0.33	0.01	-0.08	-0.08	0.00	-0.16	-0.21	0.05	-0.08	-0.03	-0.04	0.01
	SO2	-1.39	-1.82	0.43	-0.17	-0.21	0.04	-0.96	-1.19	0.22	-0.25	-0.42	0.17	-0.07
SON	aer	-1.70	-1.86	0.15	-0.03	-0.07	0.04	-1.62	-1.75	0.13	-0.06	-0.03	-0.02	0.00
	BC	-0.03	0.22	-0.24	0.29	0.29	0.00	-0.22	-0.08	-0.14	-0.09	0.01	-0.10	0.02
	OC	-0.74	-0.68	-0.06	-0.14	-0.14	0.00	-0.54	-0.51	-0.02	-0.06	-0.02	-0.04	-0.01
	SO2	-1.27	-1.69	0.42	-0.23	-0.26	0.04	-0.98	-1.38	0.40	-0.06	-0.04	-0.02	0.01

APPENDIX C: Barplots of field means for each model

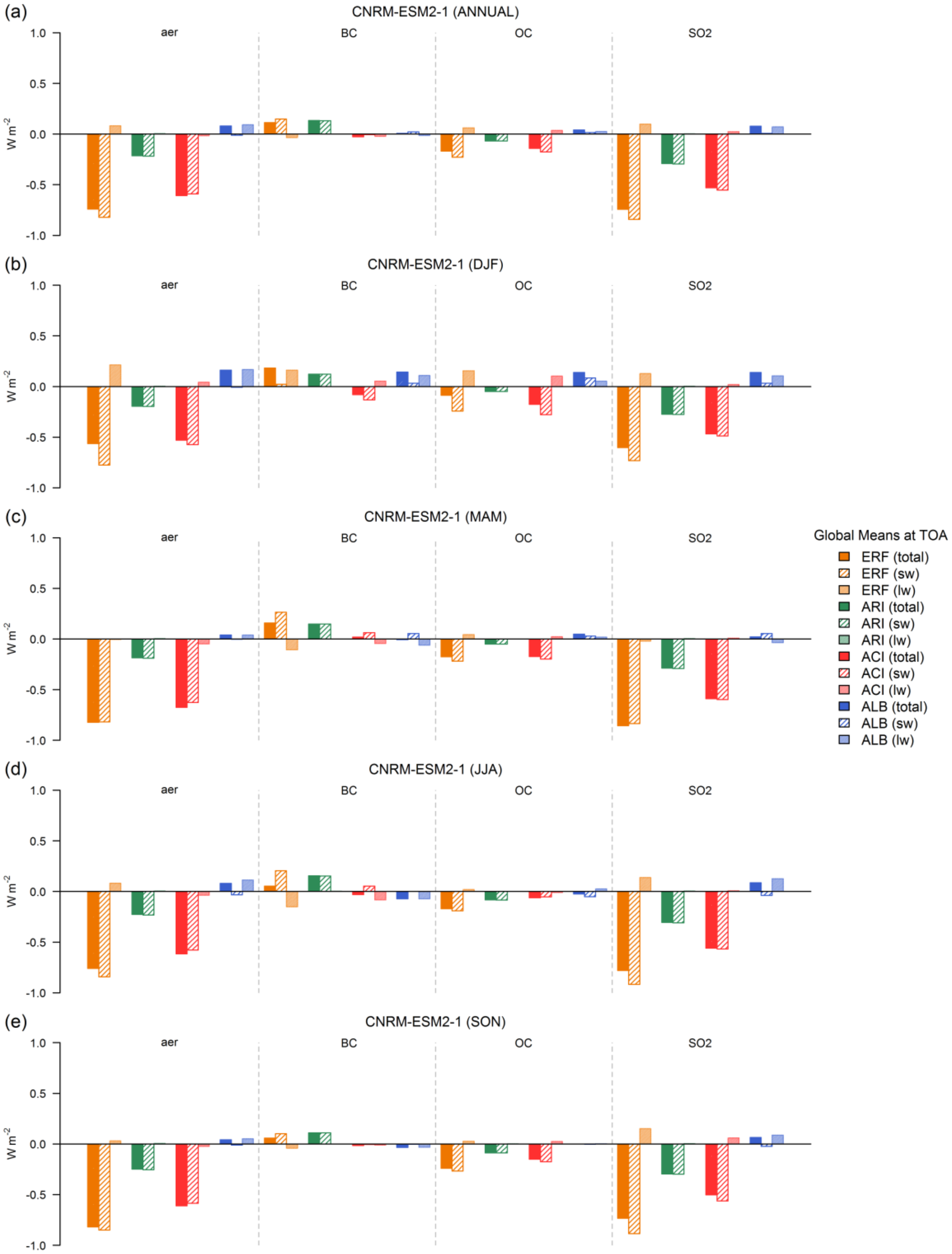

Figure C1. Barplots of the globally averaged (a) annual, (b) DJF, (c) MAM, (d) JJA, and (e) SON SW, LW, and total (SW + LW) TOA ERF components (overall ERF, ERFari, ERFaci, ERFalb) for the piClim-aer, piClim-BC, piClim-OC, and piClim-SO_2 simulations for the CNRM-ESM2-1 model.

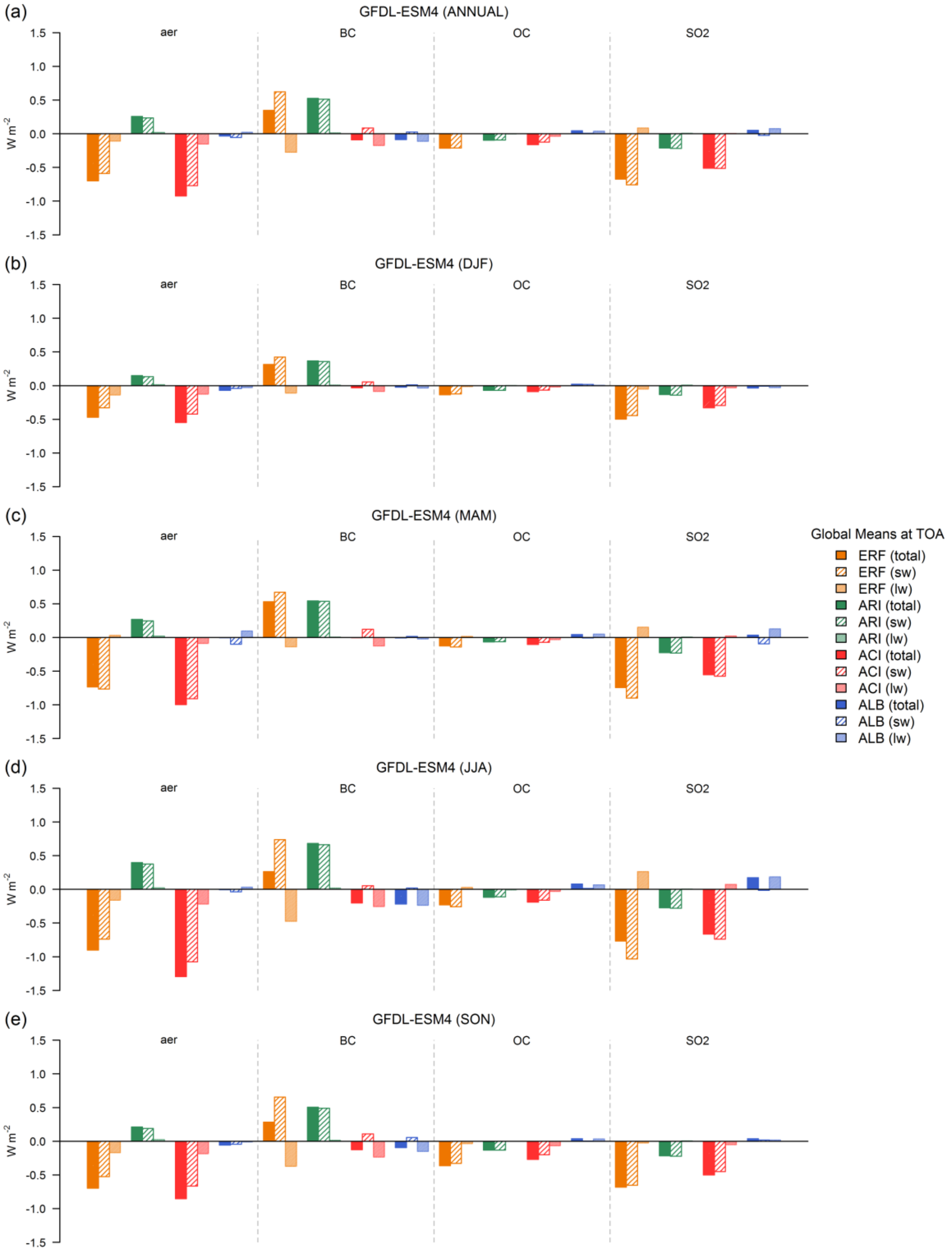

Figure C2. As in Fig. C1, but for GFDL-ESM4.

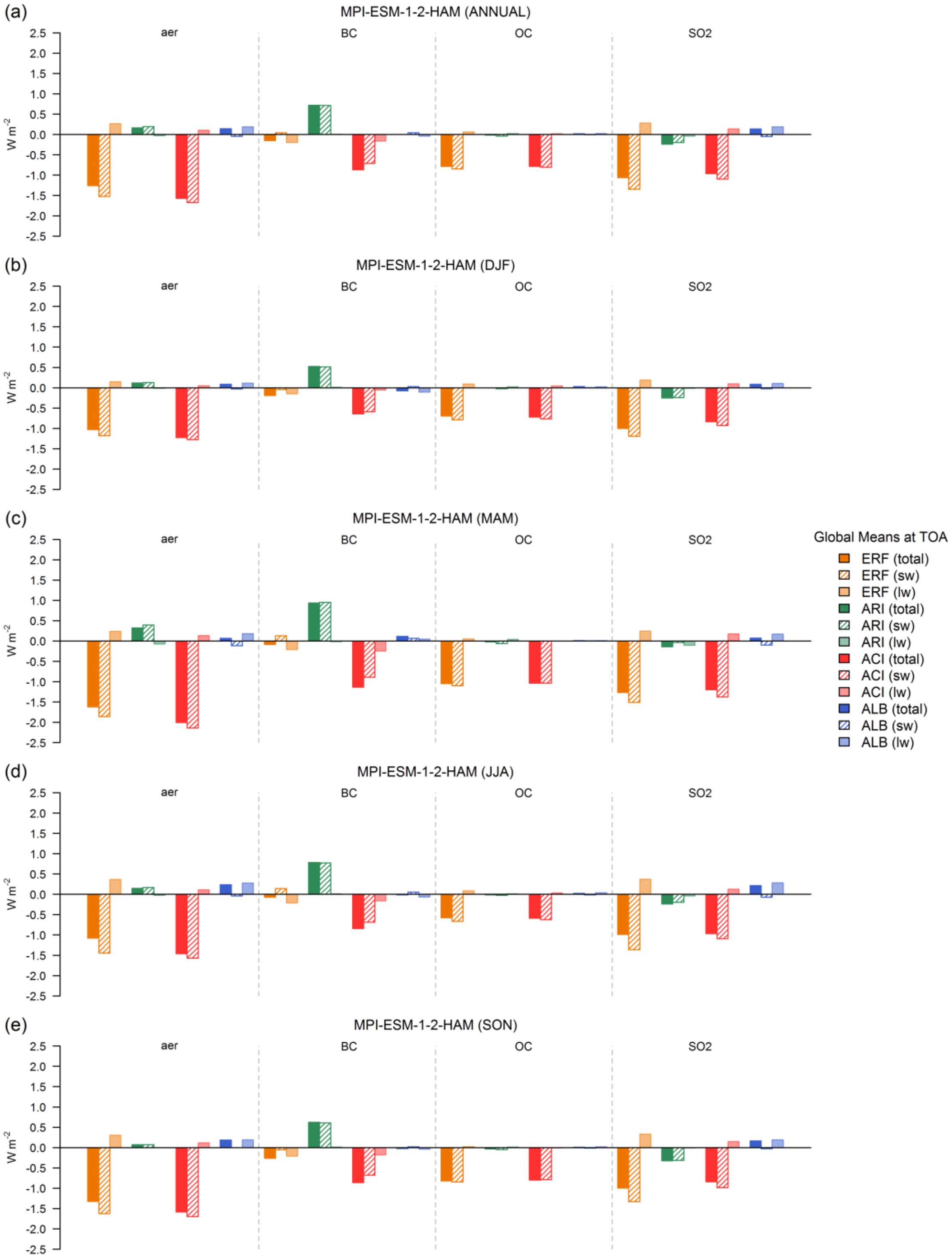

Figure C3. As in Fig. C1, but for MPI-ESM-1-2-HAM.

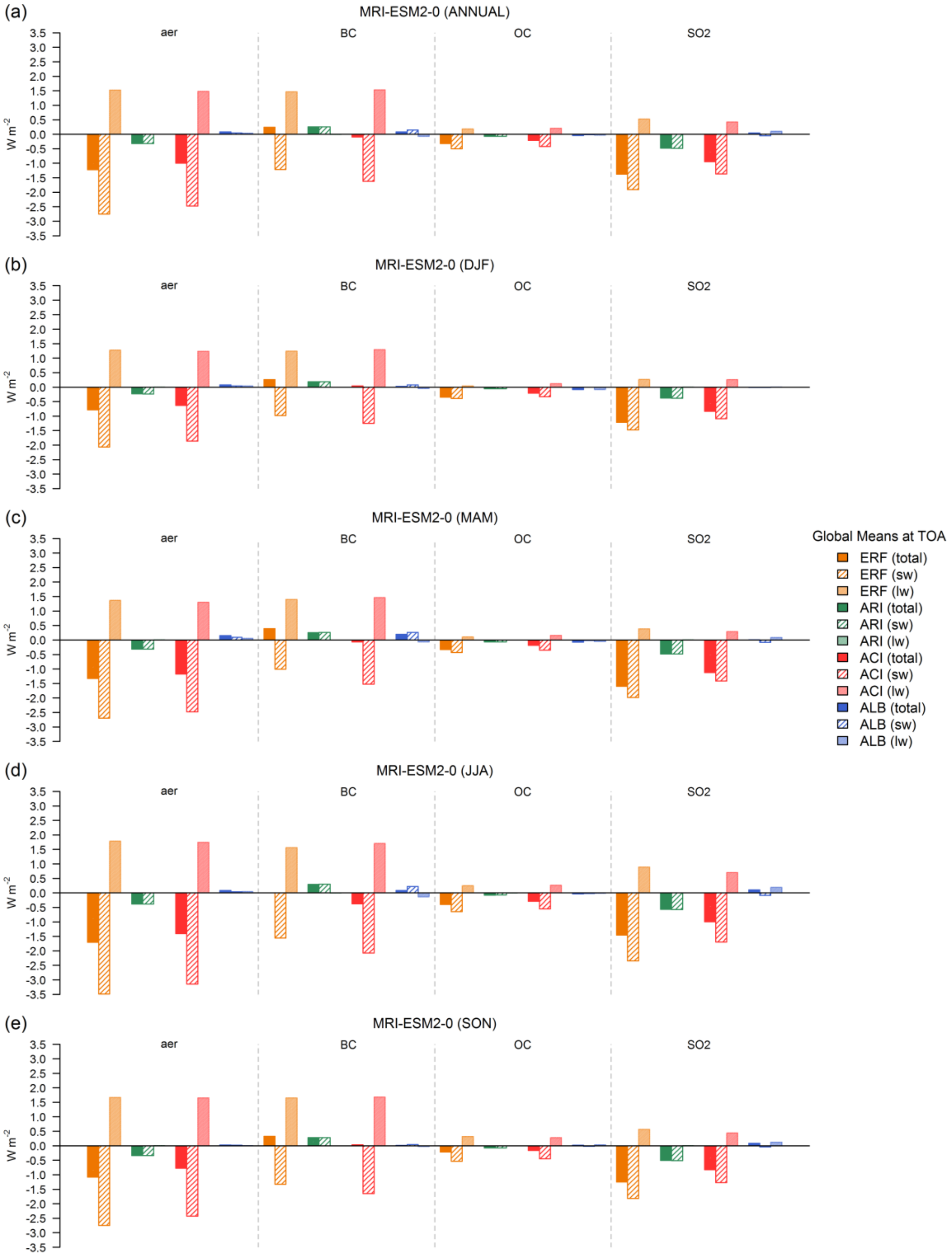

Figure C4. As in Fig. C1, but for MRI-ESM2-0.

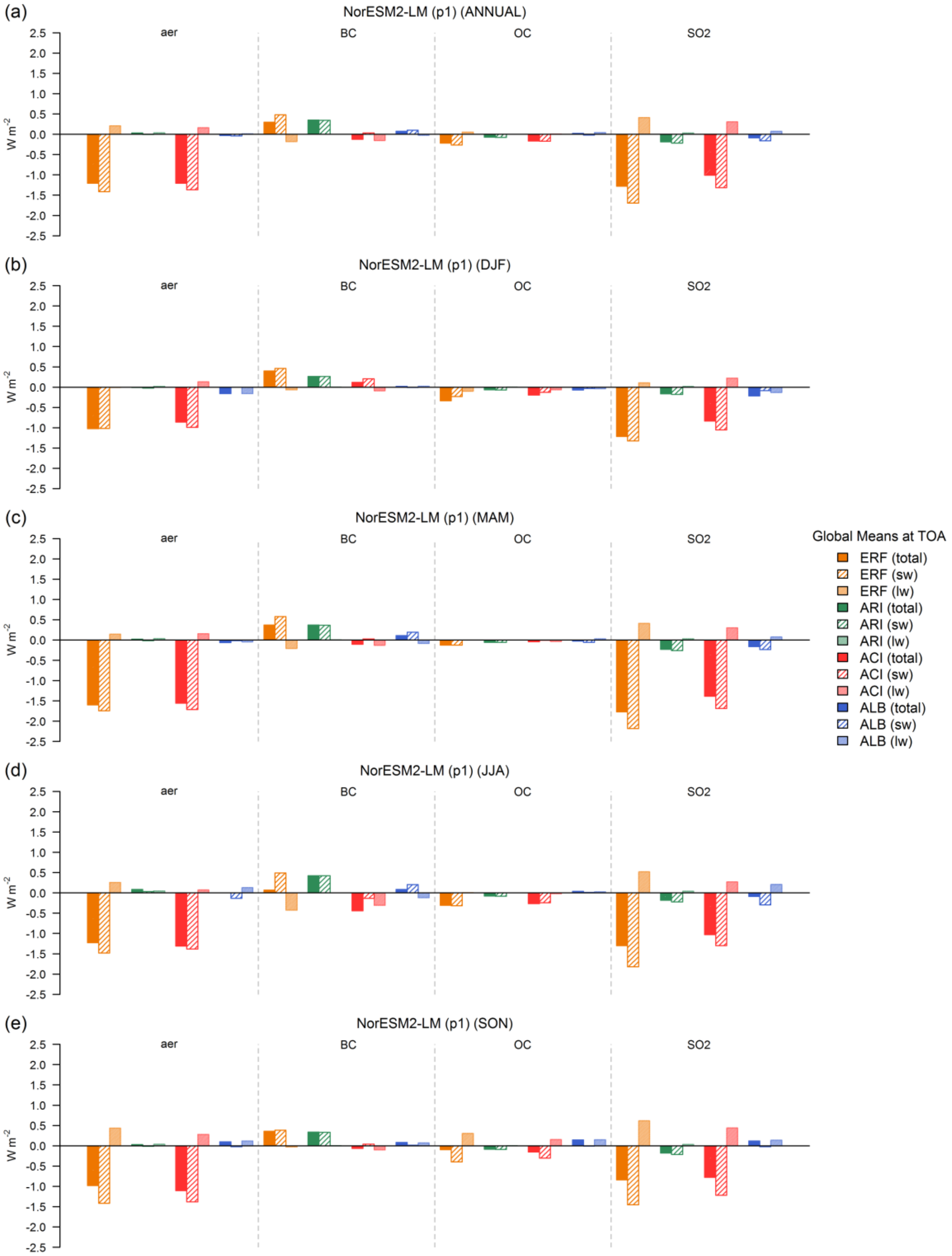

Figure C5. As in Fig. C1, but for NorESM2-LM (p1).

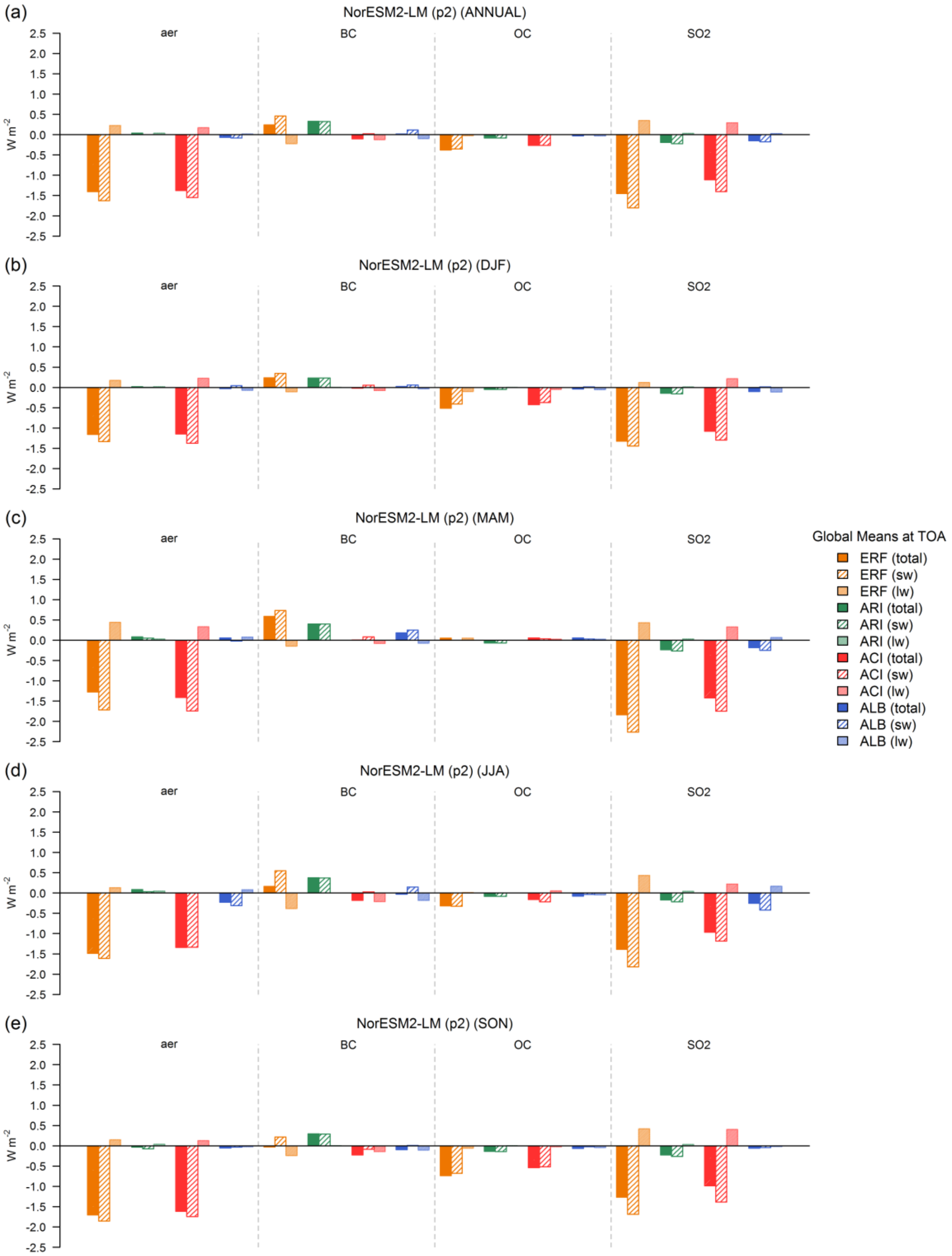

Figure C6. As in Fig. C1, but for NorESM2-LM (p2).

APPENDIX D: Boxplots for each model

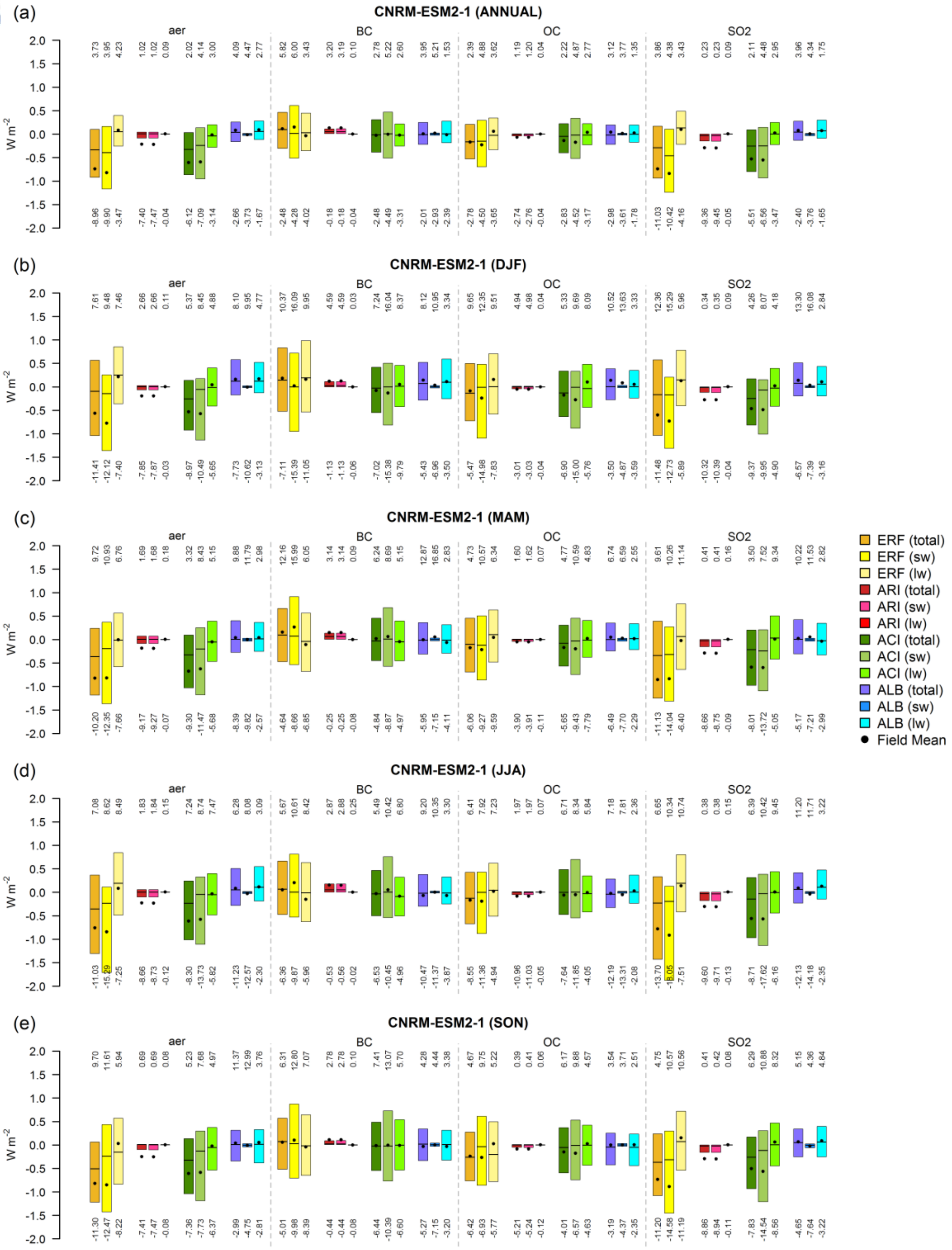

Figure D1. Boxplots of the (a) annual, (b) DJF, (c) MAM, (d) JJA, and (e) SON SW, LW, and total (SW + LW) TOA ERF components (overall ERF, ERFari, ERFaci, ERFalb) for the piClim-aer, piClim-BC, piClim-OC, and piClim-SO2 simulations for the CNRM-ESM2-1 model. Each box's lower (upper) limit is the 25th (75th) percentile, the black horizontal lines denote the median (50th percentile), the black circles are the global field means at TOA, and the numbers on the lower (upper) bounds of each subplot denote the minimum (maximum) field values.

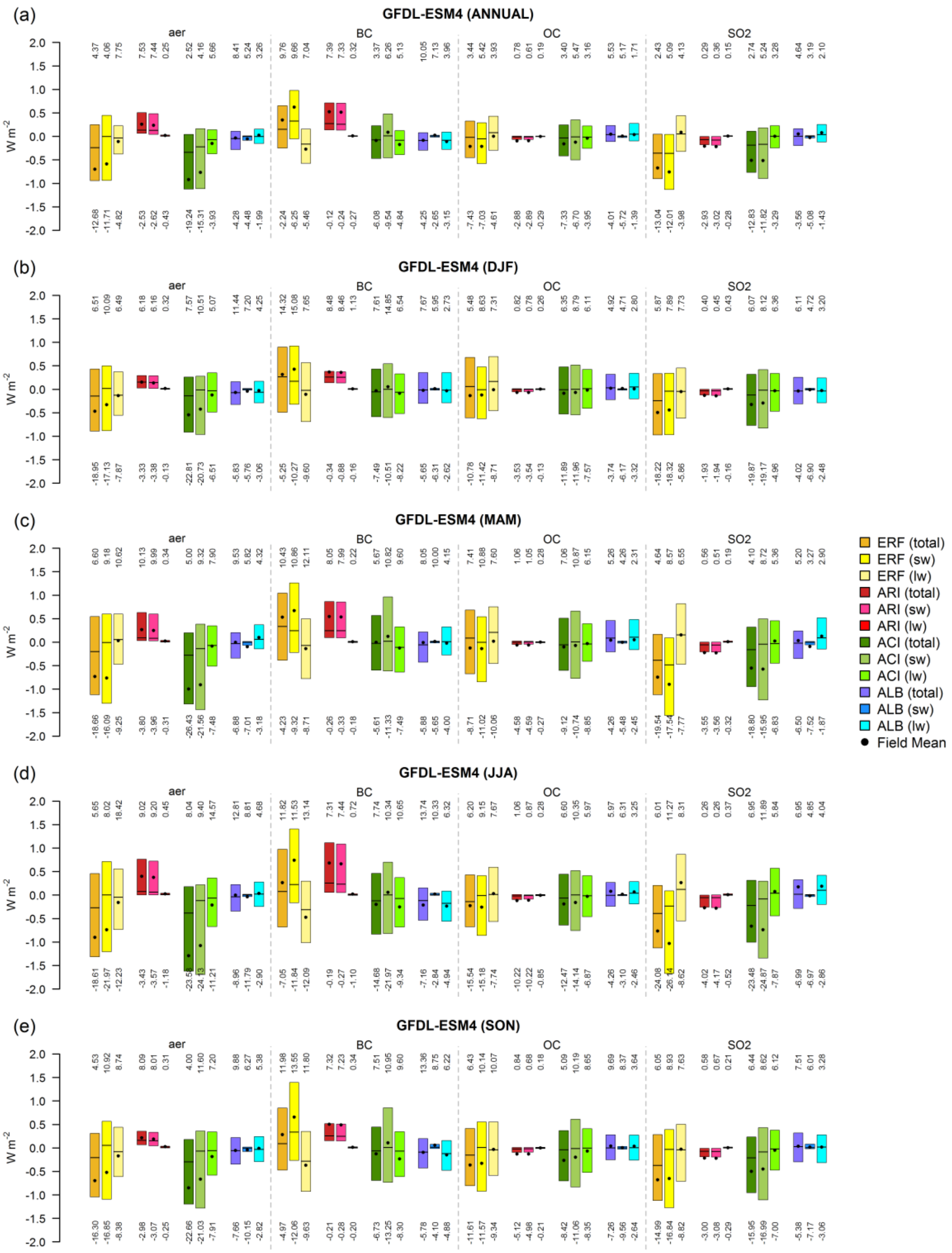

Figure D2. As in Fig. D1, but for GFDL-ESM4.

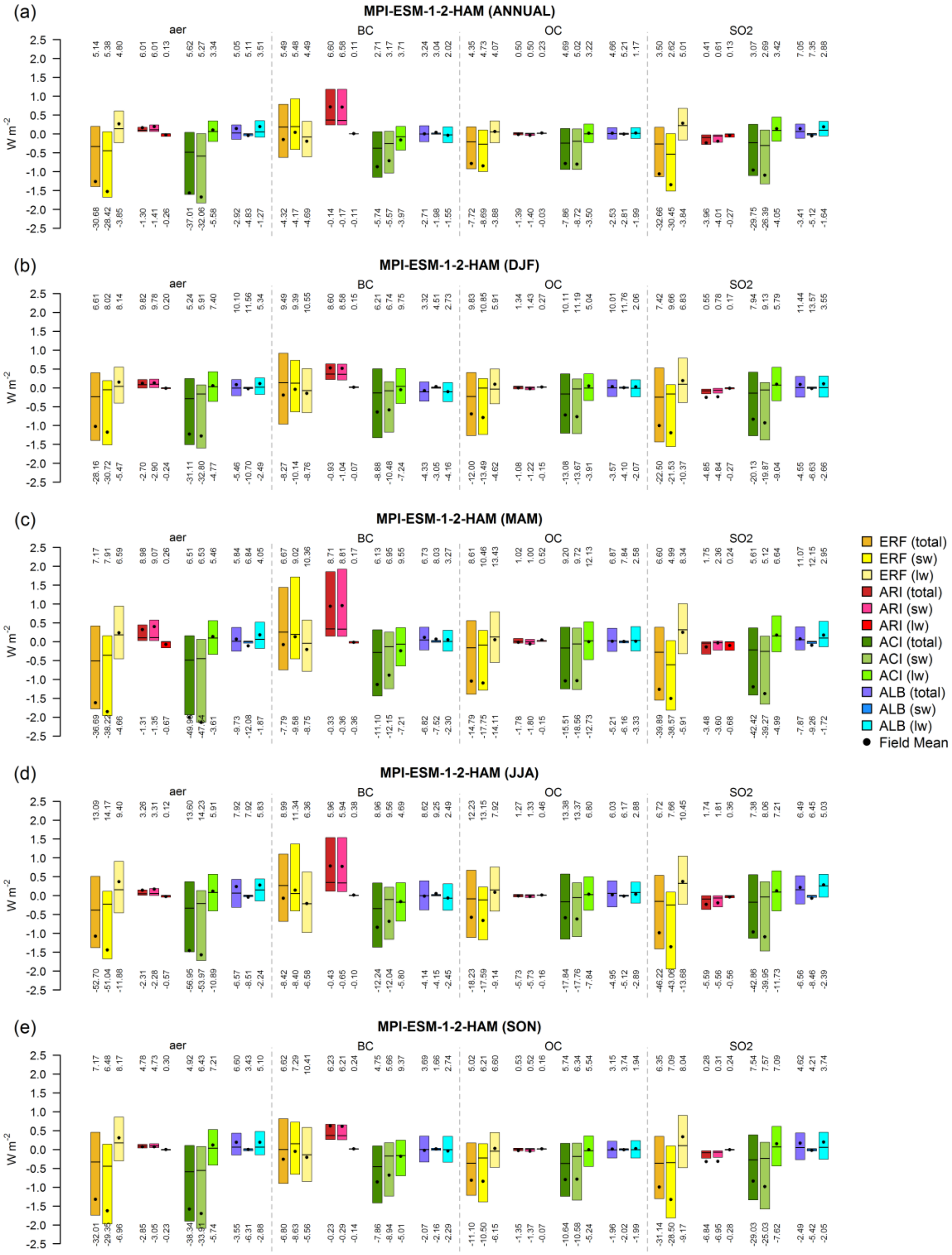

Figure D3. As in Fig. D1, but for MPI-ESM-1-2-HAM.

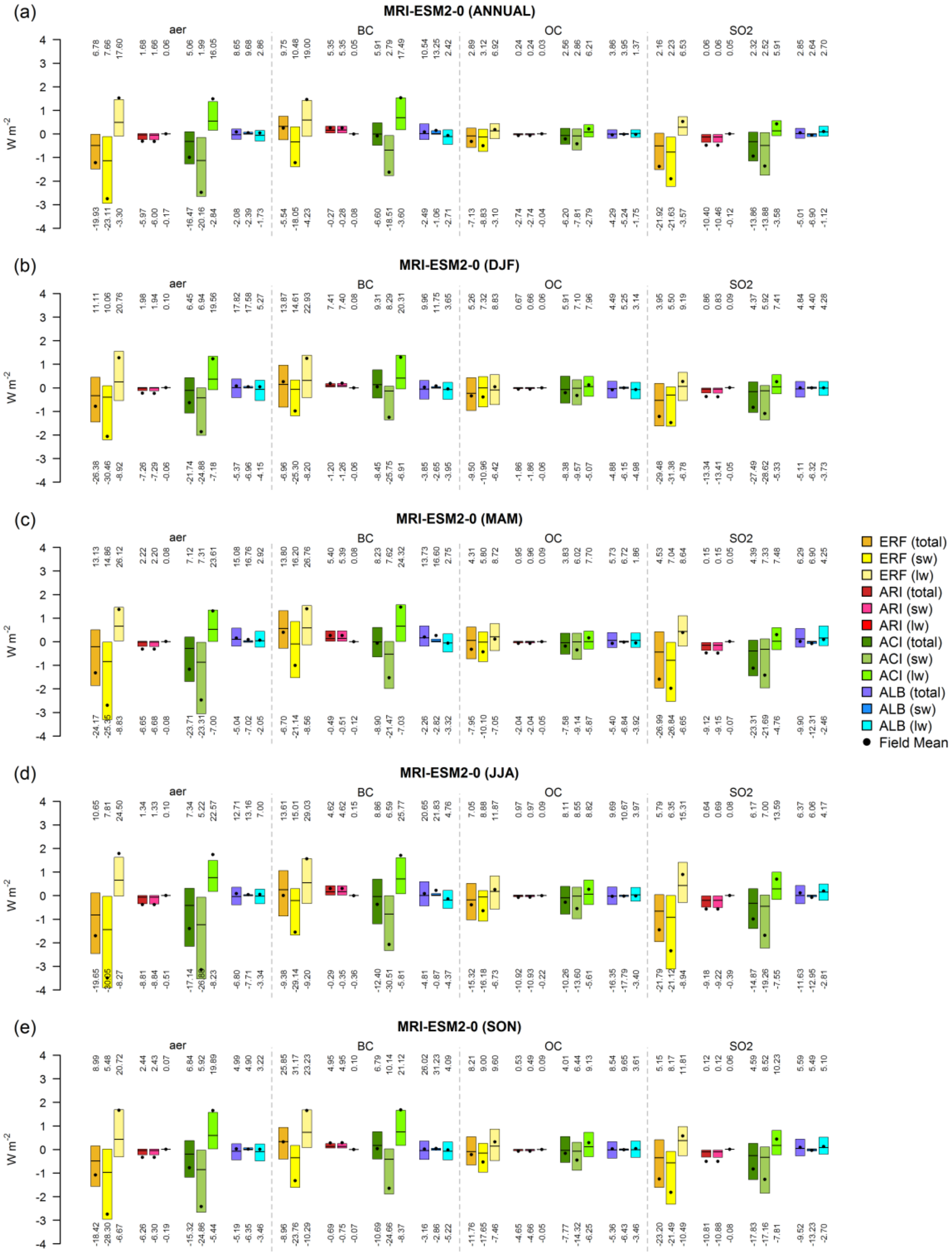

Figure D4. As in Fig. D1, but for MRI-ESM2-0.

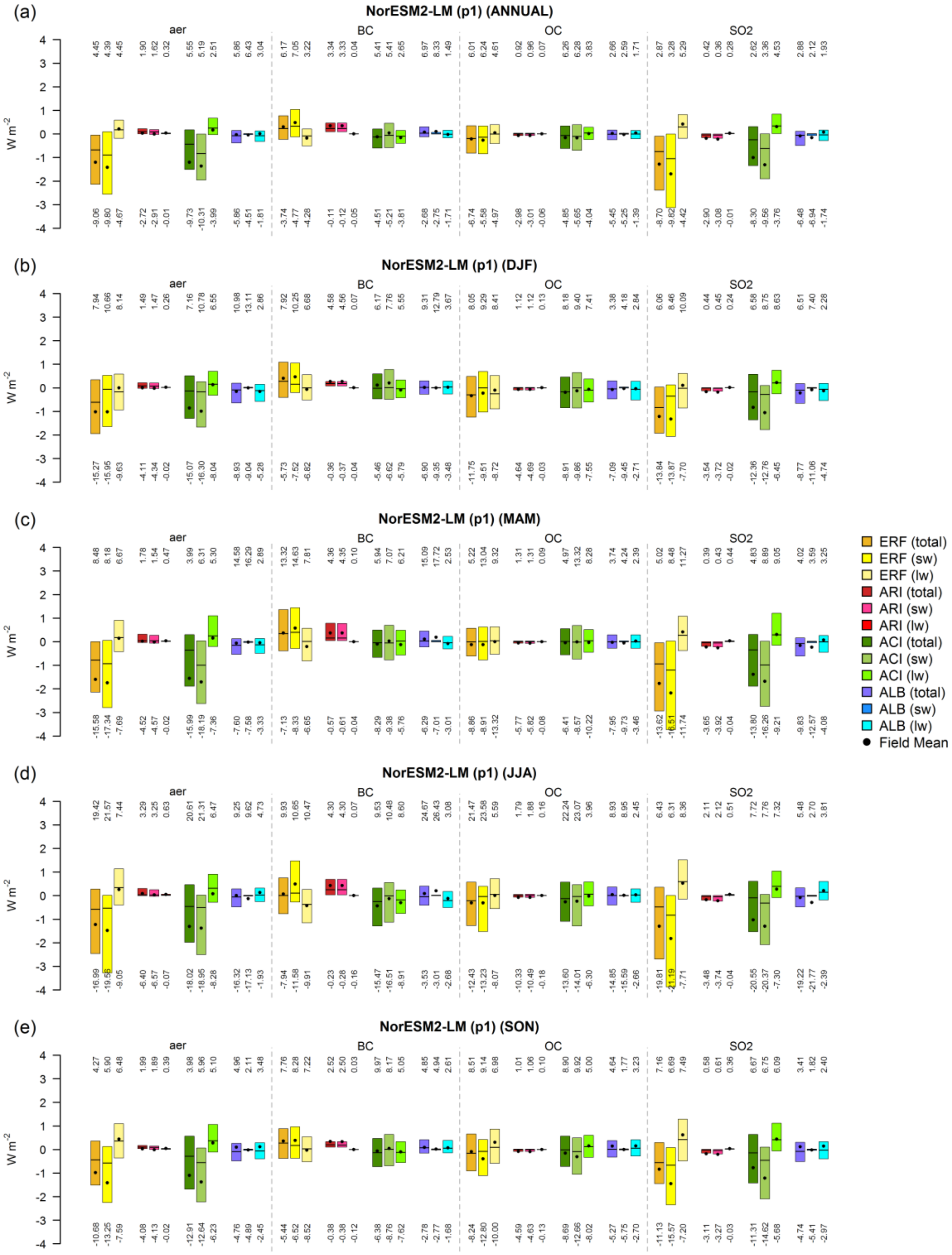

Figure D5. As in Fig. D1, but for NorESM2-LM (p1).

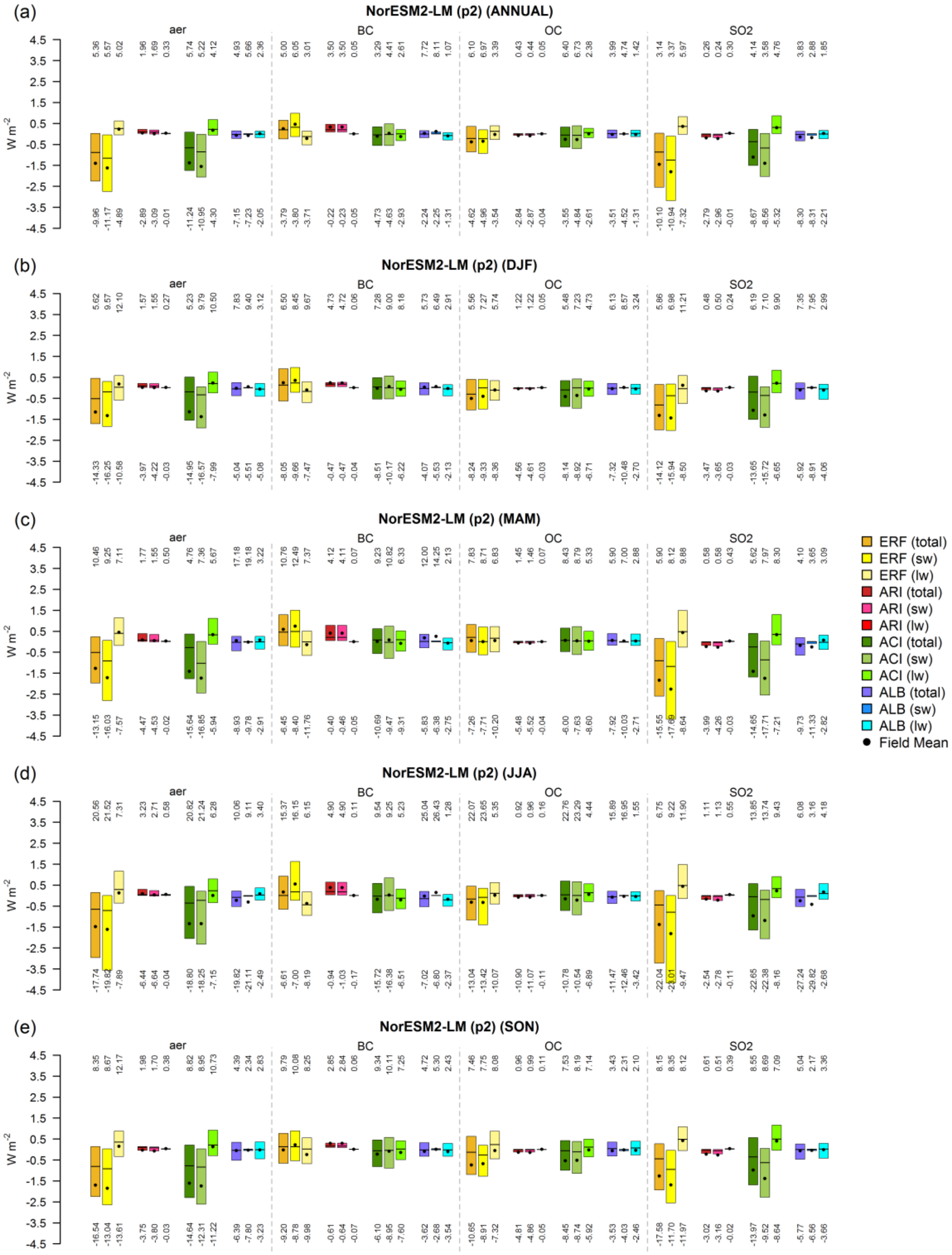

Figure D6. As in Fig. D1, but for NorESM2-LM (p2).

APPENDIX E: Temperature spatial pattern for each model

CNRM-ESM2-1

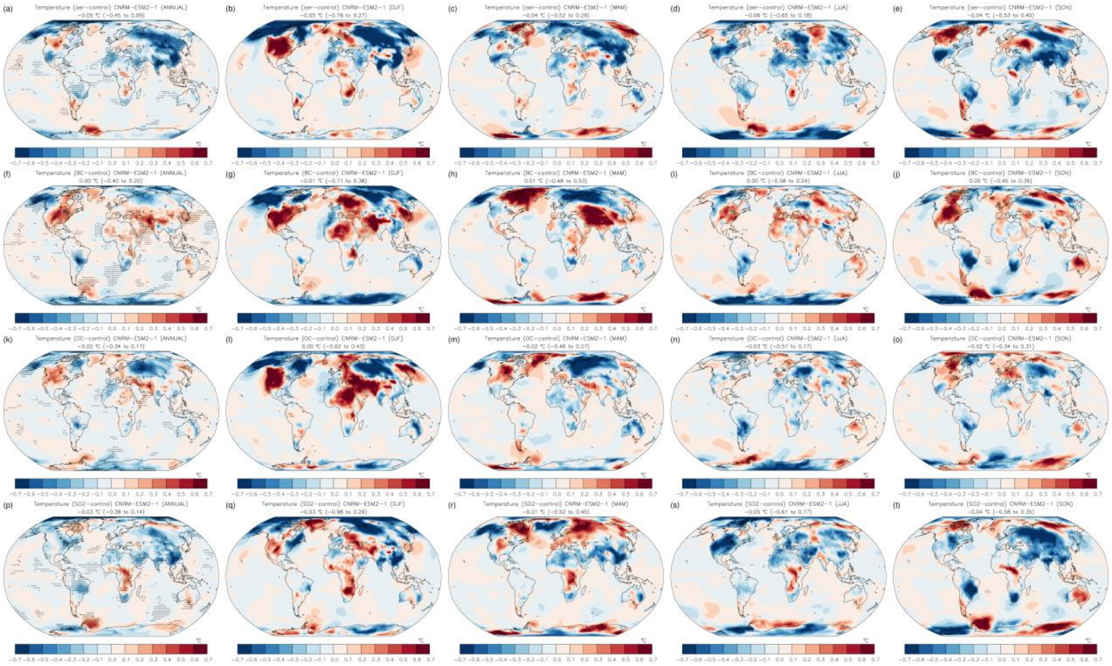

Figure E1. Spatial pattern of the annual (first column), DJF (second column), MAM (third column), JJA (fourth column), and SON (fifth column) global mean surface temperature response in the piClim-aer (first row), piClim-BC (second row), piClim-OC (third row), and piClim-SO_2 (fourth column) experiment for the CNRM-ESM2-1 model. The black crosses indicate the statistically important values in the 95% confidence level. The global field means (5th to 95th percentiles in the parenthesis) are shown in degrees Celsius.

GFDL-ESM4

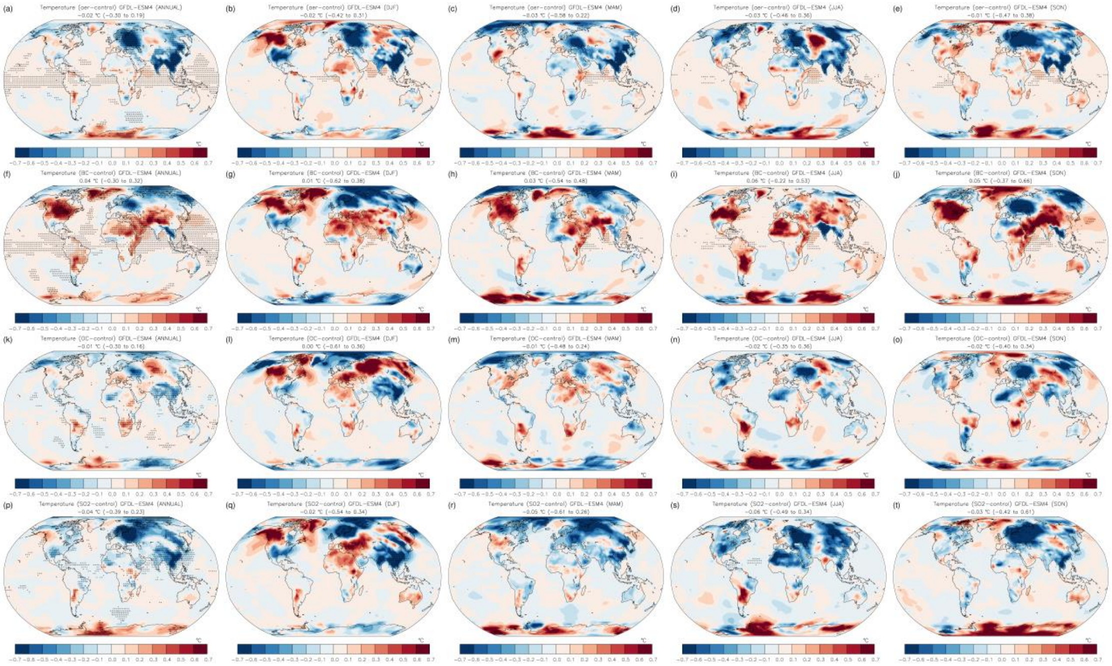

Figure E2. As in Fig. E1, but for GFDL-ESM4.

MPI-ESM-1-2-HAM

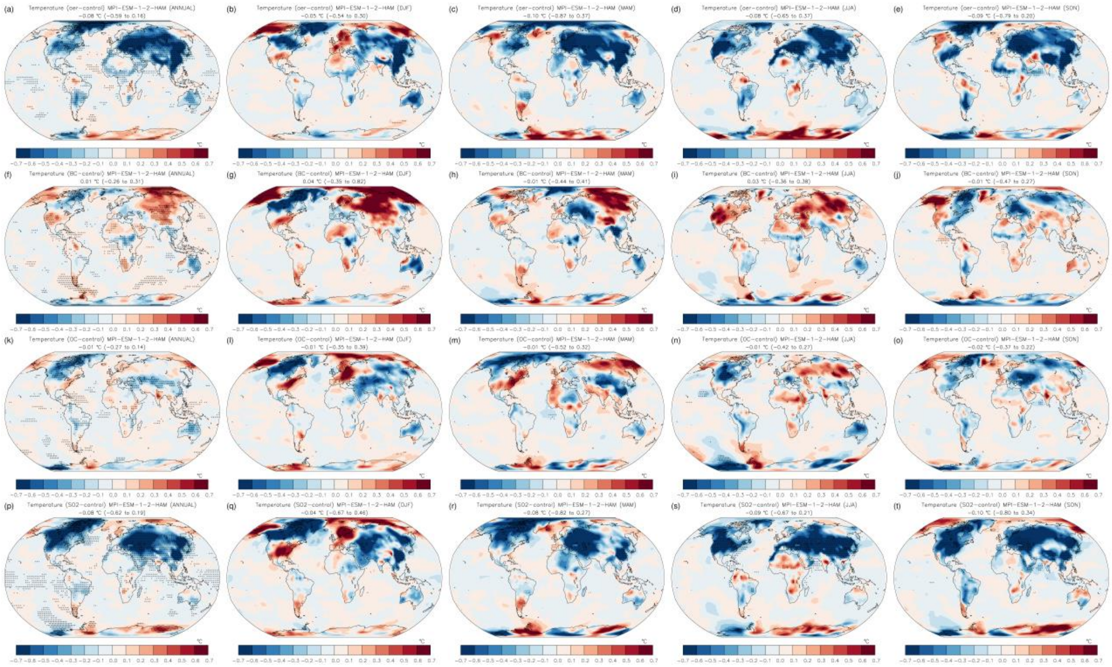

Figure E3. As in Fig. E1, but for MPI-ESM-1-2-HAM.

MRI-ESM2-0

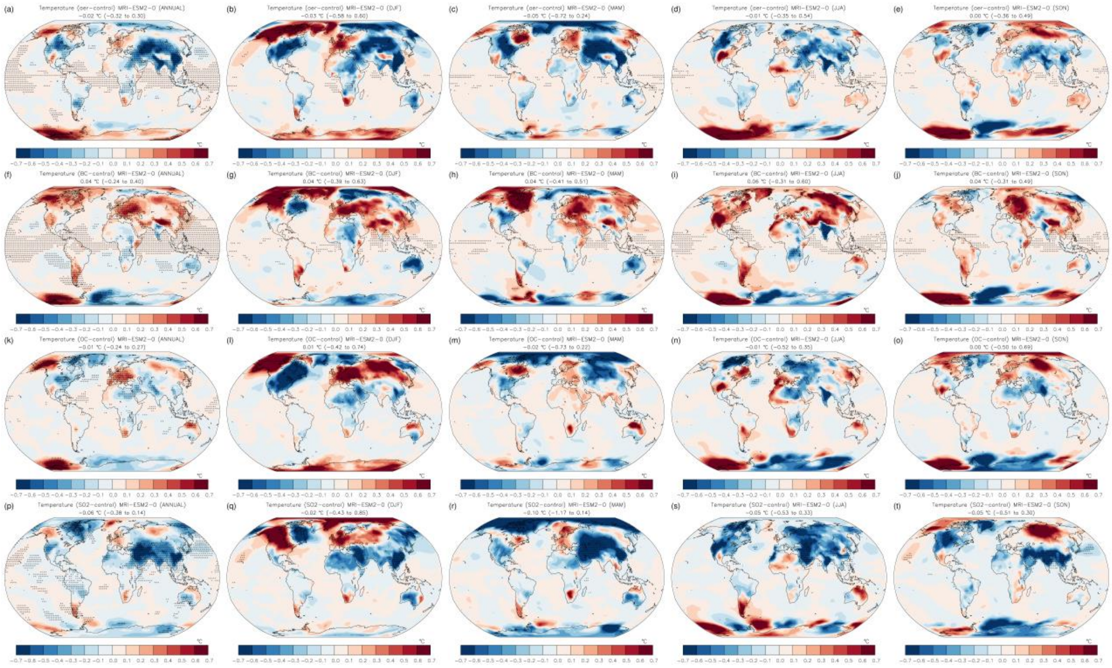

Figure E4. As in Fig. E1, but for MRI-ESM2-0.

NorESM2-LM (p1)

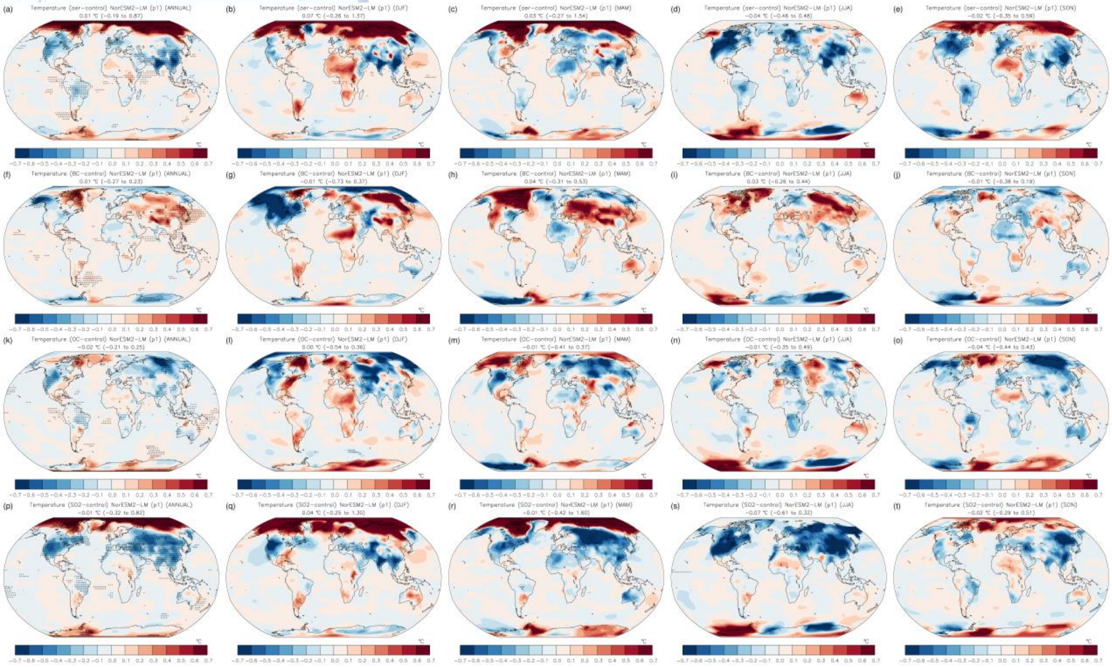

Figure E5. As in Fig. E1, but for NorESM2-LM (p1).

NorESM2-LM (p2)

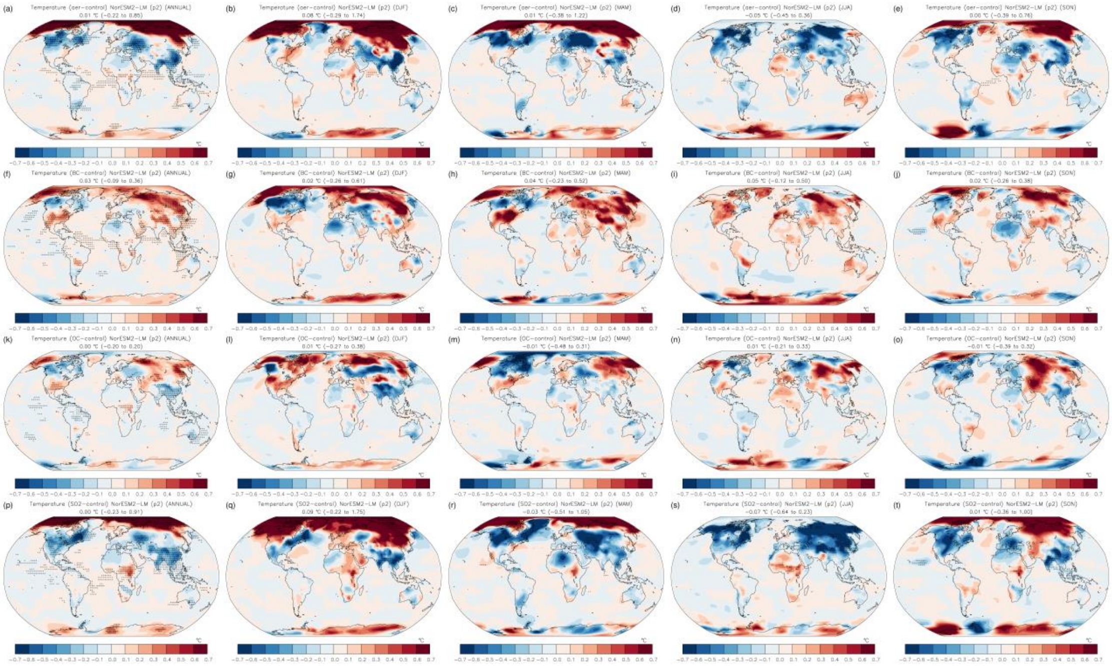

Figure E6. As in Fig. E1, but for NorESM2-LM (p2).